DISS. ETH NO. 27383

PETASCALE SIMULATIONS OF CLOUD CAVITATION COLLAPSE

A dissertation submitted to attain the degree of

DOCTOR OF SCIENCES of ETH ZURICH
(Dr. sc. ETH Zurich)

presented by

FABIAN WERMELINGER
MSc, ETH Zurich

born on 17 June 1983
citizen of Luzern LU, Switzerland

accepted on the recommendation of

Prof. Dr. P. Koumoutsakos, examiner
Prof. Dr. N. A. Adams, co-examiner

2021

To my family

ABSTRACT

The generation of a gaseous bubble, its violent collapse and rebound in a liquid that we believe is almost incompressible is another beauty of nature known as cavitation. The phenomenon appears in a wide range of applications—desired or undesired—where it is observed in arrangements involving not just one but many bubbles, broadly termed cloud cavitation. Experimental and theoretical insights to cloud cavitation are limited due to the spatial and temporal scales as well as the high non-linearity inherent to the physics of cavitation. A remedy is found in recent technological advances of High Performance Computing (HPC) architectures that enable the numerical investigation of this phenomenon.

Past as well as many recent modeling approaches employ complexity reductions to cope with the high cost of fully resolved simulations. The expense of such simplifications are reduced accuracy or even inaccurate predictions of certain dynamics in the multi-phase flow. The first part of this thesis, therefore, develops a computational framework that is designed for large scale stencil computations on recent HPC systems. The framework carefully implements optimizations that enable massively parallel simulations.

The second part of the thesis is devoted to the development of a high throughput, compressible multi-phase flow solver for petascale simulations of cloud cavitation. We simulate the collapse of an unprecedented cloud with 12500 bubbles and perform an extensive analysis of the involved microjet formation and shock wave formation in bubbly liquids. Finally, the technology developed in this thesis is used to perform a parametric study of cloud cavitation collapse with particular emphasis on the kinetic energy allocation within the bubble cloud that is affected by local bubble deformations. The results of the study are further used to asses the limitations of reduced order models commonly used in practice.

v

ZUSAMMENFASSUNG

Die Entstehung von gasartigen Blasen, deren Kollaps und Rückstoss in einer Flüssigkeit, die wir zu glauben pflegen sei praktisch inkomressibel, ist eine weitere Schönheit der Natur, bekannt als Kavitation. Das Phänomen entsteht in einer breiten Reihe von Anwendungen—erwünscht oder unerwünscht—wobei man es ausschliesslich in Anordnungen von mehreren Blasen beobachtet, weitgehend als Wolkenkavitation bezeichnet. Experimenteller als auch theoretischer Zugang zur Wolkenkavitation ist beschränkt möglich aufgrund der involvierten Längen- und Zeitskalen sowohl auch die nicht-lineare Physik der Kavitation erhebliche Schwierigkeiten bereitet. Abhilfe bieten kürzliche Fortschritte in dem Bereich der Hochleistungsrechner (HPC), welche die numerische Untersuchung des Phänomens ermöglichen.

Ältere als auch kürzliche Modellierungsansätze nutzen Vereinfachungen damit die hohen Kosten im Vergleich zu gänzlich aufgelösten Simulationen reduziert werden können. Der Nachteil darin liegt in der reduzierten Genauigkeit oder gar falsche Vorhersagen der dynamischen unbekannten in der Mehrphasenströmung. Der erste Teil dieser Arbeit befasst sich darum mit der Entwicklung von einem Berechnungsmodell, dass spezifisch für die Anwendung von räumlichen Schablonenberechnungen auf heutigen Hochleistungsrechner konstruiert wurde. Das neue Berechnungsmodell implementiert diverse Optimierungen welche schlussendlich hoch parallelisierte Simulationen ermöglichen.

Der zweite Teil der Arbeit beschäftigt sich mit der Entwicklung eines numerischen Lösers für kompressible Mehrphasenströmungen, der für petascale fähige Simulationen der Wolkenkavitation eingesetzt wird. Hierzu simulieren wir eine noch nie dagewesene Wolke mit 12500 Blasen und führen eine umfangreiche Analyse der involvierten Entstehung von Mikrojets und Schockwellen im Blasen-Wassergemisch durch. Zum Schluss verwenden wir die neu entwickelte Technologie für eine Parameterstudie der Wolkenkavitation mit besonderem Schwerpunkt auf die kinetische Energieverteilung in der Blasenwolke, welche von der Deformierung einzelner Blasen beeinträchtigt wird. Im Weiteren benutzen wir die erhaltenen Daten für die Bestimmung der Anwendungsgrenzen herkömmlicher Modelle mit reduzierter komplexität, die oft in der Praxis anzutreffen sind.

ACKNOWLEDGEMENTS

CONTENTS

NOMENCLATURE

Mathematical conventions

$\frac{\mathrm{d}}{\mathrm{d}t}$	Ordinary derivative
$\frac{\partial}{\partial t}$	Partial derivative
∂_j	Index notation for partial derivative with respect to coordinate j
$\frac{\mathrm{D}}{\mathrm{D}t}$	Material derivative $\frac{\partial}{\partial t} + (\boldsymbol{u} \cdot \boldsymbol{\nabla})$
$\dot{f}$	Time derivative of function f
$\bar{f}$	Mean of f
$\tilde{f}$	Non-dimensional quantity f
$\boldsymbol{\nabla} \cdot f$	Divergence
$\boldsymbol{\nabla} f$	Gradient
$f \cdot g$	Inner product
$f \otimes g$	Outer product
f^{T}	Transpose
$\boldsymbol{I}$	Identity tensor
δ_{ij}	Kronecker delta

Numerical conventions

i, j, k	Cell center indices; e. g. $\phi_{i,j,k}$
$i + 1/2$	Face center indices; e. g. $\phi_{i+1/2,j,k}$
$n^x_{i,j,k}$	First component of vector $\boldsymbol{n}$ at given location[1]
$(\cdot)^h_i$	Denotes a numerical approximation; $()_i$ may be omitted
h	Characteristic grid spacing
h_x, h_y, h_z	Grid spacing along x, y and z coordinates, respectively
$\mathcal{C}_i$	Control volume i (same as "cell" i)
$\mathcal{S}_i$	Closed surface on boundary of $\mathcal{C}_i$
$\mathcal{S}_{i+1/2}$	Face on boundary of cell $\mathcal{C}_i$ where $\mathcal{S}_{i+1/2}$ is part of $\mathcal{S}_i$
Δt	Time step size
ϕ^r	Reconstruction of exact variable ϕ
ϕ^n	Time level n of variable ϕ

---

1 Throughout this thesis, the first component x is analogous to the first dimension, the second component y is analogous the second dimension and the third component z is analogous to the third dimension.

V_i	Volume of cell $\mathcal{C}_i$	

Greek symbols

$\boldsymbol{\tau}$	Viscous stress tensor	Pa
Ω	Physical domain	
α_C	Gas volume fraction of bubble cloud	
α_k	Volume fraction of phase k	
β_C	Cloud interaction parameter	
γ_k	Ratio of specific heats in phase k	
γ	Mixture ratio of specific heats	
κ	Curvature	m^{-1}
μ	Mixture dynamic viscosity	Pa s
ν	Mixture kinematic viscosity	$\mathrm{m}^2\,\mathrm{s}^{-1}$
ν_k	Kinematic viscosity of phase k	$\mathrm{m}^2\,\mathrm{s}^{-1}$
ω	Frequency	s^{-1}
ϕ	Shape porosity	
φ	Microjet bulk flow deviation angle	rad
ρ_k	Density of phase k	$\mathrm{kg}\,\mathrm{m}^{-3}$
$\rho_k c_k^2$	Isentropic bulk modulus of phase k	Pa
$\rho_k e_k$	Total energy per unit volume of phase k	$\mathrm{J}\,\mathrm{m}^{-3}$
$\rho_k \varepsilon_k$	Internal energy per unit volume of phase k	$\mathrm{J}\,\mathrm{m}^{-3}$
ρ	Mixture density	$\mathrm{kg}\,\mathrm{m}^{-3}$
ρc^2	Mixture isentropic bulk modulus	Pa
ρe	Mixture total energy per unit volume (also E)	$\mathrm{J}\,\mathrm{m}^{-3}$
$\rho \varepsilon$	Mixture internal energy per unit volume	$\mathrm{J}\,\mathrm{m}^{-3}$
$\rho \varepsilon_\sigma$	Capillary potential energy per unit volume	$\mathrm{J}\,\mathrm{m}^{-3}$
σ	Surface tension coefficient	$\mathrm{N}\,\mathrm{m}^{-1}$
θ	Microjet inclination angle	rad

Latin symbols

$\boldsymbol{D}$	Deformation rate tensor	s^{-1}
$\boldsymbol{T}$	Capillary stress tensor	Pa
$\boldsymbol{m}$	Approximation to surface normal vector $\boldsymbol{n}$	
$\boldsymbol{n}$	Surface normal vector	
$\boldsymbol{u}$	Velocity vector	$\mathrm{m}\,\mathrm{s}^{-1}$
$\boldsymbol{u}_{\mathrm{tip}}$	Microjet velocity vector	$\mathrm{m}\,\mathrm{s}^{-1}$
$\boldsymbol{x}$	Position vector	m

x_B	Coordinate for bubble center of mass	m
x_C	Coordinate of cloud center	m
$E = \rho e$	Mixture total energy per unit volume	$\mathrm{J\,m^{-3}}$
L	Length	m
N	Number of countable entities	
R	Radius	m
R_F	Radial wave position	m
$\dot{R}_F$	Radial wave propagation speed	$\mathrm{m\,s^{-1}}$
T_k	Temperature of phase k	K
V	Volume	$\mathrm{m^3}$
c_k	Speed of sound in phase k	$\mathrm{m\,s^{-1}}$
c	Mixture speed of sound	$\mathrm{m\,s^{-1}}$
d	Distance; shock thickness	m
p	Pressure (also for mixture)	Pa
$p_{c,k}$	Correction pressure for phase k	Pa
p_c	Mixture correction pressure	Pa
$r = |x|$	Radial distance	m
s_k	Specific entropy of phase k	$\mathrm{J\,kg^{-1}\,K^{-1}}$
t	Time	s
t_C	Cloud collapse time (minimum gas volume)	s
v_k	Specific volume of phase k	$\mathrm{m^3\,kg^{-1}}$

Superscripts

DK	Doinikov
KM	Keller-Miksis
a	Advective phenomena
d	Diffusive phenomena
(i)	Iteration
h	Numerical approximation
r	Reconstructed value
res	Resolved 3D simulation
$*$	Characteristic state or value
n	Time level

Subscripts

0	Initial state
1	Index of the less compressible phase (liquid)

2	Index of the more compressible phase (gas)
B	Bubble
C	Cloud of bubbles
F	Wave front
I	Interface
L	Left state
R	Right state
avg	Average value for a set of entities
imp	Microjet impact on opposite wall of bubble
ijk	Tensor indices[2]
k	Phase index
kin	Kinematic
max	Maximum element in a set of entities
min	Minimum element in a set of entities
tip	Microjet tip location

Dimensionless numbers

Ma	Mach number
Oh	Ohnesorge number
Re	Reynolds number
We	Weber number

Acronyms

1D	One-Dimensional
2D	Two-Dimensional
3D	Three-Dimensional
AMR	Adaptive mesh refinement
ANL	Argonne National Laboratory
AoS	Array of structures
API	Application Programming Interface
AVX	Advanced Vector Extensions
BGQ	BlueGene/Q
C/T	Compute/Transfer
CFD	Computational Fluid Dynamics

---

2 The distinction between the phase index k and usage of a tensor component indexed with k should be clear from the context. The summation convention is assumed for indices that appear in pairs: $a_{jk}b_k = \sum_k a_{jk}b_k$.

CFL	Courant-Friedrichs-Lewy
CPU	Central Processing Unit
CSCS	Swiss National Supercomputing Center
Cubism	Cube-based stencil framework for structured grids
CUDA	Compute Unified Device Architecture
D2H	Device to host
DK	Doinikov
DLP	Data-level parallelism
DMA	Direct memory access
DNS	Direct numerical simulation
DOD	Data-oriented design
ECC	Error correcting code
ENO	Essentially-Non-Oscillatory
EOS	Equation of state
FMA	Fused multiply-add
FVM	Finite Volume Method
GPU	Graphics Processing Unit
H2D	Host to device
HLL	Harten-Lax-van Leer
HLLC	Harten-Lax-van Leer-Contact
HPC	High Performance Computing
HT	Intel Hyper-Threading Technology
I/O	Input/output
ILP	Instruction-level parallelism
ISA	Instruction set architecture
IVP	Initial value problem
KM	Keller-Miksis
LLC	Last level cache
LSRK3	Low-storage 3rd-order Runge-Kutta
MLMC	Multi-level Monte Carlo
MPI	Message Passing Interface
MPMD	Multiple program multiple data
MUSCL	Monotonic Upstream-centered Scheme for Conservation Laws
NS	Navier-Stokes
OCN	On-chip network
ODE	Ordinary Differential Equation
OI	Operational intensity

OOP	Object-oriented programming
OpenMP	Open Multi-Processing
PCIe	Peripheral component interconnect express
PDE	Partial Differential Equation
PDF	Probability density function
PID	Proportional-integral-derivative
PPM	Piecewise Parabolic Method
QPX	Quad Processing eXtensions
REA	Reconstruct/Evolve/Average
RK	Runge-Kutta
RKV	Runge-Kutta-Verner
RMS	Root-Mean-Square
RP	Rayleigh-Plesset
SAN	System area network
SFC	Space filling curve
SGEOS	Stiffened gas equation of state
SIMD	Single instruction multiple data
SIMT	Single instruction multiple threads
SMP	Symmetric multi-processing
SoA	Structure of arrays
SPMD	Single program multiple data
SSE	Streaming SIMD Extensions
TLP	Thread-level parallelism
TtS	Time to solution
TVD	Total Variation Diminishing
UQ	Uncertainty quantification
VOF	Volume of fluid
WENO	Weighted Essentially-Non-Oscillatory

1

INTRODUCTION

> *Hope is not the conviction that something will turn out*
> *well but the certainty that something makes sense,*
> *regardless of how it turns out.*
>
> — Václav Havel

Collapsing and interacting bubbles are encountered in a variety of industrial and scientific applications ranging from cavitation phenomena associated with engineering devices, such as marine propellers, hydroelectric turbines and fuel injectors (Escaler et al., 2006; Kumar et al., 2010; Mitroglou et al., 2017; Örley et al., 2015), to non-invasive biomedical procedures, for instance, dental cleansing, kidney stone lithotripsy, drug delivery and tissue ablation histotripsy (Coussios et al., 2008; Ikeda et al., 2006; Xu et al., 2008). An overview of applications in medicine that are based on cavitation is found in Brennen (2015).

In practice, the phenomenon of cavitation is observed in arrangements of multiple bubbles, referred to as a cloud of bubbles in the following. It is well known that the destructive potential of cavitation—amplified when bubbles interact with each—causes material erosion or tissue damage which is the main property of its utility in the aforementioned applications, either mitigated (Gonzalez-Avila et al., 2020) or harnessed. The thorough understanding of cavitation is therefore fundamental for its efficient exploitation and control. Past experimental studies have contributed extensively to this effort. The length scales associated with typical bubble clouds is in the order of millimeters which poses serious challenges to manufacturers of measurement devices. Furthermore, the time scale associated to the collapse of such clouds is in the order of microseconds, which requires high temporal resolution and often expensive high-speed cameras. Consequently, many such experimental studies provide results on the macroscopic scale of the cloud and rather diffuse interpretations of microscopic quantities. Only the recent study of Bremond et al. (2006) achieved a reproducible experimental setup for Two-Dimensional (2D) cloud cavitation collapse. Furthermore, Obreschkow et al. (2011) provided experimental insight for the microjet

formation in a single collapsing bubble by conducting the investigation by means of parabolic flights.

Similar to experimental studies, numerical investigations of cloud cavitation have contributed equally to the understanding of the phenomenon. Arriving at a computer informed conclusion, however, imposes similar difficulties as already encountered for the experimental conduct. Cavitation is one of the richest phenomenons that arise in fluid mechanics. For one, cavitation involves multiple phases which have to be modeled somehow. Multiple phases, in general, means multiple materials for which separate constitutive laws must be used to obtain the thermodynamic states of the materials, or fluids in our case. These laws are highly non-linear and, again, must be determined empirically. A second difficulty of cavitating flows is that its governing equations allow for discontinuous solutions. Those discontinuities emerge in the form of shock waves and, if combined with multiple fluids, such waves propagate in flow regions where the acoustic impedance can be orders of magnitudes apart within a small region in space. Detailed numerical modeling of this broad physical spectrum can become expensive, both computationally and economically. Past and present numerical studies therefore employ simplifications that reduce this burden, which on the other hand produces numerical results that represent a blurred reality. Research in mathematical models and numerical methods for compressible multi-phase flows is an active field of research (Saurel and Pantano, 2018) which is one of the reasons why no standard model has established for this particular flow problem. A part of this thesis, therefore, addresses the numerical investigation and performance of a recent model for compressible multi-phase flows that has not yet been applied to cloud cavitation collapse.

Manufacturing processes of contemporary computer architecture has progressed to the point where the transistor size on the die is only that of about 25 silicone atoms (5 nm technology). Transistor densities are therefore reaching the physical limit and Moore's law will cease to be valid. Instead, the breadth is exposed by increasing hardware parallelism. This introduces an efficiency gap (Cameron et al., 2005) because parallelism can not be exploited efficiently without considering certain design principles in the software development stage. Understanding those principles requires understanding of individual hardware components that bond together data flow paths and control flow paths. The former is the foundation of all programs, whose sole purpose is to transform data. The latter is guided by algorithms that eventually solve a problem. Efficient programs employ

design principles that ensure best interplay between the two. Most often algorithms can be divided into smaller parts. The smaller pieces furthermore employ operations that are common between parts, but operate on different data paths. The computational framework developed in this thesis aims to provide tools that perform such operations on the high-level and implement the aforementioned design principles for HPC on the low-level hidden from the caller. The envisioned outcome of this effort is to narrow the efficiency gap in today's computing landscape, improve exploitation of economical value and ensure readiness for next generation compute architectures.

1.1 STRUCTURE AND SUMMARY OF CONTRIBUTIONS

The work in this thesis presents a computational framework specifically developed for HPC architectures targeting large scale compressible multiphase flows problems with application to cloud cavitation collapse including unprecedented simulations of clouds with $O(10000)$ bubbles. The presented computational framework has been generalized such that it is not limited to compressible multi-phase flows only and aims to offer its optimized computational tools to the broader scientific community that is exposed to large scale problems. A list of publications is appended to this thesis.

Chapter 2: Physics of cloud cavitation collapse

This chapter provides a brief introduction of the physics involved in cloud cavitation. An extensive literature body exists for the study of single bubble cavitation. On the other hand, a much smaller theoretical understanding for the collapse of many nearby bubbles in cloud cavitation is available today. Moreover, our understanding is mostly limited to the analysis of linearizations that are valid only for weak pressure perturbations and small degrees of bubble-bubble interactions. Nevertheless, these simplified views provide valuable understanding of the physical phenomena which are used extensively in the remaining chapters of the thesis and aid in the analysis of the highly non-linear phenomenon of cloud cavitation collapse by means of numerical simulation.

Chapter 3: Governing equations

This chapter introduces the compressible multi-phase flow model used for the large scale simulations performed in this thesis. The model equations consist of a variation of the general non-equilibrium multi-phase flow model introduced by Baer et al. (1986). We then reformulate the model used in Hejazialhosseini, Rossinelli, et al. (2012) and extend it by an improved limit case of the general non-equilibrium model. The new model is further extended with viscous and capillary stresses. The chapter concludes with the discussion of appropriate numerical methods for the solution of the hyperbolic balance laws that arise in multi-phase flow problems.

Chapter 4: Software design

A program consists of algorithms and data structures. This chapter is concerned with the data structures used in the software design of the computational framework developed in this thesis. The core design principles for stencil based applications are discussed in detail and special emphasis is given on high memory bandwidth utilization, the main bottleneck of computing architectures today. The new framework is designed such that temporal and spatial locality of the data is utilized efficiently by the low-level computational kernels that perform the work. Furthermore, the data structures are designed such that vectorized Central Processing Unit (CPU) instructions can be exploited efficiently. Implementations of such optimized kernels are provided as a black box to the library user, who is mainly concerned with algorithm and application development. Finally, advanced HPC architectures consist of compute accelerators such as Graphics Processing Units (GPUs). These accelerators are designed for massive data-level parallelism (DLP) which is non-trivial to exploit efficiently in stencil codes. With this in mind, a heterogeneous CPU/GPU algorithm is designed that is capable to exploit the faster memory bandwidth on GPU architectures. The algorithm is evaluated with a benchmark for the solution of approximate Riemann problems.

Chapter 5: Model validation

This chapter provides validation cases for individual features of the extended multi-phase model. In particular, superior resolution of velocities

at interfaces is demonstrated and compared to the existing literature. It is further shown that the multi-phase heritage of the new model is capable of generating an almost pure gas phase from a liquid that is homogeneously mixed with a small amount of gas. A feature that can not be captured by the previous work in Hejazialhosseini, Rossinelli, et al. (2012). The modeling of the stress tensor is validated by a range of test cases that address capillary waves of various amplitude as well as a compressible turbulent channel flow for the validation of viscous dissipation and incorporation of no-slip boundary conditions.

Chapter 6: Parametric study of cloud cavitation collapse

This chapter provides data and analysis of fully resolved Three-Dimensional (3D) numerical simulations for cloud cavitation collapse, where the simulation cases are parametrized by the forcing pressure, the degree of bubble-bubble interaction and the length scale of the cloud. To the best of the authors knowledge, a systematic parameter study of this kind is currently not found in the literature. The considered number of bubbles ranges from 5 to 630 for which reduced order models with bubble-bubble interactions are typically used in industrial applications. The gathered simulation data is therefore applied to assess the performance of two reduced order models with particular emphasis on bubble deformation and its effect on translational bubble motion during collapse. The former is not accounted for in any of the two simplified models, while the latter is modeled by one of the two. It is shown that modeling bubble translation leads to an improved prediction of the collapse time for individual bubbles. Furthermore, strong bubble deformation caused by microjet penetration decelerates linear bubble motion after pierce through, which in turn leads to a reduced energy requirement for liquid mass displacement in the bubble cluster. The excess energy resulting from this process is released in the form of larger pressure peaks. Due to the inherent spherical collapse of bubbles in the employed reduced order models, it is shown that deceleration of bubbles does not take place which leads to incorrect energy allocations between translational motion and radial interface motion, and eventually wrong predictions for observed peak pressures.

Chapter 7: Large scale simulation of cloud cavitation collapse

Here we present unprecedented simulations of cloud cavitation collapse utilizing clouds with $O(10000)$ bubbles, two orders of magnitude larger than what is currently reported in the literature. The obtained simulation results allow to study the involved dynamics on the macroscopic scale of the cloud, as well as local dynamics at the scale of the bubble radii. The analysis of the data reveals the formation of a bubbly shock wave at the outskirts of the cloud with propagation speed slightly higher than what is predicted by simpler homogeneous models. The computed leading front of the bubbly shock is shown to be in agreement with experimental results while larger attenuation is found downstream of the shock in case of radial propagation in spherical clouds. Microjet data for individual bubbles is quantified by statistical analysis, where a dependence of microjet strength on the radial bubble position was established. The orientation of microjets in collapsing bubbles is of particular interest for mitigating the erosion effects that follow from jet impact on solid surfaces and is actively researched (E.-A. Brujan, Noda, et al., 2018; E.-A. Brujan, Takahira, et al., 2019; Kiyama et al., 2020; Molefe et al., 2019; Onuki et al., 2018; Tagawa et al., 2018). The present simulations reveal that microjet orientation in cloud cavitation depends on the size and distribution of neighboring bubbles, resulting in scattered jet focusing in the cloud center with localized peaks that confirm the experimental observations reported in Hansson et al. (1980).

PHYSICS OF CLOUD CAVITATION COLLAPSE

It is not easy to become an educated person.
— Richard Hamming

This chapter reviews the theoretical aspects of the involved physics in cloud cavitation collapse. The research history of cavitating liquids is briefly summarized, followed by discussions of the additional physics for multiple bubbles in close vicinity to each other. The mutual interactions exerted in these configurations influence the collapse dynamics of individual bubbles and also the collective cloud dynamics. The chapter concludes with a scaling analysis that relates the spatiotemporal scales in cavitating bubble clouds and bubbly shock waves.

2.1 EARLY THEORY OF CAVITATION

One of the earliest formulation of a problem involving a collapsing cavity in an infinite and incompressible liquid was given in Besant (1859). Later Rayleigh (1917) proposed a solution to this problem by using conservation principles to derive

$$\frac{p_B(t) - p_\infty(t)}{\rho_1} = R_B \ddot{R}_B + \frac{3}{2} \dot{R}_B^2 + \frac{4\nu_1}{R_B} \dot{R}_B + \frac{2\sigma}{\rho_1 R_B}, \qquad (2.1)$$

known as the Rayleigh-Plesset equation.[1] The first two terms on the right-hand side are inertia terms obtained from the momentum equation in radial coordinates and the last two terms describe viscous and surface tension effects at the bubble interface. The equation is balanced by dynamic pressure forces acting on the bubble interface whereas ρ_1 and ν_1 are the density and kinematic viscosity of the liquid, respectively. Its solution describes the temporal evolution of a spherical bubble with radius $R_B(t)$ provided that the pressure $p_B(t)$ inside the bubble is known (Brennen, 2013). Although highly non-linear, equation 2.1 incorporates the assumptions of

---

1 Lord Rayleigh's solution assumed $p_B(t) = 0\,\text{Pa}$ and considered only the two inertia terms on the right-hand side.

an incompressible liquid, perfect sphericity of the bubble at all times and no mass transfer across the interface.

Given these limitations, various modifications of equation 2.1 have been proposed in the literature (Gilmore, 1952; Keller et al., 1980; Plesset and Prosperetti, 1977; Plesset, 1949). Most notably the work of Gilmore (1952) considered 2nd-order compressibility terms that account for losses in the bubble energy due to pressure wave radiation. Later Keller et al. (1980) proposed an extended model for large amplitude perturbations. To date, these models are still extensively used to solve various problems in single-bubble or multi-bubble cavitation. Moreover, these One-Dimensional (1D) models are often the building blocks in more sophisticated higher order modeling approaches.

2.2 BUBBLE-BUBBLE INTERACTIONS

2.2.1 *Bjerknes forces*

In the early work of Bjerknes (1906) and his father, the interaction of expanding and contracting bodies submerged in an incompressible liquid is described by analogy of charged particles for which the field of force is given by the principle of superposition. One key difference, however, is that a submerged object in a liquid can not expand or contract indefinitely. Hence, the analogy of "charge" in a hydrodynamic field is attributed to periodic oscillation in radial or translational direction. By this simple analogy, it is shown that a hydrodynamic field exhibits similar geometric properties than that of an electric or magnetic field. Their reasoning is based on the notion of a vector field at a surface of separation, where flux, field intensity and inductivity are brought in relation with velocity, specific momentum and mobility, respectively. The latter corresponds to specific density and is thought of as the "readiness" of matter to take motion. Since the specific volume is the inverse of density, the density then is a measure of inertial resistance. For example, a spherical object with high mobility submerged in a container of water is much more willing to adapt the motion of the surrounding water than the same object with low mobility. In their work, they define kinematic buoyancy as the product of the liquid mass displaced by an object submerged in the liquid times the acceleration of the object. By this definition, they find an analogy to the Archimedean principle which states that: *any body that participates in the translatory motion of a fluid is subject*

to a kinematic buoyancy (or force) that is equal to the liquid mass displaced by the body times the acceleration of the translatory motion. Assuming two spherical bodies in an incompressible liquid, both exhibit radial oscillation and are separated at a distance *r*, if they oscillate in phase they produce field lines similar to those in a magnetic field with two poles of the same sign. Conversely, if they oscillate out of phase the field lines correspond to those of a magnetic field with poles of opposite sign. The argument is then further extended to ask the question whether a hydrodynamic field exhibits similar dynamical properties than that in an electrodynamic field. Indeed they find striking similarity with Coulomb's law in which the hydrodynamic case only differs by sign inversion. Bjerknes (1906) then formulates laws of two kinds:

PRIMARY BJERKNES FORCES act on a single bubble in an oscillating pressure field if the volume change of the bubble is non-zero over some period.

SECONDARY BJERKNES FORCES act between two oscillating bubbles and is proportional to the product of the oscillation amplitudes and inversely proportional to the square of the distance between the bubbles. Bubbles that oscillate in phase attract each other; bubbles that oscillate out of phase repulse each other.

The instantaneous Bjerknes force is given by

$$F = -V_B \nabla p, \tag{2.2}$$

where $V_B(t)$ is the volume of the bubble and ∇p is the pressure gradient along the bubble surface. The resultant force is obtained from a time averaging filter applied to equation 2.2 (Leighton et al., 1990). These simple relations further explain why small bubbles with large mobility accumulate at the anti-nodes in a standing oscillating pressure field and, vice versa, large bubbles with small mobility accumulate at pressure nodes in the same field (Crum, 1975; Crum and Eller, 1970; Mitome, 2003).

2.2.2 *Microjet formation in a cloud of bubbles*

In general, microjet formation may not necessarily be initiated due interaction with nearby bubbles. For example, both a single bubble near a wall or a shock induced bubble in the free field collapse non-spherically. Studying the temporal evolution of such collapsing cavities, it is observed that one side of the bubble begins to form a dent from which a microjet

emerges and eventually penetrates through the bubble (Benjamin et al., 1966; Obreschkow et al., 2011; Plesset and Prosperetti, 1977). The mechanism of microjet formation is explained by equation 2.2. In presence of a wall or a pressure shock, a pressure gradient exists that points away from the wall or from the pre-shocked fluid to the post-shocked fluid, respectively. Initially the change in volume of the bubble is small if we assume it is in equilibrium with the surrounding fluid at time $t = 0$ s. The slight imbalance of pressure along the bubble surface causes small variations in volume which, by equation 2.2, results in a force at the bubble surface acting in the opposite direction of the pressure gradient. This initially generates a small dent that further induces change in volume and amplifies the acting force. The process accelerates the bubble interface towards the wall or in direction of the pressure shock, respectively, and results in the formation of the microjet.

The same phenomenon is observed in a collapsing cloud of bubbles. In the context of this thesis, these clouds are forced to collapse by a higher pressure in the liquid far-field. For the sake of argument we assume this forcing pressure is constant. Since there is no pressure gradient, why do bubbles form a microjet? The reason is the presence of other bubbles that are close by to each other. The many nearby bubbles cause a change of the acoustic impedance in the bubbly mixture that generates a "shielding" effect in the bubble collective. This shielding effect indeed induces a pressure gradient across the first few (depending on the number density of bubbles) layers of bubbles at the outskirts of the cloud. The strength of this gradient depends on the distance between neighboring bubbles and on the magnitude of the forcing pressure in the far-field. The direction of the gradient points from the inside of the cloud into the pure liquid and the same mechanism of microjet formation takes place as discussed for the cases above. Because of the geometrical arrangement and the shielding effect of the bubbles in the cloud, individual spherical "layers" of bubbles do not collapse simultaneously. This gives rise to the formation of a shock wave in the bubbly medium, which amplifies as it propagates from the outskirts of the cloud towards the cloud center. This phenomenon is investigated further by means of numerical simulation in the later chapters 6 and 7 of this thesis.

In the following work, the geometrical description of a microjet associated to a bubble i is based on the sketch shown in figure 2.1. The center of mass of the bubble at any time instant is denoted by $x_{B,i}(t)$ and the center of the bubble cloud is denoted by x_C. The vector $x_C - x_{B,i}(t = 0)$ points to the cloud center and provides a reference for the initial orientation of the
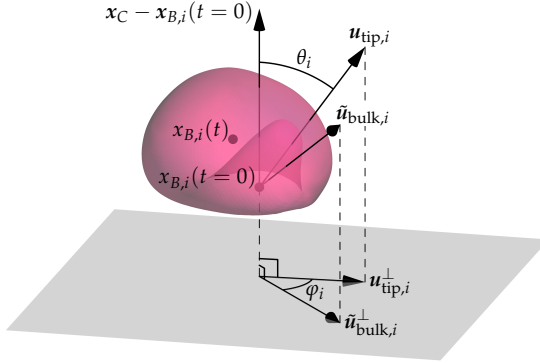
FIGURE 2.1: Microjet orientation in space: $u_{\text{tip},i}$, microjet tip velocity; $\tilde{u}_{\text{bulk},i}$, bulk velocity indicator. Projections onto a plane perpendicular to the radial direction: $u_{\text{tip},i}^{\perp}$, projection of microjet tip velocity; $\tilde{u}_{\text{bulk},i}^{\perp}$, projection of bulk velocity indicator.

bubble. At a time t the direction of the microjet is defined by its velocity vector $u_{\text{tip},i}$ computed from the initial center of mass and the coordinate of minimum curvature on the surface in the microjet pit. Its magnitude $|u_{\text{tip},i}|$ corresponds to the speed at the location of minimum curvature. The deviation of the microjet from the reference vector is quantified by the inclination angle θ_i.

Larger bubbles have a stronger influence on the liquid flow. Assuming potential flow away from the bubbles, the velocity in the surrounding liquid is given by (Mettin et al., 1997)

$$u(x,t) = \sum_{j=1}^{N_B} \frac{R_{B,j}^2 \dot{R}_{B,j}}{|x - x_{B,j}|^3}(x - x_{B,j}). \tag{2.3}$$

Furthermore, the bubble compression rate $\dot{R}_{B,j}$ in equation 2.3 is taken to be constant and negative, leading to a non-dimensional bulk velocity

$$\tilde{u}_{\text{bulk},i} = \sum_{\substack{j=1 \\ j \neq i}}^{N_B} \frac{-R_{B,j}^2(t=0)}{|x_{B,i}(t=0) - x_{B,j}(t=0)|^3}\big(x_{B,i}(t=0) - x_{B,j}(t=0)\big) \tag{2.4}$$

at the center $x_{B,i}$ of bubble i. Equation 2.4 provides an estimation for the bulk flow direction and its strength which is purely based on the initial geometrical arrangement. The assumption of constant $\dot{R}_{B,j}$ does not exactly

hold for cloud collapses since the bubbles behind the forming collapse front compress but remain at rest ahead of it. Therefore, equation 2.4 characterizes only the flow velocity perpendicular to the direction of the reference vector and is governed by the arrangement of bubbles along the collapse front. To examine the influence of the bulk flow induced by the collapse of the surrounding bubbles on the microjet direction, $u_{\text{tip},i}$ and $\tilde{u}_{\text{bulk},i}$ are projected onto a plane perpendicular to the radial direction. The resulting velocity components are marked by the superscript $\perp$ and are also schematically drawn in figure 2.1. The bulk flow deviation angle between $u_{\text{tip},i}^{\perp}$ and $\tilde{u}_{\text{bulk},i}^{\perp}$ is denoted φ_i.

2.2.3   *Linear theory of cloud cavitation collapse*

The governing equations that describe compressible multi-phase flows are introduced in chapter 3. The equations introduced there provide an accurate flow description including the chemical, mechanical and thermodynamic non-equilibrium at bubble interfaces. An exact solution, however, is not known to exist which renders their mathematical interpretation difficult. The theoretical description of cloud cavitation must therefore be simplified for mathematical accessibility. This is achieved by analysis of small perturbations and simplified representations of disperse bubble clouds by homogeneous mixtures (van Wijngaarden, 1972a). Homogeneous models can describe the macroscopic scales of cloud cavitation associated to the duration of the cloud collapse and wave propagation in the mixture. On the other hand, they fully neglect the bubbly character of the real mixture. Mørch (1980) presents a simple homogeneous model that is based on Rayleigh's solution in equation 2.1. It is assumed that the gas volume fraction α_C of a homogeneous bubble cluster is reduced to zero behind the bubbly shock, meaning that cavities are completely annihilated. In this case the cluster boundary propagates with the speed of sound in the homogeneous mixture and the bubble radius R_B in equation 2.1 is substituted with the homogeneous cloud radius R_C, that is

$$R_C \ddot{R}_C + \left(1 + \frac{\alpha_C}{2}\right) \dot{R}_C^2 = -\frac{p_\infty}{\rho_1 \alpha_C}. \tag{2.5}$$

For $\alpha_C \rightarrow 1$ the homogeneous mixture becomes a pure gas phase and equation 2.5 reduces to the single bubble case in equation 2.1.
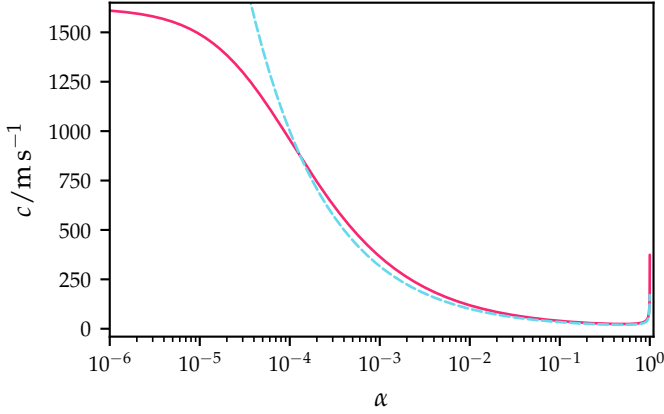
FIGURE 2.2: Mixture speed of sound for water-air at 1 bar: ——— harmonic mixture (Wood, 1930); – – – – homogeneous mixture (van Wijngaarden, 1972a).

The effective homogeneous mixture speed of sound, c_H, for the corresponding assumptions is given by (van Wijngaarden, 1972a)

$$c_H = \sqrt{\frac{p_1}{\rho_1 \alpha_C (1 - \alpha_C)}} \tag{2.6}$$

and is a crucial component for the description of cloud cavitation collapse. The speed of sound in a real bubbly mixture was first investigated in Mallock (1910) and later in Wood (1930) and later confirmed experimentally (Campbell et al., 1958; Fox et al., 1955; Karplus, 1957; Silberman, 1957; Wilson et al., 2008). Figure 2.2 compares the harmonic speed of sound for a real mixture (Wood, 1930) with the homogeneous speed of sound used in equation 2.5. It is seen that the homogenization of the bubble cloud is only valid if α_C is not too close to zero, nor unity. The simplification of cloud cavitation in equation 2.5 was later extended to account for the energy potential stored in the bubble cluster (Mørch, 1989) and further linearized treatments of cloud cavitation collapse were discussed in d'Agostino et al. (1989) and Kubota et al. (1992).

The simplifications discussed above completely neglect bubble-bubble interactions. Analysis of those dynamics is carried out with potential flow theory. The bubble wall velocities are described by a superposition of velocity potentials, ϕ_i, for which an analytical description is available (Lamb, 1879). By using Lagrange's equations, the derived equations of motion result

in a system of non-linear Ordinary Differential Equations (ODEs) where the bubble dynamics is governed by the type of equation 2.1 with additional coupling terms that describe the bubble-bubble interactions. Although the ODEs can not be solved analytically, they are often combined with a homogeneous mixture approach and then solved numerically. Chapter 6 provides further context for potential flow based models and addresses their accuracy with data from realistic bubble-bubble interactions.

2.3   SCALING LAWS FOR CAVITATING BUBBLE CLOUDS

This section presents a scaling argument for the variables that determine the dynamics of collapsing gas bubble clouds. The following variables are included in the scaling argument:

- Liquid and gas densities ρ_k with $k \in \{1, 2\}$
- Liquid and gas sound speeds c_k with $k \in \{1, 2\}$
- Initial bubble and liquid pressure p_C in the sphere defining the cloud
- Initial gas volume fraction of the cloud α_C
- Initial cloud and bubble radii R_C and R_B, respectively

The variables are non-dimensionalized following the approach presented in Bolotnov et al. (2011), where a physically significant quantity q is written as $q = q^* \tilde{q}$ with q^* its characteristic dimensional value and $\tilde{q}$ its non-dimensional value. The problem is further simplified by the following two assumptions:

1. The inertia of the gas is neglected ($\rho_2 \ll \rho_1$)
2. The liquid is treated as incompressible ($c_1 \to \infty$)

The non-dimensional parameters are set to

$$\tilde{\rho}_1 = 1, \quad \tilde{c}_2 = 1, \quad \tilde{R}_B = 1,$$

which determines the characteristic values

$$\rho^* = \frac{\rho_1}{\tilde{\rho}_1}, \tag{2.7}$$

$$c^* = \frac{c_2}{\tilde{c}_2}, \tag{2.8}$$

$$R^* = \frac{R_B}{\tilde{R}_B}. \tag{2.9}$$

The remaining non-dimensional numbers for the cloud radius, pressure and gas volume fraction then follow by

$$\tilde{R}_C = \frac{R_C}{R^*}, \quad \tilde{p} = \frac{p}{p^*},$$

and α_C, respectively. The characteristic pressure in the bubble cloud, $p^* = p_C$, is obtained from the characteristic speed of sound $c^* = \sqrt{\gamma_2 p^*/\rho_2}$ and p is a reference pressure. A time-scale for the characteristic bubble dynamics is estimated by

$$t_B^* \sim \frac{1}{\omega_B}, \tag{2.10}$$

where the bubble oscillation frequency ω_B is given by

$$\omega_B = \frac{1}{R_B}\sqrt{\frac{3\gamma_2 p}{\rho_1}}, \tag{2.11}$$

see for example Brennen (2013). Substituting the scaled variables leads to

$$t_B^* \sim \frac{1}{\omega_B} \sim R_B\sqrt{\frac{\rho_1}{\rho_2}\frac{\rho_2}{p}} \sim \frac{R^*}{c^*}\tilde{R}_B\sqrt{\frac{1}{\tilde{p}}}. \tag{2.12}$$

The macroscopic time-scale of the cloud collapse, t_C^*, is governed by the wave speed of the bubbly shock front, also referred to as effective speed of sound, given by

$$\dot{R}_F \sim \sqrt{\frac{p}{\rho_1(1-\alpha_C)\alpha_C}}, \tag{2.13}$$

which is valid for α_C neither close to zero nor close to unity as well as no relative velocity between the gas and liquid (Crespo, 1969; van Wijngaarden, 1968, 1972a). Proceeding similar as above, the characteristic time-scale scales by

$$t_C^* \sim \frac{R_C}{\dot{R}_F} \sim R_C\sqrt{\frac{\rho_1}{\rho_2}\frac{\rho_2}{p}(1-\alpha_C)\alpha_C} \sim \frac{R^*}{c^*}\tilde{R}_C\sqrt{\frac{(1-\alpha_C)\alpha_C}{\tilde{p}}}, \tag{2.14}$$

where experimental work published in Hansson et al. (1980) show good agreement with this macroscopic scaling. Computing the ratio of the two time-scales yields

$$\frac{t_C^*}{t_B^*} \sim \frac{\tilde{R}_C}{\tilde{R}_B}\sqrt{(1-\alpha_C)\alpha_C} \sim \sqrt{\beta_C}, \tag{2.15}$$

which is identical to the result presented in Wang et al. (1999). Finally, estimates for the characteristic microjet tip velocity and bubbly shock speed are obtained by combining equations 2.9, 2.12 and 2.14 such that

$$u_{\text{tip}}^* \sim \frac{R^*}{t_B^*} \sim c^* \frac{1}{\tilde{R}_B} \sqrt{\tilde{p}}, \tag{2.16}$$

$$\dot{R}_F^* \sim \frac{R^*}{t_C^*} \sim c^* \frac{1}{\tilde{R}_C} \sqrt{\frac{\tilde{p}}{(1-\alpha_C)\alpha_C}}. \tag{2.17}$$

It is interesting to note that equation 2.15 can further be discussed by following a similar argument given in van Wijngaarden (1970). Let d_F be the thickness of the bubbly shock that propagates with the effective speed $\dot{R}_F$ given by equation 2.13. The change of the bubble radius R_B induced by the shock passage happens at the time scale t_B^* given by equation 2.10, where the time scale of the shock passage is of the order $d_F/\dot{R}_F$. Requiring that the time scale of shock passage is at least of the order of the bubble response leads to the scaling

$$\tilde{d}_F \sim \frac{\tilde{R}_B}{\sqrt{(1-\alpha_C)\alpha_C}}, \tag{2.18}$$

after using equation 2.9 for conversion to non-dimensional form. Under the given assumptions, a useful estimate of the bubbly shock thickness then follows by

$$d_F \geq \frac{R_B}{\sqrt{(1-\alpha_C)\alpha_C}}. \tag{2.19}$$

Finally, the scaling argument for the ratio of the macroscopic and microscopic characteristic time in equation 2.15 can further be expressed in terms of the non-dimensional shock thickness

$$\frac{t_C^*}{t_B^*} \sim \frac{\tilde{R}_C}{\tilde{d}_F} \sim \sqrt{\beta_C}, \tag{2.20}$$

where equation 2.18 has been used.

3

GOVERNING EQUATIONS

> *Our knowledge can only be finite, while our ignorance must necessarily be infinite.*
>
> — Karl Popper

This chapter summarizes the equations that govern compressible multiphase flow in a general setting. A relaxed system in the limit of mechanical equilibrium at the interface is derived and forms the basis for the numerical calculations performed in this thesis. The chapter concludes with a discussion of the numerical methods used for the discretization of the underlying hyperbolic conservation laws.

3.1 NON-EQUILIBRIUM TWO-PHASE FLOW

The governing equations for a discrete two-phase flow were first described by Baer et al. (1986) for a reactive granular system. A variation of these equations form the basis for the compressible flow systems discussed in this thesis. Each phase $k \in \{1, 2\}$ is described by a set of balance laws for mass, momentum and energy according to

$$\frac{\partial \alpha_1 \rho_1}{\partial t} + \boldsymbol{\nabla} \cdot (\alpha_1 \rho_1 \boldsymbol{u}_1) = 0, \tag{3.1}$$

$$\frac{\partial \alpha_1 \rho_1 \boldsymbol{u}_1}{\partial t} + \boldsymbol{\nabla} \cdot (\alpha_1 \rho_1 \boldsymbol{u}_1 \otimes \boldsymbol{u}_1 + \alpha_1 p_1 \boldsymbol{I}) = -p_I \boldsymbol{\nabla} \alpha_2 + \lambda (\boldsymbol{u}_2 - \boldsymbol{u}_1), \tag{3.2}$$

$$\frac{\partial \alpha_1 \rho_1 e_1}{\partial t} + \boldsymbol{\nabla} \cdot ((\alpha_1 \rho_1 e_1 + \alpha_1 p_1) \boldsymbol{u}_1) = p_I \frac{\partial \alpha_2}{\partial t} + \lambda \boldsymbol{u}_I \cdot (\boldsymbol{u}_2 - \boldsymbol{u}_1), \tag{3.3}$$

$$\frac{\partial \alpha_2 \rho_2}{\partial t} + \boldsymbol{\nabla} \cdot (\alpha_2 \rho_2 \boldsymbol{u}_2) = 0, \tag{3.4}$$

$$\frac{\partial \alpha_2 \rho_2 \boldsymbol{u}_2}{\partial t} + \boldsymbol{\nabla} \cdot (\alpha_2 \rho_2 \boldsymbol{u}_2 \otimes \boldsymbol{u}_2 + \alpha_2 p_2 \boldsymbol{I}) = p_I \boldsymbol{\nabla} \alpha_2 - \lambda (\boldsymbol{u}_2 - \boldsymbol{u}_1), \tag{3.5}$$

$$\frac{\partial \alpha_2 \rho_2 e_2}{\partial t} + \boldsymbol{\nabla} \cdot ((\alpha_2 \rho_2 e_2 + \alpha_2 p_2) \boldsymbol{u}_2) = -p_I \frac{\partial \alpha_2}{\partial t} - \lambda \boldsymbol{u}_I \cdot (\boldsymbol{u}_2 - \boldsymbol{u}_1), \tag{3.6}$$

$$\frac{\partial \alpha_2}{\partial t} + (\boldsymbol{u}_I \cdot \boldsymbol{\nabla}) \alpha_2 = \mu (p_2 - p_1). \tag{3.7}$$

The terms on the right-hand side describe interactions at the interface be-
tween two phases, whereas quantities with subscript I are average values
at the interface. The parameters $\lambda > 0$ and $\mu > 0$ describe the rates for
which velocity and pressure relax towards equilibrium at the interface,
respectively. The variables α_k, ρ_k, $\boldsymbol{u}_k$, p_k and $e_k = \varepsilon_k + 1/2\,\boldsymbol{u}_k \cdot \boldsymbol{u}_k$ are volume
fraction, density, velocity, pressure and specific total energy of the pure
phase k, respectively, where ε_k denotes the specific internal energy. The
phasic pressure takes the form $\alpha_k p_k$, where the scaling with α_k is required
to ensure finite dissipation rates at the interface with respect to velocity
gradients (Baer et al., 1986). In case of a homogeneous mixture in thermo-
dynamic equilibrium, the phasic pressure equals the partial pressure of the
corresponding mixture component according to Dalton's Law.

In addition to the equation of state (EOS) discussed in section 3.3.1, the
geometric relation in equation 3.7 is augmented to the system for closure in
the eight unknowns α_k, ρ_k, $\boldsymbol{u}_k$ and e_k for $k \in \{1,2\}$. The particular choice of
α_2 as another degree of freedom is beneficial in terms of its thermodynamic
independence as well as its allowance to take into account compressibility
effects. The additional constraint $\alpha_1 + \alpha_2 = 1$ has implicitly been used to
arrive at the system of seven equations 3.1 to 3.7. The laws describe the
evolution of each phase k separately and are non-conservative due to the
disequilibrium state at the interface (mass and heat transfer have been
omitted here). Furthermore, conservation of the mixture is satisfied which
is easily verified by summing the equations of the corresponding variables
for $k \in \{1,2\}$.

3.2   TWO-PHASE FLOW IN THE LIMIT OF MECHANICAL RELAXATION

A simplification to the governing system of the previous section can be
introduced for interfacial flows which are central to this thesis. Such flows
separate pure fluids where the wave speed associated to the interface
corresponds to that of a contact wave. It is therefore necessary that pressure
and normal velocity are in equilibrium at the interface (Saurel and Abgrall,
1999a). This equilibrium state is achieved in the limit of $\lambda \to \infty$ and
$\mu \to \infty$, i.e., infinitely fast relaxation of the phasic velocities and pressures,
respectively, at the material interface. By asymptotic analysis of equations 3.1
to 3.7 with appropriate choice for p_I and $\boldsymbol{u}_I$ (Baer et al., 1986; Saurel,
Gavrilyuk, et al., 2003) as well as $\lambda = 1/\epsilon$ and $\mu = 1/\epsilon$, then for $\epsilon \to 0^+$

the non-equilibrium system in section 3.1 reduces to (Murrone et al., 2005; Perigaud et al., 2005)

$$\frac{\partial \alpha_1 \rho_1}{\partial t} + \boldsymbol{\nabla} \cdot (\alpha_1 \rho_1 \boldsymbol{u}) = 0, \tag{3.8}$$

$$\frac{\partial \alpha_2 \rho_2}{\partial t} + \boldsymbol{\nabla} \cdot (\alpha_2 \rho_2 \boldsymbol{u}) = 0, \tag{3.9}$$

$$\frac{\partial \rho \boldsymbol{u}}{\partial t} + \boldsymbol{\nabla} \cdot (\rho \boldsymbol{u} \otimes \boldsymbol{u} + p \boldsymbol{I}) = \boldsymbol{\nabla} \cdot \boldsymbol{\tau} + \boldsymbol{\nabla} \cdot \boldsymbol{T}, \tag{3.10}$$

$$\frac{\partial \rho e + \rho \varepsilon_\sigma}{\partial t} + \boldsymbol{\nabla} \cdot \big((\rho e + \rho \varepsilon_\sigma + p) \boldsymbol{u} \big) = \boldsymbol{\nabla} \cdot (\boldsymbol{\tau} \cdot \boldsymbol{u}) + \boldsymbol{\nabla} \cdot (\boldsymbol{T} \cdot \boldsymbol{u}), \tag{3.11}$$

$$\frac{\partial \alpha_2}{\partial t} + (\boldsymbol{u} \cdot \boldsymbol{\nabla}) \alpha_2 = K \boldsymbol{\nabla} \cdot \boldsymbol{u}. \tag{3.12}$$

In comparison to the non-equilibrium model in section 3.1 the asymptotic model of equations 3.8 to 3.12 conserves momentum and energy of the *mixture*. Here ρ, $\boldsymbol{u}$, p and e are density, velocity, pressure and specific total energy, respectively, with velocity and pressure in equilibrium at the interface. The phasic treatment for the conservation of mass leaves the model in thermodynamic disequilibrium and allows for different materials with separate equations of state in each phase, given appropriate data for the relaxation rates at the interface. In contrast, single-fluid models treat density in mixture state as well and evolve the system with the Euler equations. Phase components are again modeled by augmenting the system with a transport equation of a marker function usually based on mass fractions (Karni, 1994; Picone et al., 1988; Quirk et al., 1996; Saurel, P. Cocchi, et al., 1999; Shyue, 1998).

The asymptotic model is further augmented with the mixture viscous stress tensor $\boldsymbol{\tau}$ as well as mixture capillary stress tensor $\boldsymbol{T}$ and capillary potential energy $\rho \varepsilon_\sigma$, discussed further in sections 3.3.3 and 3.3.4, respectively. A variation of this model without stress tensors has first been used in Kapila et al. (2001) to model deflagration to detonation transition in granular materials. The term $K \boldsymbol{\nabla} \cdot \boldsymbol{u}$ on the right-hand side of equation 3.12 accounts for compression or expansion effects depending on the wave type, characterized by $\boldsymbol{\nabla} \cdot \boldsymbol{u}$, and the material pairing described by

$$K = \frac{\alpha_1 \alpha_2 (\rho_1 c_1^2 - \rho_2 c_2^2)}{\alpha_1 \rho_2 c_2^2 + \alpha_2 \rho_1 c_1^2}. \tag{3.13}$$

The numerator of K determines the sign by the difference of the bulk moduli in the two participating phases. If phase $k = 1$ is *less* compressible, then

$K > 0$. For this case the rate of change $\frac{D\alpha_2}{Dt}$ in equation 3.12 is negative across shock waves ($\nabla \cdot u < 0$) which causes compression of the volume fraction α_2. Across rarefaction waves the rate of change is positive ($\nabla \cdot u > 0$) which causes expansion. The factor $\alpha_1\alpha_2$ in equation 3.13 is focusing the magnitude of K towards the center of the mixture. The normalization factor in the denominator is of the same form as the harmonic averaging operator required for the mixture speed of sound, discussed in section 3.3.2. In the pure phase it is obvious that $K = 0$. Alternatively, the right-hand side in equation 3.12 can be derived from the EOS along an isentropic trajectory assuming pressure equilibrium (Saurel, Le Metayer, et al., 2007).

The literature concerned with interfacial flows often neglects the source term $K\nabla \cdot u$ in the volume fraction transport of equation 3.12 because it is inactive in the pure phase and components are assumed immiscible (Allaire et al., 2002; Coralic et al., 2014; Perigaud et al., 2005; Saurel, Gavrilyuk, et al., 2003).[1] The characteristics exhibited by this term are favorable for cavitating flows due to its capability of generating a gaseous phase from a liquid phase homogeneously mixed with a small amount of the gaseous phase. The reduced system in equations 3.8 to 3.12 form the governing equations used for the numerical simulations carried out in this thesis. Its discretization is discussed in section 3.4. A comprehensive overview of asymptotic solutions based on the full non-equilibrium two-phase model is given in Linga et al. (2019).

3.3   CONSTITUTIVE LAWS

The cavitating flow systems modeled in this work are composed of water and air (non-condensable gas). The convention adapted here is that the phase index $k = 1$ corresponds to the less compressible phase, i. e., liquid water, whereas the phase index $k = 2$ corresponds to the gaseous phase. The following provides the constitutive laws for the closure of equations 3.8 to 3.12.

---

1 If fluids are assumed immiscible, the term *multi-component* is often used in the literature.

	$\rho_k/\mathrm{kg\,m^{-3}}$	$c_k/\mathrm{m\,s^{-1}}$	$\nu_k/\mathrm{m^2\,s^{-1}}$	γ_k	$p_{c,k}/\mathrm{bar}$
Water	1000	1625	1.0×10^{-6}	4.4	6000
Air	1	374	18.5×10^{-6}	1.4	0

TABLE 3.1: Material parameter for water and air at 1 bar reference pressure.

3.3.1 *Equation of state*

The incomplete caloric stiffened gas equation of state (SGEOS) (Harlow et al., 1971; Menikoff et al., 1989) is used for water-air systems, where the pressure relation ship $p_k = p_k(\rho_k, \varepsilon_k)$ for the pure phase is given by

$$p_k = (\gamma_k - 1)\rho_k \varepsilon_k - \gamma_k p_{c,k}. \tag{3.14}$$

The parameters $\gamma_k > 1$ and $p_{c,k} \geq 0$ are, respectively, the ratio of specific heats and a correction pressure to model the stiffness of phase k. For a polytropic gas the parameter $p_{c,k} = 0$ and equation 3.14 reduces to the ideal gas law. The phasic speed of sound is derived from equation 3.14 at constant entropy

$$c_k^2 = \left(\frac{\partial p_k}{\partial \rho_k}\right)_{s_k} = \gamma_k \frac{p_k + p_{c,k}}{\rho_k}, \tag{3.15}$$

where the fundamental thermodynamic identity $\mathrm{d}\varepsilon_k = T_k\,\mathrm{d}s_k - p_k\,\mathrm{d}v_k$ with $\mathrm{d}s_k = 0$ has been used. The variables T_k, s_k and $v_k = 1/\rho_k$ are temperature, specific entropy and specific volume for phase k, respectively. The values for the material parameters used in this work are listed in table 3.1 with the parameters for the SGEOS adapted from Saurel and Abgrall (1999b).

3.3.2 *Mixture equations*

Equation 3.14 can be used to approximate the thermodynamic equilibrium in the mixture with appropriate averaging rules. The mixture conservation requirement of the non-equilibrium system in equations 3.1 to 3.7 on page 17 determines the mixture rules for the conserved quantities

$$\rho = \alpha_1 \rho_1 + \alpha_2 \rho_2, \tag{3.16}$$

$$\rho e = \alpha_1 \rho_1 e_1 + \alpha_2 \rho_2 e_2, \tag{3.17}$$

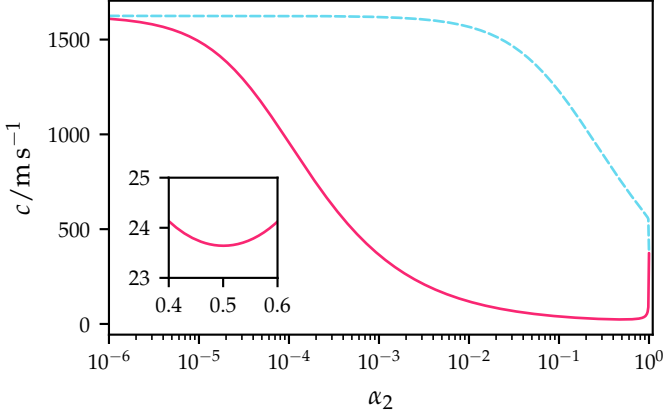$$\alpha_1 + \alpha_2 = 1, \tag{3.18}$$

FIGURE 3.1: Speed of sound for a water-air mixture: ———, equilibrium speed of sound; — — — —, frozen speed of sound.

where the interface conditions

$$u = u_I = u_1 = u_2,$$ (3.19)

$$p = p_I = p_1 = p_2,$$ (3.20)

follow from the asymptotic limit discussed in section 3.2. Velocity is a kinematic quantity and needs no further attention. The thermodynamic closure for the mixture pressure p requires consistent averaging coefficients which can be obtained from an isobaric closure (Allaire et al., 2002) of equation 3.14, resulting in

$$\frac{1}{\gamma - 1} = \sum_k \frac{\alpha_k}{\gamma_k - 1},$$ (3.21)

$$\frac{\gamma p_c}{\gamma - 1} = \sum_k \alpha_k \frac{\gamma_k p_{c,k}}{\gamma_k - 1},$$ (3.22)

where pressure positivity and the interface condition of equation 3.20 has been assumed. From these rules the mixture pressure takes the form

$$p = (\gamma - 1)\rho\varepsilon - \gamma p_c,$$ (3.23)

with $\rho\varepsilon = \rho e - 1/2 \rho u \cdot u$, γ and p_c the mixture internal energy, ratio of specific heats and correction pressure, respectively.

Equations 3.8 to 3.12 are hyperbolic for the mixture speed of sound

$$\frac{1}{\rho c^2} = \sum_k \frac{\alpha_k}{\rho_k c_k^2}.$$ (3.24)

The relation is known as the *equilibrium* mixture speed of sound and corresponds to the analytical derivations of Mallock (1910) and Wood (1930) for sound propagation in bubbly liquids. In particular, the equilibrium speed of sound in a water-air mixture is non-monotonic and below the speed of sound in the pure phases. If the source term on the right-hand side of equation 3.12 is neglected, the resulting *frozen* mixture speed of sound is monotonic but in disagreement with Wood (1930). Figure 3.1 compares the equilibrium and frozen speed of sound for a varying gas volume fraction α_2. The material parameters correspond to the values in table 3.1.

3.3.3 *Viscous stress*

Augmenting the momentum equations 3.2 and 3.5 and energy equations 3.3 and 3.6 in the non-equilibrium model with a viscous stress term, where $\mu_k = \rho_k \nu_k$ is the dynamic viscosity of phase k, leads to the equilibrium limit form (Perigaud et al., 2005)

$$\boldsymbol{\tau} = 2\mu \left(\boldsymbol{D} - \frac{1}{3}(\boldsymbol{\nabla} \cdot \boldsymbol{u})\boldsymbol{I} \right),$$ (3.25)

where

$$\mu = \alpha_1 \rho_1 \nu_1 + \alpha_2 \rho_2 \nu_2$$ (3.26)

is the dynamic viscosity of the mixture. The deformation rate tensor is given by

$$\boldsymbol{D} = \frac{1}{2}\left(\boldsymbol{\nabla}\boldsymbol{u} + (\boldsymbol{\nabla}\boldsymbol{u})^{\mathsf{T}}\right).$$ (3.27)

3.3.4 *Surface tension*

Unlike classic surface tension models for incompressible flow, where a surface tension force f_σ is added on the right-hand side of the momentum equation, a conservative formulation is necessary when the energy equation can not be neglected. For the present model the evolution of the interface geometry is described by equation 3.12 depending on the field α_2. Assuming

α_2 is continuously differentiable, then an approximation to the true surface normal $\boldsymbol{n}$ of an interface with zero thickness is given by (Brackbill et al., 1992; Sussman et al., 1994)

$$\boldsymbol{m} = -\frac{\boldsymbol{\nabla}\alpha_2}{|\boldsymbol{\nabla}\alpha_2|}, \tag{3.28}$$

where the minus sign ensures that $\boldsymbol{m}$ points towards the phase with larger mass. The local interface curvature follows from

$$\kappa = \boldsymbol{\nabla} \cdot \boldsymbol{m}. \tag{3.29}$$

One implication of a continuously differentiable field α_2 is that the interface is represented with finite thickness. This, however, is in concert with the discrete representation of α_2 such that equations 3.28 and 3.29 remain useful. Brackbill et al. (1992) then formulate the surface tension effects in terms of the volumetric force

$$\boldsymbol{f}_\sigma = \sigma\kappa\boldsymbol{m}|\boldsymbol{\nabla}\alpha_2|, \tag{3.30}$$

where σ is the surface tension coefficient. A conservative formulation in terms of a capillary stress tensor has been suggested by Gueyffier et al. (1999)

$$\boldsymbol{T} = \sigma(\boldsymbol{I} - \boldsymbol{m} \otimes \boldsymbol{m})|\boldsymbol{\nabla}\alpha_2|. \tag{3.31}$$

The energy stored in an interface due to capillary stresses, e.g. the Laplace pressure difference in a spherical bubble, must be accounted for in the energy equation. Following Perigaud et al. (2005), the capillary potential energy—based on the interface description discussed above—is given by

$$\rho\varepsilon_\sigma = \sigma|\boldsymbol{\nabla}\alpha_2|. \tag{3.32}$$

This energy corresponds to $1/2\,\mathrm{tr}\,(\boldsymbol{T})$ and can be regarded as the mechanical pressure contribution due to surface tension—following a similar argument made in Batchelor (1967) for the mechanical pressure due to the stress tensor $-p\boldsymbol{I} + \boldsymbol{\tau}$. The factor in front of the trace arises due to the 2D nature of surface tension forces. In Hu et al. (2006), the potential energy in equation 3.32 has been eliminated for an incompressible flow application by scaling the identity in equation 3.31 with an appropriate factor that accounts for the dimensionality of the problem.

3.4   DISCRETIZATION

There are two basic categories of numerical methods used for interfacial problems. The first category are methods that eliminate numerical diffusion

at the interfaces. They are also called "sharp interface methods". They may further be divided into four branches:

LAGRANGIAN METHODS and arbitrary Lagrangian-Eulerian methods describe the interface with local coordinates that advect with the local flow velocity. These methods embed a computational mesh in the fluid domain and are most natural for problems with interfaces (Benson, 1992). On the other hand, large distortions of the embedded mesh induces error and frequent re-meshing is necessary especially for problems in cavitation where large interface deformations occur. These methods are further difficult to implement in higher dimensions.

FRONT TRACKING METHODS use a fixed mesh and use different solvers for the bulk region away from interfaces and the interfacial region. These methods are not conservative in higher dimensions and pose problems when there are topological singularities at the interface, e. g., breakup or coalescence, see J.-P. Cocchi et al. (1997). A method for 1D problems was proposed in Harten and Hyman (1983). Apart from these difficulties, front tracking methods exhibit high accuracy at the cost of non-trivial implementation.

INTERFACE RECONSTRUCTION METHODS do not explicitly track the interface but perform a reconstruction based on the ideas of Hirt et al. (1981) and Youngs (1982). For incompressible flows, knowledge of the interface location is sufficient to compute the density field. For compressible problems, the determination of the densities and internal energies of phases in a mixed cell is not obvious (Saurel and Abgrall, 1999b). These methods are widely used but are not conservative.

LEVEL SET METHODS are used to compute and analyze the motion of an interface in multiple dimensions (Osher and Fedkiw, 2001; Osher and Sethian, 1988). A method for multi-fluid problems that is based on level sets is described in Fedkiw et al. (1999). In general, level set methods are not conservative.

The second category of methods allow for numerical diffusion in the interface region. These methods essentially discretize the flow fields using an Eulerian description on a single grid. The interfacial region is then necessarily described by a smooth transition zone. This implies that constitutive laws must correctly describe the thermodynamic state of the mixture in these transition zones. Derivation of such laws pose a major difficulty in such situations (Ishii et al., 1984). An equation of state that correctly describes the artificial mixture zone for simple fluids is given in Allaire et al.

(2002). The additional numerical dissipation introduced in those methods, however, is necessary to capture discontinuities in the flow field. adaptive mesh refinement (AMR), interface sharpening and high-order discretization schemes are techniques employed to counteract those weaknesses. Diffuse interface methods may further be divided into two branches:

SINGLE FLUID METHODS describe the flow fields by the conventional Euler equations. Distinction between the participating fluid components is achieved by introducing an additional marker field coupled with ideas from the level set method (Abgrall, 1996; Karni, 1996; Shyue, 1998). These methods are efficient and simple to implement. The single fluid description leads to a marker field that depends on thermodynamic quantities. These methods are therefore difficult to extend to more general constitutive laws and are not capable, for example, of generating a locally heterogeneous phase composition from a homogeneous mixture, a feature of cavitating flows.

MULTI-PHASE METHODS model the participating fluid phases independently with a separate set of Euler equations for each. Such a model was proposed in Baer et al. (1986) to study the deflagration to detonation transition in reactive materials. A variant of this model for compressible multi-phase flows was given in Saurel and Abgrall (1999a). The separate treatment of the fluid phases allows for complex fluid/solid material combinations, each governed by corresponding constitutive laws. The method is furthermore conservative for the mixture, as discussed in section 3.1. The main difficulty in solving these systems are the non-equilibrium states at interfaces. The relaxation towards mechanical, thermal, chemical and velocity equilibria happens at different rates and therefore results in stiff systems. These methods have been very successful in the past for both, model error and implementation efficiency, and are actively researched today. A comprehensive overview of the involved multi-phase flow models is given in Linga et al. (2019).

As outlined in the second category above and in section 3.2, the model and numerical method used in this thesis are based on a multi-phase flow model discretized by a diffuse interface method with Eulerian description of the flow fields. The numerical schemes involved in the diffuse interface method are described in the following sections.

3.4.1 *Spatial discretization*

The governing equations 3.8 to 3.12 are solved on structured grids using Cartesian coordinates. The basic method is a Reconstruct/Evolve/Average (REA) algorithm where space is discretized using the Finite Volume Method (FVM) followed by a time integration step (LeVeque, 2002). The separate treatment of space and time provides a flexible way to implement different numerical schemes.

For simplicity we consider the 1D system of conservation laws $\partial_t q(x,t) + \partial_x f(q(x,t)) = 0$ on a Cartesian domain $(x,t) \in \Omega \subset \mathbb{R} \times \mathbb{R}_+$ with initial condition $q_0(x)$ and appropriate boundary conditions. The volume of the spatial domain in Ω is denoted by V. The volume average of q over a control volume $\mathcal{C}_i = [x_{i-1/2}, x_{i+1/2}]$ with volume V_i is given by

$$Q_i(t) = \frac{1}{V_i} \int_{x_{i-1/2}}^{x_{i+1/2}} q(x,t)\, \mathrm{d}x. \tag{3.33}$$

Applying this averaging rule to the 1D system of conservation laws and using the divergence theorem results in

$$\frac{\mathrm{d}Q_i}{\mathrm{d}t} = -\frac{1}{V_i} \int_{\mathcal{S}_i} f(q(x,t)) \cdot n\, \mathrm{d}S, \tag{3.34}$$

where it has been assumed that the volume V_i does not change with time and $\mathcal{S}_i$ denotes the closed surface on the boundary of $\mathcal{C}_i$ with n the surface unit normal pointing outwards. For N disjoint control volumes, such that $V = \bigcup_{i=1}^{N} V_i$, equation 3.34 is a system of N ODEs whose solution is exact. Furthermore, the integral form allows for weak solutions. The semi-discrete system of equation 3.34 is the basis of the REA algorithm and its discretization requires the following approximations:

1. The time derivative is approximated with a suitable integrator at discrete time steps $\Delta t = t^{n+1} - t^n$.

2. The surface integral operator must be approximated with a suitable quadrature rule. Most often, as in this thesis, the mid-point rule is used leading to overall 2nd-order spatial accuracy. A scheme with a 4th-order Gaussian quadrature rule is presented in Coralic et al. (2014).

3. The integrand of the surface integral, i. e. the flux function, needs to be evaluated at coordinates ξ on the surface $\mathcal{S}_i$. If the solution variables are expressed in cell average form Q_i, then a reconstruction $q \approx$

$q^r(x,t) = g(x; Q_1(t), Q_2(t), \ldots, Q_N(t))$ is necessary for a point-wise evaluation of the solution variables. A zeroth-order reconstruction simply assumes $q_i^r = Q_i$ everywhere in the cell $\mathcal{C}_i$.

4. The flux function $f(q)$ depends on the solution $q(x,t)$ itself. As time progresses from a known state at t^n to t^{n+1} the solution in the time interval $(t^n, t^{n+1}]$ is unknown. This requires a numerical flux approximation of the form

$$F^n(\xi) \approx \frac{1}{\Delta t} \int_{t^n}^{t^{n+1}} f(q(\xi,t)) \, \mathrm{d}t, \tag{3.35}$$

where $\xi \in \mathcal{S}_i$ is a coordinate on the surface of control volume $\mathcal{C}_i$.

Source terms may be included in equation 3.34 as well. A detailed discussion is presented in LeVeque (2002).

To apply these techniques, equations 3.8 to 3.12 are rewritten in the compact form

$$\frac{\partial q}{\partial t} + \boldsymbol{\nabla} \cdot f^a = \boldsymbol{\nabla} \cdot f^d + s, \tag{3.36}$$

where

$$q = (\alpha_1\rho_1, \alpha_2\rho_2, \rho u_i, \rho e + \rho\varepsilon_\sigma, \alpha_2)^\mathsf{T}, \tag{3.37}$$

$$f^a = (f_x^a, f_y^a, f_z^a), \tag{3.38}$$

$$f^d = (f_x^d, f_y^d, f_z^d), \tag{3.39}$$

$$s = (0,0,0,0,0,0, [\alpha_2 + K]\partial_k u_k)^\mathsf{T}, \tag{3.40}$$

are the vectors of conserved variables, advective fluxes, diffusive fluxes and source terms, respectively. Index notation has been used for brevity. Indices that appear in pairs imply summation. The components of the flux vectors are given by

$$f_j^a = (\alpha_1\rho_1 u_j, \alpha_2\rho_2 u_j, \rho u_i u_j + p\delta_{ij}, [\rho e + \rho\varepsilon_\sigma + p]u_j, \alpha_2 u_j)^\mathsf{T}, \tag{3.41}$$

$$f_j^d = (0,0, \tau_{ij} + T_{ij}, \tau_{jk}u_k + T_{jk}u_k, 0)^\mathsf{T}. \tag{3.42}$$

The index i appearing in equations 3.37, 3.41 and 3.42 corresponds to the momentum components and is repetitive. For example, the component ρu_i in equation 3.37 repeats three times for a 3D spatial domain ($i = 1, 2, 3$), i.e., $q, s, f_j^a, f_j^d \in \mathbb{R}^7$ for $j = 1, 2, 3$. The symbol δ_{ij} denotes the Kronecker delta and u_i, τ_{ij} and T_{ij} are components of the velocity, stress and capillary stress tensors, respectively.

The numerical scheme to discretize equation 3.36 is briefly outlined in the following sections. Software design considerations for their efficient implementation targeting HPC architectures is discussed in chapter 4.

3.4.2 *Reconstruction and advective fluxes*

The advective fluxes include the non-linear terms of the governing equations. Their discretization is non-trivial and require that the numerical method is conservative, consistent and monotone. Conservation is an inherent property of the FVM. A scheme is consistent if $F(Q, \ldots, Q) = f(Q)$ where F is a numerical flux according to equation 3.35. Monotone schemes converge to entropy-satisfying weak solutions and provide stability. Godunov (1959) showed that such methods can be at most 1st-order accurate. A numerical method that is higher than 1st-order must be non-linear and Harten (1983) showed that such methods can be constructed and are stable if they obey a Total Variation Diminishing (TVD) property. In a scheme that is TVD, a local minimum or maximum is non-decreasing or non-increasing, respectively, and no new local extrema can be created. Naturally, this property is important to prevent spurious oscillations in the neighborhood of discontinuous solutions. For example, the classic 2nd-order accurate Lax-Wendroff scheme (P. Lax et al., 1960) is not TVD and consequently artificial viscosity must be added for stability. Yet, oscillations in the vicinity of discontinuities can not be avoided. The commonality of all such methods is that they generate Gibbs-like oscillations due to the high-order interpolation across discontinuities and a scheme that is TVD eliminates these oscillations (Harten, 1983, 1984, 1986; Harten and Osher, 1987).

Here we are interested in a high-order accurate scheme based on Godunov's idea to solve individual Riemann problems at the boundary $\mathcal{S}_i$ of a cell $\mathcal{C}_i$. Any such method is high-order accurate in smooth regions and necessarily 1st-order accurate at discontinuities. Improved resolution of strong shock waves was first obtained in van Leer (1979) by constructing a 2nd-order extension to Godunov's scheme called Monotonic Upstream-centered Scheme for Conservation Laws (MUSCL) and later a 3rd-order variant in Colella et al. (1984) called Piecewise Parabolic Method (PPM). More sophisticated schemes are based on high-order polynomial reconstructions called Essentially-Non-Oscillatory (ENO), where the non-oscillatory property is achieved by adaptively choosing one of the reconstructed stencils based on a smoothness indicator for the field (Harten, Engquist, et al., 1987; Shu and Osher, 1988, 1989). A weighted Essentially-Non-Oscillatory (WENO)
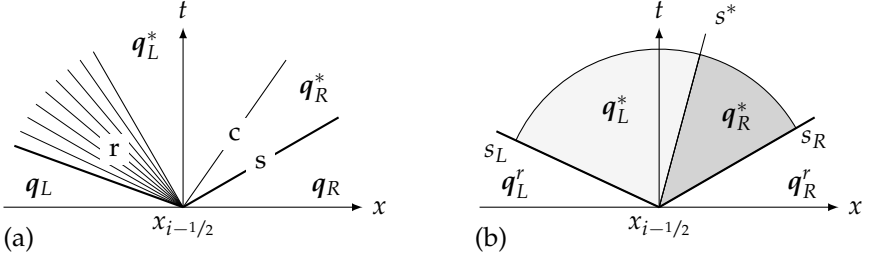
FIGURE 3.2: Riemann problem at face $\mathcal{S}_{i+1/2}$: (a) exact solution; (b) approximate solution with reconstructed initial conditions. Shock, rarefaction and contact waves are indicated by s, r and c, respectively.

scheme is a convex combination of nth-order accurate ENO stencils that leads to a $(2n-1)$th-order accurate scheme in smooth regions (Jiang et al., 1996; Liu et al., 1994). The reconstruction scheme used in the present work is a 5th-order WENO scheme for uniform grids (Jiang et al., 1996). A 3rd-order variant and their extension to non-uniform stretched grids (Coralic et al., 2014) are implemented as well.

The Riemann problem is the initial value problem (IVP) given by equation 3.36 and the initial condition

$$q_0(x) = \begin{cases} q_L & x < x_{i-1/2}, \\ q_R & x \geq x_{i-1/2}. \end{cases} \tag{3.43}$$

A typical solution $q(x,t)$ is shown in figure 3.2(a) where r, c and s correspond to rarefaction, contact and shock waves, respectively. In a 1D domain these waves propagate with speeds $u - c$, u and $u + c$, respectively. For any cell $\mathcal{C}_i$, a right-going wave from face $x_{i-1/2}$ and a left-going wave from face $x_{i+1/2}$ will interfere at time Δt for which the state vector $q(x_i, t + \Delta t)$ must change ($x_i = x_{i-1/2} + h/2$ and h is a characteristic cell size). For stability in a numerical simulation the constraint $c\Delta t < h/2$ (Courant et al., 1928), known as the Courant-Friedrichs-Lewy (CFL) condition, must hold. In case where the Riemann problem is evaluated at cell faces with averaged state variables, the stability constraint can be relaxed to $c\Delta t < h$. It is shown in section 3.4.6 that further constraints apply to the CFL number for a TVD time integration.

Solving the Riemann problem exactly (Godunov, 1959) is costly and not necessary since the solution obtained by the FVM is approximate. An approximation by a local linearization was first introduced by Roe (1981). This solver only converges to shock solutions and an appropriate entropy fix is required for rarefaction waves and sonic points. Another approximate solver due to Harten, P. D. Lax, et al. (1983) bears the name of its creators Harten-Lax-van Leer (HLL). The idea is to approximate the wave structure of the solution because only a part of the exact solution is required due to averaging. This solver is capable of resolving the non-linear waves with higher accuracy, while the contact wave suffers resolution due to approximating the wave structure with only one single state. The Harten-Lax-van Leer-Contact (HLLC) solver (Toro, 2009; Toro et al., 1994) improves this deficiency by introducing two approximate states q_L^* and q_R^* to the left and right of the contact discontinuity, respectively. This approximate solver is shown in figure 3.2(b). Here the HLLC solver is extended to the advective fluxes in equation 3.41. The flux computation is split into each spatial dimension $j = 1, 2, 3$. As indicated in figure 3.2(b) the initial condition of equation 3.43 is required at face locations and is obtained from a WENO reconstruction carried out in primitive variables to avoid pressure oscillations (Karni, 1994; Saurel and Abgrall, 1999b). In the following the notation $f_{j,k}^a = f_j^a(q_k^r)$ for $k \in \{L, R\}$ is used to indicate left and right states in the corresponding spatial direction j. Furthermore, indication of advective fluxes, time level or reconstructed states in superscripts is omitted for clarity. The numerical HLLC flux is given by

$$
\begin{aligned}
\mathcal{F}_j &= \frac{1 + \mathrm{sgn}(s^*)}{2} \left(f_{j,L} + s^- (q_{j,L}^* - q_L) \right) \\
&+ \frac{1 - \mathrm{sgn}(s^*)}{2} \left(f_{j,R} + s^+ (q_{j,R}^* - q_R) \right),
\end{aligned}
\tag{3.44}
$$

where

$$
s^- = \min(s_L, 0), \tag{3.45}
$$
$$
s^+ = \max(0, s_R), \tag{3.46}
$$

and $\mathrm{sgn}(x)$ is the signum function. The notation $\mathcal{F}_j$ is used to distinguish between the numerical flux F in equation 3.35. According to equation 3.43 the state vectors q_L and q_R correspond to locations at cell faces. Which exact face it is does not matter, only its spatial orientation j is important. The notation for a numerical flux at a specific face location in the $j = 1$ direction then follows by $F_{i-1/2,j,k} = \mathcal{F}_1((q_L)_{i-1/2,j,k}, (q_R)_{i-1/2,j,k})$ and similarly for the other two directions.

The wave speeds s_k for $k \in \{L, R\}$ are estimates for the slowest and fastest moving waves and are obtained from Einfeldt (1988). The fluxes in the intermediate states are obtained by applying the Rankine-Hugoniot jump conditions across these slowest and fastest waves

$$f^*_{j,k} = f_{j,k} + s_k(q^*_{j,k} - q_k).\tag{3.47}$$

The unknown intermediate states $q^*_{j,k}$ are obtained from these equations with the further assumption that pressure and velocity across the contact wave are equal, i.e., $p^*_k = p^*$ and $u^*_{j,k} = s^*$ for $k \in \{L, R\}$, respectively. This assumption is consistent with the mechanical equilibrium limit of the governing equations 3.8 to 3.12. Here the velocity component $u^*_{j,k}$ is the one aligned with spatial direction j. The tangential velocity components in the star-region are given by $u^*_{l,k} = u_{l,k}$ for $l \neq j$. The intermediate states are then found to be

$$q^*_{j,k} = \frac{s_k q_k - f_{j,k} + p^*_k d^*_j}{s_k - s^*},\tag{3.48}$$

with auxiliary vector $d^*_j = (0, 0, \delta_{ij}, s^*, 0)^\mathsf{T}$. The same convention for the repetitive index $i = 1, 2, 3$ applies here. The pressure in the star-region is determined from the initial condition and the wave speed estimates by

$$p^*_k = p_k + \rho_k(s_k - u_{j,k})(s^* - u_{j,k}),\tag{3.49}$$

for $k \in \{L, R\}$. The estimate for the contact wave speed s^* follows from the pressure equality $p^*_k = p^*$ and computes to

$$s^* = \frac{\rho_R u_{j,R}(s_R - u_{j,R}) - \rho_L u_{j,L}(s_L - u_{j,L}) + p_L - p_R}{\rho_R(s_R - u_{j,R}) - \rho_L(s_L - u_{j,L})}.\tag{3.50}$$

For example, in the $j = 1$ direction equation 3.48 becomes

$$q^*_{1,k} = \frac{s_k - u_{1,k}}{s_k - s^*} \begin{pmatrix} (\alpha_1\rho_1)_k \\ (\alpha_2\rho_2)_k \\ \rho_k s^* \\ (\rho u_2)_k \\ (\rho u_3)_k \\ (\rho e + \rho\varepsilon_\sigma)_k + (s^* - u_{1,k})\left(\rho_k s^* + \frac{p_k}{s_k - u_{1,k}}\right) \\ (\alpha_2)_k \end{pmatrix},\tag{3.51}$$
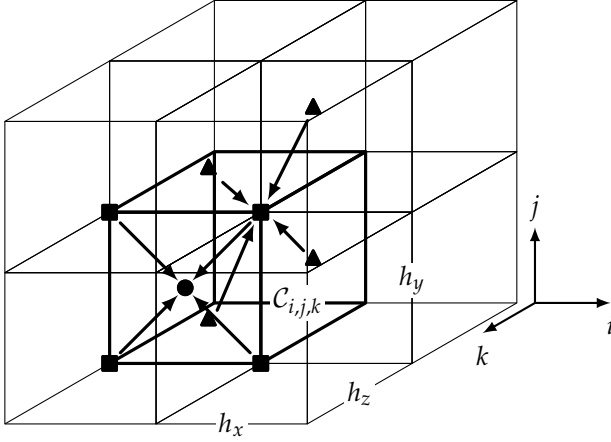
FIGURE 3.3: Approximation of gradient component $(\partial_x \phi)^h_{i,j,k+1/2}$. The target value ● is obtained by computing the cell corner values ■ from central finite differences at cell faces ▲.

where again $k \in \{L, R\}$ is either the state to the left or to the right of the contact wave. Figure 3.2(b) illustrates these intermediate states. Equation 3.49 has further been used to simplify the algebra in equation 3.51. The dependence of the wave speed estimates on the velocity component $u_{j,k}$ in the j direction implies that these estimates itself have a directional dependence. Indication of this dependence in the subscripts of s_k and s^* has been omitted for clarity. Plugging equation 3.51 into equation 3.44 results in the scheme for the numerical flux computation at the faces $\mathcal{S}_{i\pm1/2,j,k}$ of cell $\mathcal{C}_{i,j,k}$. Hence, the integral operator on the right-hand side of equation 3.34 takes the form

$$- \frac{1}{h_x}(F_{i+1/2,j,k} - F_{i-1/2,j,k}), \tag{3.52}$$

where h_x is the grid spacing for the $j = 1$ direction. The flux differences in the other two spatial directions follow likewise.

3.4.3 Diffusive fluxes

The stress tensor components τ_{ij} and T_{ij} in the diffusive flux vector components of equation 3.42 require an approximation of the gradient $\nabla^h \phi$ on the cell boundaries. This approximation is obtained by means of 2nd-order central differences (Hirsch, 1990) on Cartesian grids using a 27-point stencil

for higher robustness in regions with steep gradients or discontinuities. Approximations of the components of $\nabla^h \phi$ at the face centers of cell $\mathcal{C}_{i,j,k}$ are computed in two steps. First, their values at the corners of cell $\mathcal{C}_{i,j,k}$ are computed by

$$\left(\frac{\partial \phi}{\partial x}\right)^h_{qrs} = \sum_{l=0}^{1} \sum_{m=0}^{1} \frac{\phi_{i+q,j-1+l+r,k-1+m+s} - \phi_{i-1+q,j-1+l+r,k-1+m+s}}{4h_x}, \quad (3.53)$$

$$\left(\frac{\partial \phi}{\partial y}\right)^h_{qrs} = \sum_{l=0}^{1} \sum_{m=0}^{1} \frac{\phi_{i-1+l+q,j+r,k-1+m+s} - \phi_{i-1+l+q,j-1+r,k-1+m+s}}{4h_y}, \quad (3.54)$$

$$\left(\frac{\partial \phi}{\partial z}\right)^h_{qrs} = \sum_{l=0}^{1} \sum_{m=0}^{1} \frac{\phi_{i-1+l+q,j-1+m+r,k+s} - \phi_{i-1+l+q,j-1+m+r,k-1+s}}{4h_z}, \quad (3.55)$$

where $q, r, s \in \{0, 1\}$ denote the local cell corner coordinates. For example, $(\partial_x \phi)^h_{000}$ denotes the lower left corner and $(\partial_x \phi)^h_{111}$ the upper right corner. The grid spacing along the x, y and z coordinates is denoted by h_x, h_y and h_z, respectively. The second step computes the value at the face center from the cell corners. The first component of $\nabla^h \phi$ at the 6 faces of cell $\mathcal{C}_{i,j,k}$ is then given by

$$\left(\frac{\partial \phi}{\partial x}\right)^h_{i-1/2+q,j,k} = \frac{1}{4} \sum_{r=0}^{1} \sum_{s=0}^{1} \left(\frac{\partial \phi}{\partial x}\right)^h_{qrs}, \quad (3.56)$$

$$\left(\frac{\partial \phi}{\partial x}\right)^h_{i,j-1/2+r,k} = \frac{1}{4} \sum_{q=0}^{1} \sum_{s=0}^{1} \left(\frac{\partial \phi}{\partial x}\right)^h_{qrs}, \quad (3.57)$$

$$\left(\frac{\partial \phi}{\partial x}\right)^h_{i,j,k-1/2+s} = \frac{1}{4} \sum_{q=0}^{1} \sum_{r=0}^{1} \left(\frac{\partial \phi}{\partial x}\right)^h_{qrs}. \quad (3.58)$$

The second and third components follow by analogy. Figure 3.3 illustrates this procedure for $(\partial_x \phi)^h_{i,j,k+1/2}$. Indication of the time level has been omitted in the above notation. The face values of the velocity components for the power products in the diffusive energy flux of equation 3.42 are obtained from arithmetic averages of the adjacent cell centered data.

Extension of equations 3.53 to 3.55 to 4th-order accurate central differences is straightforward and has been implemented in the present work as well.

3.4.4 *Source terms*

The source terms in equation 3.40 are discretized using a 2nd-order accurate method. The volume average of the source terms in cell $\mathcal{C}_i$ is computed analogous to equation 3.33, that is

$$S_i = \frac{1}{V_i} \int_{\mathcal{C}_i} s \, dV, \tag{3.59}$$

where only the last component of s has a non-zero contribution (see equation 3.40). Following Johnsen and Colonius (2006) this term is approximated by

$$\left(\overline{\phi(\nabla \cdot u)}\right)_i \approx \overline{\phi}_i(\nabla \cdot u)_i^h, \tag{3.60}$$

where $\overline{\phi}_i$ denotes the volume average of scalar ϕ in cell $\mathcal{C}_i$. The velocity divergence term is approximated using 2nd-order central differences

$$(\nabla \cdot u)_{i,j,k}^h = \frac{u_{i+1/2,j,k}^x - u_{i-1/2,j,k}^x}{h_x} + \frac{u_{i,j+1/2,k}^y - u_{i,j-1/2,k}^y}{h_y} + \frac{u_{i,j,k+1/2}^z - u_{i,j,k-1/2}^z}{h_z}. \tag{3.61}$$

To ensure consistency with the advective fluxes discussed in section 3.4.2, the velocities to compute the divergence are obtained from the numerical flux Jacobian $\partial \mathcal{F}_j/\partial q$ (Johnsen and Colonius, 2006). Using equations 3.44 and 3.48 they compute to

$$\begin{aligned}
u^j = &\frac{1 + \mathrm{sgn}(s^*)}{2}\left(u_{j,L} + s^-\left(\frac{s_L - u_{j,L}}{s_L - s^*} - 1\right)\right) \\
&+ \frac{1 - \mathrm{sgn}(s^*)}{2}\left(u_{j,R} + s^+\left(\frac{s_R - u_{j,R}}{s_R - s^*} - 1\right)\right),
\end{aligned} \tag{3.62}$$

where the superscript j corresponds to the spatial velocity components in equation 3.61. Similarly, the volume average $\overline{\phi}_i$ is computed from the average of the reconstructed face values in the cell interior

$$\begin{aligned}
\overline{\phi}_{i,j,k} = \frac{1}{6}\big(&(\phi_R^r)_{i-1/2,j,k} + (\phi_L^r)_{i+1/2,j,k} \\
&+ (\phi_R^r)_{i,j-1/2,k} + (\phi_L^r)_{i,j+1/2,k} \\
&+ (\phi_R^r)_{i,j,k-1/2} + (\phi_L^r)_{i,j,k+1/2}\big).
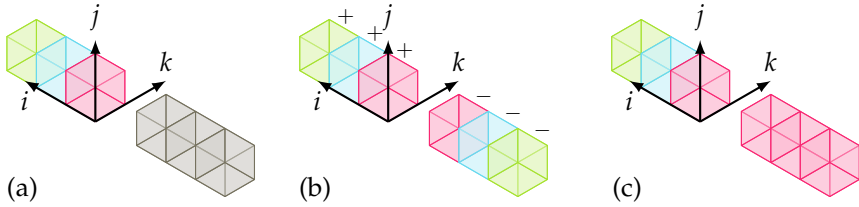\end{aligned} \tag{3.63}$$

FIGURE 3.4: Ghost cells for standard boundary conditions: (a) Dirichlet boundary with prescribed ghost cell values; (b) reflecting boundary; (c) absorbing boundary with zeroth-order extrapolation.

3.4.5 *Boundary treatment*

Apart from default periodic boundaries, standard boundary treatment for wave reflection on walls with infinite impedance, zeroth-order extrapolation for wave absorption and Dirichlet-type boundaries are implemented as well (Laney, 1998; LeVeque, 2002). The realization of boundaries is achieved using ghost cells that are filled with either known physical data or data that is obtained from the interior domain. The boundary condition for a reflecting wall consists of mirroring the interior cell data into the ghost cells and inverting the sign of the wall-normal component in vector fields. Absorbing boundaries extrapolate the cell that is adjacent to the boundary surface into the ghost cells. First-order extrapolations do not exhibit favorable properties especially for discontinuous waves that hit the boundary. These basic concepts are illustrated in figure 3.4.

In general the zeroth-order absorbing boundaries perform well in terms or stability. However, some artificial reflections can not be avoided especially in the case of oblique incoming waves. To counteract this defect, characteristic based non-reflecting boundary conditions are further considered (Engquist et al., 1977; Poinsot et al., 1992; Thompson, 1987, 1990) and have been used for the large scale simulation of cloud cavitation collapse presented in chapter 7.

For viscous flow simulations no-slip boundaries are obtained by adding further conditions for the tangential velocity components. In contrast to the reflecting (slip) wall boundary, the tangential waves in the plane of the no-slip boundary are further constrained from free propagation by sign inversion of the corresponding velocity component in the ghost cell image.

	● 6, Williamson (1980)	Gottlieb et al. (1998)
a_1	0.000 000 000	0.000 000 000
a_2	−0.531 250 000	−2.915 492 525
a_3	−1.185 185 185	−0.000 000 094
b_1	0.250 000 000	0.924 574 000
b_2	0.888 888 889	0.287 713 063
b_3	0.750 000 000	0.626 538 110

TABLE 3.2: LSRK3 coefficients a_i and b_i.

3.4.6 *Time integration*

Time integration is performed using an explicit low-storage 3rd-order Runge-Kutta (LSRK3) method (Williamson, 1980). The memory requirement for this scheme is $2NB$ bytes for N computational cells where each cell $\mathcal{C}_i$ has a memory footprint of B bytes. The minimum storage requirement per cell $\mathcal{C}_i$ are the 5 conserved fields of equations 3.8 to 3.12 which are 7 scalars total. Due to vectorization of the compute kernels, discussed in chapter 4, the total memory footprint per cell is $B = 8P$ bytes, where P is the chosen floating point precision.[2] The vector $Q = (Q_1, \ldots, Q_N)^\mathsf{T}$ denotes the collection of N cells $\mathcal{C}_i$ with Q_i the volume averages of the conserved field values in cell $\mathcal{C}_i$ according to equations 3.33 and 3.37. The right-hand side required for the LSRK3 scheme is denoted by R where $\dim R = \dim Q$. An integration stage $i = 1, 2, 3$ is given by the Euler-step

$$R^{(i)} = a_i R^{(i-1)} + \Delta t \mathcal{L}^h(Q^{(i-1)}), \tag{3.64}$$

$$Q^{(i)} = Q^{(i-1)} + b_i R^{(i)}, \tag{3.65}$$

with coefficients a_i, b_i and $\mathcal{L}^h$ the numerical operator that approximates the right-hand side of equation 3.34 (see sections 3.4.2 to 3.4.4). The integrated state corresponds to $Q^{n+1} = Q^{(3)}$ with $Q^{(0)} = Q^n$. Third-order Runge-Kutta (RK) schemes require the determination of 6 coefficients from 4 independent equations (Kopal, 1961). The coefficients a_i and b_i can therefore be chosen arbitrarily based on two parameters η_1 and η_2. Furthermore, the low-storage property is only satisfied if the parameter pairs (η_1, η_2)

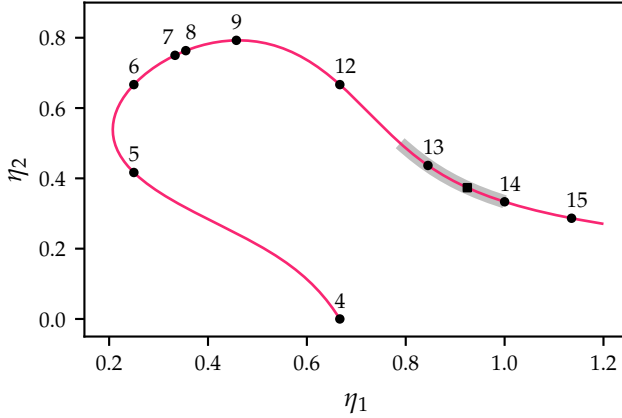2 $P = 4$ bytes for single precision or $P = 8$ bytes for double precision.

FIGURE 3.5: Locus of points (η_1, η_2) for which the low-storage property of a 3rd-order RK scheme is satisfied: ●, LSRK3 coefficients of Williamson (1980); ■, optimized TVD LSRK3 coefficients of Gottlieb et al. (1998). The shaded region corresponds to coefficients that are TVD.

describe the locus shown in figure 3.5. Williamson (1980) proposed different sets of coefficients which are indicated in figure 3.5 by the ● symbols. The case numbers as given in Williamson (1980) are shown next to the symbols. Gottlieb et al. (1998) optimized the CFL number along this locus with the constraint that the resulting LSRK3 scheme is TVD. The optimum they found corresponds to

$$\text{CFL} = 0.32 \tag{3.66}$$

and is indicated in figure 3.5 by the ■ symbol. The numerical values for the parameter set 6 in Williamson (1980) and the optimized parameters of Gottlieb et al. (1998) are listed in table 3.2. The coefficients based on Gottlieb et al. (1998) together with the CFL condition in equation 3.66 are used for the numerical calculations presented in this thesis. A further discussion about TVD RK schemes is given in (Shu, 1988). Parameter sets for TVD schemes that result in more favorable CFL conditions other than the optimum found in Gottlieb et al. (1998) are currently not known.

For a time dependent right-hand side in equation 3.34 the coefficient combinations to compute the current time are given, for example, in Shu

and Osher (1988). Expressed in terms of the LSRK3 coefficients a_i and b_i, the time values of the three stages in equation 3.64 are given by

$$t^{(0)} = t^n, \tag{3.67}$$

$$t^{(1)} = t^n + b_1 \Delta t, \tag{3.68}$$

$$t^{(2)} = t^n + \left(b_1 + (a_2 + 1)b_2\right)\Delta t, \tag{3.69}$$

respectively. In general, $t^{(i-1)}$ may not necessarily be monotonically increasing for $i = 1, 2, 3$.

4

SOFTWARE DESIGN FOR PETASCALE SIMULATIONS OF
CLOUD CAVITATION COLLAPSE

*Software is getting slower more rapidly than hardware
becomes faster.*

— Niklaus Wirth

This chapter presents the software design principles employed in the code development with aim for execution on High Performance Computing (HPC) architectures. The main task is an efficient implementation of the underlying stencil problem for the particular Computational Fluid Dynamics (CFD) application in this thesis. The software framework introduced here is therefore a modular composition of a part that takes care of the ghost cell exchange for both, intra-node and inter-node communication and a second part that implements the computational kernels of the specific problem to be solved. The former part is generic and can be used for any problem that involves stencil computations. The former framework part is called Cubism and the multi-phase compressible flow solver that builds on top of it Cubism-MPCF.

4.1 RELATED WORK

Stencil computations are operations that require information from neighboring compute elements when traversing an array of data. Such multidimensional data is represented in memory by a linear address mapping. Efficient stencil codes on multi-core architectures must therefore exploit spatial and temporal locality of the data in order to reach high performance. Spatial locality is achieved by blocking techniques either at runtime in loop structures or by blocking the data layout (Lim et al., 2001; Rivera et al., 2000; Treibig et al., 2011; Wellein et al., 2009). Temporal locality aims at reuse of data without re-accessing the slow memory modules (Datta, Murphy, et al., 2008; Datta, Kamil, et al., 2009; Günther et al., 2006; Kamil, Chan, et al., 2010; Kamil, Datta, et al., 2006; Kamil, Husbands, et al., 2005; Leopold, 2002; Oliker et al., 2003; Zhao et al., 2019).

The work of Brandvik et al. (2008) is one of the first to add GPU accelerators in a stencil based turbomachinery code. Elsen et al. (2008) performed GPU accelerated computations of hypersonic flows with all data resident on the GPU. Thibault et al. (2009) and Jacobsen et al. (2010) have implemented the incompressible Navier-Stokes equations on multiple GPUs using the Message Passing Interface (MPI). A discussion of a GPU accelerated solver using unstructured grids is given in Duffy et al. (2012).

4.2   DISTRIBUTED STENCIL COMPUTATIONS ON STRUCTURED GRIDS

Stencil computations occur very frequent in scientific computations. Yet, a generic framework that provides efficient HPC tools for point-wise and stencil operations is not trivial to build from scratch and requires time to be accepted for application in the scientific community. Often the accepted solution is a self-made implementation without paying attention to efficient resource exploitation. The result is higher cost, extended time to solution and ultimately energy inefficiency. Two frameworks for AMR with the same origin are described in W. Zhang et al. (2019) and M. Adams et al. (2019). These tools provide the algorithms for AMR and users implement the numerical scheme on top of it with the possibility of similar outcomes mentioned above if the practitioner is not skilled enough. Furthermore, the added complexity of AMR algorithms may not always be necessary or desired. This section provides a brief review of the high-level design principles of the structured grid framework Cubism which were first discussed in the context of the multi-phase compressible flow solver Cubism-MPCF (Hejazialhosseini, Conti, et al., 2013; Hejazialhosseini, Rossinelli, et al., 2012) which was later further optimized to win the Gordon Bell Prize (Rossinelli et al., 2013). The software presented in these references is tightly bound to the particular application and straightforward access to its underlying HPC principles is difficult. Therefore, the last part of this section introduces the newly written template C++ software CubismNova with the aim of separating HPC related design principles from a particular target application. This separation allows to develop an optimized set of HPC tools which are accessible to the general user who is mainly concerned with algorithm and application development.

The Cubism design considerations discussed in the remainder of this section are the ones that are the least bound to a particular application and are referred to as cluster-layer in the aforementioned references.

4.2.1 *Block-structured data layout*

Efficient cache utilization is the most important principle for stencil applications. Algorithms can either be cache-aware or cache-oblivious (Frigo, Leiserson, et al., 1999; Frigo and Strumpen, 2005). It has been shown in Datta, Kamil, et al. (2009) that cache-aware stencil algorithms are faster than their cache-oblivious counterparts. This motivates the use of a block-structured memory layout where the block size is chosen such that the data fits into (preferably) at most the L2 cache. Cubism enforces the block-structured layout in the memory space while other frameworks employ software based blocking techniques (W. Zhang et al., 2019). Both impose spatial locality of the data where the former imposes more control for the granularity of individual contiguous memory segments. This way a "block" is treated as an isolated computational entity which becomes the input/output (I/O) of computational kernels that perform certain transformation of the data. The computational kernels implement the low-level optimizations and can be created by code generation methods that target different architectures such as multi-core CPUs or accelerator hardware such as GPUs. A compute block is a generic entity that can carry either built-in or user defined data types. It is worthwhile to note that, while object-oriented programming (OOP) is preferable for software structure and modularity at the high-level, its paradigm is performance adverse for which a data-oriented design (DOD) is preferred.

This data layout is well suited for the multiple program multiple data (MPMD) programming model (Hennessy et al., 2017) that is implemented in Cubism using MPI. A Cartesian MPI topology is chosen for uniform grids such that load imbalance is minimized. The block-structured data layout described above is also well suited for AMR algorithms where load balancing becomes a non-trivial task (van Straalen et al., 2009). The MPI process mapping further plays a role for inter-node performance considering the block-structured memory layout described above. In particular, compute blocks are designed to fit into the fast cache memories nearby the CPU which means the block size is in the order of kilobytes. Inter-node communication traffic is routed through the system area network (SAN) for which bandwidth saturation is only achieved after a certain message size. Figure 4.1 shows bandwidth measurements[1] corresponding to various message sizes sent through the on-chip network (OCN), where the two communicating processes are located on the same node, the SAN, where

---

1 OSU Micro-Benchmarks 5.6.3 `https://mvapich.cse.ohio-state.edu/benchmarks`
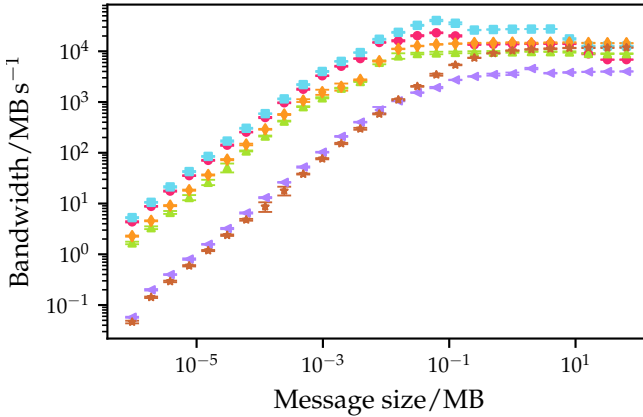
FIGURE 4.1: OCN on a Cray XC50 node: ●, sustainable bandwidth; ■, sustainable aggregate bandwidth. SAN between two Cray XC50 nodes and Cray Aries interconnect: ▲, sustainable bandwidth; ◆, sustainable aggregate bandwidth. Gen. 3 PCIe on a Cray XC50 node: ◀, pageable; ★, page-locked.

the two communicating processes are located on two different nodes, and through the peripheral component interconnect express (PCIe) which is commonly used to connect accelerator devices such as GPUs. A 5th-order WENO reconstruction requires 3 ghost cells at the boundary which results in a message size of 24 kB for one double precision field and a block size of 32^3 cells. It is difficult to consistently saturate the system bandwidth with such small message sizes. This problem is alleviated by the use of a Cartesian grid of compute blocks on the MPI process level. Messages to neighboring processes are then explicitly buffered in communication buffers to reach a satisfactory bandwidth saturation. Spatial block locality in the Cartesian block grid is enhanced by a space filling curve (SFC) such as a Morton (1966) ordering.

4.2.2 *Ghost cell treatment*

Extra storage for ghost cells is not embedded in the main block-structured data layout. Instead, blocks that require ghosts for stencil computations are loaded into an auxiliary block that is extended with the appropriate stencil size. This allows for more flexible treatment of non-symmetric stencils and
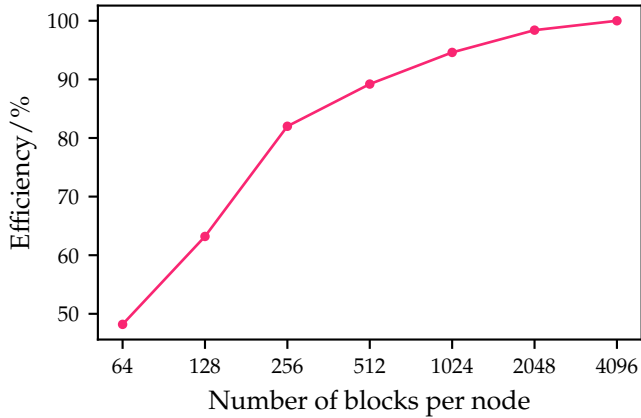
FIGURE 4.2: Efficiency of C/T overlap measured on the MIRA BGQ machine using 512 nodes.

minimizes the excessive memory footprint of auxiliary padded structures. This excess becomes even more pronounced for low-level optimizations where the efficiency of useful memory is 61 % for a stencil with 2 ghost cells in a block of 32^3 cells, optimized by using Advanced Vector Extensions (AVX) instructions. The extra memory copies associated to filling an extended block come at no extra cost due to compulsory cache misses. Once the block is ready for kernel dispatch, the cache is already populated with the necessary data.

Synchronization of ghost cells that require MPI is explicitly managed using communication buffers in asynchronous mode. Parallel entities can query the synchronization state to receive a list of blocks that do not have data dependencies beyond the owning process. This enables a Compute/Transfer (C/T) overlap that can be used efficiently to hide latencies due to MPI communication. The packing of ghost cells into larger buffers further helps to reduce these latencies by minimizing the transmission time due to fully sustained bandwidths as shown in figure 4.1. Figure 4.2 shows measured data for the efficiency of the C/T overlap using 512 nodes on the MIRA BlueGene/Q (BGQ) machine at Argonne National Laboratory (ANL). For this experiment, the MPI ranks were mapped to nodes and the 64 cores on each BGQ node were used in a symmetric multiprocessing (SMP) configuration. The low efficiency at small block counts is due to underutilization of the processor cores.

4.2.3   *CubismNova*

A number of different applications for incompressible flow and data compression have emerged based on the principles outlined above (Hadjidoukas and Wermelinger, 2019; Karnakov, Litvinov, et al., 2020; Karnakov, Wermelinger, Chatzimanolakis, et al., 2019; Karnakov, Wermelinger, Litvinov, et al., 2020; Verma et al., 2018). They all have in common some changes to the Cubism framework to fit application specific needs. These individual adjustments lead to divergence of the same code base but the main library routines for synchronization and block management remain the same.

For these reasons, the Cubism library has been rewritten to increase its application spectrum and make its underlying HPC concepts more accessible to a wider audience. The rewritten library is named CubismNova and its full documentation is hosted at `https://cubismnova.readthedocs.io`.

The core changes in its redesign address the underlying data structures that are hidden from library user. The user implements physical models based on tensor fields that are provided by CubismNova. Tensor fields are composed of compute blocks following section 4.2.1. At the low-level, tensor fields are described by an index space that depends on the resolution scheme which in turn determines a suitable memory allocator for the data. A uniform grid solver, for example, utilizes a global Cartesian index space for which the data is static. An AMR application, on the other hand, requires a dynamic allocation scheme that must minimize overhead due to frequent requests to the operating system kernel. Furthermore, fragmentation can become an issue in this case.

On the high-level, every application requires physical coordinates of the computational elements in order to perform its calculations. This requires a mapping of the low-level index space coordinates onto a mesh that describes the discrete coordinates in the computational domain. CubismNova uses generic mesh classes that may describe a trivial Cartesian mesh for uniform or stretched grid applications or more advanced mesh classes for an AMR solver or tensor fields that describe moving particles instead of Cartesian grids. Another important consideration is the entity type that the data represents. The mesh classes that wrap around tensor fields in CubismNova support cell centered, face centered or node (vertex) centered data.

Finally, compute blocks are the arguments to the computational kernels which are not concerned with the higher level representation of fields. This

allows to implement different kernels for basic operations such as finite differences, interpolation or data compression and offer them in a toolbox to the application developing user. Implementations can further be optimized by using single program multiple data (SPMD) programming models such as the Intel ISPC compiler (Pharr et al., 2012) to generate vectorized code for various architectures more efficiently. Lastly, inclusion of accelerator devices such as GPUs is readily supported in this model as well.

The development of CubismNova is ongoing. Its current state has implemented and tested the high-level concepts of sections 4.2.1 and 4.2.2 for Cartesian fields by following the generalized concepts introduced in this section.

4.3 HIGH THROUGHPUT SIMULATIONS OF COMPRESSIBLE TWO-PHASE FLOW

The multi-phase compressible flow solver Cubism-MPCF was initially presented in Hejazialhosseini, Rossinelli, et al. (2012) for a system of conservation laws that describes the evolution of the mixture density instead of the phasic densities. Furthermore, this system describes the fluid components with two transport equations for the mixture averaged parameter of the SGEOS (Shyue, 1998). In contrast to section 3.1, the chosen degrees of freedom for the interface description freeze the thermodynamic state of the mixture and do not allow to take into account compressibility effects in the interface zone. The approximate Riemann solver used in this code was based on an earlier HLL-type solver with only one approximate state for the intermediate wave structure, see figure 3.2(b) for the HLLC solver where two intermediate states are used.

The core compute kernels of Cubism-MPCF have been rewritten to implement the system of equations 3.8 to 3.12 as well as the HLLC solver described in section 3.4.2. The results of this work are presented in the remainder of this section. The results for the optimized HLLC implementation have been published in Hadjidoukas, Rossinelli, et al. (2015) and scaling results were published in Rasthofer, Wermelinger, Hadjidoukas, et al. (2017). The solver is open-source and can be downloaded from `https://github.com/cselab/Cubism-MPCF`.
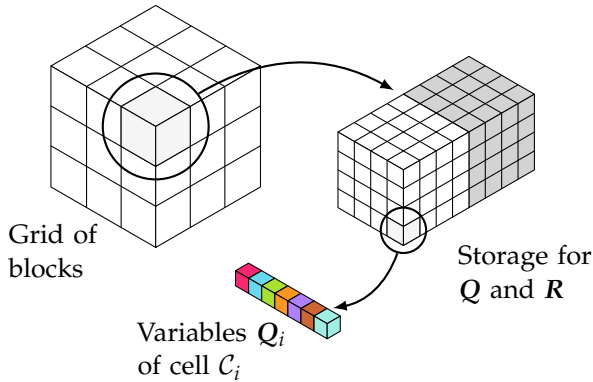
Grid of
blocks

Storage for
Q and R

Variables Q_i
of cell $\mathcal{C}_i$

FIGURE 4.3: AoS compute block structure used for the Cubism-MPCF solver with additional storage for the LSRK3 integrator.

4.3.1 *Low-level optimizations*

The data structure to represent a compute block in Cubism-MPCF is shown in figure 4.3. Each process hosts a Cartesian grid of blocks which is distributed according to section 4.2.1. Any cell $\mathcal{C}_i$ stores the volume averaged field values of the conserved quantities given in equation 3.37. Such data arrangement results in an array of structures (AoS) layout in memory. In cases where a compute kernel requires all cell values to perform a particular task, the AoS and the structure of arrays (SoA) layouts perform similar in regard to memory access efficiency. In general, however, the DOD principle is enforced by the SoA layout and should be preferred for performance reasons. The CubismNova library, introduced in section 4.2.3, implements the DOD principle hidden from the application oriented user. Lastly, the storage requirement in each block is doubled to allocate memory for the LSRK3 integrator. In order to exploit the full floating point performance of recent CPUs, the compute kernels must employ vector instructions for the data transformations. This requires that the block data is aligned at byte boundaries that are integer multiples of the vector register width. The 7 components of Q_i (see figure 4.3) clearly violate this requirement. This issue, however, is readily resolved by padding the data structure stored in cell $\mathcal{C}_i$ to the nearest power of two. The total memory footprint for a block in double precision then amounts to 1331 kB for a 16^3 base block size in an auxiliary stencil structure with 3 ghost cells on each side (e. g. 5th-order WENO reconstruction).
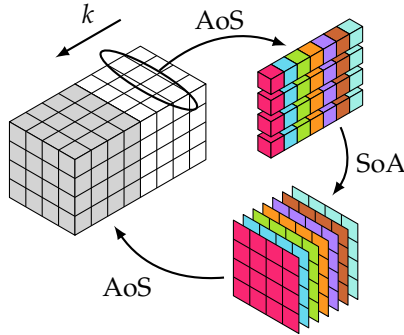
FIGURE 4.4: Explicit data reordering for SIMD vectorization.

The solver is utilizing the C/T overlap capabilities mentioned in section 4.2.2 by mapping MPI processes to either nodes or sockets. The thread-level parallelism (TLP) on the compute nodes is further exploited using the Open Multi-Processing (OpenMP) programming model for SMP architectures. The target systems for this work are the IBM BGQ and the Cray XC30/XC50 architectures. The PowerPC A2 on the BGQ is a 16-core CPU with 2 MB last level cache (LLC) per core (Haring et al., 2012). Similarly, the Cray XC30 hosts a 8-core Intel Xeon E3-2670 CPU with 2.5 MB LLC per core and the Cray XC50 hosts a 12-core Intel Xeon E5-2690 v3 CPU with 2.5 MB LLC per core. For each of those architectures the 1331 kB compute blocks fit into the shared LLC when TLP is employed.

All of the target CPUs feature instruction set architecture (ISA) extensions that are used for vectorization of the compute kernels. The multiply-add operations in equations 3.64 and 3.65 are point-wise operations and trivial to vectorize. Most recent compilers would auto-vectorize them if intermediate or aggressive optimization options are passed. Vectorization of the operator $\mathcal{L}^h$ is non-trivial and compilers can not automatically generate satisfactory results. The operator is therefore explicitly vectorized on a single instruction multiple data (SIMD) friendly 2D data structure. The data reordering from AoS into 2D SoA slices is shown in figure 4.4. Individual slices of a field are arranged in a ring buffer which contains as the number of slices required to populate stencil width along the k-index direction. The block data is processed by iterating along k where the ring buffer is rotated and updated with a new slice in every iteration. Note that the k-index is the slowest moving index in the block data array. Slices are special structures that are properly byte aligned and padded to support the Intel x86-64 Streaming

Level	Description
0	No fusion, 8 micro-kernels.
1	As level 0 with reduced accuracy of WENO smoothness indicators.
2	Fusion of energy flux with wave speed estimator, as well as fusion of mass flux with the diagonal entry of the momentum flux, 6 micro-kernels.
3	As level 2 with reduced accuracy of WENO smoothness indicators.
4	Aggressive fusion of all micro-kernels into a single macro-kernel with code transformations and reduced accuracy of WENO smoothness indicators.

TABLE 4.1: Code-fusion levels used for the computation of the numerical flux $\mathcal{F}_j$.

SIMD Extensions (SSE) and Advanced Vector Extensions (AVX) instructions as well as the IBM Quad Processing eXtensions (QPX) instructions. The AoS to SoA data reordering is combined with the conversion from conservative to primitive variables and does impose additional overhead.

Additional reduction of cache misses can be achieved by increasing the instruction-level parallelism (ILP) of compute kernels and eliminating common sub-expressions that are otherwise not visible to the compiler. Such optimizations are at the cost of additional register usage which may result in worse performance if there are excessive amounts of register spills. The multi-purpose design of CPUs is more amenable for such code-fusion optimizations than the massively parallel GPU architectures addressed in section 4.4.2. Computing the numerical flux in equation 3.52 requires 7 compute kernels for each of the flux components and an additional kernel to compute the wave speed estimates (Batten et al., 1997; Einfeldt, 1988). The naive implementation averages at 22 lines of code per kernel. Table 4.1 shows the various code-fusion levels considered for the 8 kernels used in the numerical flux computation with level 4 being the most aggressive. In addition to fusing the micro-kernels associated to the operator $\mathcal{L}^h$, reduction of complexity for the WENO smoothness indicators allows for further code optimizations. Optimizations for floating point division based on one and two iterations of the Netwon-Raphson scheme as well as the IBM intrinsic SWDIV for software floating point division (IBM, 2018) have been considered
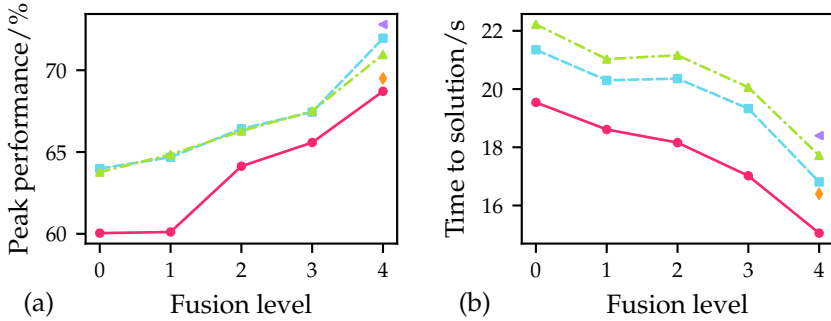
FIGURE 4.5: Single precision performance of the HLL and HLLC numerical fluxes: (a) percentage of nominal peak performance; (b) time to solution for one time step. ●, HLL with one Newton-Raphson iteration; ■, HLL with two Netwon-Raphson iterations; ▲, HLL with IBM SWDIV intrinsic; ♦, HLLC with one Netwon-Raphson iteration; ◄, HLLC with two Newton-Raphson iterations.

as well. The performance of these low-level optimizations has been evaluated on a single BGQ chip without MPI synchronization overhead. A total of 4096 blocks are used for the benchmark, corresponding to 134 Million computational cells $\mathcal{C}_i$ processed on 16 cores. The performance figures have been collected using the IBM Hardware Performance Monitor Toolkit and the executable has been generated with the IBM XL C/C++ compiler (v12.1) for single precision data. Figure 4.5 shows the results for the different code fusion levels. It is shown in figure 4.5(a) that the most aggressive optimization of the HLLC flux implementation can achieve 72.8 % of the nominal peak performance on BGQ. This corresponds to an improvement of 8 % relative to the naive implementation. Compared to the HLL flux, the HLLC flux achieves better peak performance due to the more complex algorithm that induces more fused multiply-add (FMA) instructions (but also more branching). Although the HLLC flux improves the resource utilization, its higher complexity results in an increase of the measured time to solution (TtS) of about 9 % compared to the previous HLL flux. The measured TtS for the different code-fusion levels is shown in figure 4.5(b).

The total cell throughput for the HLLC implementation with level 4 code fusion and two Newton-Raphson iterations for divisions is $455\,902\,\mathcal{C}\,\mathrm{s}^{-1}$ per core and $511\,500\,\mathcal{C}\,\mathrm{s}^{-1}$ per core for one Newton-Raphson iteration. For comparison, the cell throughput of the previous implementation of Cubism-MPCF (Rossinelli et al., 2013) is $458\,394\,\mathcal{C}\,\mathrm{s}^{-1}$ per core and HLL-type flux
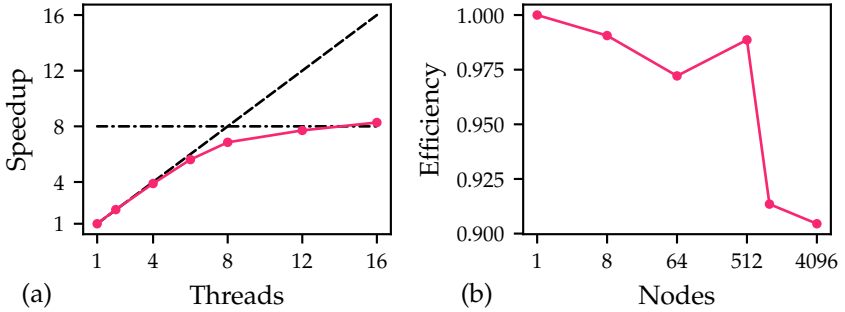
FIGURE 4.6: Scaling of Cubism-MPCF on Piz Daint: (a) strong scaling speedup on a Cray XC30 node; (b) weak scaling efficiency for 4096 Cray XC30 nodes.

kernels. The numerical results in the following sections of this thesis are computed using the code-fusion level 2, i. e., no approximate floating point divisions.

4.3.2 *Scaling analysis*

The previous sections addressed the high-level and low-level HPC design considerations for the Cubism-MPCF solver. The scaling analysis is performed using 4096 Cray XC30 nodes on the Piz Daint supercomputer at Swiss National Supercomputing Center (CSCS), where each node is equipped with an 8-core Intel Xeon E5-2670 CPU. The executable code has been generated with the GNU C++ compiler (v4.8). The block size consists of 32^3 cells and each node hosts 4096 blocks. The total memory footprint for this configuration is 8 GB per node.

Figure 4.6(a) shows the strong scaling on a single node with Intel Hyper-Threading Technology (HT) enabled. The solver exhibits an excellent node-level performance also for the Intel x86-64 architecture. Additional gain due to HT is almost zero because of the high cache utilization (see section 4.2.1). The Craypat profiler reports a 95.3 % hit ratio for the L1D cache and 99.5 % for the L1D and L2 caches combined. The cheap context switches of hardware threads in HT can hide latencies when threads need to wait for data to arrive. Because of the high temporal locality achieved here, such context switches rarely happen which is the reason for the asymptotic behavior seen in figure 4.6(a).

The weak scaling efficiency for 4096 Cray XC30 nodes (78 % of the machine capacity) is shown in figure 4.6(b). The TtS for a time step averages at 18.4 s. This result is similar to the BGQ performance shown in figure 4.5(b). It is noteworthy that the 16 cores on a BGQ node are clocked at 1.6 GHz (Haring et al., 2012) while the 8 cores on a Cray XC30 node are clocked at 3.3 GHz maximum. The loss in efficiency is due to the collective MPI all-reduce operation required to synchronize the admissible Δt for each time step. This global operation can not be hidden efficiently by computation and becomes more pronounced for larger node counts which span larger portions of the Dragonfly network topology used on Cray systems. Considering these inefficiencies, the solver exhibits a satisfactory 90 % weak efficiency on almost all of Piz Daint. The average time to execute one LSRK3 stage is 6.05 s for a single node and 6.13 s for 4096 nodes which demonstrates the almost perfect 0.987 C/T overlap when performing the stencil computations.

4.4 HETEROGENEOUS CPU/GPU ARCHITECTURES

Recent and future HPC platforms employ compute accelerators such as GPUs in order to reach into the exa-scale era. This section presents a hybrid CPU/GPU algorithm that is designed to offload the compute intensive right-hand side computation in equation 3.64 onto an accelerator device. The algorithm is designed for hybrid execution of 3D problems with large memory requirements. Typical memory available on recent GPUs ranges from 16 GB to 32 GB while the available memory on the host node is usually 2–4 times larger. In order to scale a problem on large HPC systems, the main memory must be kept on the host node and the GPUs are used for acceleration.

Mapping the right-hand side computation of the operator $\mathcal{L}^h$ in equation 3.64 to GPUs requires different considerations regarding the memory layout discussed in section 4.2.1. In particular, GPUs are massive DLP devices and require large data streams in order to maximize the hardware utilization. The classification of GPUs is similar to SIMD except that the primitive is a thread which are grouped into thread blocks for collective execution. Instead of instructions, so called *warps* are scheduled where a warp consists of 32 threads that execute in lockstep. Nvidia classifies this execution model as single instruction multiple threads (SIMT). The number of threads that can run concurrently on a GPU is determined by the complexity of the computational task. Lightweight kernels with low

resource requirements can run with large concurrency. Therefore, suitable applications for GPU porting must be decomposable into smaller tasks with a high number of (arithmetic) operations relative to accessed bytes. This is especially true for high-order numerical methods. On the downside, such methods are often stencil schemes that impose restrictions on the exploitable DLP. The GPU approach introduced in the sections below aims at maximizing this parallelism until the hardware limit is reached. It is easily verified by calculating the operational intensity (OI) of the target operator $\mathcal{L}^h$ that the problem is memory bound on any recent GPU. The memory modules on GPU have about 5-times larger bandwidths than their CPU counterpart. A maximum improvement of $5\times$ can therefore be expected when comparing to the multi-core code. Any larger improvement can only be due to benchmarking against a CPU code that is not fully optimized (V. W. Lee et al., 2010).

The main difficulty for a heterogeneous code is therefore to provide a C/T overlap between the CPU and GPU such that the latency of the connecting network is hidden efficiently (Williams, Shalf, et al., 2007). The work presented in the following sections has been published in Wermelinger, Hejazialhosseini, et al. (2016). Its target accelerators are Nvidia architectures with compute capability 3 or higher. The GPU relevant code is written using the Compute Unified Device Architecture (CUDA) language extension for C++ (Hwu et al., 2009; Lindholm et al., 2008; Nickolls et al., 2008).

4.4.1   *Heterogeneous algorithm for stencil problems*

In contrast to the memory layout discussed in section 4.2.1, the computational blocks dispatched onto GPU accelerators are designed for optimal memory utilization. Their memory footprint is therefore in the order of gigabytes to provide enough DLP for efficient resource utilization. A method for efficient GPU cache exploitation for 3D problems is discussed in the next section. The algorithm presented in this section applies to a single compute node with access to a Nvidia GPU accelerator. The management of ghost cells and inter-node communication is analogous to the multi-core code discussed in section 4.2.

Figure 4.7 shows the partitioning of the computational domain on a host node into smaller segments s for GPU scheduling. The size of the segments is parametrized by the number of cells $N_{z,s}$ along the k-coordinate in index space. The computational domain on the host consists of N cells
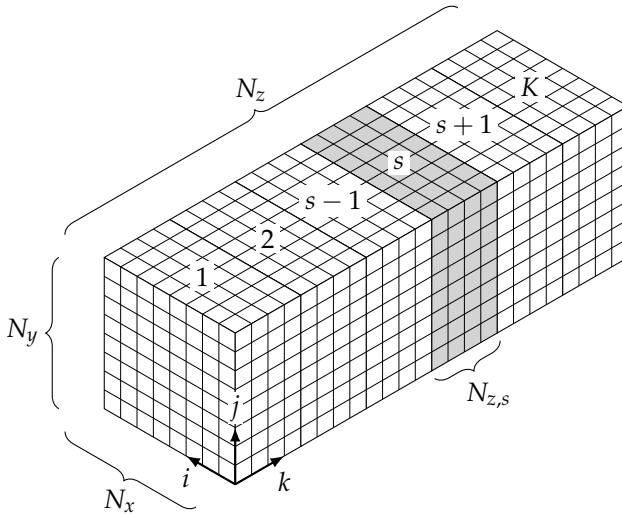
FIGURE 4.7: Partition of the computational domain on the host node into segments s.

where k is the slowest moving index. Let vector V denote a scalar field for N volume averaged cells which are stored in a SoA memory layout. Its elements are scalar values while the elements of the volume averaged vector Q are state vectors of the conserved variables (see equation 3.37). The data that corresponds to segment s is denoted by V_s and consists of $N_s = N_x \times N_y \times N_{z,s}$ cells. The communication with the GPU is performed by using a pair of page-locked memory buffers for P segments V_s. Page-locked memory allows for direct memory access (DMA) which improves memory bandwidth by circumventing certain CPU overhead. Figure 4.1 shows the sustainable bandwidth for pageable and page-locked memory of the PCIe on a Cray XC50 compute node. Note that for the SoA layout, 7 individual arrays V are required to represent the conserved variables. The heterogeneous algorithm discussed here is agnostic to them and so they are not distinguished any further. The asynchronous copy-engines on GPUs with compute capability 3 or higher are used to transfer the data between host and device. The first page-locked buffer is mapped to host to device (H2D) transfers while the second buffer is mapped to device to host (D2H) transfers. The dual copy-engines on these devices allow for overlapping data transfers in either direction. This feature is exploited by grouping the page-locked buffer pairs and arranging them on a ring with a
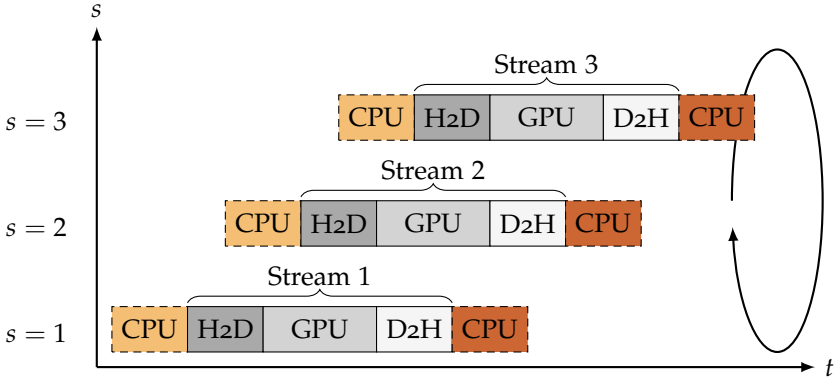
FIGURE 4.8: CUDA streams mapped to segment data V_s for task scheduling on a GPU. The streams are arranged on a ring structure used to iterate over the segments s.

total of P pairs. The ring structure allows to optimize for the C/T overlap by mapping each buffer pair to a CUDA stream that is used to schedule the tasks for execution on the GPU (Nvidia, 2020). For this application it is found that $P = 3$ buffer pairs are enough for contention free iteration over the K data segments. Figure 4.8 shows the ring arrangement of CUDA streams and the C/T overlap achieved by using individual streams. Since the execution order of CUDA streams is undefined, a preferred execution order is imposed using CUDA events. However, the tasks in a stream that occupy the GPU compute engine can not overlap with similar tasks in other streams. This sequential execution order of the GPU compute engine is further indicated in figure 4.8.

The distribution of work between the host CPU and the GPU is achieved by offloading the work of equation 3.64 and performing the cheaper update of equation 3.65 on vectorized CPU code. Hence, the initial CPU work performed on a segment stream corresponds to copying the segment data into the page-locked memory buffer for dispatch to the GPU. After the processed data is returned from the GPU the host CPU performs the final update according to equation 3.65. These initial and terminal CPU tasks are further shown in figure 4.8. The sequence of steps involved for a heterogeneous processing of K segments is summarized in algorithm 1.

Algorithm 1: Heterogeneous processing of LSRK3 stage i

Input: $V^{(i-1)}$ for all conserved variables where $V^{(0)} = V^n$.
Output: $V^{(i)}$ for all conserved variables.

1   $s \leftarrow 1$
2   Copy $V_s^{(i-1)}$ into page-locked buffer of stream s mod P
3   Enqueue GPU tasks on stream s mod P
4   **while** $s < K$ **do**
5   **if** $s > 1$ **then**
6       $\mathcal{L}_{s-1}^{h,(i)} \leftarrow$ Synchronize with stream $(s-1)$ mod P
7       $V_{s-1}^{(i)} \leftarrow$ Update on host using equation 3.65 and $R_{s-1}^{(i-1)}$ from host memory
8     $s \leftarrow s + 1$
9   Copy $V_s^{(i-1)}$ into page-locked buffer of stream s mod P
10   Enqueue GPU tasks on stream s mod P
11   $\mathcal{L}_s^{h,(i)} \leftarrow$ Synchronize with stream s mod P
12   $V_s^{(i)} \leftarrow$ Update on host using equation 3.65 and $R_s^{(i-1)}$ from host memory

---

4.4.2   *GPU kernels for the HLLC solver*

The goal of the GPU computation is the accelerated evaluation of the operator $\mathcal{L}^h$ in equation 3.64. The implementation discussed here is focusing on the advective fluxes in equation 3.41 but readily extends to diffusive fluxes as well. The complexity of a certain compute task determines the number of registers required to perform the arithmetic operations. The register file on a GPU is a scarce resource and the compute kernels must be written with that in mind. The evaluation of the numerical flux $\mathcal{F}_j$ along split spatial directions $j = 1, 2, 3$ is important for the GPU implementation as it leads to compute kernels with manageable register counts.

The page-locked buffer pairs of the previous section are matched with two global memory buffers A and B in GPU memory. Buffer A is used for I/O correspondence with the host CPU. The second buffer B is a read-only 3D CUDA array that is bound to texture references. Texture memory is used to maximize temporal locality while the CUDA array improves spatial locality. The number of buffer pairs on the GPU matches the P pairs used

---
Algorithm 2: Approximation of Riemann problem on the GPU

> **Input:** V_s for all conserved variables.
> **Output:** $\mathcal{L}_s^h$ for advective fluxes.

1 Convert data in A to primitive variables (in-place)
2 Copy data in A into CUDA 3D array B
3 Bind B to global texture reference
4 **forall** $j \in \{1, 2, 3\}$ **do**
5 $\quad$ WENO reconstruction from texture B in direction j
6 $\quad$ HLLC flux divergence in direction j

---

on the host CPU. Hence, P determines the granularity and determines the maximum segment size N_s. The main steps performed in the GPU compute engine are summarized in algorithm 2.

The stencil problem is addressed by using 2D thread blocks with 4 warps in each block. The slim tiles allows for efficient use of the texture cache along the direction normal to the tiles. This method is different than the usual 3D thread block approach which are used together with shared memory (Kamil, Datta, et al., 2006; Micikevicius, 2009). The latter approach imposes a larger restriction on the total active thread blocks due to limited shared memory and therefore reduces exploitable parallelism. The issue becomes more pronounced if high-order numerical methods are used, such as the 5th-order WENO reconstruction. The use of shared memory ensures spatial locality, however, the approach discussed here enforces spatial locality by using CUDA arrays with a suitable SFC. The main benefit of the smaller 2D thread blocks then results in a higher utilization of the GPU texture cache. Furthermore, the large 3D stencil imposes high pressure on the register file which may result in expensive register spills. An overview of the lightweight GPU kernels mapped to 2D thread blocks is given in table 4.2. The WENO reconstruction kernels are written using C++ templates to generate compiled code that maps to a specific texture memory reference. The computation of the numerical flux and the flux divergence is fused into one kernel to avoid excessive access to global memory. The fused kernel increases ILP at the cost of reduced occupancy. The increased ILP still helps with hiding latency and no significant performance impact occurs due to the reduced amount of active thread blocks (Volkov, 2010). The high-order WENO reconstruction reaches full occupancy and it is shown in the

Kernel	Registers per thread	Occupancy
Convert	24	100 %
WENO (x, y)	29	100 %
WENO (z)	32	100 %
HLLC (x)	32	100 %
HLLC (y, z)	56	56 %
Transpose (x)	64	50 %

TABLE 4.2: GPU register usage per thread and occupancy for thread blocks with 4 warps. The WENO reconstruction corresponds to a 5th-order scheme.

next section that this kernel indeed operates at the nominal performance limit of the hardware.

The arrangement of 2D thread blocks on the kernel grid is shown in figure 4.9 for execution along the x-direction (index i). Fluxes must be evaluated at the bounding faces $\mathcal{S}_{i-1/2,j,k}$ of the computational cells. Thread blocks are therefore mapped onto face locations $i - 1/2$ resulting in $N_x + 1$ thread blocks. To benefit from vectorized code on the host CPU the number of cells N_x is usually a power of two. Hence, the 2D thread block design further helps to overcome the $N_x + 1$ irregularities resulting in less complex code. Ghost cell data for thread blocks in boundary zones is obtained from a global memory buffer instead of textures (indicated by the blue cells in figure 4.9). Interior ghost cells are loaded into the texture cache by neighboring thread blocks and can be accessed in cache from nearby threads without overhead. This is the case for most of the thread blocks in the kernel grid. The result of the WENO reconstruction is written back to auxiliary arrays in global memory. The HLLC kernel is then launched on the same kernel grid to compute the numerical flux and the divergence. The result is written back into the I/O buffer in global memory. A transposition kernel is required for computations along the x-direction to ensure coalesced global memory access. The data transposition is implemented using shared memory.
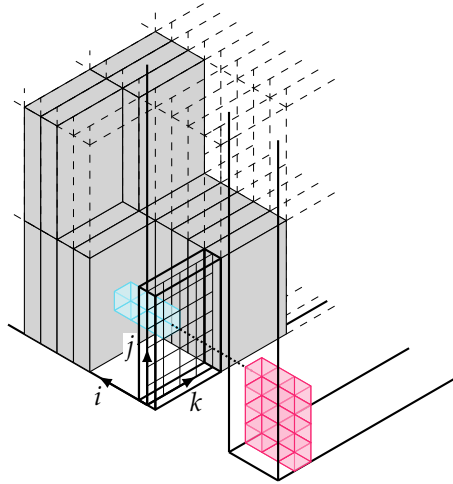
FIGURE 4.9: 2D thread block mapping for stencil evaluation at cell faces. The case for kernel execution along the *x*-direction is shown.

4.4.3   *Performance analysis*

The performance evaluation of the GPU compute kernels has been carried out using the Cray XC30 compute nodes on the Piz Daint supercomputer of CSCS. Each of these nodes hosts an 8-core Intel Xeon E3-2670 CPU and a Nvidia Tesla K20X GPU. The compute kernels are benchmarked using single precision floating point data and the Roofline model of Williams, Waterman, et al. (2009). The measured performance is shown in figure 4.10. The attainable peak performance on a GPU device is lower than the nominal hardware limits, mainly due to voltage fluctuations and error correcting codes (ECCs). The attainable bandwidth when ECC is enabled is usually around 70 % of the nominal value. The attainable ceilings, ——, are obtained by using a micro benchmark (Danalis et al., 2010). The OI of the GPU kernels is computed under the assumption of compulsory cache misses only. The executed floating point instructions and kernel execution time are measured using the Nvidia profiler. The performance of the WENO reconstruction is 907.6 Gflop s^{-1} and shows uniform behavior for all spatial directions. However, a 5th-order WENO reconstruction can at most reach about 23 % of the nominal peak performance on the tested GPUs. The overall performance for computing $\mathcal{L}_s^h$ is 462.4 Gflop s^{-1} and corresponds to a total improvement of 3.1× relative to the BGQ performance of the
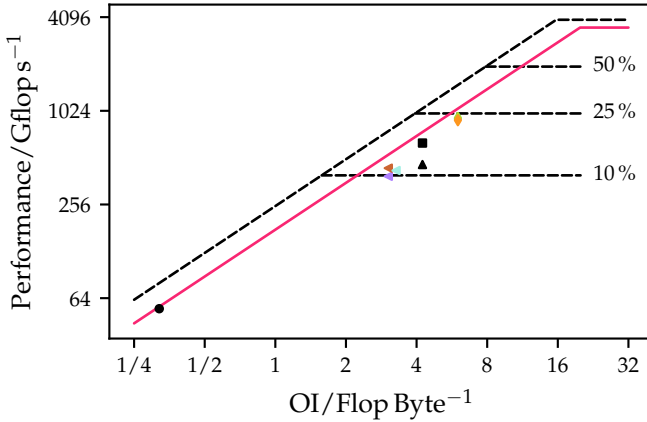
FIGURE 4.10: Roofline of the compute kernel performance on a Nvidia K20X GPU for single precision: ▬ ▬ ▬ ▬, nominal hardware ceiling; ▬▬▬▬, attainable ceiling obtained by micro benchmarks; ●, convert kernel; ■, estimate for computation of $\mathcal{L}_s^h$ using linear textures; ▲, measured performance for computation of $\mathcal{L}_s^h$ using CUDA 3D arrays; 5th-order WENO reconstruction kernels along: ▲, x; ▲, y; ▲, z; HLLC flux kernels along: ◆, x; ◆, y; ◆, z.

optimized multi-core code (Hadjidoukas, Rossinelli, et al., 2015). This result is shown by the symbol ▲ in figure 4.10.

The average time distribution for the execution of one time step Δt using algorithm 1 is shown in figure 4.11. The work performed in figure 4.11(a) corresponds to the queued tasks in the CUDA streams shown in figure 4.8. The computation of Δt at the beginning of the time step is performed using a vectorized kernel on the host CPU. The copies into the DMA buffers and the final LSRK3 update of equation 3.65 are almost in balance which is advantageous for C/T overlap. Slightly more time is spent in the H2D transfers because of the larger message sizes due to ghost cells. The main issue on the GPU are the expensive CUDA Application Programming Interface (API) calls associated to populating the texture buffers by a SFC for spatial locality. This is evident from figure 4.11(b). Due to the proprietary nature of the CUDA toolkit, the specific details of the API implementation are not clear. In order to circumvent these expensive function calls, the CUDA 3D arrays can be replaced by 1D arrays that can be filled with data directly through the H2D data transfer. Binding the arrays to textures is at no cost. To maintain spatial locality, it is required that the arrays used with
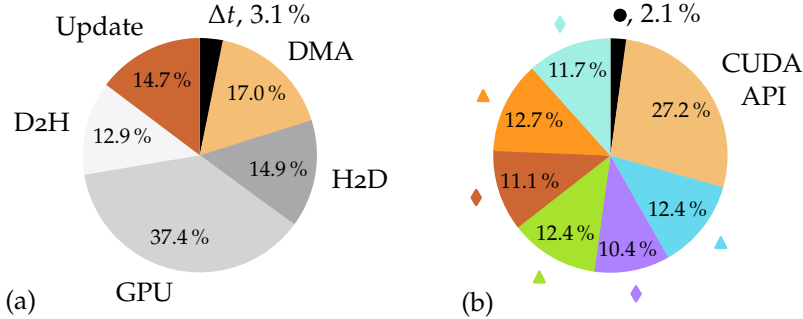
FIGURE 4.11: Time distribution of the heterogeneous algorithm: (a) average time for one LSRK3 time step; (b) average time spent for the GPU kernels and CUDA API. ●, conversion to primitive variables; 5th-order WENO reconstruction along: ▲, x; ▲, y; ▲, z; HLLC flux along: ◆, x; ◆, y; ◆, z. See figures 4.8 and 4.10 as well.

the GPU accelerated solver implement a block-structured data layout at the granularity of the segments shown in figure 4.7. The CPU related tasks in figure 4.11(a) are only point-wise operations which means that working with memory blocks larger than the LLC will not degrade the performance of the CPU kernels. The estimate for the improvement of the right-hand side computation, when neglecting the overhead of the CUDA API calls, corresponds to 4.7× (symbol ■ in figure 4.10) and is in concert with the hardware limit of 5× for memory bound problems.

4.5   SUMMARY

This chapter has introduced the multi-phase compressible flow solver Cubism-MPCF which is used for the large scale numerical simulation of cavitating flows presented in this thesis. The solver has been modified by the HLLC numerical flux which has superior resolution of interfaces in multi-phase flows compared to the HLL-type flux of an earlier implementation. The modified implementation has a computational cell throughput of $455\,902\,\mathcal{C}\,\mathrm{s}^{-1}$ per core with almost perfect C/T overlap and exhibits excellent scaling on state of the art HPC platforms. The solver can be downloaded from https://github.com/cselab/Cubism-MPCF.

To increase the application spectrum and make its underlying HPC concepts accessible to a wider audience, the core Cubism stencil framework has

been refactored into CubismNova. The rewritten framework inherits the concepts of optimal cache utilization as well as the methods for ghost synchronization from its predecessor. It uncouples itself from Cubism-MPCF by introducing the more general concept of tensor fields which are exposed to the user as building blocks for algorithm and application development. The HPC principles are hidden from the user and indirectly accessible by a toolbox of basic operations such as finite difference kernels, data interpolation or data compression tools. The development of CubismNova is ongoing. Support for structured uniform discretization on Cartesian grids has been implemented and tested. The code and documentation can be obtained from `https://cubismnova.readthedocs.io`.

In order to exploit GPU accelerators on current HPC architectures, a heterogeneous CPU/GPU algorithm has been presented that exhibits a current $3.1\times$ improvement compared to the highly optimized multi-core version of Cubism-MPCF. The GPU kernels used in the algorithm are mapped to 2D thread blocks designed for higher utilization of the texture cache. This reduces the requirements on shared memory and allows to run the GPU code at higher occupancy. The algorithm is generic and not only applicable to the compressible multi-phase flow problem used in this work. The CubismNova library has further been designed to allow for data structures that can be used for the heterogeneous CPU/GPU algorithm presented in this chapter. These structures combine the necessity for efficient cache utilization on multi-core CPUs and consider a block-structured data layout at larger granularity that ensures efficient use of the GPU global memory and texture mapping.

5

MODEL VALIDATION

> *The successful solution of a realistic problem in applied*
> *mathematics requires the fusion of four distinct*
> *ingredients: (1) knowledge of the subject area;*
> *(2) knowledge of the relevant mathematics;*
> *(3) knowledge of the relevant computer science; (4) a*
> *talent for selecting just what part of all this knowledge*
> *will actually solve the problem, and ignoring the rest.*
> — George Forsythe

The content of this chapter is concerned with the validation of the model introduced in section 3.2 with the discrete representation discussed in section 3.4. Sections 5.1 to 5.3 address the multi-phase flow capabilities of the model. Sections 5.4 to 5.6 are test cases for the surface tension model discussed in section 3.3.4. The last sections 5.7 and 5.8 provide single-phase test cases for viscous diffusion. Part of this work was used for validation in Rasthofer, Wermelinger, Hadjidoukas, et al. (2017) and Wermelinger, Rasthofer, et al. (2018).

5.1 SINGLE BUBBLE COLLAPSE

Single spherical bubble collapse is addressed in this section. The test problem consists of a spherical air cavity with radius $R_{B,0} = 10\,\mu\text{m}$ at density $\rho_2 = 1\,\text{kg}\,\text{m}^{-3}$ and a pressure $p_{B,0} = 1\,\text{bar}$. The air bubble is submerged in liquid water with density $\rho_1 = 1000\,\text{kg}\,\text{m}^{-3}$. Two cases are considered for liquid far-field pressures of 10 bar and 100 bar, respectively. The initial velocity field is equal to zero where the gas volume fraction and pressure fields are given by

$$\alpha_{2,0}(x) = \frac{1}{2}\left[1 - \tanh\left(\frac{r - R_{B,0}}{3/2\,h}\right)\right],\tag{5.1}$$

$$p_0(x) = \begin{cases} p_{B,0} & r \leq R_{B,0}, \\ p_\infty + \frac{R_{B,0}}{r}\left(p_{B,0} - p_\infty\right) & r > R_{B,0}, \end{cases}\tag{5.2}$$
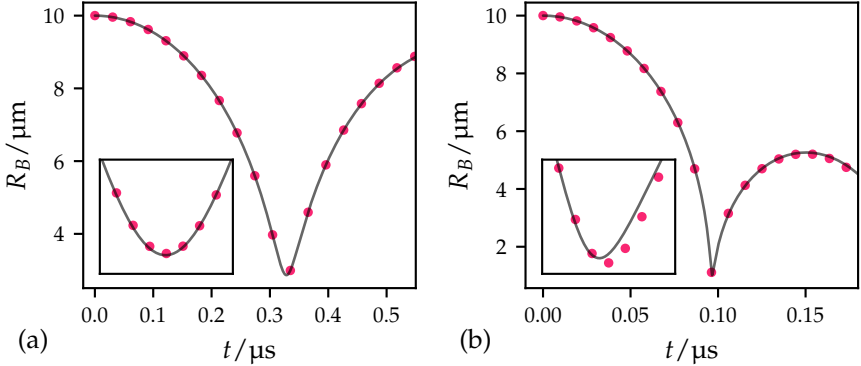
FIGURE 5.1: Single bubble collapse: (a) $p_\infty = 10\,\text{bar}$; (b) $p_\infty = 100\,\text{bar}$. ⎯⎯⎯⎯, analytical solution (Keller et al., 1980); ●, present solver.

respectively. The computational domain consists of a cubic box with length $L = 1\,\text{mm}$ and absorbing boundary conditions on cube faces as well as a symmetry boundary in the z-direction. A stretched mesh is used with a total of $576 \times 576 \times 288$ cells and initial bubble resolution of 104 cells along $R_{B,0}$. Fluids are treated inviscid and without surface tension effects. The reference solution for this problem is obtained from the weakly compressible Keller et al. (1980) model, integrated with a Runge-Kutta-Verner (RKV) 5th-6th-order variable step method.

Figure 5.1(a) shows the simulation results for $p_\infty = 10\,\text{bar}$. The minimum bubble radius is well captured and resolved by 29 cells. Figure 5.1(b) illustrates the simulation results for $p_\infty = 100\,\text{bar}$. The minimum bubble radius is well captured at a resolution of 10 cells. A slight delay of the simulation results is observed due to the much stronger change of momentum at the extrema. The small error is then carried on into the rebound phase. A grid refinement study for the case of $p_\infty = 10\,\text{bar}$ is given in appendix A.2.

5.2   SHOCK INDUCED BUBBLE COLLAPSE NEAR RIGID WALL

The main goal of this validation case is to asses the resolution of bubble wall velocities during non-spherical collapse. A sketch of the problem setup is shown in figure 5.2. The focus is on the shock distal and shock proximal points on the gas-liquid interface, as indicated in the sketch of the problem configuration. The bubble is initialized with radius $R_{B,0}$ and its center is
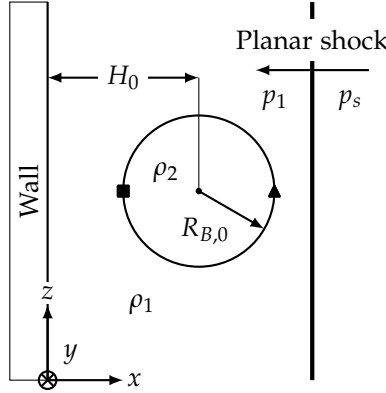
FIGURE 5.2: Initial configuration for shock induced bubble collapse near rigid wall: ■, shock distal bubble side; ▲, shock proximal bubble side.

located a distance $H_0 = 2R_{B,0}$ away from the rigid wall. A planar shock wave normal to the x-direction is initialized at coordinate $x = 3.15\,R_{B,0}$ and a strength of $p_s/p_1 = 353$. The initial densities in the liquid and air are $\rho_1 = 998\,\mathrm{kg\,m^{-3}}$ and $\rho_2 = 1\,\mathrm{kg\,m^{-3}}$, respectively. The pre-shocked fluids are initially at rest with pressure $p_1 = 1\,\mathrm{bar}$, resulting in a liquid speed of sound $c_1 = 1658\,\mathrm{m\,s^{-1}}$. The material parameter for the SGEOS are $\gamma_1 = 6.68$ and $p_{c,1} = 4.103 \times 10^3\,\mathrm{bar}$ for the liquid and $\gamma_2 = 1.4$ and $p_{c,2} = 0\,\mathrm{bar}$ for air. The problem is treated with inviscid fluids and without surface tension effects (Obreschkow et al., 2011; Plesset and Chapman, 1971). Time is expressed in non-dimensional form by $\tilde{t} = tc_1/R_{B,0}$. Extents of the domain are given by $[L_x \times L_y \times L_z] = [12 \times 15 \times 30]$, where all spatial dimensions are normalized with $R_{B,0}$. The problem is discretized using $1728 \times 1280 \times 2560$ cells on a stretched Cartesian grid with an initial bubble resolution of 250 cells along $R_{B,0}$. The wall at $x = 0$ is modeled with a reflecting boundary, where the impedance of the wall is assumed infinite. A symmetry boundary condition is used at $y = 0$ and absorbing boundaries at the remaining faces. A similar problem in a 2D domain was discussed in Johnsen and Colonius (2009).

Figure 5.3(a) shows the evolution of the distal and proximal bubble wall velocities computed for $\alpha_2 = 0.1$ on the liquid side of the interface. The comparison of the results for the present solver with Johnsen and Colonius (2009) illustrates the superior resolution of interfacial regions in contrast to the method used therein. The present method is more sensitive to com-
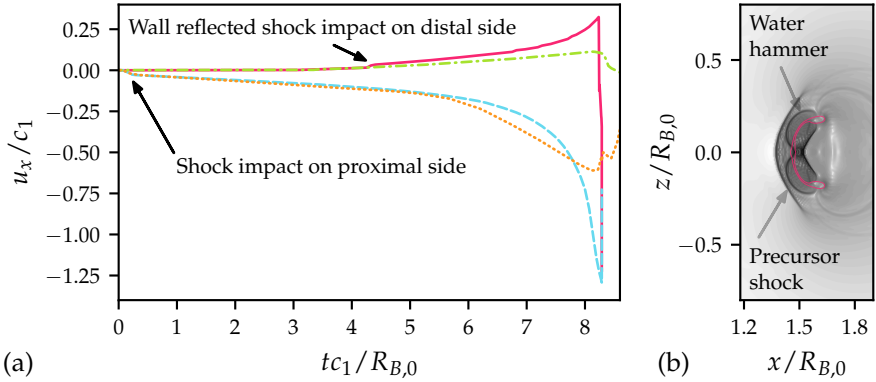
FIGURE 5.3: (a) Bubble wall velocities in x-direction for non-spherical collapse. Present solver: ——, distal bubble wall; ----, proximal bubble wall. Johnsen and Colonius (2009): —·—·—, distal bubble wall; ··········, proximal bubble wall. (b) Schlieren image of $|\nabla p|$ and bubble interface for $\alpha_2 = 0.5$ in the plane $y/R_{B,0} = 0$ for time $tc_1/R_{B,0} = 8.295$ corresponding to microjet impact on the distal bubble wall.

pression waves due to the $K\nabla \cdot u$ source term in equation 3.12. This effect is seen in figure 5.3(a) by the acceleration of the distal bubble wall, slightly after $tc_1/R_{B,0} = 4$ which corresponds to the impact of the wall reflected initial shock. The wall reflected shock is in the shadow of the bubble and therefore weaker than the initial planar shock. The present method, however, is capable of resolving this perturbation. Moreover, the bubble wall that is proximal to the initial shock, see figure 5.2, experiences a very high acceleration only in the final collapse stage, leading to a supersonic interface velocity upon impact on the distal wall. Studies on shock induced bubble collapse for cavity sizes of about 3 mm report on maximum microjet velocities in the range of $400 \, \mathrm{m \, s^{-1}}$ (Dear and Field, 1988; Dear, Field, and Walton, 1988). It is noted, however, that measuring the effective microjet velocity is a difficult task (Supponen et al., 2016). Another modeling approach by Katz (1999) suggests a cut-off kinetic energy that avoids focusing all the energy at an infinitesimal point mass. This cut-off suggests a maximum jet velocity in water of about $2000 \, \mathrm{m \, s^{-1}}$. This estimate agrees well with the $2143 \, \mathrm{m \, s^{-1}}$ peak jet velocity computed in the present case. Moreover, experimental results confirming supersonic bubble wall velocities in the case of spherical collapse have been reported in Mellen (1956). Finally, the measured wall pressures of the present case coincide with the results reported in

Johnsen and Colonius (2009) which hints that the effects of the $K\nabla \cdot u$ term remain local to interfacial regions in the case of compression waves. Effects associated to expansion waves are shown by the next validation case.

5.3 CAVITATION TUBE

The cavitation tube generates two strong rarefaction waves that propagate in opposite direction. This test is useful to assess the multi-phase flow capabilities of the model used in this work. A region of strong relaxation is created behind the parting rarefaction waves, causing a significant pressure reduction until the liquid evaporates when the pressure falls below the vapor pressure. The generation of gas volume fraction is modeled by the $K\nabla \cdot u$ source term in equation 3.12. The initial conditions in the 1D domain $x \in [0, L]$, where $L = 1\,\mathrm{m}$, are given by

$$(\rho, u, p, \alpha_2)_0 = \begin{cases} (1150\,\mathrm{kg\,m^{-3}}, -100\,\mathrm{m\,s^{-1}}, 1\,\mathrm{bar}, 0.02) & 0 \leq x \leq 0.5\,\mathrm{m}, \\ (1150\,\mathrm{kg\,m^{-3}}, 100\,\mathrm{m\,s^{-1}}, 1\,\mathrm{bar}, 0.02) & 0.5 < x \leq 1\,\mathrm{m}. \end{cases}$$
$$(5.3)$$

The domain is discretized using 1000 cells with absorbing boundaries. Since mass transfer is not modeled, a small amount of homogeneously mixed gas volume fraction must be present in the initial liquid. The parameters of the SGEOS are set to $\gamma_1 = 2.35$ and $p_{c,1} = 1 \times 10^4\,\mathrm{bar}$ for the liquid and to $\gamma_2 = 1.43$ and $p_{c,2} = 0\,\mathrm{bar}$ for the gas. Figure 5.4 shows the flow variables at time instants $t = 0\,\mathrm{ms}$, $t = 0.6\,\mathrm{ms}$, $t = 1.2\,\mathrm{ms}$ and $t = 1.8\,\mathrm{ms}$. The results of the present solver compare well to Saurel, Petitpas, et al. (2009) where a 6 equation model with pressure relaxation is used. The strong rarefaction waves cause a significant pressure reduction for which density must rarefy accordingly. As mentioned above, the created gas phase shown in figure 5.4(d) is due to the $K\nabla \cdot u$ term and reaches a maximum value of $\alpha_2 = 0.998$ at time $t = 1.8\,\mathrm{ms}$. Positivity of pressure, density and gas volume fraction is maintained for all times in this validation case with minimum values of $26.0\,\mathrm{Pa}$, $2.0\,\mathrm{kg\,m^{-3}}$ and 0.01, respectively.

5.4 EQUILIBRATION OF SQUARE CYLINDER

The purpose of this validation is to test the recovery of the equilibrium shape of a square column in a two-fluid setup due to surface tension effects.
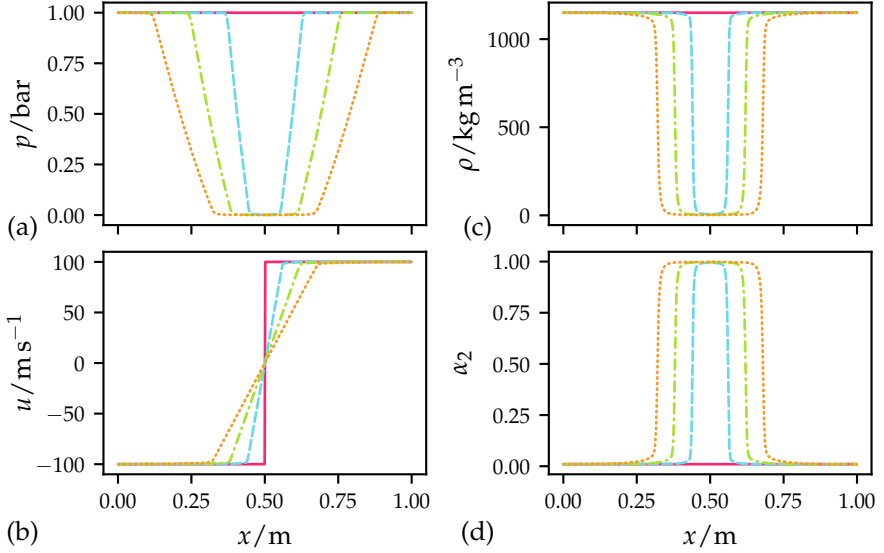
FIGURE 5.4: Spatial wave evolution in cavitation tube: (a) pressure; (b) velocity; (c) density; (d) gas volume fraction. ———, $t = 0\,\text{ms}$; − − − −, $t = 0.6\,\text{ms}$; − · − · −, $t = 1.2\,\text{ms}$; ·········, $t = 1.8\,\text{ms}$.

The problem is characterized by the length L that describes the square, the dispersion relation

$$\omega_0^2 = \frac{\sigma}{2\rho L^3} \tag{5.4}$$

and the ratio of capillary to viscous time scales

$$\varepsilon = \frac{t_\sigma}{t_\nu} = \frac{\nu}{\omega_0 L^2}. \tag{5.5}$$

The capillary time scale is defined by $t_\sigma = \omega_0^{-1}$ and the viscous time scale by $t_\nu = L^2/\nu$. The capillary time scale accounts for both, capillary and inertia effects due to its relation to equation 5.4 via ω_0. In the absence of viscous effects, t_σ expresses the time scale for reversible energy exchange between surface tension effects and inertia. Furthermore, the ratio ε scales with the Ohnesorge number $\varepsilon \sim \text{Oh}$. The following assumptions are made:

1. the two fluids are of equal density $\rho = \rho_1 = \rho_2$,
2. the kinematic viscosity $\nu = \nu_1 = \nu_2$ is the same for both fluids,
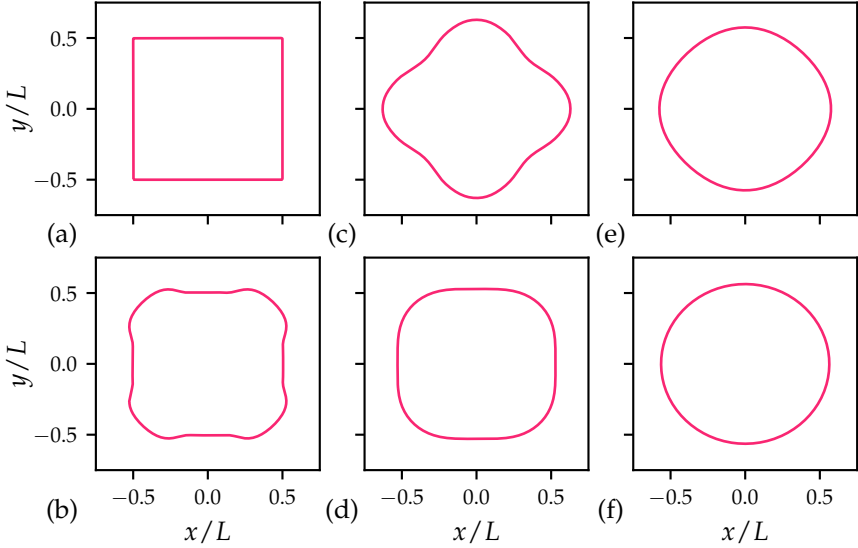3. the two fluids share identical thermodynamic properties.

FIGURE 5.5: Mode shapes: (a) $\omega_0 t = 0$; (b) $\omega_0 t = 0.05$; (c) $\omega_0 t = 0.2$; (d) $\omega_0 t = 0.7$; (e) $\omega_0 t = 1.7$; (f) $\omega_0 t = 10$. Iso-lines are shown for $\alpha_2 = 0.5$.

The problem is initialized in a 2D domain with absorbing boundary conditions. A stretched mesh is used to increase the separation of the artificial boundaries from the region of interest. The resolution is characterized by the initial number of cells along L. Initial pressure p_0 is uniform and the sharp square corners of the initial α_2 field are smoothed with a 27-point Laplacian kernel (two sweeps). The equilibrium is expected that take on a circular shape with volume V_e and radius R_e. The pressure inside the equilibrium shape follows from the Laplace pressure for a cylinder

$$p_e = p_0 + \frac{\sigma}{R_e}. \tag{5.6}$$

The equilibrium volume is computed from the isentropic relation (Schmidmayer, Petitpas, et al., 2017)

$$V_e = V_0 \left(\frac{p_0}{p_e} \right)^{\frac{1}{\gamma}} = L^2 \left(\frac{p_0}{p_0 + \frac{\sigma}{R_e}} \right)^{\frac{1}{\gamma}}, \tag{5.7}$$

where $L = 1\,\text{m}$, $p_0 = 1\,\text{bar}$, $\gamma = 1.4$ and $\sigma = 200\,\text{N}\,\text{m}^{-1}$.

Figure 5.5 shows a sequence of mode shapes at non-dimensional times $\tilde{t} = \omega_0 t$. The results shown in the figure correspond to the parameters
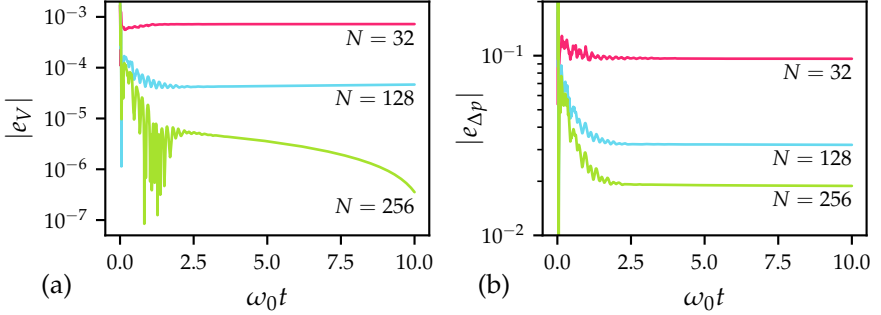
FIGURE 5.6: Temporal evolution of error with respect to number of cells N along L at fixed $\varepsilon = 0.01$: (a) relative error to equilibrium volume V_e; (b) relative error to equilibrium Laplace pressure jump Δp_e.
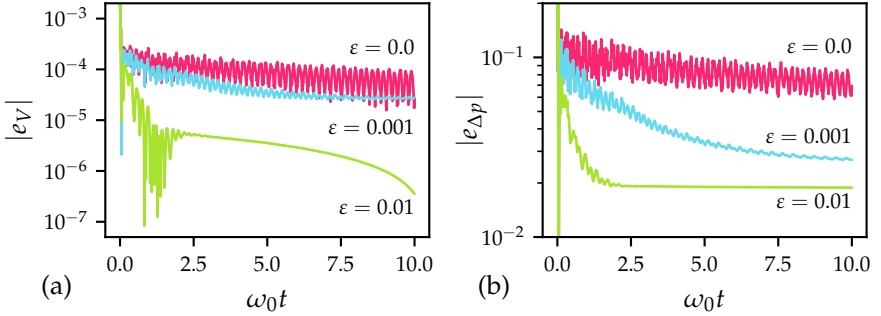
FIGURE 5.7: Temporal evolution of error with respect to viscosity ε at fixed number of cells $N = 256$: (a) relative error to equilibrium volume V_e; (b) relative error to equilibrium Laplace pressure jump Δp_e.

$\omega_0 = 10\,\mathrm{s}^{-1}$ and $\varepsilon = 0.01$. The error in the equilibrium volume is quantified by the relative measure

$$e_V = \frac{V - V_e}{V_e} \tag{5.8}$$

and the relative error in the Laplace pressure jump by

$$e_{\Delta p} = \frac{\Delta p - \Delta p_e}{\Delta p_e}, \tag{5.9}$$

where $\Delta p_e = \sigma / R_e$. The volume V and pressure difference Δp are computed from the simulation data at time $\omega_0 t = 10$ using

$$V = \int_{\Omega} \alpha_2 \, dV, \tag{5.10}$$

for the volume and

$$\Delta p = \frac{1}{V} \int_{\Omega} \alpha_2 p \, dV - p_0 \tag{5.11}$$

for the pressure jump across the interface. The temporal evolution of the error e_V and $e_{\Delta p}$ is shown in figure 5.6 for a varying resolution and in figure 5.7 for varying viscosity. For the inviscid configuration, $\varepsilon = 0$, the equilibrium solution is oscillatory due to reversible energy exchange between surface energy and inertia (neglecting numerical diffusion). The observed results converge towards the isentropic limit, where the average pressure inside the equilibrium configuration is associated with an error of 2 % on the finest grid. The error reduction of the average pressure is roughly linear with respect to grid resolution, where the error of geometric quantities such as the volume decays exponentially.

5.5 CAPILLARY WAVES

This validation case aims at the accuracy of the surface tension model for small amplitude interface motion, where the resolution of the contact wave motion is of the same order as the number of cells in the diffuse interface. This is in contrast to the previous square column validation case where the interface motion is large. Capillary forces, viscous forces as well as inertia are all relevant for this case. Assuming that the two fluids share the same kinematic viscosity, the existence of a closed form analytical solution has been shown in Prosperetti (1981). A sinusoidal interface perturbation of the form

$$y(x) = \frac{L_y}{2} + A_0 \sin kx \tag{5.12}$$

is used to initialize the problem, where the wavelength is $\lambda = 2\pi$ and the domain extent $L_x = \lambda$. The wave number is defined by $k = 2\pi/\lambda$. The initial amplitude of the perturbation corresponds to A_0. Periodic boundary conditions are applied in the x-direction and absorbing boundaries in the y-direction. A uniform resolution is used for the x-direction and a stretched mesh in the y-direction with a window of uniform resolution in the region of the perturbed interface. The same fluid assumptions as in section 5.4

	$N_x = 64$	$N_x = 128$	$N_x = 256$	$N_x = 512$
A_0/h	0.64	1.28	2.56	5.12
L_2	1.10×10^{-3}	5.44×10^{-4}	2.67×10^{-4}	1.75×10^{-4}
L_∞	2.40×10^{-3}	1.34×10^{-3}	6.81×10^{-4}	3.76×10^{-4}

TABLE 5.1: L_p error norms computed for the capillary wave amplitude on varying number of cells N_x along wavelength λ.

hold here as well. The problem is characterized by the parameters given in equations 5.4 and 5.5 with characteristic length $L = \lambda$. The simulations are initialized with $A_0 = 0.01\,\lambda$, $\omega_0 = 1\,\mathrm{s}^{-1}$ and $\varepsilon = 0.064720863$ in accordance with Gueyffier et al. (1999) and Mirjalili et al. (2019). Table 5.1 provides an overview of the different resolutions applied to this problem as well as the initial number of cells along the wave amplitude A_0. The reduction of the wave amplitude error is linear with respect to refining the grid.

Figure 5.8 shows the temporal evolution of the amplitude $A(t)/A_0$ for different numbers of cells N_x along the x-direction. Furthermore, the relative amplitude error

$$e_A = \frac{A - A_{\mathrm{exact}}}{A_{\mathrm{exact}}} \tag{5.13}$$

is shown in figure 5.8(b). The amplitude A_{exact} corresponds to the analytical solution given in Prosperetti (1981). Considering the low resolution of the capillary wave motion, the deviation from the analytical solution is less than 0.5 % on the coarsest grid. The error grows as time progresses, which is expected due to viscous damping of the amplitude for which the amplitude motion eventually falls below the resolution limit of the solver. Moreover, explicit time integration further contributes to the growing error as the problem evolves slowly.

5.6 BUBBLE COALESCENCE

The final validation case for surface tension is concerned with high interface curvature which is relevant for highly deformed bubbles. To this end the coalescence of two bubbles in free space is simulated. Experimental data for the coalescence of two bubbles that diffusively grow near a surface is provided in Soto et al. (2018). The initial conditions consist of two air bubbles
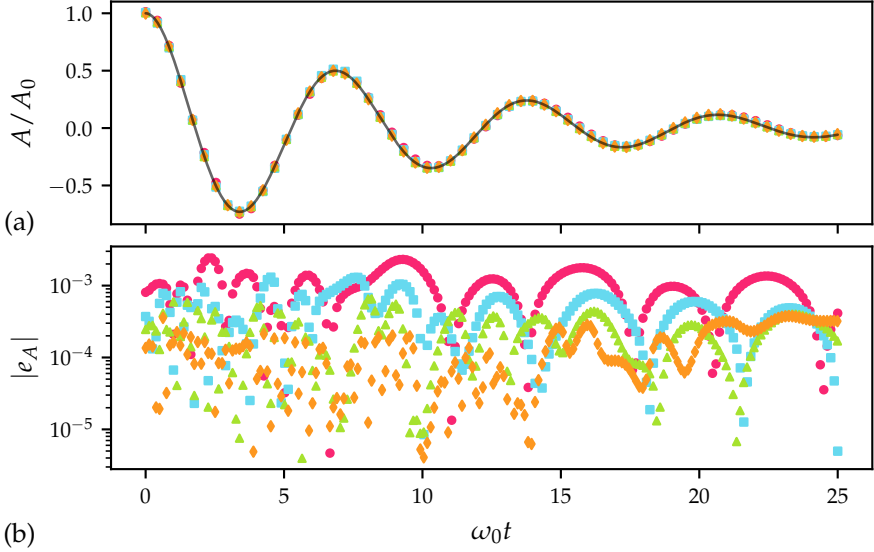
FIGURE 5.8: Capillary wave motion: (a) evolution of wave amplitude; (b) relative amplitude error. ———, exact solution (Prosperetti, 1981); •, $N_x = 64$; ■, $N_x = 128$; ▲, $N_x = 256$; ♦, $N_x = 512$.

with radius $R_{B,0} = 10\,\mu\text{m}$ submerged in water with densities $\rho_2 = 1\,\text{kg m}^{-3}$ and $\rho_1 = 1000\,\text{kg m}^{-3}$, respectively. The material parameter of the fluids are given in table 3.1. The pressure in the liquid is $p_\infty = 1\,\text{bar}$ and for the bubbles the pressure is $p_{B,0} = 1.144\,\text{bar}$ due to the Laplace pressure. The surface tension coefficient is $\sigma = 0.072\,\text{N m}^{-1}$ and fluid viscosities are $\mu_1 = 1 \times 10^{-3}\,\text{Pa s}$ and $\mu_2 = 1.813 \times 10^{-5}\,\text{Pa s}$ for water and air, respectively. The bubble centers are initially separated by a distance $d = 2R_{B,0}$. The computational domain is a cube with edge length $L = 0.24\,\text{mm}$ with a symmetry boundary in the z-direction and absorbing boundaries at the remaining faces. The initial bubbles are resolved with 152 cells along the radius. The time for this problem is normalized using the capillary time scale

$$t_\sigma = \sqrt{\frac{\rho_1 d^3}{8\sigma}}. \tag{5.14}$$

Figure 5.9 shows the computed coalescence sequence for $t/t_\sigma = 0, 0.11, 0.22, 0.33, 0.44,$ and 0.55. The iso-line of the interface shown in that figure corresponds to $\alpha_2 = 0.5$. The computed states are compared with the experimental results of Soto et al. (2018). Good agreement is observed for
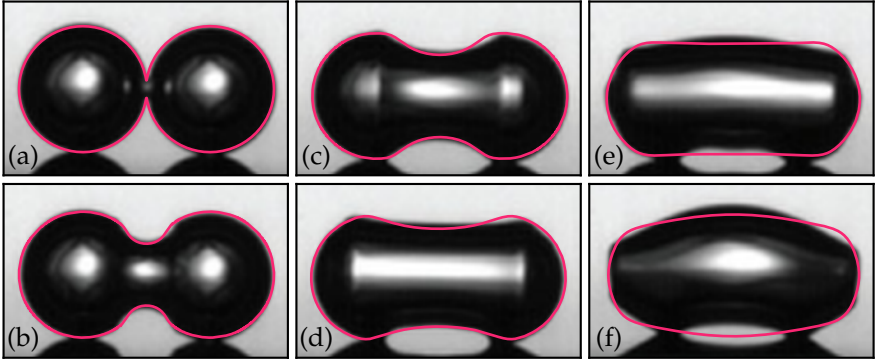
FIGURE 5.9: Bubble coalescence: (a) $t/t_\sigma = 0$; (b) $t/t_\sigma = 0.11$; (c) $t/t_\sigma = 0.22$; (d) $t/t_\sigma = 0.33$; (e) $t/t_\sigma = 0.44$; (f) $t/t_\sigma = 0.55$. ———, interface at $\alpha_2 = 0.5$ of present simulation. Experimental images are taken from Soto et al. (2018).

the states shown in figures 5.9(a) to 5.9(c). At later times, the symmetrical simulations in the free field start to deviate due to the presence of the wall in the experiments, as is seen in figures 5.9(d) to 5.9(f). It is further found that the resolution of the capillary wave on the interface is slightly diffused compared to the experiment. Figure 5.10 shows the temporal evolution of the upper neck radius r_n, see Soto et al. (2018) for a definition. The figure shows three different resolutions for 56, 104, and 152 cells along the initial radius. The shown time captures the shapes shown in figures 5.9(a) to 5.9(d). Overall good agreement is found for the finest resolution with largest deviations compared to the experimental data of Soto et al. (2018) at the initial stages of the coalescence where the interface curvature and acceleration is the largest.

5.7 TAYLOR-GREEN VORTEX

The Taylor-Green problem is used to assess the accuracy of viscous dissipation in a single-phase fluid at low Mach number. The problem is setup in
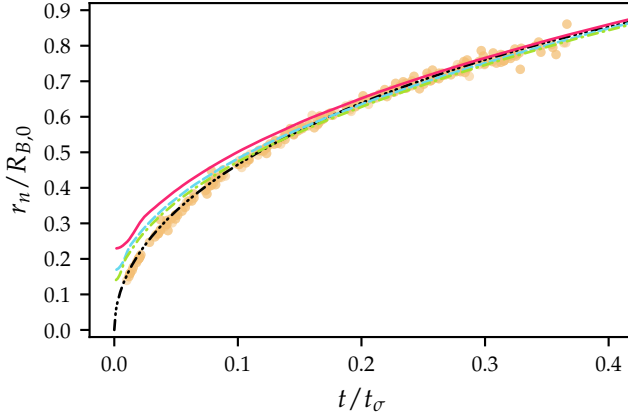
FIGURE 5.10: Evolution of neck radius r_n: •, experiments Soto et al. (2018); ▬·▬·▬·, model by Thoroddsen et al. (2005). Present simulation: ▬▬▬, 56 cells per radius; ▬ ▬ ▬, 104 cells per radius; ▬·▬·▬, 152 cells per radius.

a 3D periodic domain $\Omega = [-\pi, \pi]^3$ where coordinates are normalized by the domain length L. The initial velocity components are given by

$$u_1 = u_0 \sin(x_1) \cos(x_2) \cos(x_3), \tag{5.15}$$

$$u_2 = -u_0 \cos(x_1) \sin(x_2) \cos(x_3), \tag{5.16}$$

$$u_3 = 0 \tag{5.17}$$

and the initial pressure field follows

$$p = p_0 + \frac{\rho_0 u_0^2}{16} \left(\cos(2x_1) + \cos(2x_2) \right) \left(\cos(2x_3) + 2 \right), \tag{5.18}$$

with Re $= 1600$, Ma $= 0.1$, $L = 1\,\mathrm{m}$, $u_0 = 1\,\mathrm{m\,s^{-1}}$ and $\rho_0 = 1\,\mathrm{kg\,m^{-3}}$. The simulation is evolved until $\tilde{t} = 20$ for a normalized time $\tilde{t} = tu_0/L$. For a general compressible fluid, the kinetic energy dissipation rate is the sum of three components

$$\varepsilon_1 = \frac{1}{2\mu} \frac{1}{\rho_0 V} \int_\Omega \boldsymbol{\tau} : \boldsymbol{\tau} \, \mathrm{d}V \tag{5.19}$$

$$\varepsilon_2 = \mu_v \frac{1}{\rho_0 V} \int_\Omega (\boldsymbol{\nabla} \cdot \boldsymbol{u})^2 \, \mathrm{d}V \tag{5.20}$$

$$\varepsilon_3 = -\frac{1}{\rho_0 V} \int_\Omega p(\boldsymbol{\nabla} \cdot \boldsymbol{u}) \, \mathrm{d}V. \tag{5.21}$$
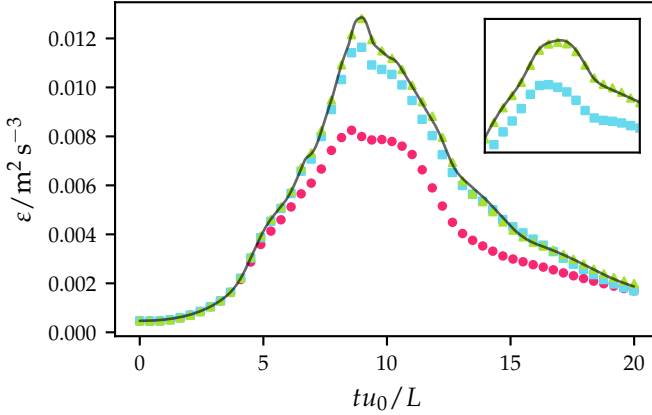
FIGURE 5.11: Kinetic energy dissipation rate for Taylor-Green vortex: ———, spectral reference; ●, $N = 256$; ■, $N = 512$; ▲, $N = 1024$.

It is assumed that the bulk viscosity $\mu_v = 0\,\mathrm{Pa\,s}$ such that $\varepsilon = \varepsilon_1 + \varepsilon_3$. The first term accounts for viscous dissipation and the second term for compressibility effects, which are small for low Mach number flows.

Figure 5.11 shows the results for the kinetic dissipation rate obtained for different resolutions using the present solver. The reference data is obtained from a dealiased pseudo-spectral code for a grid with 512^3 cells.[1] A grid convergence study for this method has been carried out in van Rees et al. (2011). Convergence is achieved for $N = 1024$ cells along the length L of the cubic domain. The resolution requirement is relatively large due to the shock capturing scheme as well as the explicit time stepping of the present solver. This method is designed for interfacial flows with biased stencils for shock capturing. For the resolution of turbulent flow structures, centered schemes are better suited methods.

5.8 COMPRESSIBLE TURBULENT CHANNEL FLOW

The previous validation case demonstrated the resolution capabilities of the present scheme for turbulent structures in a periodic domain. Here the solver is validated for a turbulent channel flow with no-slip boundaries, see section 3.4.5. The simulation is setup in a rectangular domain $[L_x \times L_y \times$

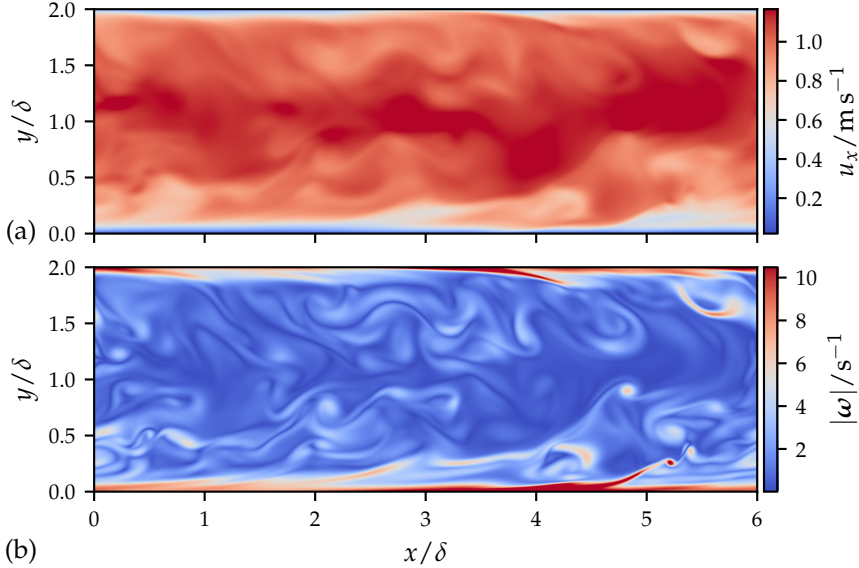---

1 https://cfd.ku.edu/hiocfd/spectral_Re1600_512.gdiag

FIGURE 5.12: Instantaneous flow fields of fully developed channel flow: (a) stream-wise velocity component u_1; (b) vorticity magnitude.

$L_z] = [6 \times 2 \times 4]$ where length scales are normalized with the channel half-width $\delta = 1\,\mathrm{m}$. The friction Reynolds number is set to $\mathrm{Re}_\tau = 180$ and the Mach number to $\mathrm{Ma} = 0.3$. The fluid is assumed single phase with density $\rho = 1\,\mathrm{kg\,m^{-3}}$ and kinematic viscosity $\nu = 3.5 \times 10^{-4}\,\mathrm{m^2\,s^{-1}}$. The Reynolds number based on these quantities is $\mathrm{Re} = 5637$ (Pope, 2000) with a mean stream-wise velocity of $\bar{U} \approx 1\,\mathrm{m\,s^{-1}}$. The problem is non-dimensionalized by the parameters

$$\tilde{\delta} = 1, \quad \tilde{\rho} = 1, \quad \tilde{\mu} = 3.5 \times 10^{-4},$$

where the dynamic viscosity is given by $\mu = \rho\nu$. Discretization of the domain corresponds to $1152 \times 384 \times 768$ cells along the x, y and z dimensions, respectively, using a uniform grid. The parameter setting and discretization lead to $y^+ = 0.470$ for the grid spacing from the wall to the first grid cell. Boundaries are treated periodic in the x (stream-wise) and z (span-wise) directions, whereas no-slip walls are imposed in the wall normal y direction.

The flow in the channel is maintained by a spatially invariant volumetric forcing term

$$f(t) = (f_x(t), 0, 0)^\mathsf{T} \tag{5.22}$$
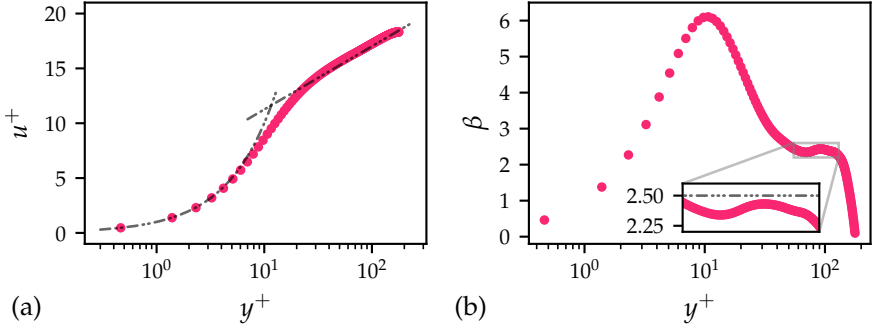
FIGURE 5.13: Mean stream-wise velocity: (a) mean velocity profile; (b) indicator function. ●, present simulation; —··—··, viscous sub-layer reference; —··—·, logarithmic law of the wall.

that is added to the right-hand side of equations 3.10 and 3.11. The mass flow in the stream-wise direction is then given by

$$\dot{m} = \int_{S_x} \rho \boldsymbol{u} \cdot \boldsymbol{n} \, dS = \frac{2\rho}{3\mu} f_x \delta^3, \tag{5.23}$$

where the last term is obtained by integrating the Navier-Stokes (NS) momentum equation. The mass flow is computed during the simulation by averaging the data over four yz-planes S_x at locations $x = 0$, $x = L_x/4$, $x = L_x/2$ and $L_x = 3L_x/4$. The error in the x-component of the forcing term in equation 5.22 is then defined by

$$\Delta f_x = f_{x,\text{ref}} - f_x = \frac{3}{2} \frac{\mu}{\delta^3} \left(2\delta \bar{U} - \frac{\dot{m}}{\rho} \right), \tag{5.24}$$

where the term $\dot{m}/\rho$ is computed from the average over planes S_x as described above and the reference forcing term $f_{x,\text{ref}}$ is obtained from $\bar{U}$ and equation 5.23. The x-component of the forcing term in equation 5.22 is then corrected every time step with the signal $\zeta(t)$ obtained from a proportional-integral-derivative (PID) controller

$$\zeta(t) = K_p e(t) + K_i \int_0^t e(\xi) \, d\xi + K_d \frac{de(t)}{dt}, \tag{5.25}$$

where $e(t) = \Delta f_x$.

Figure 5.12 shows the instantaneous stream-wise velocity $u_1 = \bar{u}_1 + u_1'$ and vorticity magnitude $|\boldsymbol{\omega}|$ in the channel for fully developed flow. The
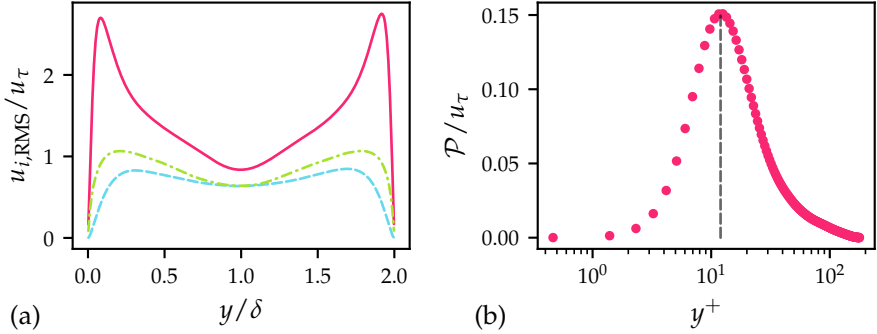
FIGURE 5.14: (a) Root-Mean-Square velocity fluctuations; ————, $u_{1,\text{RMS}}$; –––––, $u_{2,\text{RMS}}$; –·–·–, $u_{3,\text{RMS}}$. (b) Turbulent production; ●, present simulation; ————, peak production at 12 wall units corresponding to the observed peaks of $u_{1,\text{RMS}}$ in (a).

mean velocity for the data shown in figure 5.12(a) is $\bar{U} = 0.96 \pm 0.22\,\text{m\,s}^{-1}$. Statistics are collected over intervals of 5000 steps using Reynolds averages. For the present simulation at low Mach number, the differences between Reynolds and Favre averaged statistics are negligible. The friction Reynolds number averaged over 10 data sets with 5000 samples each is $\text{Re}_\tau = 178$. The mean velocity profile for the fully developed flow is shown in figure 5.13(a). The indicated references correspond to

$$\frac{\bar{u}_1}{u_\tau} = u^+ = y^+ \tag{5.26}$$

for the viscous sub-layer and

$$u^+ = 2.5 \ln y^+ + 5.5 \tag{5.27}$$

for the logarithmic law of the wall, where the von Kármán constant is set to $\kappa = 0.4$. Values with superscript $+$ are normalized by the friction velocity $u_\tau = \sqrt{\tau_w/\rho}$ where τ_w is the mean wall shear stress. Figure 5.13(b) shows the indicator function β (M. Lee et al., 2015)

$$\beta(y^+) = y^+ \frac{\mathrm{d}u^+}{\mathrm{d}y^+}, \tag{5.28}$$

which is constant and equal to $1/\kappa$ in the log-law region. Figure 5.13(b) indicates a slight deviation from the target value in the present simulation.

The Root-Mean-Square (RMS) of the velocity fluctuations u'_i is shown in figure 5.14(a), whereas the turbulent production

$$\mathcal{P} = -\overline{u'_1 u'_2} \frac{\mathrm{d}\bar{u}_1}{\mathrm{d}y} \tag{5.29}$$

is shown in figure 5.14(b). The peak of turbulent production is found 12 wall units away from the wall which is in agreement with the results presented in Kim et al. (1987).

<div align="right">

6

</div>

PARAMETRIC STUDY OF CLOUD CAVITATION COLLAPSE WITH PERFORMANCE COMPARISON OF REDUCED ORDER MODELS

> *Adopt the pace of nature: her secret is patience.*
> — Ralph Waldo Emerson

This chapter presents a parameter study for 15 collapsing bubble clouds with varying cloud radius, gas volume fraction and far-field forcing pressure. The collapse dynamics of fully resolved 3D simulations are compared with two reduced order models (Doinikov, 2004; Keller et al., 1980) that are based on the Rayleigh-Plesset (RP) equation with additional terms to model bubble-bubble interactions. The model of Doinikov (2004) adds additional degrees of freedom by modeling the translation of the center of mass for individual bubbles. The work in this chapter highlights the limitations of such advanced reduced order models with respect to fully resolved simulations of highly non-spherical bubble collapse in cluster arrangements.

6.1 RELATED WORK

Cloud cavitation collapse presents a formidable challenge to computational studies due to its geometric complexity and disparity of spatiotemporal scales. For instance, bubbles typically occur in clouds whose extent is orders of magnitude larger than the bubble radius. Direct numerical simulation (DNS) of cloud cavitation collapse aims at resolving each individual bubble and its deformation. The associated computational cost, however, is very high and impedes any detailed computational investigations for engineering applications. Mainly for this reason, simplifying assumptions and modeling are unavoidable to account for cavitation effects in numerical simulations that support the engineering design process. Frequently used simplified approaches may be roughly classified into homogeneous mixture models neglecting the resolution of bubbles entirely (Egerer, Schmidt, et al., 2016; Koukouvinis et al., 2016; Schnerr et al., 2008) and approaches making use of RP type ODEs (Flynn, 1975; Gilmore, 1952; Keller et al., 1980; Plesset and

Prosperetti, 1977; Prosperetti and Lezzi, 1986; Rayleigh, 1917; Trilling, 1952) which govern the evolution of the radius of a spherical bubble.

Euler-Lagrange approaches embed particle-like spherical bubbles into a flow field obtained from averaged Navier-Stokes equations which are solved on a fixed grid covering the computational domain (Ando et al., 2011; Fuster and Colonius, 2011; Kubota et al., 1992; Ma et al., 2015; Seo et al., 2010; van Wijngaarden, 1968; D. Z. Zhang et al., 1994). The radius of the bubbles, which is typically smaller than a grid cell, is determined by a RP type equation. This procedure significantly lowers the resolution requirements and, thus, the computational costs as the bubbles do not have to be resolved. Seo et al. (2010) showed a comparison of their proposed bubbly mixture model with fully resolved simulations for bubbly shock flows in a rectangular container. The results predicted by their model agreed well with DNS results. The study was restricted, however, to parameters for which the bubbles remained spherical also in the DNS. Other approaches use systems of particle-like spherical bubbles only (Doinikov, 2004; Mettin et al., 1997; Parlitz et al., 1999; Stricker et al., 2013; Yasui et al., 2008; Zeravcic et al., 2011). In doing so, these bubble-particle approaches even further reduce the computational costs.

Although the aforementioned applications rely on accurate predictions for clouds of bubbles, merely the collapse of a single bubble governed by RP type equations was examined in detail, both, experimentally and numerically (Fuster, Dopazo, et al., 2011; Hilgenfeldt et al., 1998; Obreschkow et al., 2013). Comprehensive comparisons for extensions of RP type equations applied to collapsing clouds of interacting bubbles with experimental or DNS studies are barely considered in literature. Bremond et al. (2006), for instance, experimentally investigated the collapse process of a planar arrangement of 37 bubbles. Their study reports predictions obtained by the incompressible RP equation with extension to account for bubble-bubble interactions and revealed that the maximum size of the bubbles, their lifetime as well as the chronological order of the bubble collapses are well captured by a bubble-particle approach. They further observed deviations of their results for collapse phases where the assumption of spherical bubble collapse was violated. Later, Chahine, Hsiao, et al. (2014) reproduced the experiment of Bremond et al. (2006) to illustrate their Euler-Lagrange approach with bubble interactions. Tiwari et al. (2015) provided a comparison for the gas volume evolution and the peak pressure using DNS data. A hemispherical cloud of 50 bubbles adjacent to a solid wall was considered. While the gas volume evolution obtained from the bubble-particle approach

was close to the one from the DNS for the growth stage of the bubbles, the bubble-particle predictions increasingly became less accurate and deviated from the reference data during the cloud collapse. Furthermore, Tiwari et al., 2015 observed that the employed bubble-particle approach notably overestimated the peak pressure.

Those studies as well as many others (N. A. Adams et al., 2013; Brennen, 2002; Chahine and Duraiswami, 1992) revealed the non-spherical collapse in cavitating bubble clouds and, hence, raise the question about the range of validity of RP type reduced order models applied in cloud cavitation. The parametric study of this chapter discusses the results obtained from two such reduced order models applied to 15 bubble clouds with up to 630 bubbles in the largest configuration. The results are further compared with resolved 3D simulations. It is found that modeling the translational motion of bubbles during the collapse enhances the accuracy of the predicted collapse time of individual bubbles. Moreover, the degree of bubble deformation affects the accuracy of predicted bubble radii and peak pressures, especially for larger systems.

6.2 BUBBLE CLOUD CONFIGURATIONS

The bubbles considered for this parameter study are initially spherical and all of equal radius $R_{B,0} = 0.75\,\text{mm}$ which is based on similar sizes considered in N. A. Adams et al. (2013) and Tiwari et al. (2015). The bubble clouds are created by randomly positioning bubbles within a sphere of radius R_C. These coordinates are obtained by following a uniform distribution with the constraint that the minimum distance between any two bubbles is not smaller than the distance $d_G = 0.4\,\text{mm}$. Bubble surfaces may tangent the hull of the spherical cloud. A 2D sketch for this cloud configuration with arbitrary bubble radii is shown in figure 7.1 on page 122.

The clouds are characterized by the gas volume fraction α_C and the cloud interaction parameter β_C (Wang et al., 1999); see equation 2.15 for their scaling dependence. The parameters are defined as

$$\alpha_C = N_B \left(\frac{R_{B,0}}{R_C} \right)^3, \tag{6.1}$$

$$\beta_C = \alpha_C \left(\frac{R_{\text{eq}}}{R_{B,0}} \right)^2, \tag{6.2}$$

Cloud	R_C/mm	β_C	α_C	N_B
1	7.5	0.015	0.005	5
2	7.5	0.1	0.016	16
3	7.5	0.2	0.025	25
4	7.5	0.5	0.042	42
5	7.5	1.0	0.064	64
6	7.5	2.5	0.110	110
7	10.0	0.2	0.017	41
8	10.0	0.5	0.030	70
9	10.0	1.0	0.045	106
10	10.0	2.5	0.078	184
11	10.0	5.0	0.118	279
12	10.0	7.5	0.150	355
13	12.5	5.0	0.090	416
14	12.5	7.5	0.115	531
15	12.5	10.0	0.136	630

TABLE 6.1: Bubble cloud configurations.

where N_B denotes the number of bubbles in the cloud and $R_{eq} = N_B^{1/3} R_{B,0}$ the equivalent radius, i.e., the radius of a single spherical bubble with the same gas volume as the cloud. Large values of β_C indicate strong interactions among the bubbles and low β_C values weak interactions (Brennen, 1998; Wang et al., 1999).

Three different cloud radii $R_C = 7.5$, 10 and 12.5 mm, each with a wide variety of β_C, are considered. The resulting number of bubbles in the cloud ranges from $N_B = 5$ to 630 and the gas volume fraction from $\alpha_C = 0.5$ to 15 %. The details of all cloud configurations are summarized in table 6.1.

The parameter study is focused on the collapse process of the bubble clouds as well as the effect of bubble deformation on the predictions obtained by the reduced order models. These models are derived based on potential flow theory (Fuster and Colonius, 2011) where the effects of bubble-bubble interactions are captured in the velocity and pressure fields. The individual bubble collapses remain spherical. Strong forcing pressure

R_C/mm	L/mm	N_L	$R_{B,0}/h$
7.5	55.0	1792	24.44
10.0	60.0	2048	25.60
12.5	65.0	2304	26.58

TABLE 6.2: Spatial domain discretization and bubble resolution. N_L is the number of computational cells along L.

in the far-field of the cloud result in highly non-spherical bubble collapses which influence the overall collapse dynamics. An important parameter, therefore, is the pressure ratio

$$\Pi = \frac{p_\infty}{p_{B,0}}, \tag{6.3}$$

where p_∞ is the constant ambient pressure in the far-field and $p_{B,0} < p_\infty$ the initial bubble pressure. The forcing pressure ratios considered in this study are $\Pi = 2$, 4.5 and 10 corresponding to $p_{B,0} = 10$ bar. The material properties for water and air are shown in table 3.1, where the air density at 10 bar corresponds to $\rho_2 = 5.180 \, \text{kg m}^{-3}$.

6.3 DISCRETE DOMAIN OF RESOLVED SIMULATIONS

The resolved 3D simulations are discretized in a cubic domain of size $\Omega = [-L/2, L/2]^3$, where the length L depends on the cloud radius. An overview of the discrete domains for the 3 cloud radii is provided in table 6.2. Clouds are at least a distance of 20 mm apart from the domain boundaries, where space is discretized on a uniform Cartesian grid with cell size h. The initial resolution of the bubbles is furthermore shown in table 6.2. Appendix A provides a convergence analysis with resolution requirements for cavitating bubble clouds. It is remarked that below the resolution limit, the mathematical model smoothly transfers into a homogeneous mixture model due to the $K\nabla \cdot \boldsymbol{u}$ source term in equation 3.12.

The initial velocity field is assumed zero everywhere, while the pressure field is initially smooth (Tiwari et al., 2015) with continuous pressure increase towards the domain boundaries. Initial pressure inside the bubbles is constant and equal to $p_{B,0} = 10$ bar. The smooth pressure increase towards

p_∞ at the boundaries is computed from the liquid side bubble surfaces following a hyperbolic tangent given by

$$p_0(x) = \begin{cases} p_{B,0} & r \leq R_{B,0}, \\ p_{B,0} + \tanh\left(\frac{r - R_{B,0}}{\lambda}\right)(p_\infty - p_{B,0}) & r > R_{B,0}, \end{cases} \tag{6.4}$$

where

$$r = \min_{1 \leq i \leq N_B} |x - x_{B,i}|$$

is the distance of point x in the domain from the nearest bubble center $x_{B,i}$. The parameter $\lambda = 12\,\text{mm}$ defines how fast the pressure increases from the bubble surface.

The numerical method used for the resolved simulations corresponds to section 3.4 with the model described in equations 3.8 to 3.12 where viscous and surface tension effects are neglected. Neglect of viscosity is justified by the estimated Reynolds number of 23 700 based on the characteristic length of $R_{B,0}$ and characteristic velocity $\sqrt{p_{B,0}/\rho_1}$, where ρ_1 is the density of the liquid. The kinematic viscosity in liquid is assumed $1.0 \times 10^{-6}\,\text{m}^2\,\text{s}^{-1}$. Similarly, the estimated Weber number is 10 400 assuming the surface tension of $0.072\,\text{N}\,\text{m}^{-1}$ for an air-water composition, suggesting that fluid inertia dominates surface tension effects. Non-reflecting, characteristic-based boundary conditions (Engquist et al., 1977; Poinsot et al., 1992; Thompson, 1987, 1990) are used. Additionally, the ambient pressure p_∞ is imposed in the far-field by adding the term $C_{bc}(p - p_\infty)$ to the incoming wave (Rudy et al., 1980). Coefficient $C_{bc} = \sigma(1 - \text{Ma}^2)c_1/\ell \approx \sigma c_1/\ell$ depends on a characteristic length $\ell = 10\,\text{mm}$, the speed of sound c_1 in the liquid at the boundary, the Mach number Ma at the boundary, which is assumed negligible, and a user defined parameter $\sigma = 1\,\text{s}$. The CFL number of the simulation is set to 0.3.

6.4   BUBBLE RECONSTRUCTION AND SHAPE CHARACTERIZATION

Individual bubble deformations are analyzed by reconstruction of the bubble surface from the gas volume fraction field. The set of points

$$\Gamma(t) = \{x \in \Omega \mid \alpha_2(x, t) = 0.5\} \tag{6.5}$$

defines a surface on which the gas volume fraction is equal to $\alpha_2 = 0.5$, i.e., centered in the diffuse interface region. The surface Γ is computed
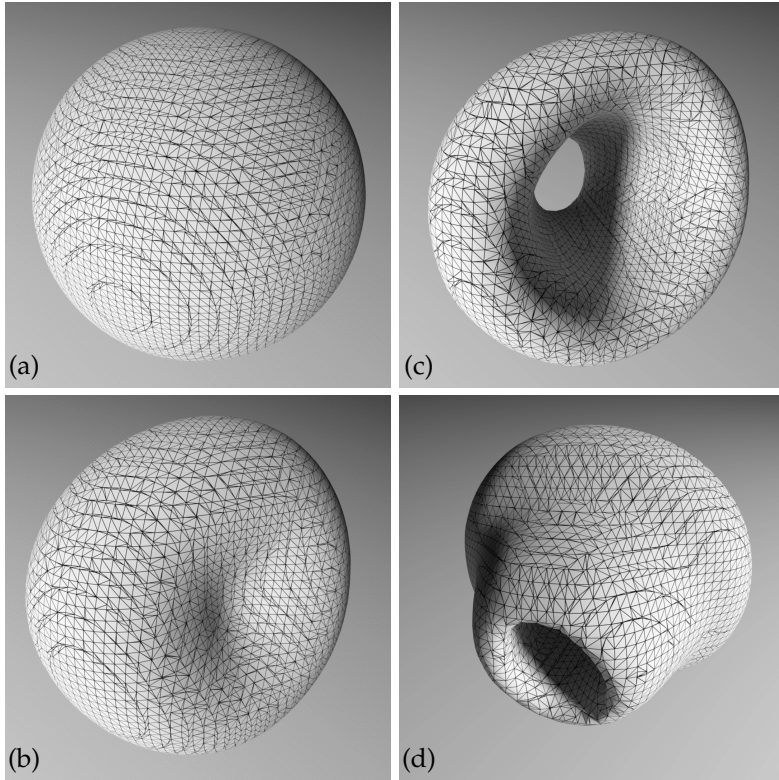
FIGURE 6.1: Reconstructed interface of a collapsing bubble: (a) $t = 0\,\mu s$, $R_{B,0} = 0.75\,mm$, $\phi = 1$; (b) $t = 31.6\,\mu s$, $\phi = 0.98$; (c) $t = 52.9\,\mu s$, $\phi = 0.67$ (back view); (d) $t = 52.9\,\mu s$, $\phi = 0.67$ (front view).

with a marching cube algorithm (Dietrich et al., 2009; Lorensen et al., 1987), where the cubes are identical to grid cells. The surface is reconstructed by computing triangular patches in cubes where $0 < \alpha_2 < 1$ such that the triangle vertices satisfy the constraint $\alpha_2 = 0.5$. The first step consists of interpolating the cell centered data onto the vertices of the cubes using the techniques described in Monaghan (1985). Linear hat kernels were used for the analysis carried out in this study. Once the values on the cube vertices are known, the vertices of the triangular patches are computed along cube edges where the values of the two edge vertices satisfy $v_1 < 0.5 < v_2$. The triangle vertex position is then linearly interpolated between v_1 and v_2. Higher order interpolation along cube edges did not yield

improved reconstructions. The individual bubbles in a cloud are obtained by computing the connected components of Γ. Figure 6.1 shows an interface reconstruction for $\alpha_2 = 0.5$ of a collapsing bubble at evolving instances of time using the method described above.

The bubble surface area and volume are readily obtained from the reconstruction. These metrics are used to characterize the shape of a bubble during non-spherical collapse. The transition to a non-convex shape is of particular interest to identify the formation of microjets which lead to highly deformed bubbles. This transition is measured by the porosity

$$\phi = \frac{V_B}{V_{B,\text{hull}}}, \tag{6.6}$$

where $V_{B,\text{hull}}$ denotes the volume of the convex bubble hull. A convex bubble shape is characterized by $\phi = 1$ and non-convex shapes by $\phi < 1$. The degree of bubble deformation is indicated by the magnitude of ϕ, where values closer to zero indicate large deformations. Figure 6.1 provides a reference for the porosity associated with the shown bubbles.

Although the computation of Γ involves additional work, performing the bubble reconstruction with a dedicated C++ code allows for higher processing throughput compared to visualization tools such as ParaView.[1] Higher processing throughput becomes especially important when the number of bubbles to be analyzed grows beyond $O(10^3)$. The surface reconstruction tool described here has further been used for shock wave visualization.

6.5   REDUCED ORDER RAYLEIGH-PLESSET TYPE MODELS

The reduced order models considered for comparison with the resolved simulations are based on the Keller-Miksis (KM) equation (Keller et al., 1980) with an additional extension for modeling bubble-bubble interactions (Mettin et al., 1997). The KM equation takes weak compressibility of the liquid into account in contrast to the classic RP equation (Plesset and Prosperetti, 1977; Rayleigh, 1917) and is therefore the preferred model for comparison with the compressible 3D simulations. Compressibility effects in the coupling terms for bubble-bubble interactions are usually neglected (Doinikov, 2004; Mettin et al., 1997; Tiwari et al., 2015; Yasui et al., 2008). An extended model that takes into account first order terms for these compressibility

---

1 https://www.paraview.org

effects was suggested in Fuster and Colonius (2011). The models described above account for the interactions of nearby bubbles, describing the effective dynamics of the gas-liquid interface. Additional degrees of freedom for bubble translations were described in the model of Doinikov (2004) and Ilinskii et al. (2007). These models extend the velocity potential by the translational motion $\dot{x}_{B,i}$ for each bubble i which is then used to formulate expressions for the kinetic and potential energies of the bubble cluster. The equations of motion for the bubbles can then be derived with Lagrange's equations. Following Doinikov (2004), these equations of motion are

$$
\begin{aligned}
\left(1 - \frac{\dot{R}_{B,i}}{c_1}\right) & R_{B,i} \ddot{R}_{B,i} + \left(\frac{3}{2} - \frac{\dot{R}_{B,i}}{2c_1}\right) \dot{R}_{B,i}^2 \\
&= \frac{1}{\rho_1} \left(1 + \frac{\dot{R}_{B,i}}{c_1}\right) (p_{B,i} - p_\infty) + \frac{R_{B,i}}{\rho_1 c_1} \frac{\mathrm{d}}{\mathrm{d}t}(p_{B,i} - p_\infty) \\
&\quad + \frac{1}{4} \dot{x}_{B,i}^2 - \sum_{\substack{j=1 \\ j \neq i}}^{N_B} \Bigg\{ \frac{1}{d_{ij}} \left(R_{B,j}^2 \ddot{R}_{B,j} + 2 R_{B,j} \dot{R}_{B,j}^2 \right) \\
&\quad + \frac{R_{B,j}^2}{2 d_{ij}^3} (x_{B,i} - x_{B,j}) \cdot (R_{B,j} \ddot{x}_{B,j} + \dot{R}_{B,j} \dot{x}_{B,i} + 5 \dot{R}_{B,j} \dot{x}_{B,j}) \\
&\quad - \frac{R_{B,j}^3}{4 d_{ij}^3} \Big[\dot{x}_{B,j} \cdot (\dot{x}_{B,i} + 2 \dot{x}_{B,j}) \\
&\quad + \frac{3}{d_{ij}^2} \left(\dot{x}_{B,j} \cdot (x_{B,j} - x_{B,i}) \right) \left((x_{B,i} - x_{B,j}) \cdot (\dot{x}_{B,i} + 2 \dot{x}_{B,j}) \right) \Big] \Bigg\},
\end{aligned}
\tag{6.7}
$$

$$
\begin{aligned}
\frac{1}{3} R_{B,i} \ddot{x}_{B,i} + & \dot{R}_{B,i} \dot{x}_{B,i} \\
&= \sum_{\substack{j=1 \\ j \neq i}}^{N_B} \Bigg\{ \frac{1}{d_{ij}^3} (x_{B,i} - x_{B,j}) \left(R_{B,i} R_{B,j}^2 \ddot{R}_{B,j} + 2 R_{B,i} R_{B,j} \dot{R}_{B,j}^2 + \dot{R}_{B,i} \dot{R}_{B,j} R_{B,j}^2 \right) \\
&\quad - \frac{R_{B,j}^2}{2 d_{ij}^3} \left(R_{B,i} R_{B,j} \ddot{x}_{B,j} + (\dot{R}_{B,i} R_{B,j} + 5 R_{B,i} \dot{R}_{B,j}) \dot{x}_{B,j} \right) \\
&\quad + \frac{3 R_{B,j}^2}{2 d_{ij}^5} (x_{B,i} - x_{B,j}) \Big[(x_{B,i} - x_{B,j}) \cdot \Big(R_{B,i} R_{B,j} \ddot{x}_{B,j} \\
&\quad + (\dot{R}_{B,i} R_{B,j} + 5 R_{B,i} \dot{R}_{B,j}) \dot{x}_{B,j} \Big) \Big] \Bigg\},
\end{aligned}
\tag{6.8}
$$

where $R_{B,i}$ denotes the radius of bubble i, $x_{B,i}$ its position, $p_{B,i}$ its pressure, d_{ij} the distance between bubble i and any other bubble j, ρ_1 and c_1 the liquid density and speed of sound, respectively, and p_∞ the constant far-field pressure. The bubble pressure $p_{B,i}$ is given by

$$p_{B,i} = p_{B,i}(t = 0) \left(\frac{R_{B,i}(t = 0)}{R_{B,i}} \right)^{3\gamma_2} \tag{6.9}$$

with γ_2 the ratio of specific heats in the gas. The liquid speed of sound c_1 is computed by equation 3.15 based on the far-field pressure p_∞ and the liquid material parameter in table 3.1. Equations 6.7 and 6.8 are a coupled system of $2N_B$ 2nd-order non-linear ODEs in the $2N_B$ unknowns $R_{B,i}$ and $x_{B,i}$ with $i = 1, \ldots, N_B$ and N_B the number of bubbles in the cloud. The unknowns $R_{B,i} = R_{B,i}(t)$ and $x_{B,i} = x_{B,i}(t)$ are the bubble radius and center of mass coordinates, respectively. In accord with the resolved simulation setup, viscous and surface tension effects are neglected. For brevity, the model in equations 6.7 and 6.8 is abbreviated by DK (Doinikov, 2004).

In the limit of spatially constrained bubbles where $x_{B,i} = \dot{x}_{B,i} = 0$, equations 6.7 and 6.8 to the KM equations with bubble-bubble interaction terms as used for example in Tiwari et al. (2015). This limit model will be denoted as KM in the following whereas the coupled system of equations 6.7 and 6.8 is denoted as DK. Quantities of the fully resolved 3D simulations are denoted by the superscript "res" in the following sections.

The solver used for these reduced models is based on an explicit RKV 5th-6th-order variable step integrator implemented in C++. The linear systems due to the bubble-bubble interactions are solved with a Householder rank-revealing QR decomposition and column-pivoting; implemented in the Eigen library.[2] The initial conditions for the interface velocities, $\dot{R}_{B,i} = 0$, and additionally for DK the translational velocities, $\dot{x}_{B,i} = 0$, are in correspondence with the initial conditions of the resolved simulations. The initial bubble radii are $R_{B,i} = 0.75\,\text{mm}$ whereas the initial bubble positions $x_{B,i}$ depend on the cloud configurations shown in table 6.1.

---

2 http://eigen.tuxfamily.org

6.6 RESULTS

6.6.1 *Parameter impact on holistic cloud collapse*

This section provides a comparison on the observed holistic cloud collapse dynamics for different parameters. An illustration of the highly non-linear relationship between 6 parameter sets is shown in figure 6.2. The time of minimum gas volume in the cloud is denoted by t_C and referred to as the cloud collapse time in the following. The figure shows the state of 3 clouds selected from table 6.1 for the two pressure ratios $\Pi = 2$ and $\Pi = 10$ at time $t/t_C = 0.95$. In all of the cases the bubbles are focusing towards the cloud center, while in the case of small β_C and weak pressure ratio Π the bubbles exhibit a small degree of deformation and all shapes conserve convexity; see figure 6.2(a). In particular, the focusing of bubbles towards the cloud center is mainly determined by geometrical parameters and β_C, where the focal point becomes sharper at increasing values of β_C. On the other hand, the degree of bubble deformation is mainly determined by the forcing pressure ratio Π, especially at moderate values of β_C. The mean degree of bubble deformation in a collapsing cloud is estimated by the average porosity

$$\bar{\phi} = \frac{1}{N_B} \sum_{i=1}^{N_B} \phi_i, \qquad (6.10)$$

where ϕ_i is the porosity of bubble i determined by equation 6.6. Figure 6.3 shows the mean temporally evolving porosity corresponding to the cases shown in figure 6.2. The cases with $\Pi = 10$ exhibit about 2–9 times stronger deformation rates, where the case with large β_C shows a less dramatic increase of the deformation rate when compared to the case with $\Pi = 2$. This weaker dependence when the far-field pressure increases is attributed to the higher number density of bubbles in the cloud, which cause stronger shielding. This also explains the observation that bubble shapes turn non-convex at almost the same time, regardless of the forcing pressure magnitude; see figures 6.3(c) and 6.3(f). Furthermore, the maximum degree of deformation is only observed for the pressure ratio $\Pi = 10$, as seen in figures 6.3(d) to 6.3(f). The recording of the maximum degree of deformation roughly coincides with the time of minimum gas volume t_C. After this time the rate of bubble deformations remains approximately constant in the case of strong forcing pressures.

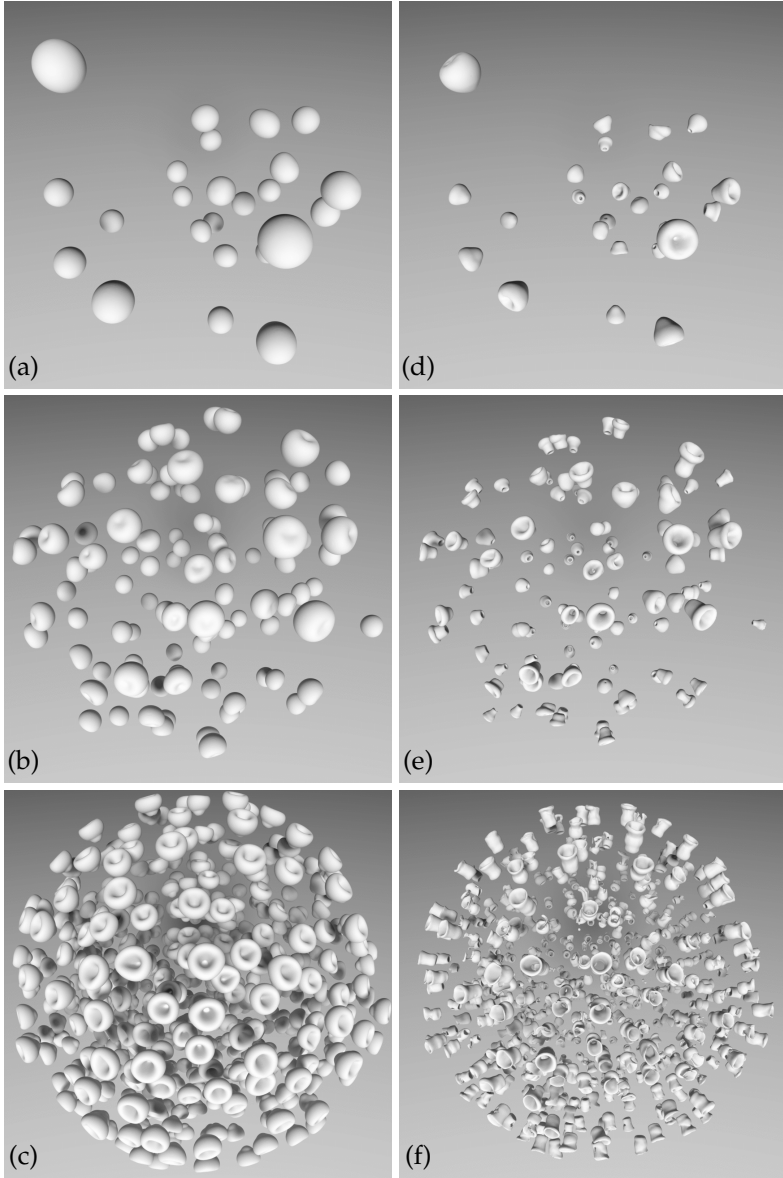FIGURE 6.2: Comparison of collective bubble collapse state at time $t/t_C = 0.95$: (a)–(c) $\Pi = 2$; (d)–(f) $\Pi = 10$. Cloud configurations correspond to table 6.1: (a) and (d) cloud 3; (b) and (e) cloud 9; (c) and (f) cloud 14.
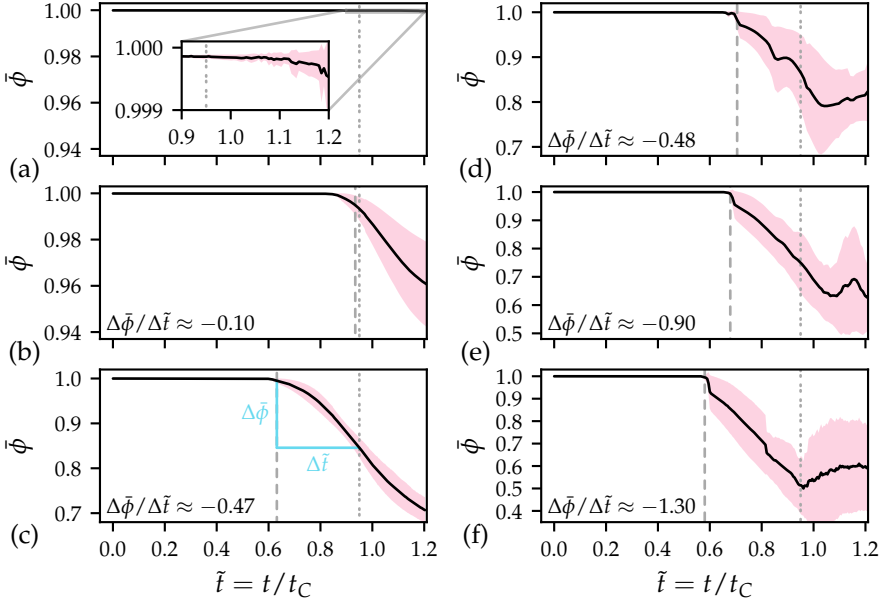
FIGURE 6.3: Temporal evolution of the mean porosity $\bar{\phi}$ (degree of bubble deformations): (a)–(c) $\Pi = 2$; (d)–(f) $\Pi = 10$. Cloud configurations correspond to table 6.1: (a) and (d) cloud 3; (b) and (e) cloud 9; (c) and (f) cloud 14. $\cdots\cdots$, $t/t_C = 0.95$ (see figure 6.2); $- - -$, $\bar{\phi} = 0.995$.

The bubble collapse is initiated at the cloud perimeter due higher forcing pressure in the far-field of the liquid. The magnitude of the forcing pressure Π as well as the cloud interaction parameter β_C determine the collapse dynamics of the bubble cluster. In particular, for clouds with sufficiently large β_C and pressure ratios Π, a bubbly shock wave with thickness d_F forms at the outskirts of the cloud and is magnified as it propagates towards the cloud center. The magnification is caused by local bubble collapses that emit strong pressure shocks upon collapse. Part of the released energy radiates towards the cloud center which is transferred into collapse energy of the following bubbles. This is in accordance with the hypotheses in Hansson et al. (1980) and Mørch (1980). Visualizations for the collapse of cloud 8 and 12 are shown in figures 6.4 and 6.5, respectively. The images correspond to the *xy*-plane through the cloud center at $z = 0\,\text{mm}$ and show streamlines based on the velocity field and schlieren visualizations computed from the pressure gradient $|\nabla p|$. The collapse shown in figure 6.4 corresponds to

FIGURE 6.4: Collapse chronology of cloud 8 in the xy-plane at $z = 0\,\text{mm}$: (a) initial bubble distribution; (b) $t = 11.25\,\mu\text{s}$; (c) $t = 22.5\,\mu\text{s}$; (d) $t = 33.75\,\mu\text{s}$; (e) $t = 45\,\mu\text{s}$; (f) $t = 52.22\,\mu\text{s}$. Streamlines of the instantaneous velocity field and schlieren images of $|\boldsymbol{\nabla} p|$ are superimposed on the bubble interfaces shown for $\alpha_2 = 0.5$. Configuration parameter: $R_C = 10\,\text{mm}$; $\beta_C = 0.5$; $\Pi = 2$.
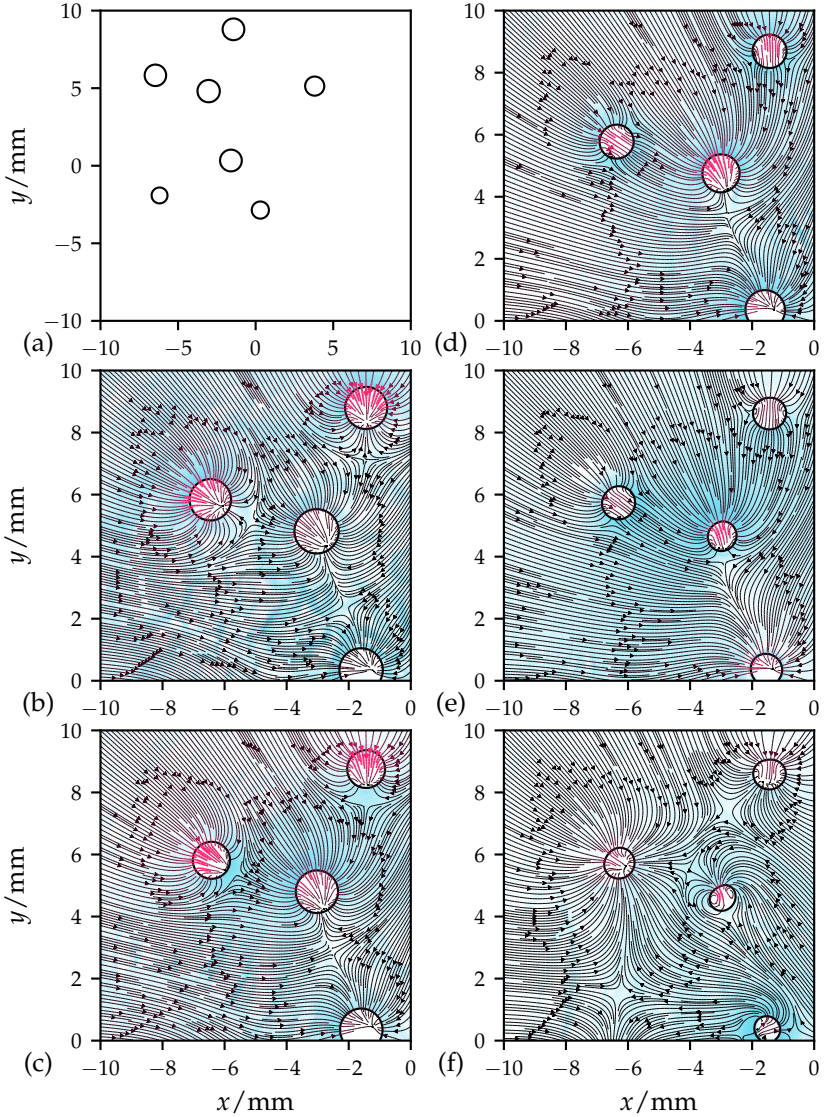
FIGURE 6.5: Collapse chronology of cloud 12 in the xy-plane at $z = 0\,\text{mm}$: (a) initial bubble distribution; (b) $t = 12.5\,\mu s$; (c) $t = 25\,\mu s$; (d) $t = 37.5\,\mu s$; (e) $t = 50\,\mu s$; (f) $t = 57.55\,\mu s$. Streamlines of the instantaneous velocity field and schlieren images of $|\boldsymbol{\nabla} p|$ are superimposed on the bubble interfaces shown for $\alpha_2 = 0.5$. Configuration parameter: $R_C = 10\,\text{mm}$; $\beta_C = 7.5$; $\Pi = 4.5$.
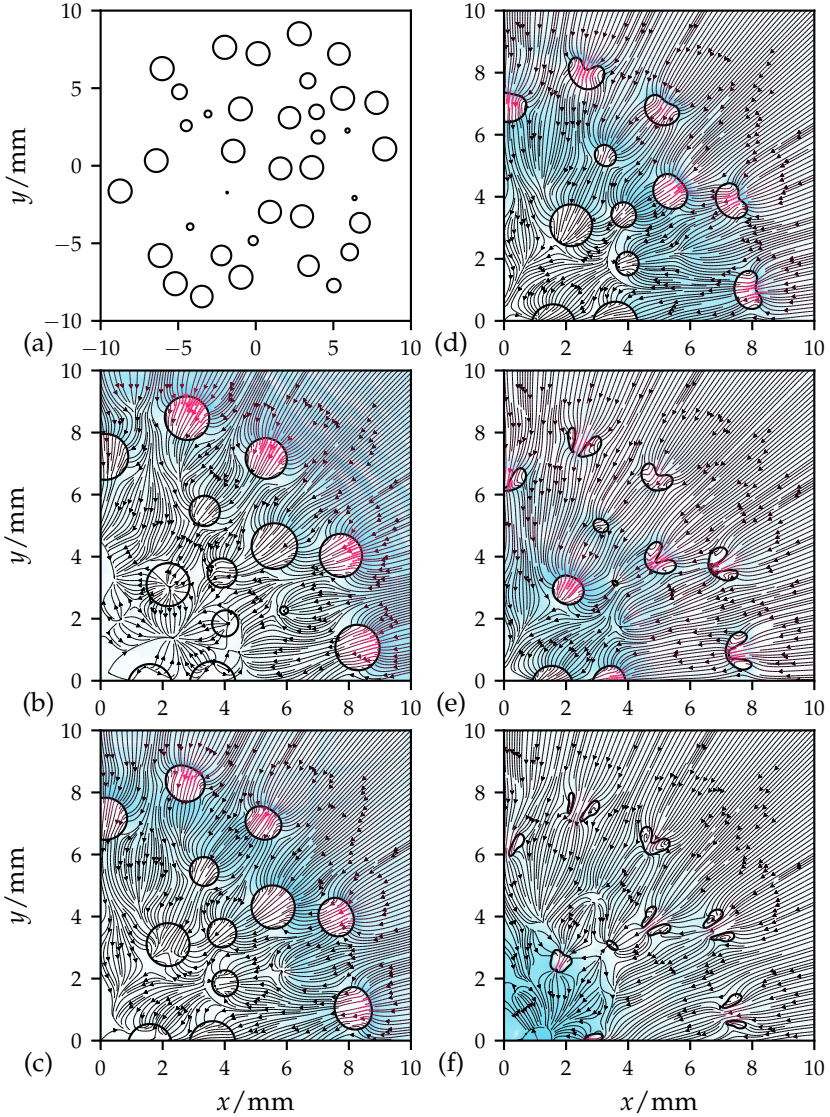
cloud 8 with $\Pi = 2$ and time instants $t = 11.25, 22.5, 33.75, 45$ and $52.22\,\mu s$. It is evident from the schlieren visualization in the background that the formation of a bubbly shock wave does not take place for this configuration. There is, however, a chronology of flow acceleration inside bubbles which starts at the outskirts of the cloud. The direction of the acceleration inside the bubbles is towards its closest neighbor due to secondary Bjerknes forces (Bjerknes, 1906; Pelekasis et al., 1993). The bulk flow tends towards the cloud center while streamlines in direction away from the cloud center coexist. On the contrary, the collapse shown in figure 6.5 corresponds to cloud 12 with $\Pi = 4.5$ and time instants $t = 12.5, 25, 37.5, 50$ and $57.55\,\mu s$. The configuration for this case causes the formation of a bubbly shock wave, as seen in figures 6.5(c) and 6.5(d). Here β_C is one order of magnitude lager than for the previous case, while the forcing pressure is about two time larger. This leads to a violent evident based on the indicated streamlines that the cloud collapse is charged at the cloud perimeter by a build up of kinetic energy in the first bubble layer. The kinetic energy increases the momentum in the liquid which transports the kinetic energy in wards as the collapse progresses. The potential energy released by individual bubble collapses magnify the strength of the bubbly shock wave as the cloud collapse proceeds. This is in concert with Hansson et al. (1980) and Mørch (1980).

The initial charging of kinetic energy at the cloud perimeter and the subsequent propagation of the kinetic energy wave is shown by the example of cloud 14, see figures 6.2(c) and 6.2(f). The kinetic energy in the mixture is computed along radial lines that start from the cloud center in the xy-plane through the cloud center $z = 0\,mm$. To average out the random bubble positions, the kinetic energy is averaged over 360 samples obtained at $1°$ increments along the positive z-axis. Figure 6.6 shows the temporal evolution of the average kinetic energy wave in the rt-space for cloud 14 at the pressure ratio $\Pi = 2$. The vertical dimension indicates the logarithm of the average kinetic energy $\bar{E}_{kin}$. The figure shows the initial charging with kinetic energy at the cloud perimeter $r/R_C = 1$ within the time interval $t/t_C < 0.3$. Additional energy peaks appear for $t/t_C \geq 0.3$ where the spatial separation of the energy peaks is of the order $2R_{B,0}$. Although β_C is large in this cloud configuration, the weak forcing pressure in the liquid far-field does not impose enough potential for a bubbly shock formation. The increase of kinetic energy is governed by the bubble length scale and the elasticity of the present gas phase, which attenuates the incoming pressure perturbation. For this reason, no wave amplification is observed towards the
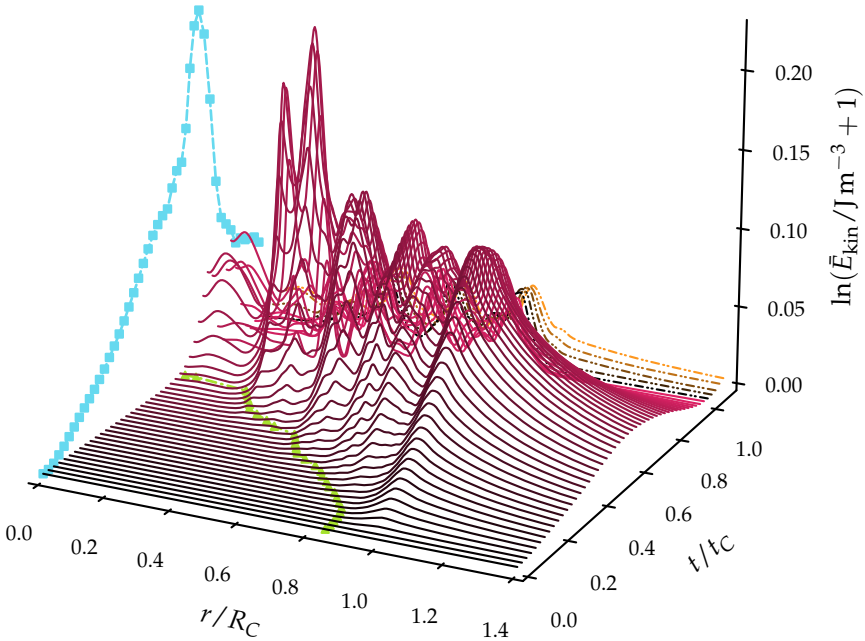
FIGURE 6.6: Radially averaged kinetic energy wave in *rt*-space for cloud 14: ——, energy wave before cloud collapse ($t/t_C < 1$); —··—··, energy wave after cloud collapse ($t/t_C > 1$); —■—, projection of $\max_r \bar{E}_{\mathrm{kin}}(r,t)$; —·▲·—, wave trajectory corresponding to the radial coordinate R_F such that $\bar{E}_{\mathrm{kin}}(R_F,t) = 0.05 \max_r \bar{E}_{\mathrm{kin}}(r,t)$. Configuration parameter: $R_C = 12.5\,\mathrm{mm}$; $\beta_C = 7.5$; $\Pi = 2$.

core of the cloud. Moreover, the wave profiles are almost standing which indicates a stronger dependence on the temporal coordinate as the wave magnitude merely amplifies and attenuates along the time axis. The state at $t/t_C = 0.95$ for this cloud configuration is shown in figure 6.2(c).

Figure 6.7 shows the same case as before at pressure ratio $\Pi = 4.5$. The initial charging at the cloud perimeter takes slightly longer up to about $t/t_C < 0.4$. The pressure perturbation in the liquid far-field is strong enough in this case to cause the formation of a bubbly shock wave. The wave profiles reveal, however, a slightly rippled shape along the r axis for time $t/t_C \geq 0.4$, indicating that the length scales of the bubbles cause local energy relaxation effects and thus a more oscillatory propagation of the bubbly shock wave.
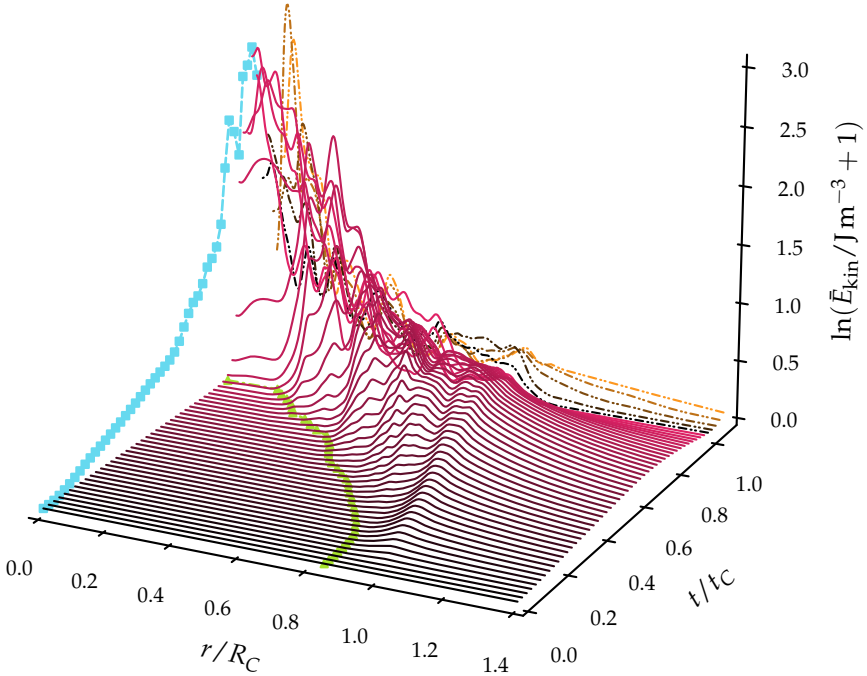
FIGURE 6.7: Radially averaged kinetic energy wave in rt-space for cloud 14: ———, energy wave before cloud collapse ($t/t_C < 1$); —··—··, energy wave after cloud collapse ($t/t_C > 1$); —■—, projection of $\max_r \bar{E}_{kin}(r, t)$; —▲—, wave trajectory corresponding to the radial coordinate R_F such that $\bar{E}_{kin}(R_F, t) = 0.05 \max_r \bar{E}_{kin}(r, t)$. Configuration parameter: $R_C = 12.5\,\text{mm}$; $\beta_C = 7.5$; $\Pi = 4.5$.

Finally, figure 6.8 shows the results for a pressure amplification of $\Pi = 10$. The charging at the cloud perimeter takes about the same time as for the $\Pi = 4.5$ case before. The wave profile, however, is steeper and the forming wave has a lager magnitude. The visibility of the bubble length scales disappears due to the higher gas phase compression of the resulting wave. As a result, the wave trajectory in figure 6.8 appears smoother compared to the other two cases. For both cases in figures 6.7 and 6.8, the wave amplitude is reinforced due to the cascading effects of individual bubble collapses as the wave propagates towards the core of the cloud. Slightly before $t/t_C = 1$ the kinetic energy wave reaches the singularity at the cloud center which generates a sudden change in the liquid momentum, transforming the entire kinetic energy into potential energy which is released
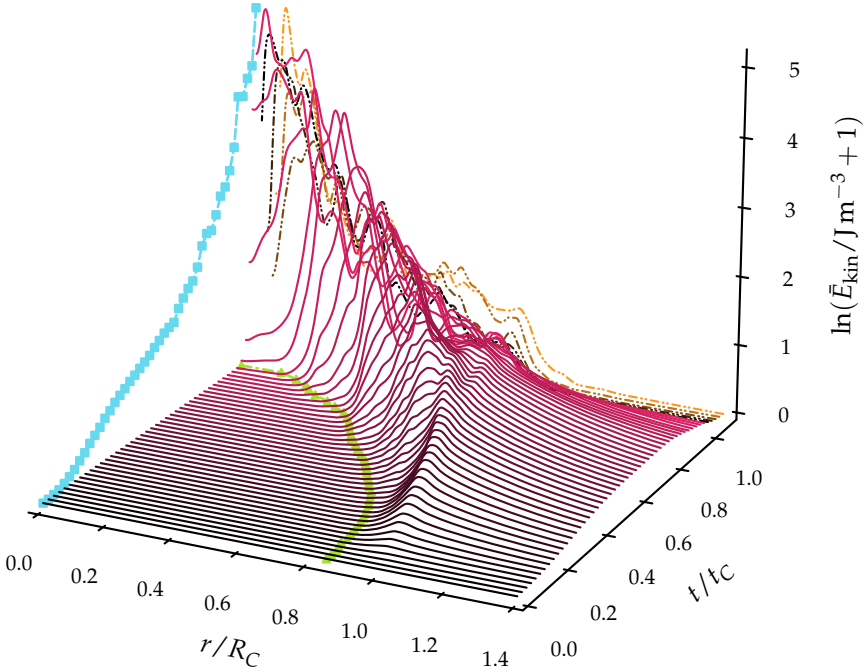
FIGURE 6.8: Radially averaged kinetic energy wave in rt-space for cloud 14: ────, energy wave before cloud collapse ($t/t_C < 1$); ──·──··, energy wave after cloud collapse ($t/t_C > 1$); ──■──, projection of $\max_r \bar{E}_{kin}(r,t)$; ──▲──, wave trajectory corresponding to the radial coordinate R_F such that $\bar{E}_{kin}(R_F, t) = 0.05 \max_r \bar{E}_{kin}(r,t)$. Configuration parameter: $R_C = 12.5$ mm; $\beta_C = 7.5$; $\Pi = 10$.

by a very strong outward propagating shock wave. This result is consistent with Mørch (1980). Due to the Rankine-Hugoniot jump conditions, the large pressure behind the outward shock induces a bulk velocity in the liquid; causing relaxation of the fluid state in the cloud core. This transfer of energy is again seen by the formation of kinetic energy for $t/t_C > 1$ in figures 6.7 and 6.8. It is noted that the 2× increase of the far-field pressure for the cases $\Pi = 2$ and $\Pi = 4.5$ results in 10× higher energy conversion due to the activation of local bubble dynamics whose energy potential is released in the form of local pressure shocks. On the other hand, increasing the forcing pressure by another 2× in the case of $\Pi = 4.5$ and $\Pi = 10$ results in a 2× increase of the energy transformation rate, suggesting a proportional relationship in the regime where bubbly shock waves develop during cloud

cavitation collapse. Analysis of the bubbly shock structure is discussed in section 7.3.1.

6.6.2 *Individual bubble collapses*

The following analysis of individual bubble collapses is based on three characteristic bubbles whose dynamics are then compared with the KM and DK models. The selection of those bubbles is based on their initial radial distance from the cloud center:

 I the bubble furthest away from the cloud center,

 II the bubble closest to the $R_C/2$ coordinate,

 III the bubble closest to the cloud center.

Figures 6.9 and 6.10 display the evolution of the bubble radius R_B for the three characteristic bubbles at the locations described above. Figure 6.9 shows the evolution for the pressure ratio $\Pi = 2$ and figure 6.10 for the pressure ratio $\Pi = 10$. The time axes are normalized by the time $t_{\mathrm{III}}^{\mathrm{res}}$ corresponding to the minimum volume (collapse time) of the bubble closest to the cloud center, see the enumeration above, computed with the resolved 3D simulation. Comparative results with time $t_{\mathrm{III}}^{m}/t_{\mathrm{III}}^{\mathrm{res}} < 1$ for $m \in \{\mathrm{KM, DK}\}$ indicate faster collapse dynamics and vice versa $t_{\mathrm{III}}^{m}/t_{\mathrm{III}}^{\mathrm{res}} > 1$ corresponds to slower collapse dynamics. The cloud radius in those figures is equal to $R_C = 10\,\mathrm{mm}$. Predictions obtained from the reduced order models KM and DK are shown as well.

For $\Pi = 2$, shown in figure 6.9, the prediction of the bubble radius by the reduced order models is in overall good agreement with the data obtained from the resolved 3D simulation for $\beta_C = 0.2$ and 0.5. The slight deviations, observed in particular at bubble location I, are attributed to the initial pressure field which cannot be prescribed fully consistent with approaches based on the RP type equations. From $\beta_C = 1$ to 7.5, increasing deviations between KM and DK as well as with respect to the 3D simulation are observed for the evolution of the bubble radius at location III and, less pronounced, also for the bubble at location II. In particular, a delayed collapse of bubble III and a smaller minimum radius than in the 3D simulation is shown by KM. Both the delay of the collapse and the underestimation of the minimum radius increase with β_C. In contrast, the results obtained from DK are able to follow the curve of bubble III predicted by the 3D simulation farther towards the minimum radius. Only a slight delay in the collapse time of bubble III is observed for DK. However, the minimum

FIGURE 6.9: Temporal evolution of bubble radius R_B for $R_C = 10$ mm and $\Pi = 2$: (a) $\beta_C = 0.2$; (b) $\beta_C = 0.5$; (c) $\beta_C = 1$; (d) $\beta_C = 2.5$; (e) $\beta_C = 5$; (f) $\beta_C = 7.5$. ⸺, resolved 3D simulation; ⸺ ⸺, Keller-Miksis (KM); ⸺·⸺·⸺, Doinikov (DK). Bubble locations: I, at cloud perimeter; II, at coordinate $R_C/2$; III, at cloud center.

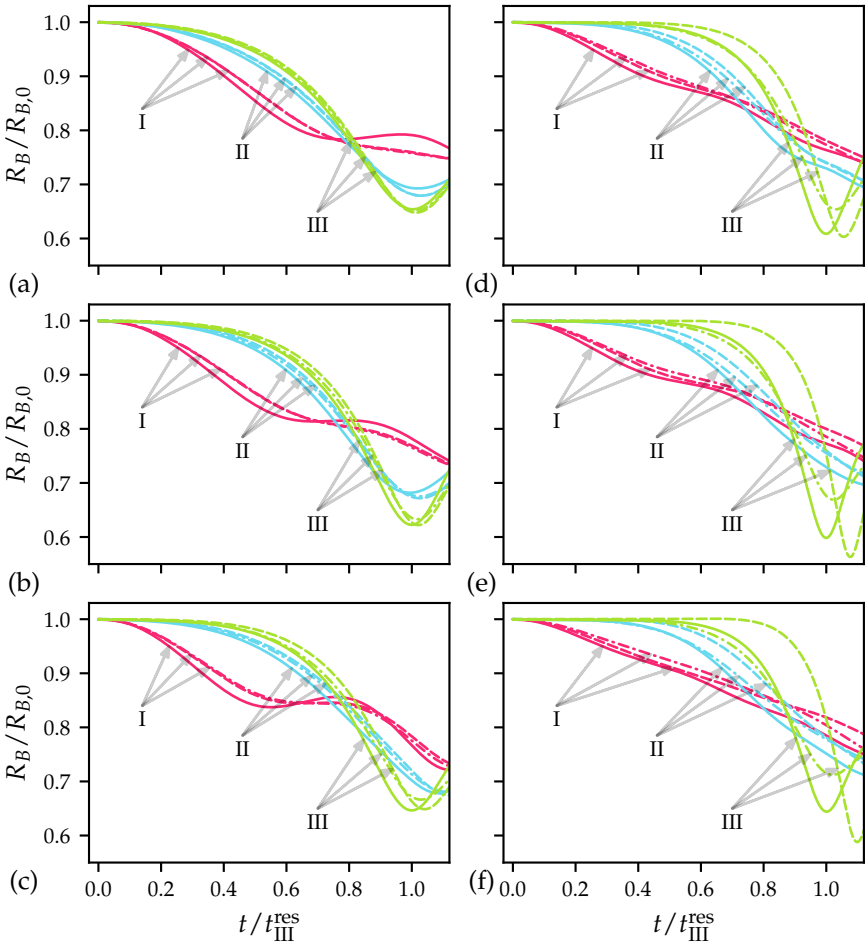FIGURE 6.10: Temporal evolution of bubble radius R_B for $R_C = 10\,\text{mm}$ and $\Pi = 4.5$: (a) $\beta_C = 0.2$; (b) $\beta_C = 0.5$; (c) $\beta_C = 1$; (d) $\beta_C = 2.5$; (e) $\beta_C = 5$; (f) $\beta_C = 7.5$. ——, resolved 3D simulation; ————, Keller-Miksis (KM); —·—·—, Doinikov (DK). Bubble locations: I, at cloud perimeter; II, at coordinate $R_C/2$; III, at cloud center.
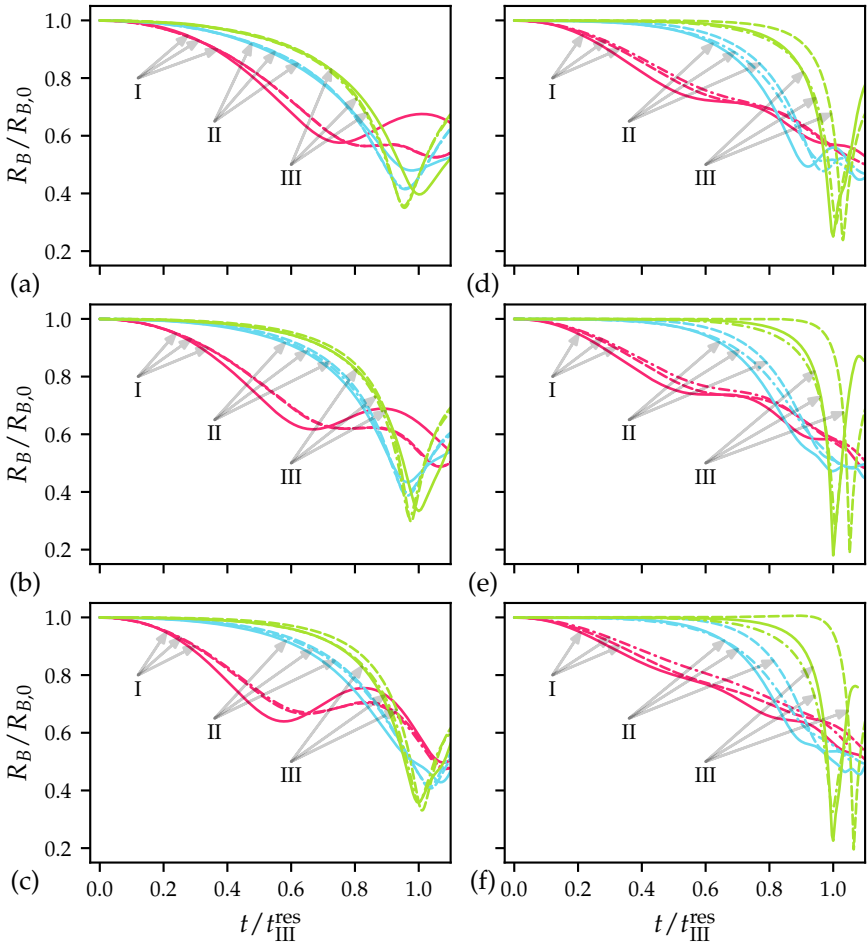
radius of bubble III is clearly overestimated. Again, the overestimation increases with β_C.

Analogous to the lower pressure ratio, KM and DK provide similar results for bubble I in the case of $\Pi = 4.5$, shown in figure 6.10, with the curves obtained from KM being slightly closer to the ones from the 3D simulation. However, somewhat larger deviations between them and the 3D simulation are observed. For bubble II and III, deviations between the results obtained with KM and DK emerge from $\beta_C = 1$ and increase with β_C as already seen for $\Pi = 2$. As observed from figures 6.10(d) to 6.10(f), numerical failure of the DK scheme is observed after the collapse of bubble III. These failures are due to bubble collisions caused by translation. To summarize, the chronological order of the collapses predicted by the considered bubble-particle approaches matches the one from the 3D simulation. A similar observation was reported in Bremond et al. (2006) using experimental data as a reference. Notable differences in the minimum radius and, for KM, also in the collapse time of bubble III, emerge with respect to increasing β_C and Π for both reduced order models. As seen from figures 6.2 and 6.3, the bubble deformation likewise increases with these parameters, leading to a violation of the assumption of spherical bubble collapse, fundamental to the bubble-particle approaches. Moreover, KM and DK also deviate from each other with increasing β_C. The consideration of bubble translation in DK significantly influences the results, and the results obtained from DK closer match the resolved 3D simulations compared to the KM model. The effects of bubble translation during collapse are addressed in the next section.

6.6.3 *Bubble translation during collapse*

The analysis of the previous section suggests that the bubble dynamics in cloud cavitation collapse are influenced by the translation of the bubbles. The purpose of this section is to provide a more detailed investigation of such translational bubble motions.

Figures 6.11 and 6.12 show the temporal evolution for the radial distance r_B of the center of bubble mass relative to the center of the cloud. The evolution of those distances are given for the three considered bubbles I, II and III, their definition was given at the beginning of section 6.6.2. The results shown in these figures correspond to a cloud with $R_C = 10\,\text{mm}$ and pressure ratios $\Pi = 2$ and $\Pi = 4.5$, respectively. The time axes are again normalized with time $t_{\text{III}}^{\text{res}}$. The positions obtained from DK are compared

FIGURE 6.11: Temporal evolution of radial distance r_B for $R_C = 10\,\text{mm}$ and $\Pi = 2$: (a) $\beta_C = 0.2$; (b) $\beta_C = 0.5$; (c) $\beta_C = 1$; (d) $\beta_C = 2.5$; (e) $\beta_C = 5$; (f) $\beta_C = 7.5$. ———, resolved 3D simulation; – – – –, Keller-Miksis (KM); – · – · –, Doinikov (DK). Bubble locations: I, at cloud perimeter; II, at coordinate $R_C/2$; III, at cloud center.
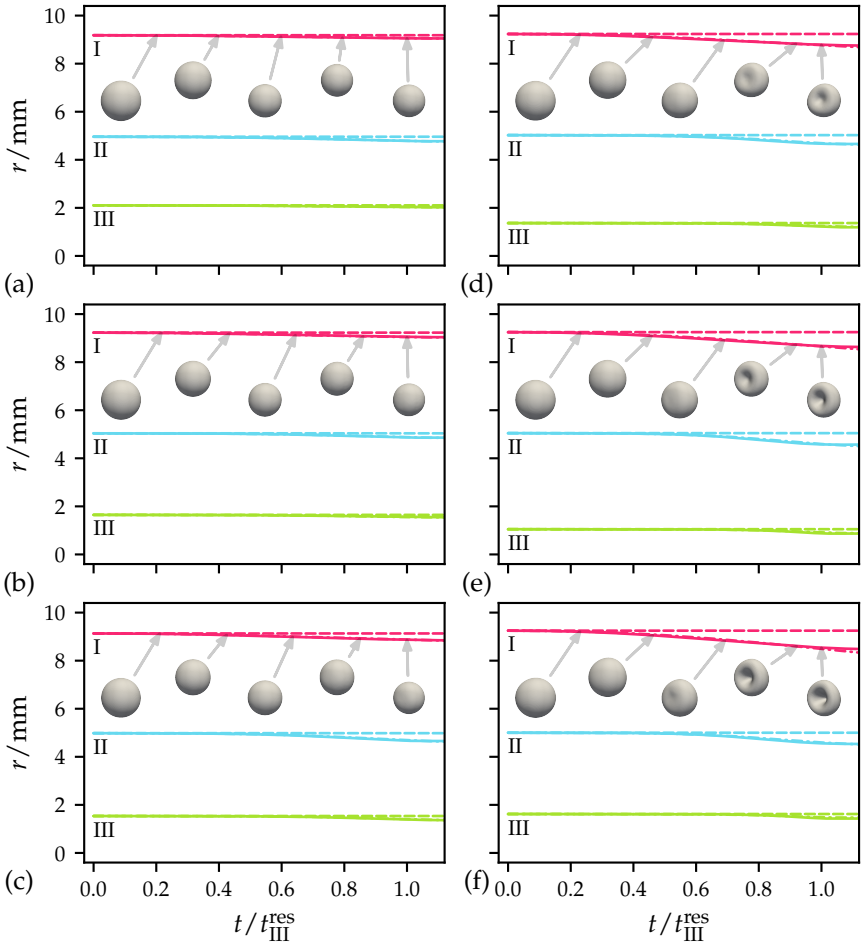
FIGURE 6.12: Temporal evolution of radial distance r_B for $R_C = 10\,\mathrm{mm}$ and $\Pi = 4.5$: (a) $\beta_C = 0.2$; (b) $\beta_C = 0.5$; (c) $\beta_C = 1$; (d) $\beta_C = 2.5$; (e) $\beta_C = 5$; (f) $\beta_C = 7.5$. ——, resolved 3D simulation; ———, Keller-Miksis (KM); —·—·—, Doinikov (DK). Bubble locations: I, at cloud perimeter; II, at coordinate $R_C/2$; III, at cloud center.

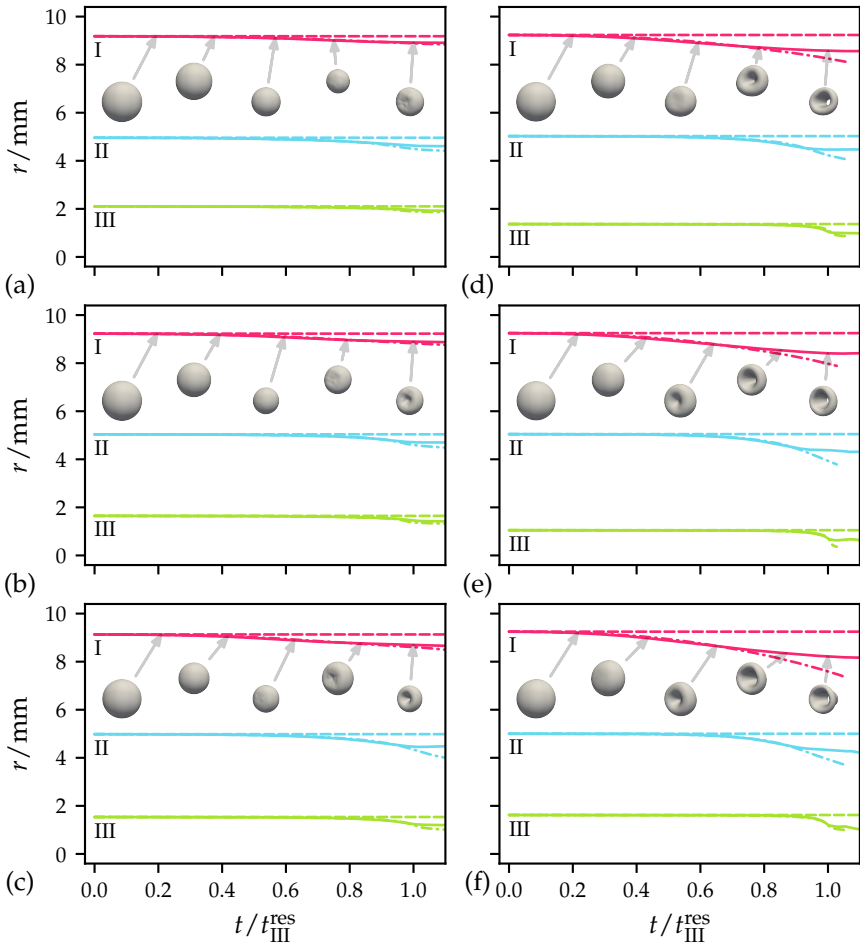to the respective data obtained from the resolved 3D simulations. Curves corresponding to the fixed bubble positions of KM are included for additional reference. The computed positions of the 3D simulations correspond to the center of mass for a generally deformed bubble. For cases with weak pressure ratio $\Pi = 2$, hardly any difference between the results obtained from DK and the 3D simulation are observable. The bubbles only slightly move for β_C values up to 1. Merely for bubble I, some slight deviations from the 3D simulation arise for the higher β_C values towards the end of the bubble collapse where the largest deformations are to be expected; see figure 6.3. Results for the stronger pressure amplification $\Pi = 4.5$ are shown in figure 6.12. Significantly larger deviations are observed, where DK clearly overestimates the displacement of bubble I and, later in time, also for bubble II. The deviations again increase with β_C. Significant translational motion of bubble III is observed only at the very end of its collapse process for sufficiently large β_C and Π. This impulsive non-linear bubble translation is again overestimated by the DK model.

Further insight into the origins of the deviations between DK and the 3D simulation is gained from the examination of bubble shapes. Selected time instances for the shape of bubble I are therefore additionally shown in figures 6.11 and 6.12. The last instance corresponds to t_{III}^{res}. When the bubble starts to develop stronger shape deformations, the deviation of the trajectories predicted by DK and the 3D simulations becomes more pronounced. At the time when the collapsing bubble takes a toroidal shape due to the penetration of microjets, it becomes more transparent to the local flow field and its motion starts to stagnate. For $\Pi = 2$ and $\beta_C \leq 1$, the bubble remains spherical during its compression and the predictions by DK perfectly match the 3D simulation results. The bubble translation in those cases is mainly attributed to slight changes in the liquid momentum that are not related to a bubbly shock. The involved dynamics are governed by primary and secondary Bjerknes forces (Bjerknes, 1906).

Only for clouds with sufficiently large interaction parameter, β_C, and correspondingly high pressure ratio Π to overcome the elasticity induced by the gas phase, a bubbly shock wave will form. Attributed to the Rankine-Hugoniot jump condition, the flow velocity behind this shock is non-zero (assuming a zero initial velocity field). The phenomenon of bubbly shock formation has been visualized in figures 6.4 and 6.5, where the two cases considered in those images correspond to the cases shown in figures 6.9(b) and 6.11(b) and figures 6.10(f) and 6.12(f), respectively. The time instants shown for bubble I in these latter figures are identical to the time instants
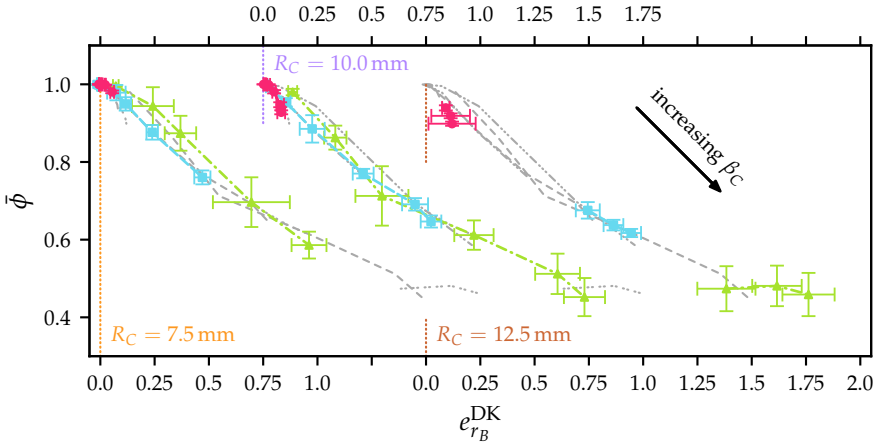
FIGURE 6.13: Radial displacement error $e_{r_B}^{DK}$ versus average bubble porosity $\bar{\phi}$ (average degree of deformation): ——●——, $\Pi = 2$; — ■ —, $\Pi = 4.5$; — ▲ —, $\Pi = 10$. Reference curves: ······, $R_C = 7.5\,\text{mm}$; — — —, $R_C = 10\,\text{mm}$; ·······, $R_C = 12.5\,\text{mm}$. Error bars indicate standard deviation.

of the slices through the cloud center shown in the former figure reference. As mentioned above, in the case of $\beta_C = 0.5$ and $\Pi = 2$, bubbly shock formation is not taking place resulting in only slight bubble movement and excellent agreement with DK. The kinetic energy wave in this case is standing in space, where formation of kinetic energy is exclusively due to local bubble wall velocities; see figure 6.6. On the contrary, a bubbly shock formation is observed for the case $\beta_C = 7.5$ and $\Pi = 10$, leading to a violent bubble collapse with high deformations and microjet formation. The evolution of the kinetic energy wave due to these effects is shown in figure 6.8. The non-zero velocity behind the bubbly shock causes the bubbles to move towards the focal point of the shock wave, seen in figure 6.12(f). The high bubble deformations lead to toroidal shapes that become more transparent to the bulk liquid momentum, causing bubbles to slow down at the later stage of the collapse. This phenomenon is not captured by the DK model and consequently bubbles continue to accelerate towards the cloud center, resulting in large deviations in predicted positions relative to the resolved simulations.

A quantitative description for the evolution of the bubble shapes can be obtained in terms of the average porosity defined in equation 6.6. To

quantify the error of bubble translation in radial direction, the following measure is defined

$$e_{r_B}^{DK} = \frac{1}{R_{B,0}N_{disp}} \sum_{i=1}^{N_{disp}} \left(r_{B,i}^{res}(t_{III}^{res}) - r_{B,i}^{DK}(t_{III}^{DK}) \right), \quad (6.11)$$

where $N_{disp} = \lfloor 0.15N_B \rfloor$ corresponds to the number of displaced bubbles used for this analysis. These bubbles are located in the outer region of the cloud where the translation trajectory is similar to that of bubble I in figures 6.11 and 6.12. Figure 6.13 shows the measured radial displacement error based on equation 6.11 for the clouds listed in table 6.1. The data is plotted against the average bubble porosity for the N_{disp} bubbles according to equation 6.6. The radial displacement errors are normalized by the initial bubble radius $R_{B,0}$, such that a value of $e_{r_B}^{DK} = 1$ means an average radial displacement error of one initial bubble radius measured between the DK model and the resolved 3D simulations. The positive number indicates that the bubble position predicted by the DK model is closer to the cloud center, i. e., $r_{B,i}^{DK} < r_{B,i}^{res}$ on average. The standard deviations for both plotted quantities are indicated in figure 6.13 as well. Data from the 3D simulation is evaluated at the collapse time t_{III}^{res} of bubble III and data from DK at the corresponding time t_{III}^{DK}. For increasing β_C, the porosity decreases, i. e., the degree of bubble deformation increases, leading to an increase in the error of the radial bubble positions. In particular, the curves of all cloud radii and pressure ratios approximately coincide. To illustrate this consistency, the curves corresponding to the other cloud radii are plotted as a reference in figure 6.13. For the largest error in the radial position, the porosity does not further decrease as a lower bound for these values is reached; see also figure 6.3. These observations clearly indicate that deviations in the radial displacement of bubbles strongly correlate with their deformation, a quantity that is not accounted for in typical RP type models.

6.6.4 Bubble pressure

This section provides an analysis of the predicted pressure for the considered computational models. In a collapsing cloud composed of non-condensable gas bubbles, the global peak pressure arises within a bubble close to the cloud center. Table 6.3 provides the bubble indices which exhibit the global peak pressure. The indices are sorted according to the bubble location, where the index 1 corresponds to the bubble closest to the center

R_C/mm	β_C	$\Pi = 2$			$\Pi = 4.5$			$\Pi = 10$		
		res	KM	DK	res	KM	DK	res	KM	DK
7.5	0.015	2	2	2	2	2	2	2	2	2
7.5	0.1	1	1	1	1	1	1	1	1	2
7.5	0.2	2	2	2	2	2	2	2	2	2
7.5	0.5	2	2	2	2	2	2	2	2	2
7.5	1.0	1	1	1	1	1	1	1	1	1
7.5	2.5	1	1	1	1	1	1	1	1	1
10.0	0.2	2	2	2	2	2	2	2	2	2
10.0	0.5	1	3	1	3	3	3	3	3	3
10.0	1.0	3	3	3	2	7	2	2	7	7
10.0	2.5	3	3	3	3	3	3	1	3	3
10.0	5.0	1	1	1	1	1	1	1	1	1
10.0	7.5	1	1	4	1	1	1	1	1	1
12.5	5.0	1	1	1	1	1	1	1	1	1
12.5	7.5	1	1	1	1	1	1	1	1	1
12.5	10.0	2	2	2	2	2	2	2	2	2

TABLE 6.3: Peak pressure location by bubble index. Bubble indices are sorted such that index 1 is closest to the cloud center.

of the cloud. By this order, bubble III corresponds to index 1 and bubble I to the largest index N_B. For most of the considered cases, KM, DK and the resolved 3D simulation predict the same peak pressure bubble. In summary, KM as well as DK provide adequate predictions for the location of the peak pressure.

Most of the locations shown in table 6.3 correspond to bubble III. It was shown in section 6.6.2 that the KM model exhibits delays in the collapse time t_{III} in particular for large β_C; see figures 6.9(f) and 6.10(f). A more quantitative evaluation for the collapse time of bubble III is given by the juxtaposition in figure 6.14. The reference curve $y = x$ corresponds to perfect agreement. All clouds in table 6.1 and all pressure ratios Π are considered in this figure. Doinikov is overall in good agreement with the resolved simulation for all configurations owing to the additional degrees of freedom
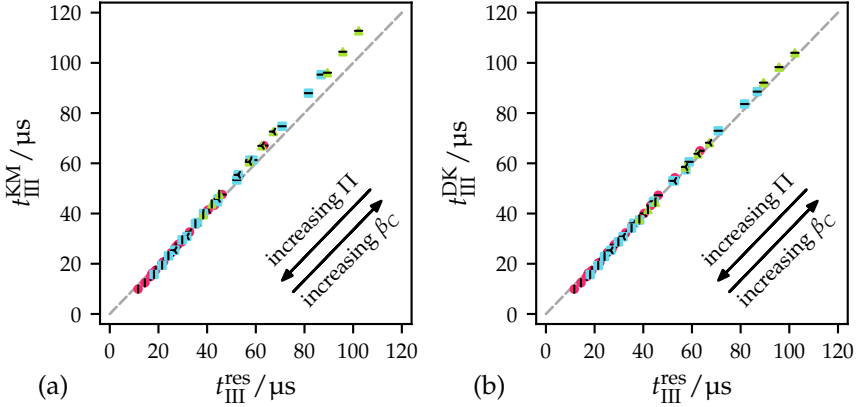
FIGURE 6.14: Collapse time of bubble III compared to the resolved 3D simulation: (a) Keller-Miksis (KM); (b) Doinikov (DK). ●, $R_C = 7.5\,\mathrm{mm}$; ■, $R_C = 10\,\mathrm{mm}$; ▲, $R_C = 12.5\,\mathrm{mm}$; –, $\Pi = 2$; ◄, $\Pi = 4.5$; ⵏ, $\Pi = 10$; - - - -, $y = x$.

for bubble translation. Notable overestimation of the collapse time $t_{\mathrm{III}}^{\mathrm{KM}}$ is observed for Keller-Miksis at $\Pi = 2$, especially for large β_C (necessarily for larger R_C). This inaccuracy vanishes at large pressure ratios Π.

The pressure inside a bubble is computed by means of spherical sensors with radius $R_{S,i} = R_{B,i}(t = 0) + 1/2\,d_G$ and concentrical with the center of mass of bubble i. This allows to capture bubble movement and avoids overlap with neighboring bubbles; see figure 7.1 on page 122 for a sketch. The bubble pressure p_{III} is then obtained by

$$p_{\mathrm{III}} = \frac{1}{V_{B,\mathrm{III}}} \int_{\Omega_{S,\mathrm{III}}} \alpha_2 p \, \mathrm{d}V, \tag{6.12}$$

where $\Omega_{S,\mathrm{III}}$ denotes the domain of the sensor for bubble III. The bubble volume is computed according to

$$V_{B,\mathrm{III}} = \int_{\Omega_{S,\mathrm{III}}} \alpha_2 \, \mathrm{d}V. \tag{6.13}$$

For the strongest cloud collapses considered in this study, which are the ones for $\Pi = 10$, $R_C = 12.5\,\mathrm{mm}$ and all considered β_C values, as well as the cases corresponding to $\Pi = 10$ and $R_C = 10\,\mathrm{mm}$ with $\beta_C = 5$ and 7.5, the shape of bubble III is strongly deformed and highly compressed. Only a thin torus with $\alpha_2 < 1$ of the thickness of the cell size remains from
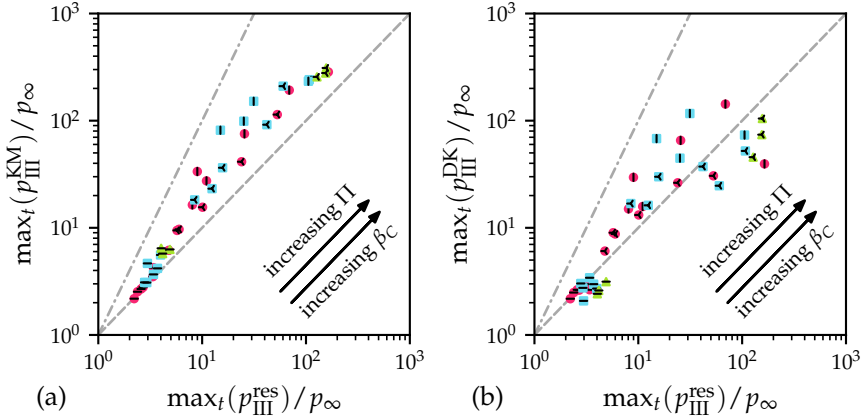
FIGURE 6.15: Collapse time of bubble III compared to the resolved 3D simulation: (a) Keller-Miksis (KM); (b) Doinikov (DK). ●, $R_C = 7.5\,\text{mm}$; ■, $R_C = 10\,\text{mm}$; ▲, $R_C = 12.5\,\text{mm}$; ▬, $\Pi = 2$; ◄, $\Pi = 4.5$; ▮, $\Pi = 10$; ▬▬▬▬, $y = x$; ▬·▬·▬·, $y = x^2$.

these bubbles. This issue prohibits any accurate computation of the bubble pressure at location III, suitable for comparison with the reduced order models. Figure 6.15 displays the peak pressure $\max_t(p_{\text{III}})$ for the bubble at location III computed by the 3D simulation and compared with KM and DK. Pressures are displayed as amplification factors by normalization with the liquid far-field pressure p_∞. The aforementioned extreme cases are excluded. For the weakest collapses ($\Pi = 2$, low β_C values and small R_C), the 3D simulation, KM and DK predict similar peak pressures for bubble III. In the remaining cases, especially the ones with medium and high pressure ratio, KM leads to overestimated peak pressures compared to the 3D simulation. For reference, curves $y = x$ and $y = x^2$ are further added in the diagrams. Tiwari et al. (2015) observed the latter scaling for KM based on hemispherical clouds with 50 bubbles and various comparable pressure ratios. The simulations of the spherical clouds in this work, however, indicate that a quadratic scaling law for the peak pressure predictions between KM and the resolved 3D simulation is more of an upper bound. In the case of KM only peak pressure overestimates have been observed. For the DK model underestimates occur as well, where underestimates are mainly observed in regions of higher β_C and R_C values.
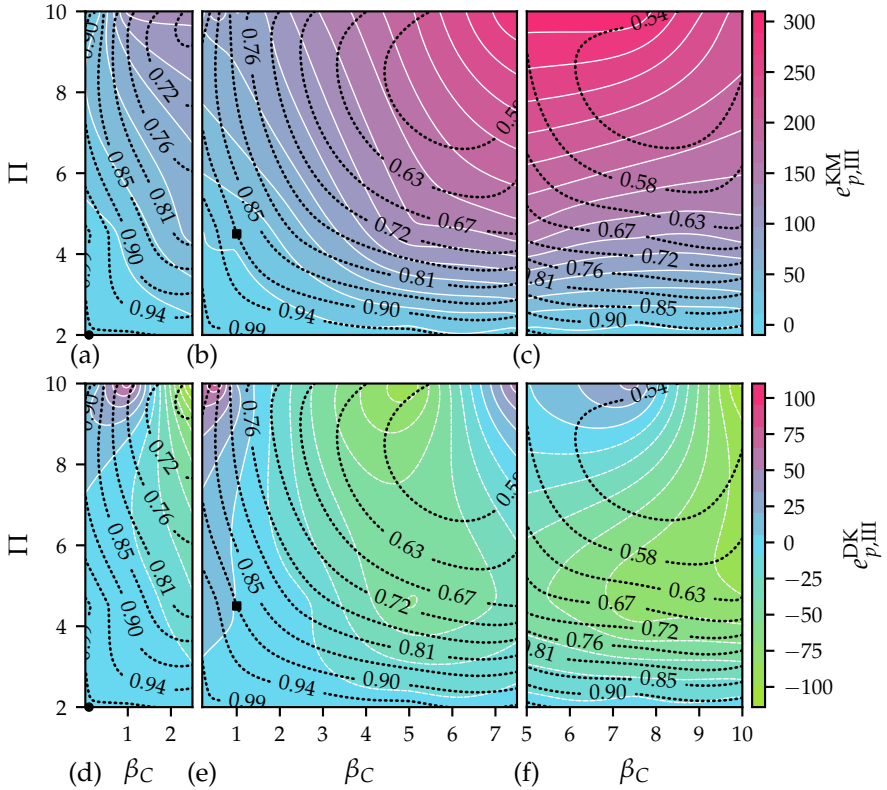
FIGURE 6.16: Error in peak pressure predictions for bubble III closest to the cloud center: (a) KM, $R_C = 7.5\,\text{mm}$; (b) KM, $R_C = 10\,\text{mm}$; (c) KM, $R_C = 12.5\,\text{mm}$; (d) DK, $R_C = 7.5\,\text{mm}$; (e) DK, $R_C = 10\,\text{mm}$; (f) DK, $R_C = 12.5\,\text{mm}$; ⋯⋯⋯, porosity $\bar{\phi}$; ●, cloud 2, $\Pi = 2$; ■, cloud 9, $\Pi = 4.5$.

A quantification of the error for the prediction of the peak pressure observed in bubble III is based on the measure

$$e_{p,\mathrm{III}}^m = \frac{\max_t(p_{\mathrm{III}}^m) - \max_t(p_{\mathrm{III}}^{\mathrm{res}})}{p_\infty}, \qquad (6.14)$$

where $m \in \{\mathrm{KM}, \mathrm{DK}\}$. The quantity $e_{p,\mathrm{III}}^m$ describes the factor by which the reduced order model m overestimates (positive) or underestimates (negative) the observed peak pressure in bubble III relative to the resolved 3D simulation. The deviations based on this measure are shown in figure 6.16 for the full parameter range. In contrast to the data shown in figure 6.15 the extreme cases not shown in that figure are included in figure 6.16. It is noted that the uncertainty for those extreme cases may be large, however, the reduced order models tend to generate already larger errors for less extreme cases in the same parameter neighborhood. Data points between simulated parameter sets are linearly interpolated. In addition to the results obtained with equation 6.14, labeled contour lines corresponding to the mean porosity based on equation 6.10 are superimposed.

The Keller-Miksis model exhibits a clear correlation between the error in the peak pressure prediction of bubble III and the degree of bubble deformation indicated by the porosity $\bar{\phi}$. The direction of the gradient of increasing error in the peak pressure prediction follows the direction of the gradient for decreasing porosity, i. e., larger bubble deformations. Figures 6.16(a) and 6.16(b) illustrate that this correlation is valid for the full set of test clouds with $R_C = 7.5\,\mathrm{mm}$ as well as over the full range of Π for clouds with $R_C = 10\,\mathrm{mm}$ and if $\beta_C < 1$, which applies to clouds 1– 8 in table 6.1. It is noted, however, that KM performs best for $\Pi < 4$ which is evident from figures 6.16(a) to 6.16(c). The model by Doinikov exhibits a similar correlation between porosity and the associated error in the peak pressure prediction. The region of best performance is similar to that observed for KM; corresponding to the blue colored regions in the diagrams of figures 6.16(d) to 6.16(f). On contrary to KM, the peak pressure predictions by DK include underestimates and overestimates, which are symmetric around the null-error point. Since the initial condition of both, KM and DK consists of identical far-field liquid pressure and bubble cluster configuration, and hence, identical potential energies, the DK model draws part of that energy budget for the translational motions. This results in an imbalance of total kinetic energy at the gas-liquid interfaces between KM
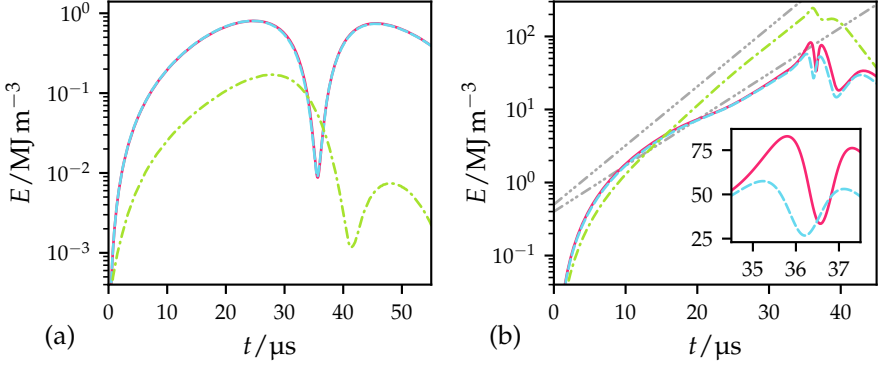
FIGURE 6.17: Temporal evolution of energy at gas-liquid interfaces as well as due to liquid mass displacement: (a) cloud 2, $\Pi = 2$, see ● in figure 6.16; (b) cloud 9, $\Pi = 4.5$, see ■ in figure 6.16. ———, $E_{\text{kin},I}^{\text{KM}}$; ─────, $E_{\text{kin},I}^{\text{DK}}$; ──·──·, $E_{\text{disp}}^{\text{DK}}$; ──···──···, exponential references.

and DK and leads to lower peak pressures measured for bubble III. The total kinetic energy at the gas-liquid interfaces is quantified by

$$E_{\text{kin},I}^m = \frac{1}{2}\rho_1 \sum_{i=1}^{N_B} \dot{R}_{B,i}^2, \tag{6.15}$$

where $m \in \{\text{KM}, \text{DK}\}$. The amount of energy required to displace the liquid mass for the translational motion in the DK model is further given by

$$E_{\text{disp}}^{\text{DK}} = \frac{1}{2}\rho_1 \sum_{i=1}^{N_B} \dot{x}_{B,i}^2. \tag{6.16}$$

The temporal evolution of those energies is shown in figure 6.17 for the two sets of parameters indicated in figure 6.16. The parameter configuration shown in figure 6.17(a) corresponds to cloud 2 with low pressure ratio $\Pi = 2$. This cloud contains only 16 bubbles and consequently the energy for the bubble displacement is about one order of magnitude smaller than the energy at the gas-liquid interfaces for bubble compression. The later energy is about identical for both KM and DK for all t, resulting in identical bubble dynamics. Figure 6.17(b) shows the case for the configuration of cloud 9 with 109 bubbles at pressure ratio $\Pi = 4.5$, furthermore indicated in figure 6.16. The figure reveals that for large enough forcing potentials, both $E_{\text{kin},I}^m$ and $E_{\text{disp}}^{\text{DK}}$ transition into an exponential growth region

after about 20 µs where $E_{\text{disp}}^{\text{DK}}$ grows at a 3.2× stronger rate. This eventually leads to less compression potential for the DK model which in turn results in smaller peak pressures in the bubbles as well as faster collapse, a deficiency of the KM model illustrated in figures 6.9 and 6.10 for the larger β_C systems. While accounting for bubble translation improves the collapse time prediction over the full range of β_C, see figure 6.14(b), the accuracy of predicted bubble radii and peak bubble pressure abates compared to the resolved 3D simulation due to the inherent assumption of spherical bubble collapse in the DK model. Moreover, it is seen from figure 6.15(b) that the partitioning of the $E_{\text{kin},I}^{\text{DK}}$ and $E_{\text{disp}}^{\text{DK}}$ energy budgets is sensitive to the random bubble positions in the initial cloud configurations, especially for denser clouds with larger β_C and higher pressure ratios Π. This sensitivity due to the energy partitioning into translatory and compressive budgets explains the over- and underestimations of the peak pressure measurements shown in figure 6.15(b) and eventually in figures 6.16(d) to 6.16(f).

6.7 CONCLUSION

Rayleigh-Plesset type reduced order models with extensions for bubble-bubble interactions are a widely used approach to model the dynamics of cloud cavitation collapse. The parametric study performed in this chapter demonstrates their limitations with regard to more realistic results obtained from resolved 3D simulations. It is shown that for small cloud interaction parameter β_C shock formation in the bubbly liquid does not take place. Naturally, these cases are limit cases with negligible bubble-bubble interaction and consequently the reduced order models considered here perform equally well and accurate. The predictions of the peak pressure locations in cloud configurations within this parameter range all coincide with the predictions resolved simulations.

By increasing β_C (or equivalently α_C) and maintaining a low forcing pressure in the liquid far-field (relative to the initial bubble pressure), the additional benefit of modeling bubble translation becomes apparent in preserving the correct collapse time of bubbles that are within a spherical region with radius half that of the cloud radius R_C. This observation holds true for far-field pressures that are about 5× larger than the initial bubble pressure. The main defect of the KM model consists of overestimating the collapse time for bubbles that are responsible for peak pressure shock emission. The reason for this time elongation is the incorrect modeling

of the energy budget available for bubble compression during collapse. This energy is too large which results in excessive bubble compression that requires more time. As a consequence, the predicted peak pressures in the KM model are too large by about a factor of 2, less than what Tiwari et al. (2015) reported for hemispherical clouds.

The modeling of bubble translation in DK allows to divide the initial energy potential into a partition allocated for liquid mass displacement during bubble translation and a second partition for bubble compression. For weak initial pressure potentials and small β_C the former energy partition is about one order of magnitude smaller than that for bubble compression for which DK and KM perform equal. By increasing β_C as well as the forcing pressure in the liquid far-field, both energy partitions transition to exponential growth after a certain initiation time. The energy associated to bubble translation grows at a too large rate, which becomes more severe at larger β_C. The reason for this energy overestimate is the inherent assumption of spherical bubble collapse. The toroidal bubble deformations in realistic cloud cavitation results in bubbles that are opaque to the bulk flow and therefore slow down their linear motion. Consequently, the deceleration of bubbles reduces the required energy for liquid displacement, which is not accounted for in the case of idealized spherical bubble collapse. Finally, the energy overestimate in the DK model leads weaker bubble compression resulting in larger minimum bubble radii and lower peak pressure estimates. It is further noted that dense clouds and high far-field pressures lead to numerical issues in the DK model due to bubble collisions.

It is found that both KM and DK perform reasonably well at far-field pressure amplifications below $\Pi \approx 4$. For low β_C the additional complexity of the DK model is not justified. For increasing β_C systems DK is the preferred model due to more accurate prediction of individual bubble collapse times. It has been shown, however, that DK is not suitable for systems with gas volume fractions of about 12 % or more, even for weak far-field pressures. For systems with high gas volume fraction, both reduced order models fail to model accurately the higher complexity of the bubble-bubble interactions. Higher order models are necessary in such cases. An interesting future investigation would be the combination of DK with data-driven approaches that are able to learn the correct evolution of the energy required for bubble displacements based on data obtained from fully resolved simulations. Such an extension would help to increase the applicability of DK to problems with large β_C at moderate far-field pressures. The effect of varying bubble sizes has further been neglected in this study.

7

LARGE SCALE SIMULATION OF CLOUD CAVITATION COLLAPSE WITH 12500 GAS BUBBLES IN WATER

> *Empty your mind, be formless, shapeless, like water.*
> *Now you put water into a cup, it becomes the cup. You*
> *put water into a bottle it becomes the bottle, you put it*
> *in a teapot it becomes the teapot. Now water can flow,*
> *or it can crash. Be water my friend.*
>
> — Bruce Lee

This chapter presents results and analysis of unprecedented simulations of cloud cavitation collapse utilizing 12500 air bubbles in liquid water. The present simulations are enabled by the HPC software design discussed in chapter 4 and performed on a Cartesian uniform grid. The formation and propagation of a bubbly shock is investigated and compared with a 1D model (Mørch, 1989), a reduced order 3D homogeneous mixture model as well as experimental data (Kameda and Matsumoto, 1996; Kameda, Shimaura, et al., 1998). The analysis of the microscopic length scales present in the flow include the formation of microjets during individual bubble collapse. It is found by statistical analysis that the velocity magnitude of the microjets depends on the local strength of the bubbly shock wave and hence on the radial position of the bubbles in the cloud. At the same time, the orientation of microjets is influenced by the size of neighboring bubbles.

7.1 RELATED WORK

The collective growth and rapid collapse of a large number of bubbles, i. e., a cloud of bubbles, in a liquid subjected to large pressure variation has been investigated both experimentally and numerically. Experiments in Mørch (1980) studied the collapse of a cloud of bubbles via the formation of an inward propagating shock wave and the geometric focusing of this shock at the center of the cloud. Experimental measurements with hydrofoils subjected to cloud cavitation, conducted in Reisman et al. (1998), showed that very large pressure pulses occur within the cloud and are radiated

outward during the collapse process. A technique developed in Bremond et al. (2006) allowed for controlling the bubble distance within a 2D cloud. The study revealed the shielding effect of the outer bubbles and showed the formation of an inward-directed microjet. The final stage of the collapse of a hemispherical cloud near a solid surface was investigated using ultra high-speed photography in E. Brujan et al. (2011). Cloud cavitation in a water jet was examined in Yamamoto (2016). Various numerical studies were also reported in the literature; for instance, early ones assuming a potential flow in the liquid in Chahine and Duraiswami (1992) and Wang et al. (1999). The recently presented study of Ma et al. (2015) used an Euler-Lagrange approach, combining the Navier-Stokes equations with subgrid-scale spherical bubbles governed by a Rayleigh-Plesset type equation, to investigate spherical clouds collapsing near a rigid wall. A similar approach was applied in Chahine, Hsiao, et al. (2014) to study the impulsive loads generated by a cloud with 400 bubbles under an imposed oscillating pressure field. Resolved and deforming bubbles were considered in N. A. Adams et al. (2013), Peng et al. (2015), Šukys et al. (2018), and Tiwari et al. (2015). A 2D simulation of the collapse of a small cluster with 7 bubbles in an incompressible liquid using a front tracking method was presented in Peng et al. (2015). The collapse dynamics of a cloud composed of 125 vapor bubbles with random radii was studied in N. A. Adams et al. (2013), while Tiwari et al. (2015) reported the evolution of a hemispherical cloud of 50 air bubbles. In Tiwari et al. (2015), a homogeneous mixture model and a coupled system of Rayleigh-Plesset type equations were considered in addition, but provided qualitatively different predictions of the pressure field.

Early studies of wave propagation in disperse bubbly liquids date back to Mallock (1910) and Wood (1930) where fundamentally different wave propagation was reported compared to the pure phases, see also figure 3.1 on page 22. These theoretical observations have later been confirmed experimentally in works of Campbell et al. (1958), Carstensen et al. (1947), Fox et al. (1955), Karplus (1957), and Silberman (1957). An early study of wave structures based on scattering was published in Foldy (1945). Further studies have investigated the structure of shock waves that emerges in disperse bubbly liquids. The small bubbles submerged in the liquid contain most of the compressibility while inertia in the flow is mostly due to the liquid phase. A discussion on this topic was given in Batchelor (1969). Approaches to model and compute the shock structure in bubbly liquids, mostly based on 1D simplifications, were discussed in Caflisch et al. (1985a,b), Crespo

(1969), Noordzij and van Wijngaarden (1974), Noordzij (1973b), and van Wijngaarden (1968, 1970, 1972a,b). An extensive report on the phenomenon of shock propagation in two-phase problems was given in Eddington (1967).

The goal of the present chapter is to advance the state of the art in studies of cloud collapse processes and wave propagation in bubbly disperse liquids by simulating thousands of gas bubbles and studying their collective interactions. The results of this study have been published in Rasthofer, Wermelinger, Karnakov, et al. (2019). An uncertainty quantification (UQ) study concerned with the initial geometrical configurations of smaller cavitating bubble clouds was published in Šukys et al. (2018). The work therein presents novel empirically optimal control variate coefficients to enhance the variance reduction in the multi-level Monte Carlo (MLMC) method used for the study.

7.2 BUBBLE CLOUD SETUP AND INITIAL CONDITIONS

This section describes the initial condition that has been implemented to simulate 12500 randomly distributed bubbles in a spherical confinement. It is further shown that the computation of an expensive initial condition for the pressure field, one that satisfies the Laplace equation $\nabla^2 p = 0$, can be substituted by a simpler initial pressure field.

7.2.1 *Bubble cloud configuration*

The bubble cloud in this simulation is initially spherical and of radius $R_C = 45\,\mathrm{mm}$, composed of $N_B = 12500$ spherical bubbles of radius $R_{B,i}$ with $i \in 1, \dots, N_B$. The cloud is generated by randomly positioning bubbles within a sphere of radius R_C using a uniform distribution and subject to the constraint that the minimum distance between the surfaces of any two bubbles is greater than $d_G = 0.4\,\mathrm{mm}$. The radius of the bubbles is chosen in the range $[R_{B,\mathrm{min}}, R_{B,\mathrm{max}}]$ using a log-normal probability distribution. The minimum and maximum bubble radii values, $R_{B,\mathrm{min}} = 0.5\,\mathrm{mm}$ and $R_{B,\mathrm{max}} = 1.25\,\mathrm{mm}$, are based on the respective values suggested in N. A. Adams et al. (2013) and Tiwari et al. (2015). The mean bubble radius is defined by

$$\bar{R}_B = \frac{2e^{\mu + \frac{1}{2}\sigma^2} - 1}{4} \left(R_{B,\mathrm{max}} - R_{B,\mathrm{min}} \right) + R_{B,\mathrm{min}} = 0.7\,\mathrm{mm}, \qquad (7.1)$$
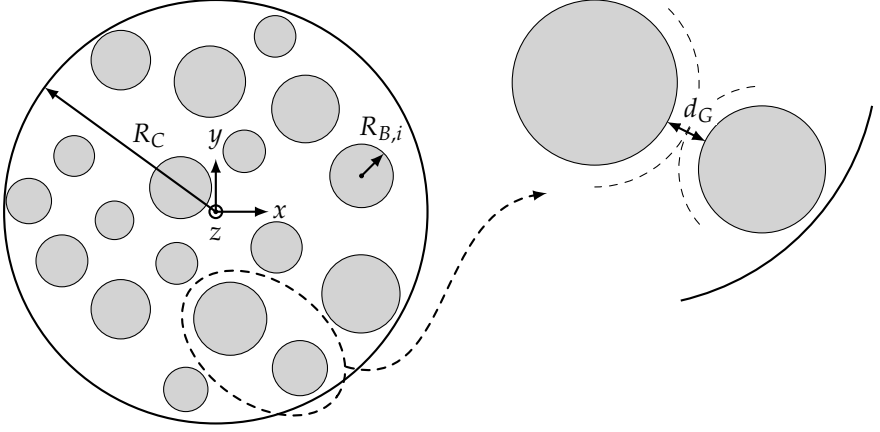
FIGURE 7.1: Sketch of spherical cloud with radius R_C composed of bubbles with radius R_B in close-up of two bubbles separated by distance d_G.

where $\mu = 0$ and $\sigma = 0.3$ are the mean and standard deviation of the log-normal distribution, respectively. A two-dimensional sketch of the cloud setup is shown in figure 7.1. The bubble cloud is characterized by the gas volume fraction α_C and the cloud interaction parameter β_C, defined as

$$\alpha_C = \frac{1}{R_C^3} \sum_{i=1}^{N_B} R_{B,i}^3, \tag{7.2}$$

$$\beta_C = \alpha_C \left(\frac{R_C}{R_{B,\text{avg}}} \right)^2, \tag{7.3}$$

where

$$R_{B,\text{avg}} = \frac{1}{N_B} \sum_{i=1}^{N_B} R_{B,i} \tag{7.4}$$

denotes the average bubble radius. Higher β_C values indicate stronger interactions among the bubbles (Brennen, 1998; Wang et al., 1999). For the present cloud, $\alpha_C = 4.9\,\%$, $\beta_C = 208$, and $R_{B,\text{avg}} = 0.69\,\text{mm}$. Figure 7.2 shows a histogram of the distribution of the bubble radius and a visualization of the generated cloud.

The cloud is centered in a cubic computational domain of size $6R_C \times 6R_C \times 6R_C$. The domain is uniformly discretized using $6144 \times 6144 \times 6144$ cells, leading to $R_{B,\text{min}}/h = 11.38$ for the minimum bubble resolution and
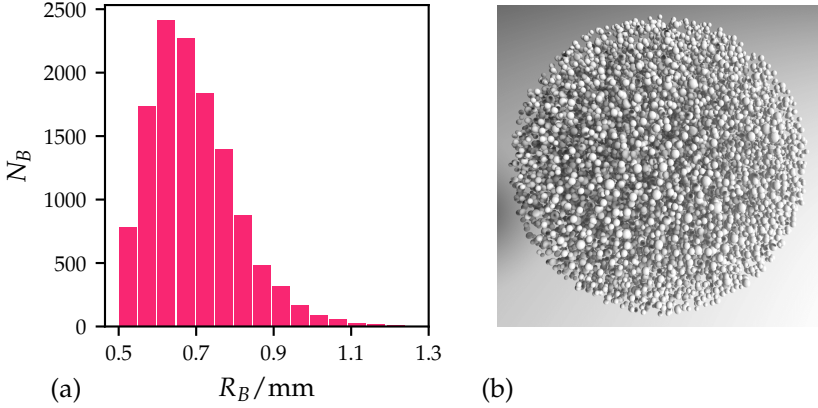
FIGURE 7.2: Model cloud with 12500 bubbles: (a) bubble radius distribution; (b) rendering of the initial cloud.

$R_{B,\max}/h = 28.44$ for the maximum bubble resolution, where the cell size is denoted by h.

Non-reflecting, characteristic-based boundary conditions (Engquist et al., 1977; Poinsot et al., 1992; Thompson, 1987, 1990) are used. Additionally, the ambient pressure p_∞ is imposed in the far-field by adding the term $C_{bc}(p - p_\infty)$ to the incoming wave (Rudy et al., 1980). Coefficient $C_{bc} = \sigma(1 - \mathrm{Ma}^2)c_1/\ell \approx \sigma c_1/\ell$ depends on a characteristic length $\ell = 3R_C$, the speed of sound c_1 in the liquid at the boundary, the Mach number Ma at the boundary, which is assumed negligible, and a user defined parameter $\sigma = 0.75\,\mathrm{s}$. The CFL number of the simulation is set to 0.3.

7.2.2 Initial condition

Initially, a zero velocity field is assumed. The density of water is set to $\rho_1 = 1000\,\mathrm{kg\,m^{-3}}$ and of air to $\rho_2 = 1\,\mathrm{kg\,m^{-3}}$. Moreover, a smoothed initial pressure field (Tiwari et al., 2015) is used which is essential in order to attenuate the emission of spurious pressure waves caused by the initial conditions. The bubble and liquid pressure in the sphere defined by R_C is set to $p_C = 0.1\,\mathrm{MPa}$ and the ambient pressure to $p_\infty = 1\,\mathrm{MPa}$. Following Tiwari

et al. (2015), the initial pressure field in the liquid outside of the cloud is then approximated by

$$p_0(\boldsymbol{x}) = \begin{cases} p_C & |\boldsymbol{x} - \boldsymbol{x}_C| \leq R_C, \\ p_C + \tanh\left(\frac{|\boldsymbol{x} - \boldsymbol{x}_C| - R_C}{\lambda}\right)(p_\infty - p_C) & |\boldsymbol{x} - \boldsymbol{x}_C| > R_C, \end{cases} \tag{7.5}$$

where $\boldsymbol{x}_C$ denotes the center of the cloud. Parameter λ defines how fast the pressure increases from the cloud surface to the ambient and is set to 50 mm. Note that equation 7.5 is a simplified statement of the condition in equation 6.4 used for the initial pressure field in the smaller clouds used for the parameter study in chapter 6. The additional detail in equation 6.4 is not justified by the computational overhead, especially for the large cloud used in this study where shielding effects and small inter-bubble distances dominate.

The validity of assuming a uniform pressure in the initial spherical hull of the bubble cloud is shown by a small cloud with 10 bubbles at similar resolution as the main cloud in section 7.2.1. Figures 7.3(a) and 7.3(b) shows the initial pressure distribution on a slice through the cloud center for the simplified approach and an initial pressure field that satisfies the Laplace equation $\nabla^2 p = 0$ with Dirichlet boundary conditions at the bubble walls and domain boundaries. The initial pressure is 0.1 MPa inside the bubbles and 1 MPa in the far-field. The boundary conditions for evolving the clouds are identical to section 7.2.1. The evolved pressure fields after 14 µs (2400 iterations) are shown in figures 7.3(c) and 7.3(d), respectively. At this point, the simplified initial pressure has relaxed towards the Laplace reference with a relative error of $0.6 \pm 0.8\,\%$.

Figures 7.4(a) and 7.4(b) show the evolution of the equivalent bubble radii $R_{B,i}$ and the average bubble pressures $p_{B,i}$, see equations 7.17 and A.2 on pages 138 and 161, respectively. A slight delay in time is observed for the case of the simplified initial condition due to the initial pressure relaxation around the bubbles in the cloud. This process does not introduce artificial pressure oscillations. The most important characteristics, such as time of minimum gas volume in the cloud, the individual time of minimum bubble volumes as well as time and magnitude of peak pressures are all preserved. This shows that the average and local features are not affected by the choice of a simplified initial pressure field, as its relaxation towards the pressure obtained for a field that initially satisfies $\nabla^2 p = 0$ takes place well before the fast scales of the cloud collapse start to dominate. The slightly increased cloud collapse time does not affect the local bubble dynamics as shown
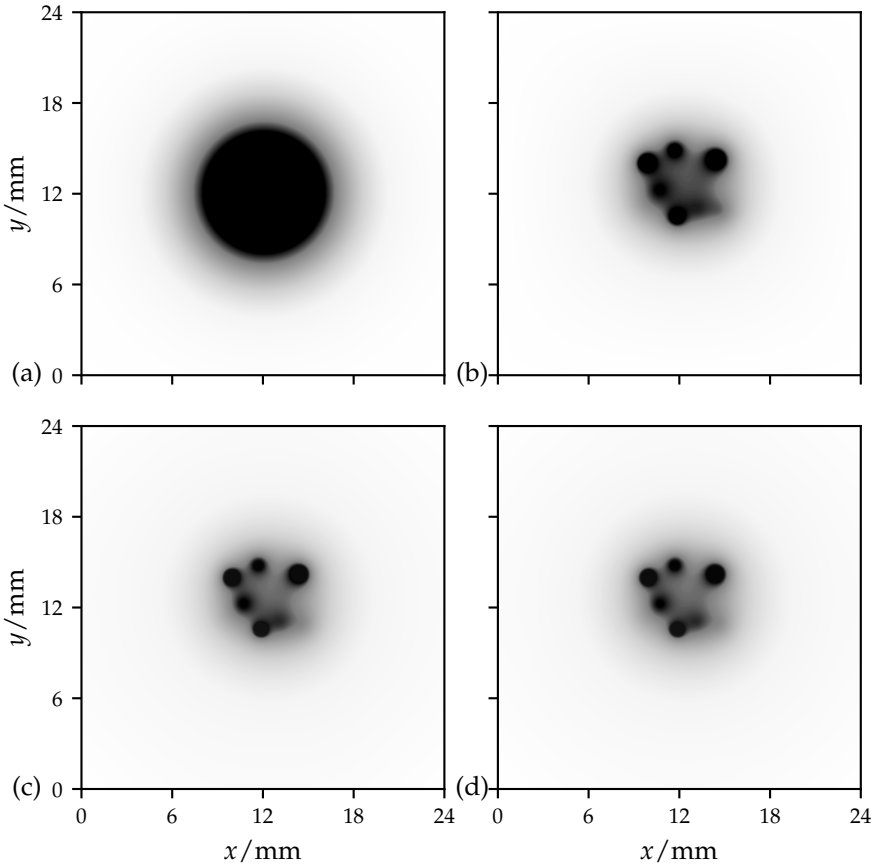
FIGURE 7.3: Initial pressure field on a slice through the cloud center: (a) simpli-
fication at $t = 0\,\mu s$; (b) solution of $\nabla^2 p = 0$ at $t = 0\,\mu s$; (c) evolved
pressure field at $t = 14\,\mu s$ with initial condition (a); (d) evolved pres-
sure field at $t = 14\,\mu s$ with initial condition (b). Dark color in the
cloud center corresponds to $0.1\,\text{MPa}$ and white color in the far-field
to $1\,\text{MPa}$.
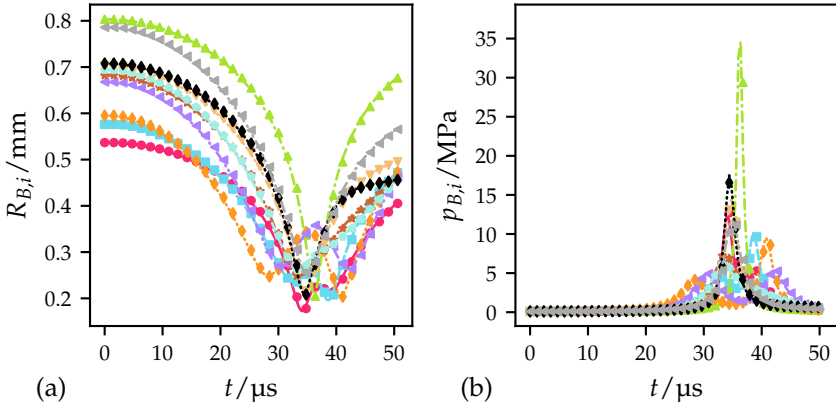
FIGURE 7.4: Temporal evolution of individual bubbles: (a) equivalent bubble radius $R_{B,i}$; (b) average bubble pressure $p_{B,i}$. Solid lines correspond to the Laplace reference that satisfies $\nabla^2 p = 0$ initially; symbols correspond to the solution obtained using the simplified pressure initial condition.

in figure 7.4 and confirms the validity of the simplified condition for the initial pressure field.

7.3   CLOUD COLLAPSE DYNAMICS

This section examines macroscopic quantities during the collapse of 12500 bubbles. These include the formation of a bubbly shock wave of finite thickness, determined by the length scale of the present bubbles. Bubble interactions and bubble dynamics of the collapse are discussed in section 7.4. Subsequently, the propagation of the collapse wave through the cloud is analyzed and compared to results from a reduced order homogeneous mixture model as well as the model of Mørch (1989) where a modified Rayleigh-Plesset type equation is derived by considering the potential energy stored in a cavity cluster.

The cloud collapse process is quantified through the temporal evolution of a number of local and global quantities. Figure 7.5 shows the development of the gas volume $V_2/V_{2,0}$, the point-wise maximum pressure p_{max}/p_{peak} within the computational domain, the average pressure $p_C/p_{C,peak}$ within the cloud, the average pressure $p_S/p_{S,peak}$ within a sen-

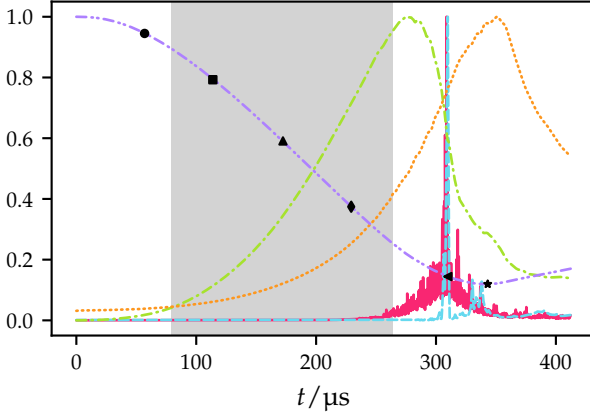FIGURE 7.5: Temporal evolution of macroscopic quantities: ———, maximum pressure over all cells p_{max}/p_{peak}; – – – –, average pressure $p_S/p_{S,peak}$ inside spherical sensor in cloud center; – · – · –, average kinetic energy $E_{kin,C}/E_{kin,C,peak}$ within cloud; ·········, average pressure $p_C/p_{C,peak}$ within cloud; – · · – · · –, gas volume $V_2/V_{2,0}$. Symbols mark time instants for the visualizations shown in figures 7.6 and 7.7. The gray shaded area indicates the time interval of data extraction for the microjet analysis in section 7.4.2.

sor at the center of the cloud, further described below, and the total kinetic energy $E_{kin,C}/E_{kin,C,peak}$ within the cloud. The peak values are defined by

$$f_{peak} = \max_{0 \leq t \leq T} f(t), \tag{7.6}$$

for some function $f(t)$ defined on the interval $t \in [0, T]$. The symbols on top of the curve for the gas volume in figure 7.5 coincide with the time instants of the collapse visualizations shown in figures 7.6 and 7.7. The pressure iso-surface shown in figure 7.6 corresponds to the pressure $p_{iso} = 0.15\,\text{MPa}$. The numerical schlieren (Quirk et al., 1996) in figure 7.7 show the magnitude of the pressure gradient $|\nabla p|$ in the xy-plane at $z = 0$. The last two symbols correspond to the time of peak pressure $p_{S,peak}$ within the cloud center sensor and the time of minimum gas volume in the cloud, respectively. The remaining symbols are spaced evenly between $t = 0\,\mu\text{s}$ and the time of occurrence of $p_{S,peak}$.

The minimum gas volume is reached at the cloud collapse time $t_C = 343.9\,\mu\text{s}$. At this time, the gas volume is reduced by 88 % relative to its initial value. The maximum pressure $p_{max} = \max_C p$ over all computational cells C

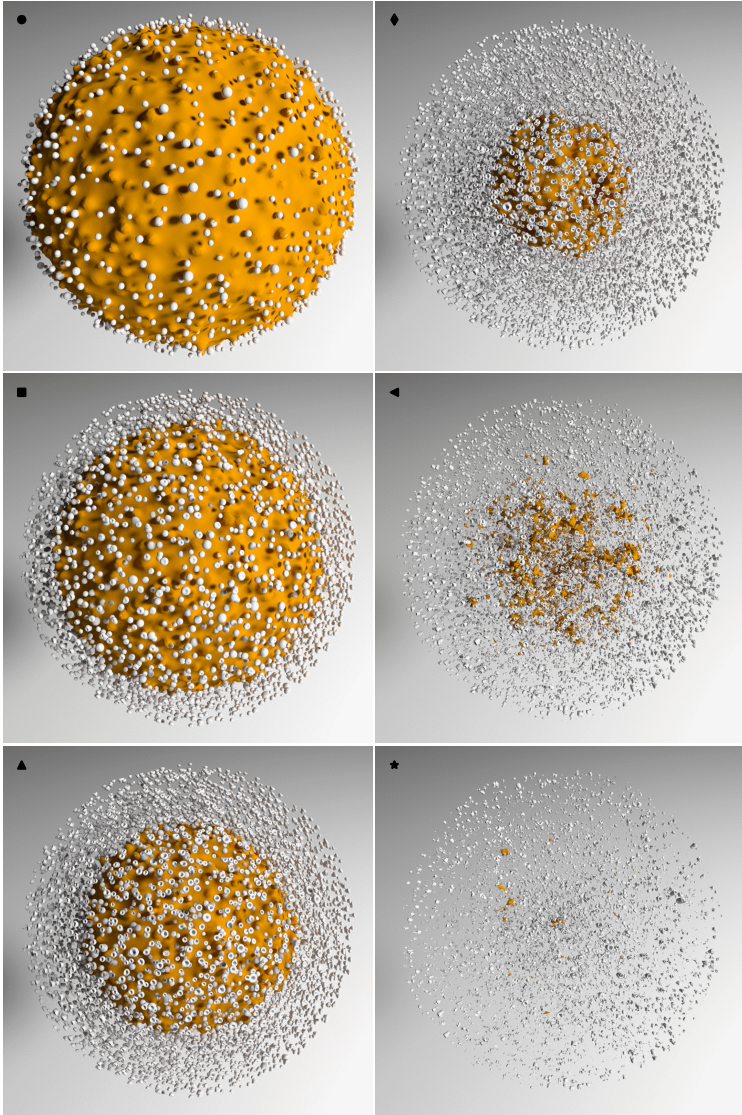FIGURE 7.6: Temporal evolution of collapsing cloud with pressure iso-surface at $p_{\text{iso}} = 0.15\,\text{MPa}$. Symbols in top left corner correspond to time instants marked figure 7.5.
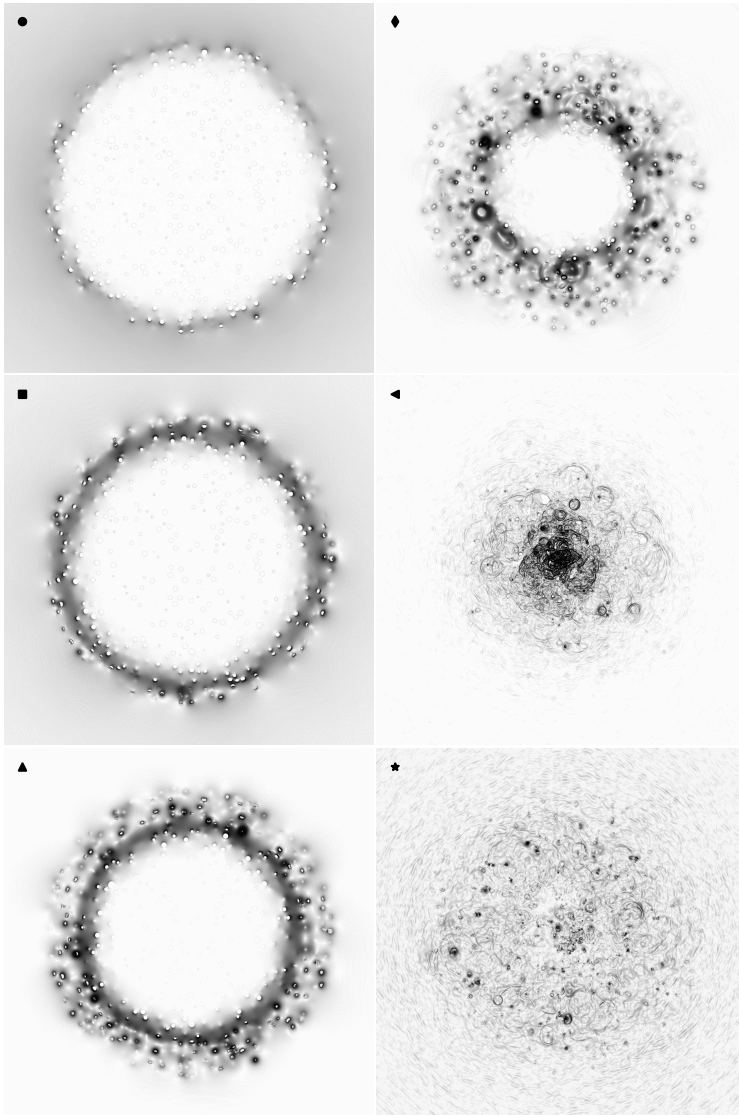
FIGURE 7.7: Temporal evolution of collapsing cloud visualized using numerical schlieren images of the $|\nabla p|$ field in the xy-plane at $z = 0$. Symbols in top left corner correspond to time instants marked in figure 7.5.

is a highly fluctuating quantity. Its peak $p_{peak} = 3.41\,\text{GPa}$ is detected at time $t/t_C = 0.898$ and occurs before the minimum gas volume is encountered. A similar observation was reported in Yamamoto (2016). To capture the behavior in the core of the cloud, a spherical sensor of radius $R_S = 1\,\text{mm}$ is placed at the center of the cloud. The sensor measures the average pressure p_S within its domain. The maximum value of p_S amounts to $p_{S,peak} = 89.5\,\text{MPa}$ and is observed at time $t/t_C = 0.901$. The pressure curve of the sensor reveals the shielding effect Brennen, 2005; d'Agostino et al., 1989 of the outer bubbles in the cloud. Although a broad time interval of high pressures is observed for p_{max}, merely the major peak and one smaller peak are detected by the sensor. Strong pressure waves emitted away from the immediate surrounding of the sensor are absorbed by bubbles between the source of the pressure wave and the sensor by contributing to the compression of these bubbles. The maximum value of the average pressure within the cloud is $p_{C,peak} = 3.69\,\text{MPa}$ and corresponds to $4\,\%$ of the value measured for $p_{S,peak}$. It is encountered at a later time $t/t_C = 1.021$, which is almost exactly the time of minimum gas volume. The kinetic energy of the mixture in the cloud region increases until it reaches its peak value of $E_{kin,C,peak} = 3.69\,\text{J}$ at $t/t_C = 0.800$, which is before the occurrence of p_{peak}. At time t_C, the kinetic energy is already reduced by $72\,\%$.

Figure 7.6 illustrates the deformation of the bubbles caused by the formation of microjets discussed in section 7.4.2. As the collapse of the cloud progresses, the extracted pressure iso-surface is moving inward with focus to the cloud center. Accordingly, an evolving circular front is detected by the numerical schlieren of the pressure gradient shown in figure 7.7. These images reveal a radially inward-propagating collapse wave and the aforementioned shielding effect. While the bubbles behind the front are subject to a collapse process, bubbles ahead of the front remain at their initial state. In the transition from frame ♦ to ◄, a break-down of the shielding effect is observed. Furthermore, strong spherical pressure waves emitted from individual bubble collapses are clearly visible in frame ◄ of figure 7.7.

7.3.1   *Wave propagation in bubbly liquid*

The large number of bubbles in the cloud renders the macroscopic flow spherically symmetric and allows for analyzing the collapse wave observed in the previous section. In order to proceed, spherical averages

$$\bar{\alpha}_2(r,t), \quad \bar{p}(r,t), \quad \bar{u}(r,t),$$
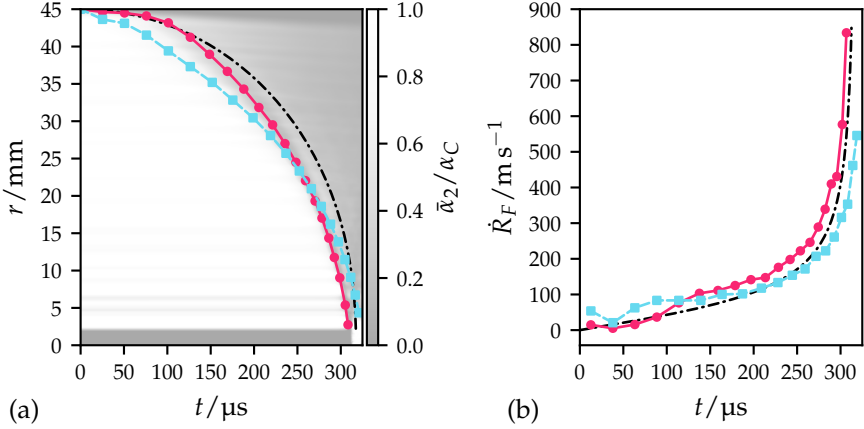
FIGURE 7.8: Temporal evolution of bubbly shock: (a) front trajectory on $\bar{\alpha}_2$ contour plot; (b) effective wave propagation speed. ──●──, simulation with resolved bubbles; ──■──, homogeneous mixture model; ──·──·──, Mørch (1989).

of the gas volume fraction, the pressure and the velocity magnitude, $u = |\boldsymbol{u}|$, are computed over spheres with radius r centered at the cloud center. The radial position of the collapse wave front is defined by the location of the maximum average velocity magnitude as

$$R_F(t) = \arg\max_r \bar{u}(r,t). \tag{7.7}$$

Figure 7.8(a) shows the front trajectory in the rt-space on top of a contour plot of $\bar{\alpha}_2(r,t)$ where the white color below the trajectory corresponds to large gas content in the liquid. The plot is related to the $\bar{E}_{\mathrm{kin}} = 0$ plane in figure 6.8 on page 101. The effective speed of the shock in the bubbly liquid, $\dot{R}_F$, is shown in figure 7.8(b). For reference, equation 2.13 estimates a wave speed of $50\,\mathrm{m\,s}^{-1}$ for a pressure of 1 bar and gas volume fraction α_C of 5 % (van Wijngaarden, 1972a). The effective speed of propagation is lower than that in the pure phases (Wood, 1930) and was already observed in figure 3.1. In addition to the resolved simulation, predictions by the model of Mørch (1989) and a homogeneous mixture approach, further addressed below, are also included in the figure.

Profiles of the spherical averages at time instants $t = 139, 183, 218, 245, 267, 285$ and $297\,\mathrm{\mu s}$ corresponding to $R_F = 40, 35, 30, 25, 20, 15$ and 10 mm are shown in figure 7.9. The profiles are normalized and plotted in the
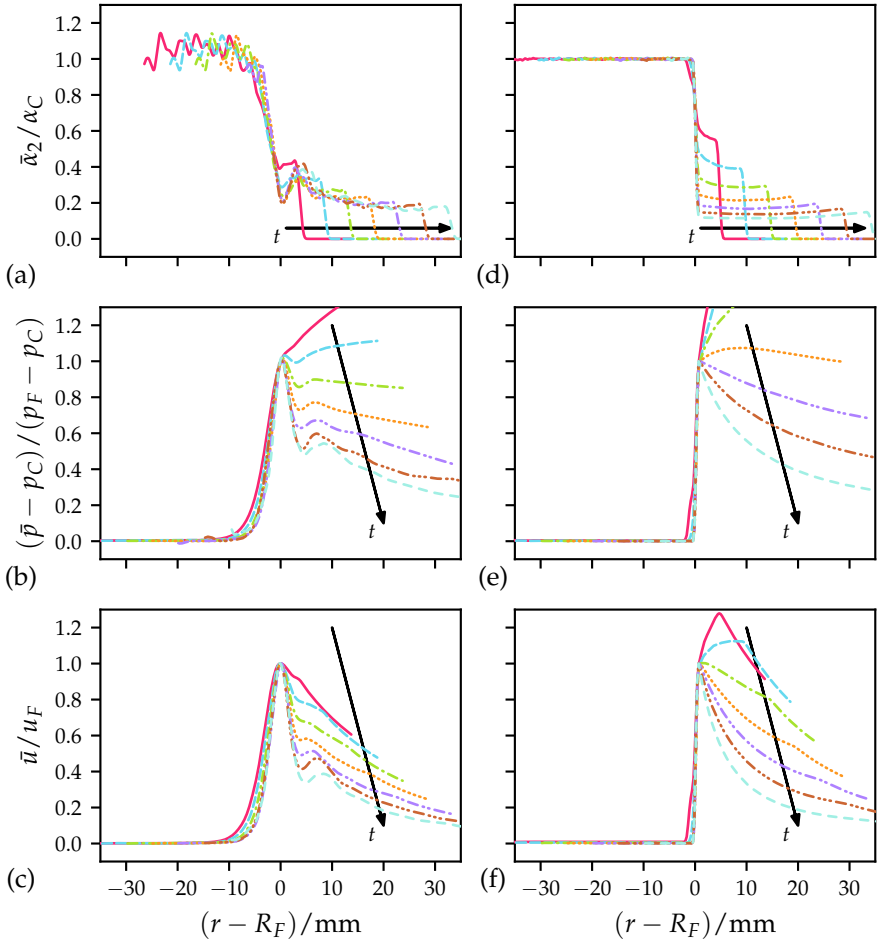
FIGURE 7.9: Normalized bubbly shock profiles of spherical averages at different radial locations: (a)–(c) resolved simulation; (d)–(f) homogeneous mixture model. ——, $R_F(139\,\mu s) = 40\,mm$; – – –, $R_F(183\,\mu s) = 35\,mm$; –·–·–, $R_F(218\,\mu s) = 30\,mm$; ·········, $R_F(245\,\mu s) = 25\,mm$; –··–··–, $R_F(267\,\mu s) = 20\,mm$; –···–···–, $R_F(285\,\mu s) = 15\,mm$; – – –, $R_F(297\,\mu s) = 10\,mm$. Arrows indicate increasing time.

frame of reference of the front, i. e., depending on the relative radial location $r - R_F(t)$. The normalized gas volume fraction, pressure and velocity are defined as

$$\frac{\bar{\alpha}_2}{\alpha_C}, \quad \frac{\bar{p} - p_C}{\bar{p}_F - p_C}, \quad \frac{\bar{u}}{\bar{u}_F},$$

where

$$\bar{p}_F(t) = \bar{p}(R_F(t), t), \tag{7.8}$$

$$\bar{u}_F(t) = \bar{u}(R_F(t), t), \tag{7.9}$$

are pressure and velocity at the bubbly shock front, respectively. Figures 7.9(a) to 7.9(c) correspond to the profiles computed from the resolved bubble simulation while figures 7.9(d) to 7.9(f) correspond to profiles obtained by the homogeneous mixture model addressed below. The gas volume fraction shows some oscillations which decay towards the cloud surface as more bubbles contribute to the averages with increasing r. The normalization of the radial profiles reveals their self-similarity in the vicinity of the front. The gas volume fraction gradually decreases to $\alpha_2/\alpha_C \approx 0.2$ in the close vicinity of the shock front, while the pressure and the velocity grow towards their peak values. Behind the bubbly shock front the pressure exhibits a drop which causes an expansive rebound of the gas volume fraction. The shock structure is further addressed below. Farther outward from the cloud center, all profiles keep declining. At the cloud surface, the gas volume fraction drops to zero in a sharp fashion whereas pressure and velocity decrease smoothly to their prescribed far field values.

For a single-phase fluid the thickness of discontinuities in the flow is in the order of the mean free path, whereas the thickness of a bubbly shock depends on the length scale of the bubbles in the disperse mixture (Hai et al., 1982; Noordzij, 1973b; van Wijngaarden, 1970). Figure 7.10 illustrates the pressure shock profile computed at 285 µs for $R_F = 15\,\mathrm{mm}$. An estimate for the bubbly shock thickness $d_F = 3.2\,\mathrm{mm}$ is obtained using equation 2.19. The thickness corresponds to about 5 bubble diameter relative to the mean radius $\bar{R}_B$. It has been shown by Crespo (1969) that planar shock propagation in disperse bubbly liquids exhibits an exponential steepening ahead of the shock and an oscillatory wave pattern behind the shock. A similar behavior is observed at the shock front for a spherical (radially inward) shock propagation. This is confirmed by fitting the exponential function

$$f(x) = A \exp\left(\sqrt{\frac{3\gamma_2(1 - \alpha_C)\alpha_C}{\bar{R}_B^2}}(x - x_0)\right)$$
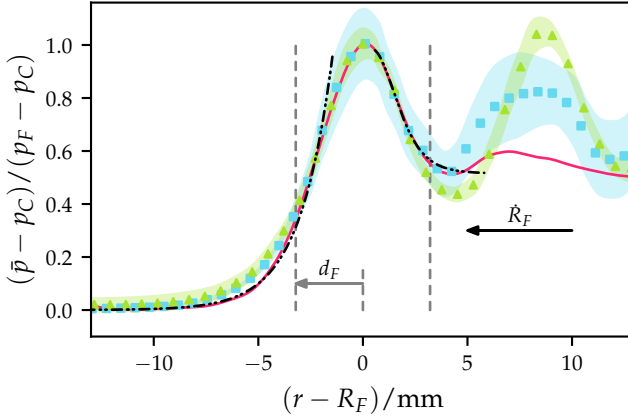
FIGURE 7.10: Bubbly shock thickness: ———, shock profile for $R_F(285\,\mu s) =$
15 mm; —··—··, fit for exponential steepening upstream; —··—·,
$(\mathrm{sech}\,x)^2$ type fit of oscillatory downstream pattern. Measurements
in a vertical shock tube: ■, spatially parabolic bubble distribu-
tion (Kameda and Matsumoto, 1996); ▲, spatially uniform bubble
distribution (Kameda, Shimaura, et al., 1998). Color shades indicate
the standard deviation of the measurements. The estimate for the
shock thickness $d_F = 3.2\,\mathrm{mm}$ is obtained from equation 2.19.

to the leading front of the shock profile in figure 7.10. The parameter A
and x_0 are determined by fitting to the simulation data. The wave pattern
behind the shock exhibits different behavior compared to the case of a
planar shock. The decay behind the wave peak is following a profile given
by

$$g(x) = A - B\left(\mathrm{sech}\left(\sqrt{\frac{3\gamma_2(1-\alpha_C)\alpha_C}{\bar{R}_B^2}}(x - x_0)\right)\right)^2,$$

which is in agreement to the solitary wave discussion in Noordzij (1973a)
and Noordzij (1973b). Here parameters A, B and x_0 are obtained by fitting
to the simulation data. The oscillatory wave pattern behind the shock un-
dergoes stronger damping compared to data presented in Crespo (1969)
and van Wijngaarden (1972b) for planar shocks. Figure 7.10 further includes
measurement data of a vertical shock tube with non-condensable gas bub-
bles for a spatially parabolic bubble distribution (Kameda and Matsumoto,
1995, 1996) and a spatially uniform bubble distribution (Kameda, Shimaura,
et al., 1998). The exponential shock steepening upstream and the shock
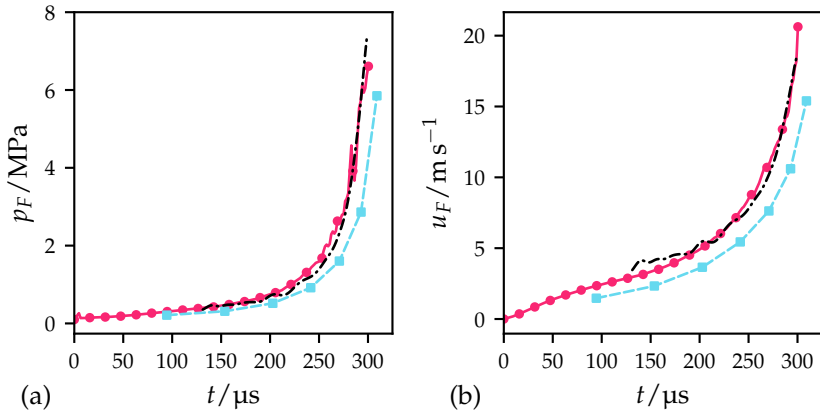
FIGURE 7.11: Temporal evolution of average flow: (a) front pressure; (b) flow velocity magnitude at the front. ●──●, simulation with resolved bubbles; ■──■, homogeneous mixture model; ▬·▬·▬, fitted equations 7.12 and 7.13 for (a) and (b), respectively.

structure within the estimated thickness d_F is very well matched by the experimental data. Major differences arise in the downstream region of the shock. The spherical geometry of the cloud causes dissipation of the outbound wave due to radiation which is one reason for the mismatch of the shock profile in the downstream region. Secondary causes on the downstream shock structure, which are currently unclear, are effects of geometry imposed by the spherical cloud and the distribution of bubbles within that confinement. Finally, numerical dissipation may cause further dissipation of the downstream shock structure since the shock capturing scheme used here is not ideal for the resolution of weak, or acoustic, waves observed in this region of the flow.

One more difference in the present simulations is the gradual build-up of the bubbly shock at the outskirt of the cloud in contrast to the planar shock experiments where a shock wave is directed onto a bubble cluster. The temporal evolution of the front pressure and flow velocity at the front during the build-up of the bubbly shock are depicted in figures 7.11(a) and 7.11(b), respectively. As derived from mass and momentum balance (Mørch, 1989;

van Wijngaarden, 1970), p_F and u_F are related to the bubbly shock speed. Approximate relations for these quantities near the front are given by

$$p_F - p_C \sim \rho_1 (1 - \alpha_C) \alpha_C \dot{R}_F^2, \tag{7.10}$$

$$u_F \sim \alpha_C \dot{R}_F, \tag{7.11}$$

up to a scaling factor which depends on the definition of the front location. Fitting these relations to the simulation data results in

$$p_F - p_C = 6.20 \, \rho_1 (1 - \alpha_C) \alpha_C \dot{R}_F^2, \tag{7.12}$$

$$u_F = 0.75 \, \alpha_C \dot{R}_F, \tag{7.13}$$

and provides a good approximation to the present results as shown in figure 7.11.

A model proposed in Mørch (1989) describes the collapse of a spherical cloud of vapor bubbles using the Rayleigh-Plesset equation extended by considering the potential energy stored in the cavity cluster. The model is given by

$$R_F \ddot{R}_F + \left(\frac{3}{2} - \frac{1}{2}(1 - \psi)(1 - \alpha_C) \right) \dot{R}_F^2 = -\frac{p_\infty - p_v}{\rho_1 \alpha_C}, \tag{7.14}$$

where p_v denotes the vapor pressure of the liquid and ψ an energy conservation factor. The energy conservation factor accounts for energy losses due to the radiation of acoustic waves and dissipation. A larger value leads to a higher front speed. According to Mørch (1989), the energy conservation factor should be in the range $0 \leq \psi \leq 0.5$. The model assumes that the bubbles are small compared to the cloud radius and that the vapor volume fraction is sufficiently high.

In contrast to the present simulation of a cloud of gas bubbles, the model by Mørch (1989) is derived for vapor bubbles which means that the pressure inside the bubbles remains constant during the collapse and that the bubbles collapse completely without rebound. When setting $p_v = p_C$, the model in equation 7.14 also provides a reasonable prediction for the front trajectory and speed of the present case, as is shown in figure 7.8. The curves shown in that figure correspond to an energy conservation factor $\psi = 0.5$. It is found, however, that ψ is only of minor influence for the case discussed here.

Furthermore, results obtained by a homogeneous mixture approach are included for comparison. Homogeneous mixture (or single fluid) models,

such as the ones proposed and/or used in Egerer, Hickel, et al. (2014), Kunz et al. (2000), Merkle et al. (1998), Schnerr et al. (2008), Senocak et al. (2002), and Singhal et al. (2002), do not consider individual bubbles, but treat the cloud region as a mixture of water and gas (or vapor), for instance, based on a cell-averaged void-fraction distribution. Such models may be used in a situation where none of the void structures are resolved on the computational grid. These situations exhibit a ratio $\bar{R}_B/h \ll 1$ of the characteristic size of the bubbles to the grid cell length. In this case, homogeneous mixture models allow the simulation of large scale flow dynamics, i. e., dynamics that are resolvable on the chosen computational grid. By increasing the grid resolution, homogeneous mixture models are able to capture the flow dynamics of decreasingly smaller scales. The mathematical model introduced in section 3.2 may also be used to describe a homogeneous mixture of gas and liquid owing to the $K\nabla \cdot \boldsymbol{u}$ term in equation 3.12. This is achieved by simply setting a uniform gas volume fraction $\alpha_2 = \alpha_C$ for all cells within the sphere of radius R_C, instead of initially computing local cell averaged values of the gas volume fraction field based on the distribution of the 12500 bubbles in the cloud and some filter kernel. The initial conditions for the velocity and the pressure as well as the applied boundary conditions remain identical to the simulation with resolved bubbles. A similar approach was used in Tiwari et al. (2015). The results obtained from the homogeneous mixture simulations are discretized on a uniform grid with 1024 cells per spatial direction. Similarly as before, spherically averaged profiles for $R_F = 40$, 35, 30, 25, 20, 15 and 10 mm corresponding to $t = 94$, 154, 203, 242, 271, 293 and 309 µs, are shown in figure 7.9. In contrast to the case with resolved bubbles, the radial profiles are discontinuous at the front. The mechanisms responsible for the formation of a bubbly shock front are amplitude dispersion which leads to steepening of the shock front and frequency dispersion responsible for the opposite phenomena (van Wijngaarden, 1972b). These physics can only take place if disperse bubbles are present in the liquid, essentially expressed by equation 2.18 on page 16. The homogeneous mixture model is not capable of resolving these length scales and consequently the observed shock profiles in figures 7.9(d) to 7.9(f) are fundamentally different compared to the profiles of the resolved simulation in figures 7.9(a) to 7.9(c). The major difference due to the comments above is the inability to resolve the finite shock thickness d_F, while the macroscopic features shown in figure 7.11 reveal a similar evolutionary trend, but are 30 % lower in magnitude compared to the results of the resolved bubble simulation. The

wave locator in equation 7.7 is not suitable for the homogeneous mixture case, instead, the wave is located from the gas volume fraction field via

$$R_F(t) = \arg\max_r \left| \frac{\partial \bar{\alpha}_2}{\partial t}(r, t) \right|, \tag{7.15}$$

which detects the discontinuity in $\bar{\alpha}_2$. The front trajectory and speed, shown in figure 7.8 are qualitatively similar compared to the resolved simulation. The effective propagation speed of the wave shown in figure 7.8(b), however, is underestimated starting from $t = 150\,\mu s$, where the deviation grows in time reaching 20 % relative error at $t = 200\,\mu s$ and 40 % relative error at $t = 300\,\mu s$.

In summary, the results indicate that the front trajectory and effective wave propagation speed observed in the simulation with large numbers of bubbles are well captured by the model of Mørch (1989) and the present homogeneous mixture approach. The evolution of the pressure and the velocity near the front matches the theoretical relations and in turn validates the present numerical results.

7.4   BUBBLE INTERACTIONS AND DYNAMICS

This section discusses the microscopic scales involved in the collapse of large bubble clusters. The first section dissects the collapse behavior of individual bubbles depending on their position in the cloud. The second part provides a statistical analysis of the microjet formation during the cloud collapse.

7.4.1   *Bubble collapses*

The shape of the bubbles is implicitly described by the gas volume fraction field α_2, which is sampled at a frequency of 0.63 MHz. The center $\mathbf{x}_{B,i}(t)$ and the equivalent radius $R_{B,i}(t)$ of bubble i are calculated as

$$\mathbf{x}_{B,i}(t) = \frac{1}{V_{B,i}(t)} \int_{\Omega_{B,i}} \alpha_2 \mathbf{x} \, dV, \tag{7.16}$$

$$R_{B,i}(t) = \left(\frac{3}{4\pi} V_{B,i}(t) \right)^{\frac{1}{3}}, \tag{7.17}$$

where

$$V_{B,i}(t) = \int_{\Omega_{B,i}} \alpha_2 \, dV \tag{7.18}$$

is the bubble volume. The integration is performed over the spherical domain $\Omega_{B,i}$ concentric with the bubble center of the previous time sample and the radius equal to the initial bubble radius $R_{B,i}(t = 0)$. In order to improve the accuracy of peak detection, the function $R_{B,i}(t)$ is interpolated in time using a cubic spline.

Figure 7.12 shows the evolution of the equivalent bubble radius for a few bubbles selected at various radial locations. All curves are normalized by the initial bubble radius. A bubble starts to collapse once it is overtaken by the inward-propagating wave. The figure illustrates that the strength of the collapses, expressed in terms of short collapse time and stronger bubble compression, increases with decreasing distance to the cloud center. In the vicinity of the center of the cloud, bubbles collapse in a highly non-linear fashion, as seen in figures 7.12(d) to 7.12(f), whereas weak oscillations are observed for bubbles located in the outskirts of the cloud, shown in figures 7.12(a) to 7.12(c).

7.4.2 *Microjet formation*

The evolving pressure gradient along the bubble surface leads to the formation of a localized liquid jet of high velocity which notably deforms the bubble and eventually pierces though it. Following Jayaprakash et al. (2012), the tip $x_{\text{tip},i}$ of the microjet associated with bubble i is identified as the location of minimum curvature on the bubble surface. Here, the interface is represented by the iso-surface $\alpha_2 = 0.5$ of the gas volume fraction field. The curvature of any iso-contour of α_2 can be calculated from equation 3.29.

Figure 7.13 illustrates the evolution of the microjet for three bubbles. The relative location of the tip, $x_{\text{tip},i} - x_{B,i}$, as well as the bubble radius $R_{B,i}$ are displayed as a function of time. Additionally, bubble shapes are shown for selected time instants. At the beginning of the collapse process, the bubble surface is largely spherical and possesses a positive curvature. Therefore, the distance between the location of minimum curvature and the bubble center is approximately equal to the equivalent radius, but the location itself is not well-defined and thus bounces from one point to another. Once the microjet starts to form, the curvature changes its sign. The location of minimum curvature then identifies the tip of the microjet. The microjet
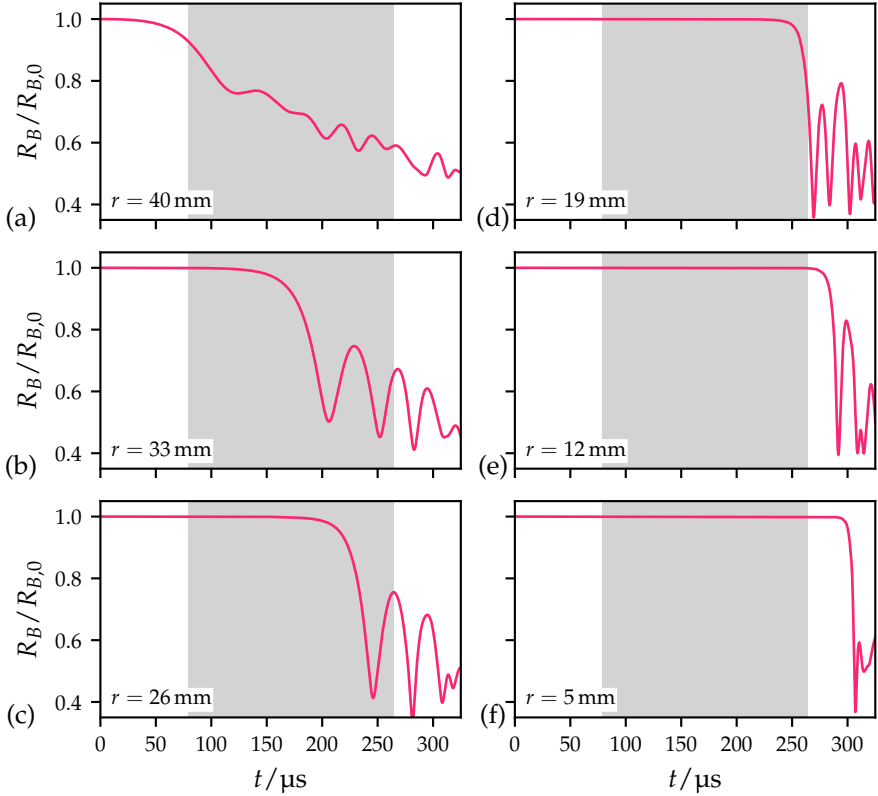
FIGURE 7.12: Temporal evolution of equivalent radius for selected bubbles: (a) $r = 40\,\text{mm}$; (b) $r = 33\,\text{mm}$; (c) $r = 26\,\text{mm}$; (d) $r = 19\,\text{mm}$; (e) $r = 12\,\text{mm}$; (f) $r = 5\,\text{mm}$. The gray shaded area corresponds to the time interval of microjet analysis.
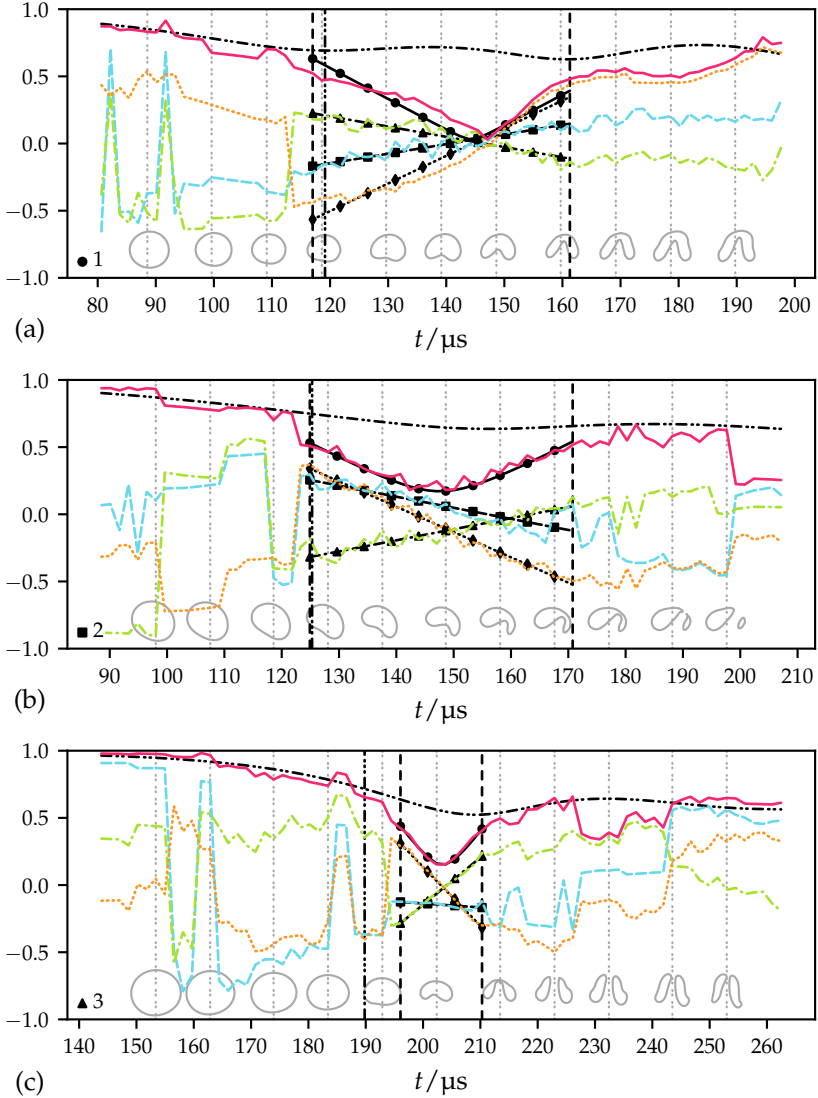
FIGURE 7.13: Temporal evolution of microjets for three selected bubbles: ———, $|x_{\text{tip}} - x_B|/R_{B,0}$, ——●——, linear fit; ———, $(x_{\text{tip}} - x_B)/R_{B,0}$, ——■——, linear fit; ———, $(y_{\text{tip}} - y_B)/R_{B,0}$, ——▲——, linear fit; ·······, $(z_{\text{tip}} - z_B)/R_{B,0}$, ····◆····, linear fit; ———·—, $R_B/R_{B,0}$; ———, fitting range $[t_{\text{tip},i}, t_{\text{imp},i}]$; ———·—, collapse wave arrival t_F. Iso-lines of $\alpha_2 = 0.5$ at 10 μs intervals are shown at the bottom for each case.

deforms the bubble into a cap-like shape until it pierces through the bubble on the opposite surface, see figure 7.13. The time of microjet impact on the opposite bubble wall is denoted by $t_{\text{imp},i}$ for bubble i. At this time, the distance between the location of minimum curvature and the bubble center again approximately equals the equivalent radius. Hence, the characteristic quantities of the microjets are evaluated during the time interval $[t_{\text{tip},i}, t_{\text{imp},i}]$ for which

$$|x_{B,i} - x_{\text{tip},i}| < 0.75\, R_{B,i} \tag{7.19}$$

holds. As observed in figure 7.13, the relative trajectory $x_{\text{tip},i} - x_{B,i}$ of the tip of the microjet propagates with approximately a constant velocity within this interval. The microjet velocity $u_{\text{tip},i}$ is defined by the time derivative of a linear fit of $x_{\text{tip},i} - x_{B,i}$ in the time interval $[t_{\text{tip},i}, t_{\text{imp},i}]$. In order to obtain reliable statistics, the fitting range is required to comprise at least 6 samples in time, i. e., is of duration of at least 10 µs and the RMS error of the fitting has to be below $0.1\, R_{B,i}(t=0)$. Due to the limited data sampling frequency and the complexity of the microjet tip trajectories, not all bubbles satisfy these requirements. Such bubbles are excluded from the subsequent analysis of the microjets, leaving about 7500 bubbles (i. e., 60 % of the bubbles) for further evaluation. The time interval considered for the microjet analyses of all bubbles is defined by the interval $[t_{M,s}, t_{M,e}]$, where

$$t_{M,s} = \min_i t_{\text{tip},i}, \tag{7.20}$$

$$t_{M,e} = \max_i t_{\text{imp},i}, \tag{7.21}$$

are the start and end times, respectively. The microjet interval is highlighted in figure 7.5 with a gray shaded region. It is noted that the end time $t_{M,e}$ corresponds to a time instant before the time of minimum cloud volume t_C. Appendix A presents a convergence study to prove that the bubble resolution in the present simulation is sufficient during the time interval of microjet analysis. The associated error of microjet velocity magnitudes is at most $10.0 \pm 5.2\,\%$ relative to a grid with twice the resolution.

As of preceding studies on cloud collapse dynamics (Bremond et al., 2006; Tiwari et al., 2015), the microjets point towards the core of the cloud. As shown in the present work, the axes of these microjets are not perfectly aligned with the radial direction $x_C - x_{B,i}(t=0)$ from the initial bubble center to the cloud center. The inclination angle θ_i denotes the angle between the radial direction and the direction of the microjet velocity corresponding to bubble i, see figure 2.1 in section 7.4.2 on page 11 for an illustration and further explanation. A microjet with $\theta_i = 0°$ is directed towards the cloud

Bubble	$\frac{r}{\mathrm{mm}}$	$\theta/°$	$\frac{u_{\mathrm{tip}}}{\mathrm{m\,s^{-1}}}$	$\frac{R_{B,0}}{\mathrm{mm}}$	$\frac{\min_t(-\dot{R}_B(t))}{\mathrm{m\,s^{-1}}}$	$\varphi/°$	$\lvert\tilde{u}^{\perp}_{\mathrm{bulk}}\rvert$
1 ●	41.9	9.8	13.4	0.58	3.9	50.6	0.005
2 ■	41.4	49.4	14.6	0.66	3.3	22.9	0.293
3 ▲	34.1	12.6	64.1	1.14	14.7	92.5	0.148

TABLE 7.1: Microjet parameters of selected bubbles.

center. Values of the inclination angle for bubbles shown in figure 7.13 are given in table 7.1 where the microjet of bubble 2 (symbol ■) is distinguished by stronger inclination. Figure 7.14(a) depicts a scatter plot of the inclination angle θ_i versus the radial distance r. All scatter plots shown in this subsection also contain the moving average and the standard deviation computed with a window length equal to 10 % of the corresponding horizontal axis range. The selected bubbles shown in figure 7.13 are further indicated by their corresponding symbol. Furthermore, figure 7.14(c) depicts the probability density function (PDF) of the simulated inclination angle.

The average inclination angle for the present cloud collapse process is 13.2°. Furthermore, 90 % of the bubbles exhibit an inclination angle smaller than 24°. Local mean values of the inclination angle range from 10° at $r = 45$ mm to 18° at $r = 26$ mm. As a result, the microjet inclination angle increases slightly towards the cloud center indicating a weak dependence on the collapse wave speed, which strongly depends on r. Very large inclination angles in the range of 35° to 61° are observed for 1 % of the bubbles. Closer examination of these microjets reveals that the microjet inclination is affected by the surrounding bubbles. Figure 7.14(b) shows the neighborhood of a bubble with an inclination angle of 50°. The microjet is inclined towards a specific neighbor bubble that has a significantly larger size, most likely due to secondary Bjerknes forces. A similar effect has been observed in Blake et al. (1997) where the microjet direction was influenced due to buoyancy.

The observed PDF for the bulk flow deviation angle φ_i is shown in figure 7.14(d). Scatter plots of φ_i versus θ_i and θ_i versus the magnitude $\lvert\tilde{u}^{\perp}_{\mathrm{bulk},i}\rvert$ of the projected bulk velocity are shown in figures 7.15(a) and 7.15(b), respectively. For 68 % of the bubbles, φ_i is smaller than 45°, which demonstrates that the microjets are inclined towards the direction of the bulk liquid flow around the bubble. This angle reduces with increasing inclina-

(a)

(b)

(c)

(d)

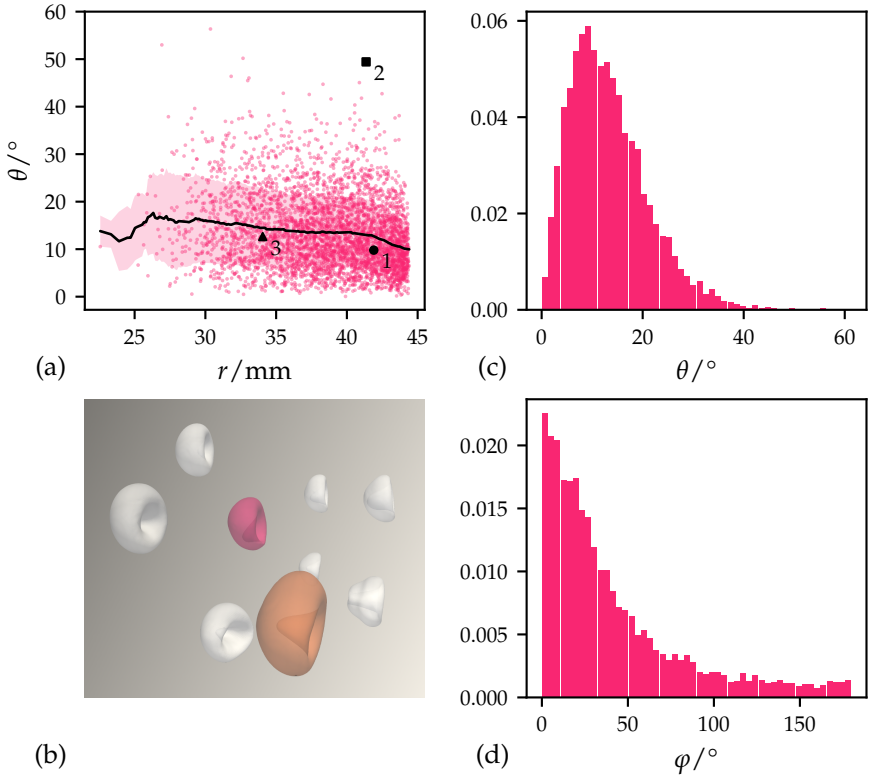FIGURE 7.14: Microjet inclination: (a) inclination angle θ_i depending on radial location of bubble; ——, moving average; (b) tendency of microjet inclination towards larger neighbor bubbles; (c) PDF of inclination angle θ_i; (d) PDF of angle φ_i between $u_{\text{tip},i}^{\perp}$ and $\tilde{u}_{\text{bulk},i}^{\perp}$. The color shades in (a) indicate the standard deviation.
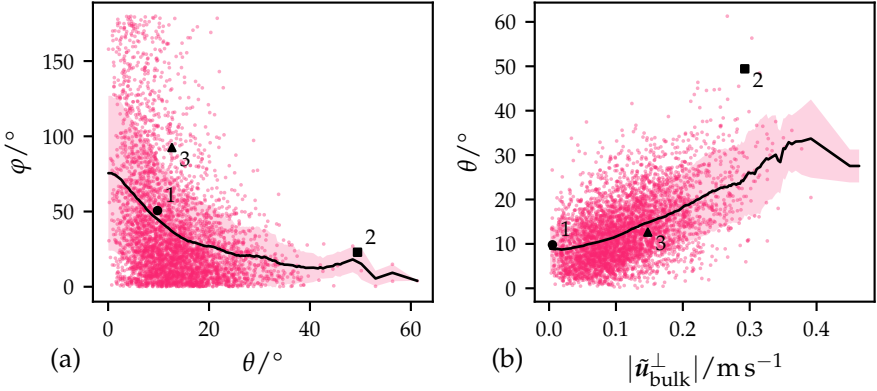
FIGURE 7.15: Deviation of microjet direction relative to cloud center: (a) angle φ_i between $\boldsymbol{u}_{\text{tip},i}^{\perp}$ and $\tilde{\boldsymbol{u}}_{\text{bulk},i}^{\perp}$ depending on inclination angle θ_i; (b) inclination angle θ_i depending on the magnitude $|\tilde{\boldsymbol{u}}_{\text{bulk},i}^{\perp}|$; ————, moving average. Color shades indicate the standard deviation.

tion. The mean value of φ_i is 45° for $\theta_i = 10°$ and 25° for $\theta_i = 40°$. Moreover, a positive correlation between the inclination angle θ_i and the magnitude of the projected component of the bulk flow indicator $|\tilde{\boldsymbol{u}}_{\text{bulk},i}^{\perp}|$ is observed.

Figure 7.16 displays scatter plots of the microjet velocity magnitude depending on various quantities. The velocity magnitude of the microjets increases with their time of initiation. For instance, the mean value amounts to $10\,\text{m s}^{-1}$ for $t_{\text{tip}} = 80\,\mu\text{s}$ and to $50\,\text{m s}^{-1}$ for $t_{\text{tip}} = 250\,\mu\text{s}$. This behavior is consistent with the acceleration of the collapse wave and the growth of the pressure at the front. One of the fastest microjets is observed for bubble 3 (symbol ▲) shown in figure 7.13(c) and table 7.1. The scatter plot of the microjet velocity magnitude versus the initial bubble radius $R_{B,0}$ shows that larger bubbles exhibit faster microjets. The mean value rises from 20 to $40\,\text{m s}^{-1}$ for bubbles with an initial radius between 0.5 and 1.2 mm. Another quantity relevant to the collapse strength of a bubble is the peak compression rate $\min_t(-\dot{R}_{B,i}(t))$ which is evaluated within the time interval $[t_{\text{tip},i}, t_{\text{imp},i}]$. A positive correlation of the compression rate with the magnitude of the microjet velocity is observed in figure 7.16(b). In contrast, the inclination angle θ_i does not affect the magnitude of the microjet velocity, as seen in figure 7.16(d). The analyzed relations reveal that the microjet velocity is influenced by both, parameters of individual bubbles (e. g., the initial bubble radius) and macroscopic parameters of the

FIGURE 7.16: Microjet tip velocity depending on: (a) microjet initiation time $t_{\text{tip},i}$; (b) bubble compression rate $\min_t -\dot{R}_{B,i}(t)$; (c) bubble initial radius $R_{B,i}(t=0)$; (d) inclination angle θ_i; ——, moving average. Color shades indicate the standard deviation.

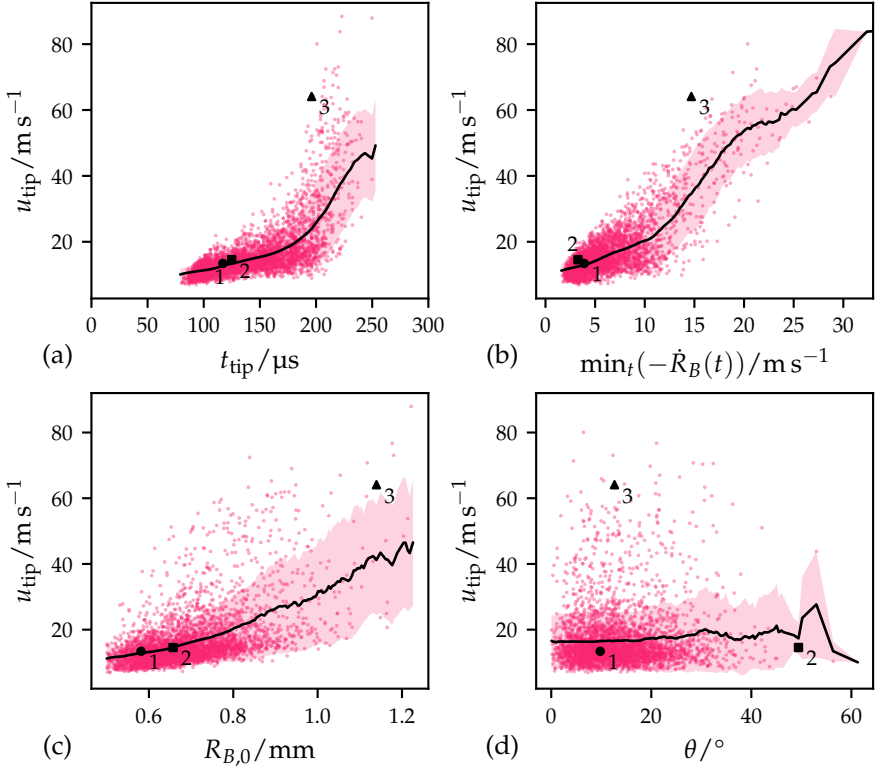cloud collapse (e. g., the effective propagation speed of the bubbly shock). The overall large dispersion of these relations, however, indicates further influence of factors such as the spatial configuration of locally surrounding bubbles.

7.5 CONCLUSION

This chapter presented a large scale simulation of cloud cavitation collapse with 12500 gas bubbles. Intensive literature research suggests that the simulation results presented here are the first of its kind. The mathematical model, numerical methods and HPC techniques are those described in chapters 3 and 4. The simulated bubble cloud corresponds to a gas volume fraction of 4.9 % and is composed of bubbles with radii following a log-normal distribution with mean radius 0.7 mm. The many small bubbles allows for proper averaging over the global system and enables a large sample count for reliable statistics on the scale of the bubbles.

The collapse process has been studied for macroscopic scales where the formation of a bubbly shock wave has been identified that starts at the surface of the cloud and propagates inward with focus on the core of the cloud. The flow has been analyzed by means of spherically averaged quantities. The bubbly shock wave advances in accordance with the 1D model of Mørch (1989) as well as a reduced order 3D homogeneous mixture approach. In contrast to these models, the detailed simulation presented in this chapter discloses the thickness of the collapse wave front which is of the order of a few bubble diameters, in agreement with the 1D theory in the literature (van Wijngaarden, 1970, 1972a,b). The computed shock structure has been compared to measurement data of simpler linear bubble configurations in shock tubes (Kameda and Matsumoto, 1995, 1996; Kameda, Shimaura, et al., 1998). The leading exponential shock steepening and the core bubbly shock structure is found to be in agreement with the measured data. Disagreement between measurement and simulation is observed in post shock region further downstream. The differences are attributed to dissipation and geometric variables in the spherical cloud configuration. Further investigation in this direction would benefit the community as the body of literature is rather sparse. The literature mainly consists of dilute or small systems with few bubbles (Ando et al., 2011; Watanabe et al., 1994) or DNS approaches where incompressible liquids are assumed simulated in domains with few bubbles (Delale, Nas, et al., 2005; Delale and Tryggvason, 2008; Tryggvason et al., 2013).

Finally, the microscopic scales have been analyzed by studying the individual bubbles in a small neighborhood. The associated microjet formation has been quantified which revealed that the microjets do in general not exactly point towards the cloud center. For the present cloud configuration, they are inclined to an angle up to 50° with respect to the radial direction. Closer examinations have demonstrated the correlation between this inclination and the bubble distribution in the vicinity of the microjets. For the velocity at the tip of the microjet, correlations with the radial location and the size of the bubble have been identified.

<div style="text-align: right; font-size: 3em;">8</div>

CONCLUSION AND OUTLOOK

> *Dealing with failure is easy: Work hard to improve.*
> *Success is also easy to handle: You've solved the wrong*
> *problem. Work hard to improve.*
>
> — Alan Perlis

The work in this thesis is engaged with the study of large scale cloud cavitation, its discrete representation and the mapping onto contemporary High Performance Computing architectures. The capability of the developed tools is demonstrated by the numerical solution of cloud cavitation that employs collapsing bubble clouds that are two orders of magnitude larger than what is currently reported in the literature.

8.1 CONCLUSION

Hyperbolic two-phase flow model

In chapter 3 we introduced the non-equilibrium two-phase flow model in the limit of infinitely fast relaxation of pressure and velocity. The hyperbolic model has further been extended to include viscous and capillary effects. The extended model has been validated and we demonstrate its superiority by means of improved resolution for interface velocities as well as its ability to generate a gaseous phase in the case of strong rarefaction. Both of these features are due the source term $K\nabla \cdot \boldsymbol{u}$ that acts in equation 3.12 on page 19 and is significant for cavitating flows. It was found that the source term further exhibits beneficial behavior in under-resolved flow regions where mixed fluids exist. In opposite to some other studies of cavitating flows (Allaire et al., 2002; Coralic et al., 2014; Perigaud et al., 2005) we explicitly retain this term and show that the resulting model is capable of resolving complex cavitating flows involving a large number of interfaces.

Moreover, we have shown—although using a biased shock capturing scheme—that the extended model is capable of resolving turbulent struc-

tures at low Mach numbers and can capture a broad range of capillary waves.

High throughput computing

In chapter 4 we have established the computational framework upon which we have implemented the compressible multi-phase flow model. The software developed in this thesis is a successor of previous work in Rossinelli et al. (2013). Major changes incorporate a redesign of the data structures that have been used previously, such that HPC concepts can be separated from algorithm development. Moreover, the new library is extensively documented. One of the main drawbacks of the predecessor is its tight coupling between algorithm and HPC, which makes it difficult to implement algorithmic changes. The new framework overcomes this difficulty by implementing an extensible set of optimized compute kernels that are commonly needed for algorithm implementation. Such kernels may be restriction or prolongation operators, finite differences, gradient computations or data compression.

The developed framework is not specific to a certain memory allocator and can therefore adapt to different paradigms such as structured grids with Cartesian ordering, static block-structured grids, adaptively refined grids, particle based discretizations which may be combined with fields that are discretized by structured grids or specialized allocators that are required to target accelerators such as GPUs. To this end, we have developed a heterogeneous algorithm that targets GPU accelerators for 3D stencil computations and demonstrated its performance by solving the approximate Riemann problem encountered in discretizations of compressible flows. Lastly, the method used in this thesis has been extended by the HLLC numerical flux and it is shown that the performance of the new method is similar to the method used in Rossinelli et al. (2013) with a throughput of 455 902 cells per second per core with the additional benefit of higher numerical accuracy in regions with interfaces.

Reduced order modeling of cloud cavitation collapse

In chapter 6 we have applied the developed methods to perform a parametric study of cloud cavitation collapse. We find that the formation of a bubbly shock within the cloud depends on a combination of the liquid

far-field pressure and the amount of gas within the bubble cluster. The elastic response of a cloud depends on the number of bubbles and their relative distances. This elasticity requires a certain potential that must be overcome by the far-field forcing potential in order to give rise to bubbly shock formation. For low far field pressures, the elasticity imposed by the interaction parameter β_C attenuates bubble-bubble interactions and prevents the formation of a bubbly shock. In configurations of high β_C and low pressure ratios Π, the shape of the kinetic energy waves within the cloud is determined by bubble length scales only. By increasing the far-field pressure, a bubbly shock begins to form at the outskirts of the cloud. For intermediate forcing pressures, the kinetic energy is found to be a superposition of two factors: bubble oscillations that cause damping and high frequency pressure waves radiated from collapsing bubbles. The latter are responsible for the amplitude accumulation in the bubbly shock wave. For large far-field pressures, the damping period associated to the frequency of bubble oscillations exceeds the collapse time of individual bubbles. In this case, the wave structure of kinetic energy does not expose bubble length scales which in turn leads to less damping in the bubbly shock and consequently a larger shock amplitude.

We have further used the data form the parametric study to asses the accuracy of reduced order models that are typically used in practice as well as in modeling approaches based on Euler-Lagrange couplings. These models are characterized by spherical bubble collapse and therefore associated with error that follows from non-spherical bubble collapse in realistic cavitation. It is found that modeling bubble translation improves the accuracy of such models. The additional degrees of freedom introduced for translation divide the total collapse potential into two parts: energy required to displace liquid mass and energy required for bubble compression. The former acts as an attenuator which reduces the peak pressure in the final collapse stage. This behavior is indeed in concert with the resolved 3D simulation. The deformation of bubbles, however, causes a deceleration of linear motion once they adopt a toroidal shape. An effect that is not captured by the reduced order model and consequently yields underestimates of peak pressures. It is found that the energy allocated for liquid mass displacement grows exponentially and becomes worse with increasing number of bubbles. In contrast, reduced order models that ignore bubble translation consistently overestimate both peak pressure and collapse time.

State of the art simulation of cloud cavitation with 12500 bubbles

In chapter 7 we have presented state of the art simulations of cloud cavitation collapse with 12500 bubbles. We have used the data to study the macroscopic dynamics and compared the captured bubbly shock with data from bubbly shock tube experiments. The leading front of the simulated shock structure corresponds with the exponential shock steepening that is observed in the experiments and the associated 1D modeling approaches therein. We further find that the back of the shock attenuates stronger in radial motion and is in better agreement with experimental data samples that follow a parabolic bubble distribution. From this we conclude that the downstream part of a bubbly shock is more sensitive to the geometrical arrangements of bubbles. Moreover, the initial condition used in the spherical cloud collapse must be accounted for as well. This uncertainty could not be investigated further in the present work.

Lastly, we have examined the microjet formation of individual bubbles by means of interface deformation and associated velocity. These investigations have revealed that the microjets do in general not exactly point towards the cloud center. For the present cloud configuration, they are inclined to an angle up to 50° with respect to the radial direction. Closer examination demonstrated the correlation between microjet inclination and size of neighboring bubbles. Microjet velocities further reveal correlation with radial location and the initial size of its originating bubble.

8.2 OUTLOOK

Modeling of compressible multi-phase flow

As mentioned earlier, the field of numerical methods for compressible multi-phase flow is actively researched. Often new methods are tested with 1D models and validated with cases that only address special features. Method validation with larger problems that involve more complex wave structures are left out due to additional effort. For example, the $K \nabla \cdot \boldsymbol{u}$ source term in equation 3.12 can lead to violation of gas volume fraction positivity because of the non-monotonic mixture speed of sound. This defect may result in negative pressure and eventually failure of the method. Instabilities of this kind did not occur during the first collapse stage of the simulations carried out in this work. For some configurations, however, nu-

merical stability issues have been encountered during the rebound phase of the cloud. Although the rebound phase was not considered in the analyses herein, the present method is not suitable for flow analysis in the rebound phase of cloud cavitation collapse. A possible remedy for this flaw may be achieved by not assuming instantaneous pressure relaxation at interfaces. Instead, balance laws for the phasic energy are considered with additional non-conservative products. Pressure equilibrium at interfaces must then be obtained by a relaxation procedure after solving the homogeneous hyperbolic problem first (Saurel, Petitpas, et al., 2009). A model of this type is likely to perform better during the cloud rebound and improve stability issues. An assessment of this method for single bubble collapse was given in Schmidmayer, Bryngelson, et al. (2020). Assessing the performance of this model with data from the present work would be informative.

Adaptive mesh refinement and mutltigrid methods

The computational framework developed in this thesis is capable to adapt data structures other than those optimal for structured memory access. In particular, adaptive mesh refinement (AMR) is readily supported as its implementation is mainly concerned with load-balancing that is acting above the node-level and further requires conservative interpolation kernels for ghost cell reconstructions at block boundaries with different resolution. The structure of computational kernels, on the other hand, remains identical to the ones already used in this work. AMR for compressible flows and multi-phase flows in particular is a high value asset and it has been taken into consideration during the present software development stages.

Secondly, the solution of linear systems is ubiquitous in most algorithms. Multigrid methods (Brandt, 1977) are fast and often used for this purpose. Their implementation in the present computational framework can be realized with ease by considering a series of Cartesian grids at power of two resolution levels. The tools to process the data on the individual grids again remain identical in structure to the ones already used here. The possibility to solve linear systems within the same computational framework is a convenience that results more structured software with less dependencies.

Data-driven reduced order modeling

In section 6.6.4 we have identified the effect of bubble deformation on kinetic energy and showed its implication on reduced order models. These models are typically used in higher order approaches such as Euler-Lagrange one-way or two-way couplings. By improving the accuracy and time to solution of RP type models, the parent models directly benefit from the improvement. A possible strategy to account for the effects of bubble deformation in RP type equations is to learn these physics from data of the resolved 3D simulations by constructing a scalar potential that is superimposed on the velocity potential of the RP type model. The learned physics may be encoded such that they account for individual bubble corrections or a global correction averaged over all bubbles. The goal is to interfere the exponential growth of kinetic energy for linear motion, as was shown in figure 6.17(b) on page 116. Since the defect of the Doinikov (DK) model mainly appears for large clouds with many bubbles, such a modification would help increase the application spectrum of the model to larger clouds. Moreover, as the number of bubbles grow, reduced order models with bubble-bubble interaction terms are notorious for their stiffness attributed to the large separation of time scales during the collective collapse. Improving the time to solution with the help of a data-driven model could render considerably cheaper model evaluation.

Turbulent flow and cavitation

In closing, the majority of flow configurations discussed in this thesis were simulated with inviscid fluids. In real flows, however, turbulence is ubiquitous and natural next steps that build on the present work is the combination of turbulent flow with cavitating bubbles. Accurate numerical methods for compressible turbulence with shock interactions are challenging because of contradicting numerical methods used in discontinuous hyperbolic flow regions and turbulent flow regions, characterized by parabolic smooth solutions (N. Adams et al., 1996; Johnsen, Larsson, et al., 2010; Larsson et al., 2013). The computational framework developed in this thesis, nevertheless, now offers improved flexibility to address both the challenging algorithmic requirements and HPC needs of turbulent flow with cavitation.

A

GRID CONVERGENCE STUDY

It is not routine practice in the multi-phase flow community to perform grid convergence studies, especially for multi-dimensional problems (Saurel and Pantano, 2018). To alleviate this issue and to prove convergence of the results presented in chapter 7, a grid refinement study for the macroscopic and microscopic scales involved in the collapse of gas bubble clouds is presented in this appendix.

The simulation setup for the resolution assessment is based on the scaling laws given in equations 2.16 and 2.17. The laws are given by

$$u^*_{\text{tip}} \sim \frac{R^*}{t^*_B} \sim c^* \frac{1}{\tilde{R}_B} \sqrt{\tilde{p}}, \qquad \text{(2.16 revisited)}$$

$$\dot{R}^*_F \sim \frac{R^*}{t^*_C} \sim c^* \frac{1}{\tilde{R}_C} \sqrt{\frac{\tilde{p}}{(1 - \alpha_C)\alpha_C}}, \qquad \text{(2.17 revisited)}$$

and describe the characteristic velocity on the microscopic and macroscopic scale, respectively. These velocity scales are retained by configuring a bubble cloud with an identical log-normal distribution for the bubble radii as well as preserving the pressure ratio $\tilde{p}$ based on a reference pressure $p = p_\infty$, see section 7.2. Taking into account a reduced computational budget for this convergence study, the cloud radius R_C and gas volume fraction α_C cannot be preserved. Changing these parameters will only affect the macroscopic scales for which convergence is achieved faster, even on coarse grids. For these reasons, a bubble cloud with radius $R_C = 9\,\text{mm}$ and $N_B = 400$ bubbles is used, which yields a gas volume fraction of $\alpha_C = 15.2\,\%$. All

Case	N_B	R_C/mm	$R_{B,\text{avg}}/\text{mm}$	$\alpha_C/\%$	t^*_C/t^*_B
Production run	12 500	45	0.69	4.9	13.9
Grid refinement	400	9	0.64	15.2	4.6

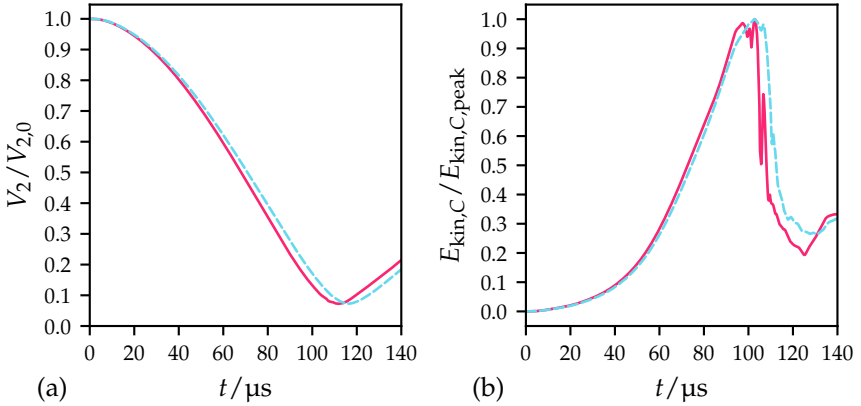TABLE A.1: Overview of altered simulation parameter for the resolution assessment study.

FIGURE A.1: Temporal evolution of macroscopic scales: (a) gas volume $V_2/V_{2,0}$; (b) average kinetic energy $E_{kin,C}/E_{kin,C,peak}$ within the cloud. ———, reduced domain approximation with symmetry boundaries; – – –, full cloud simulation.

other parameters remain unchanged and correspond to their definitions in table 3.1 and section 7.2. Table A.1 shows the simulation parameters that are changed for the resolution assessment. The computational cost is further reduced by a symmetry approximation such that only one octant of the full computational domain is simulated. Symmetry boundary conditions are used for boundaries that intersect the cloud, where the remaining boundary conditions are identical to section 7.2. The center of bubbles that initially intersect one of the symmetry planes has been shifted onto the intersecting plane such that the bubble is initially symmetric with respect to that plane. The cloud in the octant is then extracted from the full cloud. Figure A.1 shows the temporal evolution of the gas volume $V_2/V_{2,0}$ and the average kinetic energy $E_{kin,C}/E_{kin,C,peak}$ within the cloud corresponding to the grid refinement parameter shown in Table A.1. The cloud collapse time for this configuration is $t_C = 115.9\,\mu s$ which corresponds to a 2.97 times faster collapse compared to the time reported in section 7.3. In contrast, equation 2.14 estimates a 3.01 times faster cloud collapse time. Furthermore, figure A.1 shows the result for the simulation using the aforementioned symmetry approximation, which results in a slightly faster cloud collapse time. The difference stems from the mirroring of the random cloud in the octant on the symmetry planes, which does not exactly match the full random cloud in the remaining 7 octants. The resulting relative error in the cloud collapse

Grid		N	$R_{B,\min}/h$	$R_{B,\max}/h$	$t_{M,s}/\mu s$	$t_{M,e}/\mu s$
G_-	(coarse)	448	8	14	42.3	103.6
G_0	(production)	896	16	28	40.3	98.4
G_+	(fine)	1792	33	57	39.9	98.8

TABLE A.2: Grid resolutions used in the refinement study.

time is 3.8 % and does not affect the order of magnitude of the macroscopic time scale. The reduction in computational cost clearly outweighs the small error incurred by this approximation. The microscopic time scale, described by equation 2.12, remains in the same order of magnitude for all clouds presented in the manuscript.

A.1   CONVERGENCE OF MACROSCOPIC QUANTITIES

Three grid resolutions G_-, G_0 and G_+ are used, where G_0 corresponds to the initial bubble resolution described in section 7.2. The resolution on the coarse grid G_- is half of G_0 and the resolution on the fine grid G_+ is twice the resolution of G_0. Table A.2 shows the three grids used for the resolution assessment including the number of cells N along each edge of the octant and the initial number of cells per radius for the smallest and largest bubbles in the cloud. Due to the symmetry assumption, the cloud is centered at the domain origin with domain extents $3R_C \times 3R_C \times 3R_C$ for the x, y and z coordinates, respectively. Figure A.2 compares the temporal evolution of the gas volume $V_2/V_{2,0}$ and the average kinetic energy $E_{\mathrm{kin},C}/E_{\mathrm{kin},C,\mathrm{peak}}$ within the cloud for the three different resolutions. Geometric quantities such as the gas volume already converge on the coarse grid G_-. Only a weak grid dependence is identified during the post collapse of the cloud where small length scales are dominant. Stronger grid dependence is observed for velocity and quantities that depend on it. This dependence is mainly restricted to the region after the minimum cloud volume has been reached due to its sensitivity on numerical diffusion at smaller scales. The analyses presented in this thesis do not depend on data after t_C and, therefore, is not critical. During the cloud collapse we observe convergence for the integral of kinetic energy on grid G_0. The reduced cloud used for this grid refinement study consists of 62 bubbles where 49 bubbles (79 %) satisfy the quality criteria for the microjet evaluation on all three grids, see section 7.4.2. The
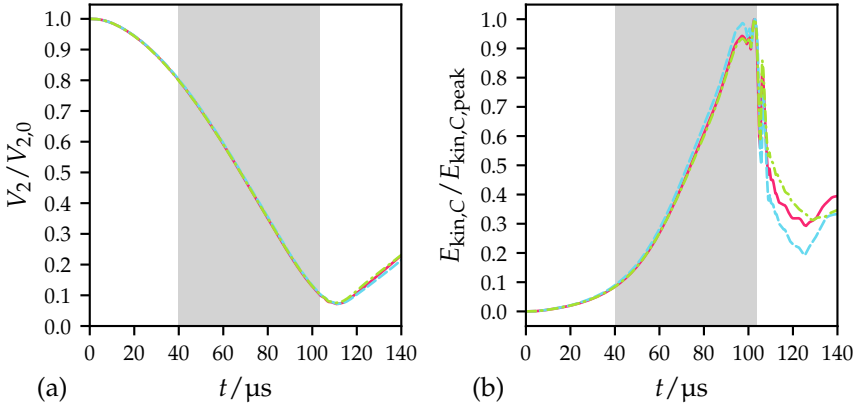
FIGURE A.2: Temporal evolution of macroscopic scales: (a) cloud gas volume $V_2/V_{2,0}$; (b) average kinetic energy $E_{\mathrm{kin},C}/E_{\mathrm{kin},C,\mathrm{peak}}$ within the cloud. – – – –, G_-; ———, G_0; – · – · –, G_+. The gray shaded area corresponds to the time interval of the data shown in figure A.3.

characteristic quantities are evaluated within the time interval $[t_{\mathrm{tip},i}, t_{\mathrm{imp},i}]$ for bubble i. The start and end time that covers the microjet analyses for all bubbles, $t_{M,s}$ and $t_{M,e}$, respectively, are furthermore shown in table A.2 for each grid. Their definition was given in equations 7.20 and 7.21 on page 142. The values associated to those quantities have converged on grid G_0.

A.2 CHARACTERISTIC MICROJET QUANTITIES

Figure A.3 shows the microjet velocity magnitudes and the inclination angles computed on the three different resolutions. The data for G_+ is sorted in increasing order while the data for G_0 and G_- are shown relative to that sort order. The gray shaded region in figure A.2 highlights the interval $[t_{M,s}, t_{M,e}]$ which corresponds to the time range of the displayed data in figure A.3. Table A.3 shows absolute errors relative to the fine grid G_+ for the microjet velocity magnitude $u_{\mathrm{tip},i}$, inclination angle θ_i and the fit range $[t_{\mathrm{tip},i}, t_{\mathrm{imp},i}]$ averaged over all bubbles. The microjet velocity magnitudes on the production grid G_0 are within a $10.0 \pm 5.2\,\%$ error margin relative to the fine grid G_+. The errors reported in table A.3 suggest that only a marginal accuracy improvement can be achieved when doubling the resolution of the production run and does not justify the $16\times$ increase in computational cost that is associated with it in regard to the scope of
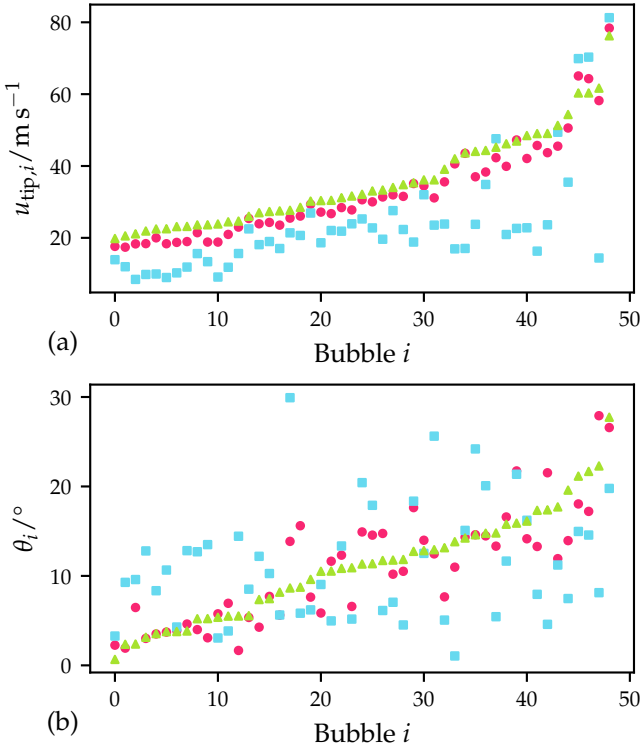
FIGURE A.3: Microscopic quantities of individual bubbles: (a) microjet velocity magnitude $u_{\text{tip},i}$; (b) microjet inclination angle θ_i. ■, G_-; ●, G_0; ▲, G_+. Both quantities clearly indicate convergence towards the finest grid G_+.

the analyses. Moreover, microjet velocity magnitudes are between $10\,\text{m}\,\text{s}^{-1}$ and $60\,\text{m}\,\text{s}^{-1}$, see figures 7.16 and A.3(a). These characteristic velocities relate to the length scale imposed by the mean bubble radius $\bar{R}_B$ defined in equation 7.1 on page 121. Based on these quantities, as well as the kinematic viscosity $\nu = 1.0 \times 10^{-6}\,\text{m}^2\,\text{s}^{-1}$ for water, the Reynolds number is in the expected range of 7000–42000. Similarly, the Weber number is in the range of 972–35000 based on a surface tension coefficient of $0.072\,\text{N}\,\text{m}^{-1}$ for air-water systems. Both of these ranges justify the neglect of viscous and surface tension forces for this study.

Figure A.4 shows the temporal evolution of the normalized bubble radius $R_B/R_{B,0}$ as well as the normalized interface thickness $(d_I - d_{I,0})/d_{I,0}$ for

Grid	$u_{\text{tip},i}/\text{m s}^{-1}$	$\theta_i/°$	$t_{\text{tip},i}/\mu\text{s}$	$t_{\text{imp},i}/\mu\text{s}$	$T_{B,i}/\mu\text{s}$
G_-	13.0 ± 8.6	6.4 ± 4.1	1.7 ± 0.9	11.1 ± 6.4	0.41 ± 0.46
G_0	3.2 ± 1.6	2.4 ± 2.0	1.0 ± 1.1	2.7 ± 1.8	0.24 ± 0.21

TABLE A.3: Absolute error averaged over all bubbles relative to the fine grid G_+.
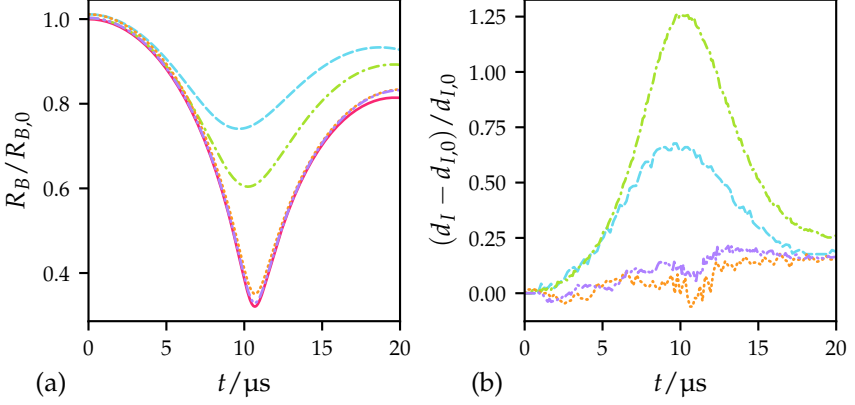
FIGURE A.4: Collapse of a single air bubble in water: (a) bubble radius R_B; (b) interface thickness d_I. ———, reference solution based on Keller et al. (1980); – – – –, $R_{B,0}/h = 12$ (without $K\boldsymbol{\nabla} \cdot \boldsymbol{u}$); –·–·–, $R_{B,0}/h = 25$ (without $K\boldsymbol{\nabla} \cdot \boldsymbol{u}$); ·········, $R_{B,0}/h = 12$; –··–··–, $R_{B,0}/h = 25$.

the collapse of a single air bubble in water at $p_\infty = 10\,\text{bar}$ (Wermelinger, Rasthofer, et al., 2018). The interface thickness is defined by

$$d_I = R_{\theta=0.1} - R_{\theta=0.9} \tag{A.1}$$

based on two equivalent bubble radii. These radii are associated with the 0.1 and 0.9 iso-contours of the gas volume fraction field α_2. The equivalent bubble radius is defined by $R_\theta = h\sqrt[3]{3/(4\pi)\sum_{i=1}^{N}\chi_\theta}$ and uses a shifted phase indicator function χ_θ with threshold value θ, which is given by $\chi_\theta = 1$ if $\alpha_2 > \theta$ and $\chi_\theta = 0$ otherwise. In the definition of R_θ, h denotes the uniform grid spacing and N the number of cells $\mathcal{C}_i$. The validation of the numerical results shown in figure A.4(a) is based on a reference solution proposed by Keller et al. (1980). The numerical results are obtained from equations 3.8 to 3.12 on two grid resolutions that correspond to the resolution of the smallest and largest bubbles in the 12 500 bubble

cloud introduced in section 7.2. Emphasis is given on the influence of the source term $K\nabla \cdot \boldsymbol{u}$ in equation 3.12. Including this term in the model improves the accuracy of the numerical result considerably, even at rather low resolutions. A similar trend is observed in the evolution of the interface thickness in figure A.4(b). The thickness of the interface increases strongly when the bubble reaches its minimum radius for simulations that do not include the $K\nabla \cdot \boldsymbol{u}$ term in the model, while an approximate linear increase of the interface thickness is observed for the case that includes the term. This linear increase can be attributed almost exclusively to numerical diffusion.

A.3 COLLAPSE PERIOD AND BUBBLE PRESSURE

Figure A.5 shows the temporal evolution the equivalent bubble radius, defined in equation 7.17, and average bubble pressure for three selected bubbles. The computation of the average bubble pressure follows the same approach used for the bubble center $x_{B,i}$ in equation 7.16. It is defined by

$$p_{B,i}(t) = \frac{1}{V_{B,i}(t)} \int_{\Omega_{B,i}} \alpha_2 p \, dV, \qquad (A.2)$$

where the bubble volume $V_{B,i}(t)$ is defined in equation 7.18. Data for the three resolutions described in table A.2 is included in each plot. The location of the first and second minimum of the equivalent bubble radius is not sensitive to the grid resolution. This observation is in correspondence with the previous statement regarding convergence of geometric quantities. The bubble collapse period T_B is derived from the equivalent bubble radius and is associated with a $1.8 \pm 1.7\,\%$ error margin on grid G_0 relative to the fine grid G_+. Absolute error values averaged over all bubbles are shown in table A.3. The fluctuating error of the evolving quantities $R_{B,i}(t)$ and $p_{B,i}(t)$ is measured by

$$L_2(y; t_s, t_e) = \sqrt{\frac{1}{t_e - t_s} \int_{t_s}^{t_e} \left| \frac{y - y_+}{y_+} \right|^2 dt}, \qquad (A.3)$$

where $y(t)$ is the subject function and $y_+(t)$ a reference associated with the fine grid G_+. A cubic spline interpolant is used to obtain a representation for y and approximate the integral in equation A.3 with a 4th-order Simpson quadrature. The data for the cubic spline interpolant is sampled at 2.53 MHz. Table A.4 shows error measures based on equation A.3 evaluated for two time intervals $[0, t_{M,e}]$ and $[t_{M,e}, t_C]$ which correspond to

Grid	$R_{B,i}; [0, t_{M,e}]$	$R_{B,i}; [t_{M,e}, t_C]$	$p_{B,i}; [0, t_{M,e}]$	$p_{B,i}; [t_{M,e}, t_C]$
G_-	1.1 ± 0.4	3.3 ± 1.6	4.9 ± 1.6	15.7 ± 10.0
G_0	0.60 ± 0.09	2.8 ± 0.9	2.4 ± 0.5	13.2 ± 5.8

TABLE A.4: L_2 error measures for $R_{B,i}$ and $p_{B,i}$ averaged over all bubbles. The values correspond to the indicated intervals and are expressed in percentages relative to the fine grid G_+.

the interval of microjet analyses and region of peak pressure in the cloud, respectively. Values for $t_{M,e}$ are shown in table A.2. The interval of the microjet evaluation $[t_{M,s}, t_{M,e}]$ and t_C are further highlighted in figure A.5. The equivalent bubble radius $R_{B,i}$ has converged in both regions of interest with a relative error of $2.8 \pm 0.9\,\%$ in the peak pressure region of the cloud, averaged over all bubbles. This is consistent with the error associated to the collapse period T_B reported above. The average bubble pressure $p_{B,i}$ shows similar convergence during the microjet evaluation interval with a relative error of $2.4 \pm 0.5\,\%$ averaged over all bubbles. The measured relative error is $13.2 \pm 5.8\,\%$ during the peak pressure interval in the cloud. Note that the pressure averages discussed in section 7.3.1 propagate through both of these regions of interest and are associated with at most $13.2 \pm 5.8\,\%$ relative error during the final stage of the cloud collapse. This peak error is in the same order as the error measured for the microjet velocity magnitudes but occurs during the second interval of interest, while the error associated with the microjets occurs in the first interval. The magnitude of the point-wise maximum pressure p_{peak}, reported in section 7.3, is determined by the local maximum measure $L_\infty(p_{B,i}; t_{M,e}, t_C) = 38.1 \pm 22.6\,\%$ on grid G_0, averaged over all bubbles. The large local error is mainly due to deviation in local pressure magnitude, not dislocation in time, see figures A.5(d) to A.5(f). This point-wise maximum pressure is only shown here to orient the reader about its appearance in time. The discussions in chapter 7 do not further elaborate on this quantity.
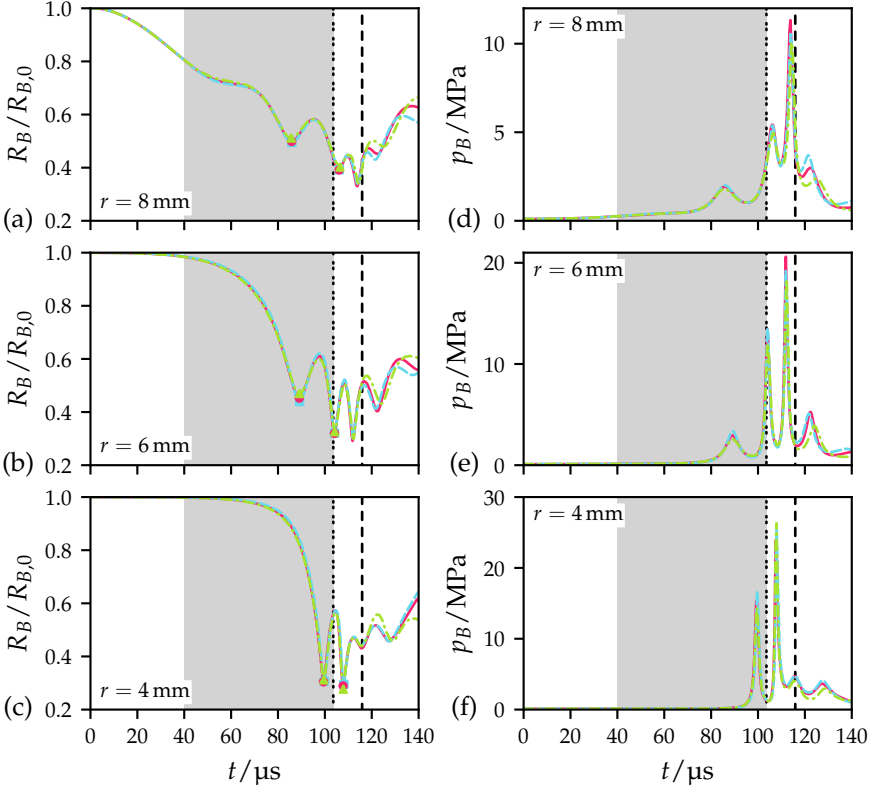
FIGURE A.5: Temporal evolution of selected bubbles at different radial distance r from the cloud center: (a)–(c) equivalent bubble radius $R_B/R_{B,0}$; (d)–(f) average bubble pressure p_B. ┅ ┅ ┅, G_-; ━━━, G_0; ┅·┅·┅, G_+; ·· ·· ·· ··, end of the microjet evaluation interval $t_{M,e}$; ┅ ┅ ┅, time of minimum cloud volume t_C. First and second minimum locations of the equivalent radius are indicated for ■, G_-; ●, G_0; ▲, G_+. The gray shaded area corresponds to the time interval of the data shown in figure A.3.

BIBLIOGRAPHY

Abgrall, R. (1996). "How to prevent pressure oscillations in multicomponent flow calculations: a quasi conservative approach". In: *Journal of Computational Physics* 125.1, 150.

Adams, M., P. Colella, D. T. Graves, J. N. Johnson, N. D. Keen, T. J. Ligocki, D. F. Martin, P. W. McCorquodale, D. Modiano, P. O. Schwartz, T. D. Sternberg, and B. van Straalen (2019). *Chombo Software Package for AMR Applications - Design Document*. Tech. rep. LBNL-6616E. Lawrence Berkeley National Laboratory.

Adams, N. and K. Shariff (1996). "A High-Resolution Hybrid Compact-ENO Scheme for Shock-Turbulence Interaction Problems". In: *Journal of Computational Physics* 127.1, 27.

Adams, N. A. and S. J. Schmidt (2013). "Shocks in Cavitating Flows". In: *Bubble Dynamics and Shock Waves*. Springer Berlin Heidelberg, 235.

Allaire, G., S. Clerc, and S. Kokh (2002). "A five-equation model for the simulation of interfaces between compressible fluids". In: *Journal of Computational Physics* 181.2, 577.

Ando, K., T. Colonius, and C. E. Brennen (2011). "Numerical simulation of shock propagation in a polydisperse bubbly liquid". In: *International Journal of Multiphase Flow* 37.6, 596.

Baer, M. R. and J. W. Nunziato (1986). "A two-phase mixture theory for the deflagration-to-detonation transition (DDT) in reactive granular materials". In: *International journal of multiphase flow* 12.6, 861.

Batchelor, G. K. (1967). *An introduction to fluid dynamics*. Cambridge University Press (CUP).

Batchelor, G. K. (1969). "Compression waves in a suspension of gas bubbles in liquid". In: *Fluid Dynamics Transactions*. Vol. 4. PWN Warszawa, 425.

Batten, P., N. Clarke, C. Lambert, and D. Causon (1997). "On the Choice of Wavespeeds for the HLLC Riemann Solver". In: *SIAM Journal on Scientific Computing* 18.6, 1553.

Benjamin, T. B. and A. T. Ellis (1966). "The Collapse of Cavitation Bubbles and the Pressures thereby Produced against Solid Boundaries". In: *Philosophical Transactions of the Royal Society A: Mathematical, Physical and Engineering Sciences* 260.1110, 221.

Benson, D. J. (1992). "Computational methods in Lagrangian and Eulerian hydrocodes". In: *Computer Methods in Applied Mechanics and Engineering* 99.2-3, 235.

Besant, W. H. (1859). *Hydrostatics and Hydrodynamics*.

Bjerknes, V. (1906). *Fields of force*. Columbia University Press.

Blake, J. R., M. C. Hooton, P. B. Robinson, and R. P. Tong (1997). "Collapsing cavities, toroidal bubbles and jet impact". In: *Philosophical Transactions of the Royal Society of London. Series A: Mathematical, Physical and Engineering Sciences* 355.1724. Ed. by S. D. Howison, J. R. Ockendon, D. H. Peregrine, and D. W. Moore, 537.

Bolotnov, I. A., K. E. Jansen, D. A. Drew, A. A. Oberai, R. T. Lahey, and M. Z. Podowski (2011). "Detached direct numerical simulations of turbulent two-phase bubbly channel flow". In: *International Journal of Multiphase Flow* 37.6, 647.

Brackbill, J. U., D. Kothe, and C. Zemach (1992). "A continuum method for modeling surface tension". In: *Journal of Computational Physics* 100.2, 335.

Brandt, A. (1977). "Multi-level adaptive solutions to boundary-value problems". In: *Mathematics of Computation* 31.138, 333.

Brandvik, T. and G. Pullan (2008). "Acceleration of a 3D Euler Solver Using Commodity Graphics Hardware". In: *46th AIAA Aerospace Sciences Meeting and Exhibit*. American Institute of Aeronautics and Astronautics.

Bremond, N., M. Arora, C.-D. Ohl, and D. Lohse (2006). "Controlled Multi-bubble Surface Cavitation". In: *Physical Review Letters* 96.22.

Brennen, C. E. (2005). *Fundamentals of multiphase flow*. Cambridge University Press.

Brennen, C. E. (2013). *Cavitation and bubble dynamics*. Cambridge University Press (CUP).

Brennen, C. E. (1998). "Cloud Cavitation: Observations, Calculations and Shock Waves". In: *Multiphase Science and Technology* 10.4, 303.

Brennen, C. E. (2002). "Fission of collapsing cavitation bubbles". In: *Journal of Fluid Mechanics* 472.

Brennen, C. E. (2015). "Cavitation in medicine". In: *Interface Focus* 5.5. eprint: http://rsfs.royalsocietypublishing.org/content/5/5/20150022.full.pdf.

Brujan, E., T. Ikeda, K. Yoshinaka, and Y. Matsumoto (2011). "The final stage of the collapse of a cloud of bubbles close to a rigid boundary". In: *Ultrasonics Sonochemistry* 18.1, 59.

Brujan, E.-A., T. Noda, A. Ishigami, T. Ogasawara, and H. Takahira (2018). "Dynamics of laser-induced cavitation bubbles near two perpendicular rigid walls". In: *Journal of Fluid Mechanics* 841, 28.

Brujan, E.-A., H. Takahira, and T. Ogasawara (2019). "Planar jets in collapsing cavitation bubbles". In: *Experimental Thermal and Fluid Science* 101, 48.

Caflisch, R. E., M. J. Miksis, G. C. Papanicolaou, and L. Ting (1985a). "Effective equations for wave propagation in bubbly liquids". In: *Journal of Fluid Mechanics* 153, 259.

Caflisch, R. E., M. J. Miksis, G. C. Papanicolaou, and L. Ting (1985b). "Wave propagation in bubbly liquids at finite volume fraction". In: *Journal of Fluid Mechanics* 160, 1.

Cameron, K., R. Ge, and X. Feng (2005). "High-performance, power-aware distributed computing for scientific applications". In: *Computer* 38.11, 40.

Campbell, I. J. and A. S. Pitcher (1958). "Shock waves in a liquid containing gas bubbles". In: *Proceedings of the Royal Society of London. Series A. Mathematical and Physical Sciences* 243.1235, 534.

Carstensen, E. L. and L. L. Foldy (1947). "Propagation of Sound Through a Liquid Containing Bubbles". In: *The Journal of the Acoustical Society of America* 19.3, 481.

Chahine, G. L. and R. Duraiswami (1992). "Dynamical interactions in a multi-bubble cloud". In: *Journal of Fluids Engineering* 114.4, 680.

Chahine, G. L., C.-T. Hsiao, and R. Raju (2014). "Scaling of Cavitation Bubble Cloud Dynamics on Propellers". In: *Advanced Experimental and Numerical Techniques for Cavitation Erosion Prediction*. Springer Netherlands, 345.

Cocchi, J.-P. and R. Saurel (1997). "A Riemann problem based method for the resolution of compressible multimaterial flows". In: *Journal of Computational Physics* 137.2, 265.

Colella, P. and P. R. Woodward (1984). "The Piecewise Parabolic Method (PPM) for gas-dynamical simulations". In: *Journal of Computational Physics* 54.1, 174.

Coralic, V. and T. Colonius (2014). "Finite-Volume WENO Scheme for Viscous Compressible Multicomponent Flows". In: *Journal of Computational Physics*.

Courant, R., K. Friedrichs, and H. Lewy (1928). "Über die partiellen Differenzengleichungen der mathematischen Physik". In: *Mathematische Annalen* 100.1, 32.

Coussios, C. C. and R. A. Roy (2008). "Applications of Acoustics and Cavitation to Noninvasive Therapy and Drug Delivery". In: *Annual Review of Fluid Mechanics* 40.1, 395.

Crespo, A. (1969). "Sound and Shock Waves in Liquids Containing Bubbles". In: *Physics of Fluids* 12.11, 2274.

Crum, L. A. (1975). "Bjerknes forces on bubbles in a stationary sound field". In: *The Journal of the Acoustical Society of America* 57.6, 1363.

Crum, L. A. and A. I. Eller (1970). "Motion of Bubbles in a Stationary Sound Field". In: *The Journal of the Acoustical Society of America* 48.1B, 181.

d'Agostino, L. and C. E. Brennen (1989). "Linearized dynamics of spherical bubble clouds". In: *Journal of Fluid Mechanics* 199, 155.

Danalis, A., G. Marin, C. McCurdy, J. S. Meredith, P. C. Roth, K. Spafford, V. Tipparaju, and J. S. Vetter (2010). "The Scalable Heterogeneous Computing (SHOC) benchmark suite". In: *Proceedings of the 3rd Workshop on General-Purpose Computation on Graphics Processing Units - GPGPU '10*. ACM Press.

Datta, K., M. Murphy, V. Volkov, S. Williams, J. Carter, L. Oliker, D. Patterson, J. Shalf, and K. Yelick (2008). "Stencil computation optimization and auto-tuning on state-of-the-art multicore architectures". In: *2008 SC - International Conference for High Performance Computing, Networking, Storage and Analysis*. IEEE.

Datta, K., S. Kamil, S. Williams, L. Oliker, J. Shalf, and K. Yelick (2009). "Optimization and Performance Modeling of Stencil Computations on Modern Microprocessors". In: *SIAM Review* 51.1, 129.

Dear, J. P. and J. E. Field (1988). "A study of the collapse of arrays of cavities". In: *Journal of Fluid Mechanics* 190, 409.

Dear, J. P., J. E. Field, and A. J. Walton (1988). "Gas compression and jet formation in cavities collapsed by a shock wave". In: *Nature* 332.6164, 505.

Delale, C. F., S. Nas, and G. Tryggvason (2005). "Direct numerical simulations of shock propagation in bubbly liquids". In: *Physics of Fluids* 17.12, 121705.

Delale, C. F. and G. Tryggvason (2008). "Shock structure in bubbly liquids: comparison of direct numerical simulations and model equations". In: *Shock Waves* 17.6, 433.

Dietrich, C. A., C. E. Scheidegger, J. L. Comba, L. P. Nedel, and C. T. Silva (2009). "Marching Cubes without Skinny Triangles". In: *Computing in Science & Engineering* 11.2, 82.

Doinikov, A. A. (2004). "Mathematical model for collective bubble dynamics in strong ultrasound fields". In: *The Journal of the Acoustical Society of America* 116.2, 821.

Duffy, A. C., D. P. Hammond, and E. J. Nielsen (2012). *Production Level CFD Code Acceleration for Hybrid Many-Core Architectures*. Tech. rep. TM-2012-217770. NASA.

Eddington, R. B. (1967). *Investigation of supersonic shock phenomena in a two-phase (liquid-gas) tunnel*. Tech. rep.

Egerer, C. P., S. Hickel, S. J. Schmidt, and N. A. Adams (2014). "Large-eddy simulation of turbulent cavitating flow in a micro channel". In: *Physics of Fluids* 26.8, 085102.

Egerer, C. P., S. J. Schmidt, S. Hickel, and N. A. Adams (2016). "Efficient implicit LES method for the simulation of turbulent cavitating flows". In: *Journal of Computational Physics* 316, 453.

Einfeldt, B. (1988). "On Godunov-Type Methods for Gas Dynamics". In: *SIAM Journal on Numerical Analysis* 25.2, 294. eprint: `http://epubs.siam.org/doi/pdf/10.1137/0725021`.

Elsen, E., P. LeGresley, and E. Darve (2008). "Large calculation of the flow over a hypersonic vehicle using a GPU". In: *Journal of Computational Physics* 227.24, 10148.

Engquist, B. and A. Majda (1977). "Absorbing boundary conditions for numerical simulation of waves". In: *Proceedings of the National Academy of Sciences* 74.5, 1765.

Escaler, X., E. Egusquiza, M. Farhat, F. Avellan, and M. Coussirat (2006). "Detection of cavitation in hydraulic turbines". In: *Mechanical Systems and Signal Processing* 20.4, 983.

Fedkiw, R. P., T. Aslam, B. Merriman, and S. Osher (1999). "A non-oscillatory Eulerian approach to interfaces in multimaterial flows (the ghost fluid method)". In: *Journal of computational physics* 152.2, 457.

Flynn, H. G. (1975). "Cavitation dynamics. I. A mathematical formulation". In: *The Journal of the Acoustical Society of America* 57.6, 1379.

Foldy, L. L. (1945). "The Multiple Scattering of Waves. I. General Theory of Isotropic Scattering by Randomly Distributed Scatterers". In: *Physical Review* 67.3-4, 107.

Fox, F. E., S. R. Curley, and G. S. Larson (1955). "Phase Velocity and Absorption Measurements in Water Containing Air Bubbles". In: *The Journal of the Acoustical Society of America* 27.3, 534.

Frigo, M., C. Leiserson, H. Prokop, and S. Ramachandran (1999). "Cache-oblivious algorithms". In: *40th Annual Symposium on Foundations of Computer Science (Cat. No.99CB37039)*. IEEE Comput. Soc.

Frigo, M. and V. Strumpen (2005). "Cache oblivious stencil computations". In: *Proceedings of the 19th annual international conference on Supercomputing - ICS '05*. ACM Press.

Fuster, D., C. Dopazo, and G. Hauke (2011). "Liquid compressibility effects during the collapse of a single cavitating bubble". In: *The Journal of the Acoustical Society of America* 129.1, 122.

Fuster, D. and T. Colonius (2011). "Modelling bubble clusters in compressible liquids". In: *Journal of Fluid Mechanics* 688, 352.

Gilmore, F. R. (1952). "The growth or collapse of a spherical bubble in a viscous compressible liquid". Technical Report. Pasadena, CA.

Godunov, S. K. (1959). "Difference method for the numerical computation of discontinuous solutions of equations of hydrodynamics". In: *Mat. Sbornik, N. S.* 47(89).3. English translation, 271.

Gonzalez-Avila, S. R., D. M. Nguyen, S. Arunachalam, E. M. Domingues, H. Mishra, and C.-D. Ohl (2020). "Mitigating cavitation erosion using biomimetic gas-entrapping microtextured surfaces (GEMS)". In: *Science Advances* 6.13, eaax6192.

Gottlieb, S. and C.-W. Shu (1998). "Total variation diminishing Runge-Kutta schemes". In: *Mathematics of Computation of the American Mathematical Society* 67.221, 73.

Gueyffier, D., J. Li, A. Nadim, R. Scardovelli, and S. Zaleski (1999). "Volume-of-Fluid Interface Tracking with Smoothed Surface Stress Methods for Three-Dimensional Flows". In: *Journal of Computational Physics* 152.2, 423.

Günther, F., M. Mehl, M. Pögl, and C. Zenger (2006). "A Cache-Aware Algorithm for PDEs on Hierarchical Data Structures Based on Space-Filling Curves". In: *SIAM Journal on Scientific Computing* 28.5, 1634.

Hadjidoukas, P. E., D. Rossinelli, F. Wermelinger, J. Šukys, U. Rasthofer, C. Conti, B. Hejazialhosseini, and P. Koumoutsakos (2015). "High throughput simulations of two-phase flows on Blue Gene/Q". In: *Parallel Computing: On the Road to Exascale*, 767.

Hadjidoukas, P. E. and F. Wermelinger (2019). *A Parallel Data Compression Framework for Large Scale 3D Scientific Data*. arXiv: 1903.07761 [cs.DC].

Hai, Z. N., R. I. Nigmatulin, and N. S. Khabeev (1982). "Structure of shock waves in a liquid with vapor bubbles". In: *Fluid Dynamics* 17.2, 253.

Hansson, I. and K. A. Mørch (1980). "The dynamics of cavity clusters in ultrasonic (vibratory) cavitation erosion". In: *Journal of Applied Physics* 51.9, 4651.

Haring, R., M. Ohmacht, T. Fox, M. Gschwind, D. Satterfield, K. Sugavanam, P. Coteus, P. Heidelberger, M. Blumrich, R. Wisniewski, A. Gara, G. Chiu, P. Boyle, N. Chist, and C. Kim (2012). "The IBM Blue Gene/Q Compute Chip". In: *IEEE Micro* 32.2, 48.

Harlow, F. and A. Amsden (1971). *Fluid Dynamics*. LANL Monograph Technical Report LA-4700. Los Alamos National Laboratory.

Harten, A. (1983). "High resolution schemes for hyperbolic conservation laws". In: *Journal of computational physics* 49.3, 357.

Harten, A. (1984). "On a Class of High Resolution Total-Variation-Stable Finite-Difference Schemes". In: *SIAM Journal on Numerical Analysis* 21.1, 1.

Harten, A. (1986). "On High-Order Accurate Interpolation for Non-Oscillatory Shock Capturing Schemes". In: *The IMA Volumes in Mathematics and Its Applications*. Springer New York, 71.

Harten, A., B. Engquist, S. Osher, and S. R. Chakravarthy (1987). "Uniformly high order accurate essentially non-oscillatory schemes, III". In: *Journal of computational physics* 71.2, 231.

Harten, A. and J. M. Hyman (1983). "Self adjusting grid methods for one-dimensional hyperbolic conservation laws". In: *Journal of computational Physics* 50.2, 235.

Harten, A. and S. Osher (1987). "Uniformly High-Order Accurate Nonoscillatory Schemes. I". In: *SIAM Journal on Numerical Analysis* 24.2, 279.

Harten, A., P. D. Lax, and B. van Leer (1983). "On upstream differencing and Godunov-type schemes for hyperbolic conservation laws". In: *SIAM review* 25.1, 35.

Hejazialhosseini, B., C. Conti, D. Rossinelli, and P. Koumoutsakos (2013). "High Performance CPU Kernels for Multiphase Compressible Flows". In: *Lecture Notes in Computer Science*. Springer Berlin Heidelberg, 216.

Hejazialhosseini, B., D. Rossinelli, C. Conti, and P. Koumoutsakos (2012). "High throughput software for direct numerical simulations of compressible two-phase flows". In: *2012 International Conference for High Performance Computing, Networking, Storage and Analysis*. IEEE.

Hennessy, J. L. and D. A. Patterson (2017). *Computer Architecture: A Quantitative Approach*. 6th ed. Morgan Kaufmann.

Hilgenfeldt, S., M. P. Brenner, S. Grossmann, and D. Lohse (1998). "Analysis of Rayleigh-Plesset dynamics for sonoluminescing bubbles". In: *Journal of Fluid Dynamics* 365, 171.

Hirsch, C. (1990). *Computational methods for inviscid and viscous flows*. Wiley.

Hirt, C. and B. Nichols (1981). "Volume of fluid (VOF) method for the dynamics of free boundaries". In: *Journal of Computational Physics* 39.1, 201.

Hu, X. and N. Adams (2006). "A multi-phase SPH method for macroscopic and mesoscopic flows". In: *Journal of Computational Physics* 213.2, 844.

Hwu, W.-M., C. Rodrigues, S. Ryoo, and J. Stratton (2009). "Compute Unified Device Architecture Application Suitability". In: *Computing in Science & Engineering* 11.3, 16.

IBM (2018). *C/C++ Compiler Reference for Linux*. SC27-8047-01. IBM.

Ikeda, T., S. Yoshizawa, M. Tosaki, J. S. Allen, S. Takagi, N. Ohta, T. Kitamura, and Y. Matsumoto (2006). "Cloud cavitation control for lithotripsy using high intensity focused ultrasound". In: *Ultrasound in Medicine & Biology* 32.9, 1383.

Ilinskii, Y. A., M. F. Hamilton, and E. A. Zabolotskaya (2007). "Bubble interaction dynamics in Lagrangian and Hamiltonian mechanics". In: *The Journal of the Acoustical Society of America* 121.2, 786.

Ishii, M. and K. Mishima (1984). "Two-fluid model and hydrodynamic constitutive relations". In: *Nuclear Engineering and Design* 82.2-3, 107.

Jacobsen, D., J. Thibault, and I. Senocak (2010). "An MPI-CUDA Implementation for Massively Parallel Incompressible Flow Computations on Multi-GPU Clusters". In: *48th AIAA Aerospace Sciences Meeting Including the New Horizons Forum and Aerospace Exposition*. American Institute of Aeronautics and Astronautics.

Jayaprakash, A., C.-T. Hsiao, and G. Chahine (2012). "Numerical and Experimental Study of the Interaction of a Spark-Generated Bubble and a Vertical Wall". In: *Journal of Fluids Engineering* 134.3.

Jiang, G.-S. and C.-W. Shu (1996). "Efficient implementation of weighted ENO schemes". In: *Journal of computational physics* 126.1, 202.

Johnsen, E. and T. Colonius (2006). "Implementation of WENO schemes in compressible multicomponent flow problems". In: *Journal of Computational Physics* 219.2, 715.

Johnsen, E. and T. Colonius (2009). "Numerical simulations of non-spherical bubble collapse". In: *Journal of fluid mechanics* 629, 231.

Johnsen, E., J. Larsson, A. V. Bhagatwala, W. H. Cabot, P. Moin, B. J. Olson, P. S. Rawat, S. K. Shankar, B. Sjgreen, H. Yee, X. Zhong, and S. K. Lele

(2010). "Assessment of high-resolution methods for numerical simulations of compressible turbulence with shock waves". In: *Journal of Computational Physics* 229.4, 1213.

Kameda, M. and Y. Matsumoto (1995). "Structure of Shock Waves in a Liquid Containing Gas Bubbles". In: *IUTAM Symposium on Waves in Liquid/Gas and Liquid/Vapour Two-Phase Systems*. Springer Netherlands, 117.

Kameda, M. and Y. Matsumoto (1996). "Shock waves in a liquid containing small gas bubbles". In: *Physics of Fluids* 8.2, 322.

Kameda, M., N. Shimaura, F. Higashino, and Y. Matsumoto (1998). "Shock waves in a uniform bubbly flow". In: *Physics of Fluids* 10.10, 2661.

Kamil, S., C. Chan, L. Oliker, J. Shalf, and S. Williams (2010). "An auto-tuning framework for parallel multicore stencil computations". In: *2010 IEEE International Symposium on Parallel & Distributed Processing (IPDPS)*. IEEE.

Kamil, S., K. Datta, S. Williams, L. Oliker, J. Shalf, and K. Yelick (2006). "Implicit and explicit optimizations for stencil computations". In: *Proceedings of the 2006 workshop on Memory system performance and correctness - MSPC '06*. ACM Press.

Kamil, S., P. Husbands, L. Oliker, J. Shalf, and K. Yelick (2005). "Impact of modern memory subsystems on cache optimizations for stencil computations". In: *Proceedings of the 2005 workshop on Memory system performance - MSP '05*. ACM Press.

Kapila, A. K., R. Menikoff, J. B. Bdzil, S. F. Son, and D. S. Stewart (2001). "Two-phase modeling of deflagration-to-detonation transition in granular materials: Reduced equations". In: *Physics of Fluids* 13.10, 3002.

Karnakov, P., S. Litvinov, and P. Koumoutsakos (2020). "A hybrid particle volume-of-fluid method for curvature estimation in multiphase flows". In: *International Journal of Multiphase Flow* 125, 103209.

Karnakov, P., F. Wermelinger, M. Chatzimanolakis, S. Litvinov, and P. Koumoutsakos (2019). "A High Performance Computing Framework for Multiphase, Turbulent Flows on Structured Grids". In: *PASC '19: Proceedings of the Platform for Advanced Scientific Computing Conference*. ACM Press.

Karnakov, P., F. Wermelinger, S. Litvinov, and P. Koumoutsakos (2020). "Aphros: High Performance Software for Multiphase Flows with Large Scale Bubble and Drop Clusters". In: *PASC '20: Proceedings of the Platform for Advanced Scientific Computing Conference*. The conference has been postponed by one year due to COVID-19. ACM Press.

Karni, S. (1994). "Multicomponent flow calculations by a consistent primitive algorithm". In: *Journal of Computational Physics* 112.1, 31.

Karni, S. (1996). "Hybrid multifluid algorithms". In: *SIAM Journal on Scientific Computing* 17.5, 1019.

Karplus, H. B. (1957). "Velocity of Sound in a Liquid Containing Gas Bubbles". In: *The Journal of the Acoustical Society of America* 29.11, 1261.

Katz, J. I. (1999). "Jets from collapsing bubbles". In: *Proceedings of the Royal Society of London. Series A: Mathematical, Physical and Engineering Sciences* 455.1981, 323.

Keller, J. B. and M. Miksis (1980). "Bubble oscillations of large amplitude". In: *The Journal of the Acoustical Society of America* 68.2, 628.

Kim, J., P. Moin, and R. Moser (1987). "Turbulence statistics in fully developed channel flow at low Reynolds number". In: *Journal of Fluid Mechanics* 177, 133.

Kiyama, A., T. Shimazaki, J. M. Gordillo, and Y. Tagawa (2020). *The direction of the microjet produced by the collapse of a cavitation bubble located in between a wall and a free surface*. arXiv: 2012.00867 [physics.flu-dyn].

Kopal, Z. (1961). *Numerical Analysis*. 2nd. John Wiley & Sons.

Koukouvinis, P., M. Gavaises, J. Li, and L. Wang (2016). "Large Eddy Simulation of Diesel injector including cavitation effects and correlation to erosion damage". In: *Fuel* 175, 26.

Kubota, A., H. Kato, and H. Yamaguchi (1992). "A new modelling of cavitating flows: a numerical study of unsteady cavitation on a hydrofoil section". In: *Journal of Fluid Mechanics* 240.1, 59.

Kumar, P. and R. Saini (2010). "Study of cavitation in hydro turbines—A review". In: *Renewable and Sustainable Energy Reviews* 14.1, 374.

Kunz, R. F., D. A. Boger, D. R. Stinebring, T. S. Chyczewski, J. W. Lindau, H. J. Gibeling, S. Venkateswaran, and T. Govindan (2000). "A preconditioned Navier-Stokes method for two-phase flows with application to cavitation prediction". In: *Computers & Fluids* 29.8, 849.

Lamb, H. (1879). *Hydrodynamics*. Cambridge University Press.

Laney, C. B. (1998). *Computational Gas Dynamics*. Cambridge University Press (CUP).

Larsson, J., I. Bermejo-Moreno, and S. K. Lele (2013). "Reynolds- and Mach-number effects in canonical shock-turbulence interaction". In: *Journal of Fluid Mechanics* 717, 293.

Lax, P. and B. Wendroff (1960). "Systems of conservation laws". In: *Communications on Pure and Applied Mathematics* 13.2, 217.

Lee, M. and R. D. Moser (2015). "Direct numerical simulation of turbulent channel flow up to $Re_\tau \approx 5200$". In: *Journal of Fluid Mechanics* 774, 395.

Lee, V. W., P. Hammarlund, R. Singhal, P. Dubey, C. Kim, J. Chhugani, M. Deisher, D. Kim, A. D. Nguyen, N. Satish, M. Smelyanskiy, and S. Chennupaty (2010). "Debunking the 100X GPU vs. CPU myth". In: *Proceedings of the 37th annual international symposium on Computer architecture - ISCA '10*. ACM Press.

Leighton, T. G., A. J. Walton, and M. J. W. Pickworth (1990). "Primary Bjerknes forces". In: *European Journal of Physics* 11.1, 47.

Leopold, C. (2002). "Tight Bounds on Capacity Misses for 3D Stencil Codes". In: *Lecture Notes in Computer Science*. Springer Berlin Heidelberg, 843.

LeVeque, R. J. (2002). *Finite Volume Methods for Hyperbolic Problems*. Cambridge University Press (CUP).

Lim, A. W., S.-W. Liao, and M. S. Lam (2001). "Blocking and array contraction across arbitrarily nested loops using affine partitioning". In: *ACM SIGPLAN Notices* 36.7, 103.

Lindholm, E., J. Nickolls, S. Oberman, and J. Montrym (2008). "NVIDIA Tesla: A unified graphics and computing architecture". In: *IEEE micro* 2, 39.

Linga, G. and T. Flåtten (2019). "A hierarchy of non-equilibrium two-phase flow models". In: *ESAIM: Proceedings and Surveys* 66. Ed. by P. Helluy, J.-M. Hérard, and N. Seguin, 109.

Liu, X.-D., S. Osher, and T. Chan (1994). "Weighted essentially non-oscillatory schemes". In: *Journal of computational physics* 115.1, 200.

Lorensen, W. E. and H. E. Cline (1987). "Marching cubes: A high resolution 3D surface construction algorithm". In: *ACM SIGGRAPH Computer Graphics* 21.4, 163.

Ma, J., C.-T. Hsiao, and G. L. Chahine (2015). "Euler-Lagrange Simulations of Bubble Cloud Dynamics Near a Wall". In: *Journal of Fluids Engineering* 137.4, 041301.

Mallock, A. (1910). "The damping of sound by frothy liquids". In: *Proceedings of the Royal Society of London. Series A, Containing Papers of a Mathematical and Physical Character* 84.572, 391.

Mellen, R. H. (1956). "An Experimental Study of the Collapse of a Spherical Cavity in Water". In: *The Journal of the Acoustical Society of America* 28.3, 447.

Menikoff, R. and B. J. Plohr (1989). "The Riemann problem for fluid flow of real materials". In: *Reviews of modern physics* 61.1, 75.

Merkle, C. L., J. Feng, and P. E. O. Buelow (1998). "Computational modeling of the dynamics of sheet cavitation". In: *Proceedings of 3rd International Symposium on Cavitation*. Ed. by J. M. Michel. Grenoble, France, 307.

Mettin, R., I. Akhatov, U. Parlitz, C. Ohl, and W. Lauterborn (1997). "Bjerknes forces between small cavitation bubbles in a strong acoustic field". In: *Physical review E* 56.3, 2924.

Micikevicius, P. (2009). "3D finite difference computation on GPUs using CUDA". In: *Proceedings of 2nd Workshop on General Purpose Processing on Graphics Processing Units - GPGPU-2*. Association for Computing Machinery (ACM).

Mirjalili, S., C. B. Ivey, and A. Mani (2019). "Comparison between the diffuse interface and volume of fluid methods for simulating two-phase flows". In: *International Journal of Multiphase Flow* 116, 221.

Mitome, H. (2003). "Action of ultrasound on particles and cavitation bubbles". In: *Proceedings of the World Congress on Ultrasonics*, 1231.

Mitroglou, N., V. Stamboliyski, I. Karathanassis, K. Nikas, and M. Gavaises (2017). "Cloud cavitation vortex shedding inside an injector nozzle". In: *Experimental Thermal and Fluid Science* 84, 179.

Molefe, L. and I. R. Peters (2019). "Jet direction in bubble collapse within rectangular and triangular channels". In: *Physical Review E* 100.6.

Monaghan, J. (1985). "Extrapolating B splines for interpolation". In: *Journal of Computational Physics* 60.2, 253.

Mørch, K. A. (1980). "On the Collapse of Cavity Clusters in Flow Cavitation". In: *Cavitation and Inhomogeneities in Underwater Acoustics*. Springer Berlin Heidelberg, 95.

Mørch, K. A. (1989). "On cavity cluster formation in a focused acoustic field". In: *Journal of Fluid Mechanics* 201.-1, 57.

Morton, G. (1966). *A computer oriented geodetic data base and a new technique in file sequencing*. Tech. rep. IBM Ltd.

Murrone, A. and H. Guillard (2005). "A five equation reduced model for compressible two phase flow problems". In: *Journal of Computational Physics* 202.2, 664.

Nickolls, J., I. Buck, M. Garland, and K. Skadron (2008). "Scalable parallel programming with CUDA". In: *ACM SIGGRAPH 2008 classes on - SIGGRAPH '08*. ACM Press.

Noordzij, L. (1973a). "Shock waves in bubble-liquid mixtures". In: *IUTAM Symposium on Non-steady Flow of Water at High Speeds*. Ed. by L. I. Sedov and G. Y. Stepanov. Nauka Moscow.

Noordzij, L. and L. van Wijngaarden (1974). "Relaxation effects, caused by relative motion, on shock waves in gas-bubble/liquid mixtures". In: *Journal of Fluid Mechanics* 66.01, 115.

Noordzij, L. (1973b). "Shock waves in mixtures of liquids and air bubbles". PhD thesis. University of Twente.

Nvidia (2020). *CUDA C Programming Guide*. PG-02829-001 v11.1. Nvidia.

Obreschkow, D., M. Tinguely, N. Dorsaz, P. Kobel, A. de Bosset, and M. Farhat (2011). "Universal Scaling Law for Jets of Collapsing Bubbles". In: *Physical Review Letters* 107.20.

Obreschkow, D., M. Tinguely, N. Dorsaz, P. Kobel, A. de Bosset, and M. Farhat (2013). "The quest for the most spherical bubble: experimental setup and data overview". In: *Experiments in Fluids* 54.4.

Oliker, L., A. Canning, J. Carter, J. Shalf, D. Skinner, E. Ethier, R. Biswas, J. Djomehri, and R. van der Wijngaart (2003). "Evaluation of Cache-based Superscalar and Cacheless Vector Architectures for Scientific Computations". In: *Proceedings of the 2003 ACM/IEEE conference on Supercomputing - SC '03*. ACM Press.

Onuki, H., Y. Oi, and Y. Tagawa (2018). "Microjet Generator for Highly Viscous Fluids". In: *Physical Review Applied* 9.1.

Örley, F., T. Trummler, S. Hickel, M. Mihatsch, S. Schmidt, and N. Adams (2015). "Large-eddy simulation of cavitating nozzle flow and primary jet break-up". In: *Physics of Fluids* 27.8, 086101.

Osher, S. and R. P. Fedkiw (2001). "Level Set Methods: An Overview and Some Recent Results". In: *Journal of Computational Physics* 169.2, 463.

Osher, S. and J. A. Sethian (1988). "Fronts propagating with curvature-dependent speed: Algorithms based on Hamilton-Jacobi formulations". In: *Journal of Computational Physics* 79.1, 12.

Parlitz, U., R. Mettin, S. Luther, I. Akhatov, M. Voss, and W. Lauterborn (1999). "Spatio-temporal dynamics of acoustic cavitation bubble clouds". In: *Philosophical Transactions of the Royal Society of London. Series A: Mathematical, Physical and Engineering Sciences* 357.1751. Ed. by J. R. Blake, 313.

Pelekasis, N. A. and J. A. Tsamopoulos (1993). "Bjerknes forces between two bubbles. Part 1. Response to a step change in pressure". In: *Journal of Fluid Mechanics* 254.-1, 467.

Peng, G., G. Tryggvason, and S. Shimizu (2015). "Two-dimensional direct numerical simulation of bubble cloud cavitation by front-tracking method". In: *IOP Conference Series: Materials Science and Engineering* 72.1, 012001.

Perigaud, G. and R. Saurel (2005). "A compressible flow model with capillary effects". In: *Journal of Computational Physics* 209.1, 139.

Pharr, M. and W. R. Mark (2012). "ispc: A SPMD compiler for high-performance CPU programming". In: *Innovative Parallel Computing (InPar)*. IEEE.

Picone, J. M. and J. P. Boris (1988). "Vorticity generation by shock propagation through bubbles in a gas". In: *Journal of Fluid Mechanics* 189, 23.

Plesset, M. S. and R. B. Chapman (1971). "Collapse of an initially spherical vapour cavity in the neighbourhood of a solid boundary". In: *Journal of Fluid Mechanics* 47.02, 283.

Plesset, M. S. and A. Prosperetti (1977). "Bubble dynamics and cavitation". In: *Annual Review of Fluid Mechanics* 9.1, 145.

Plesset, M. S. (1949). "The dynamics of cavitation bubbles". In: *Journal of Applied Mechanics* 16, 277.

Poinsot, T. J. and S. K. Lele (1992). "Boundary conditions for direct simulations of compressible viscous flows". In: *Journal of computational physics* 101.1, 104.

Pope, S. B. (2000). *Turbulent flows*. 1st ed. Cambridge University Press.

Prosperetti, A. and A. Lezzi (1986). "Bubble dynamics in a compressible liquid. Part 1. First-order theory". In: *Journal of Fluid Mechanics* 168.-1, 457.

Prosperetti, A. (1981). "Motion of two superposed viscous fluids". In: *Physics of Fluids* 24.7, 1217.

Quirk, J. J. and S. Karni (1996). "On the dynamics of a shock-bubble interaction". In: *Journal of Fluid Mechanics* 318, 129.

Rasthofer, U., F. Wermelinger, P. E. Hadjidoukas, and P. Koumoutsakos (2017). "Large Scale Simulation of Cloud Cavitation Collapse". In: *Procedia Comput. Sci.* 108, 1763.

Rasthofer, U., F. Wermelinger, P. Karnakov, J. Šukys, and P. Koumoutsakos (2019). "Computational study of the collapse of a cloud with 12500 gas bubbles in a liquid". In: *Phys. Rev. Fluids* 4 (6), 063602.

Rayleigh, L. (1917). "On the pressure developed in a liquid during the collapse of a spherical cavity". In: *Philosophical Magazine Series 6* 34.200, 94.

Reisman, G. E., Y.-C. Wang, and C. E. Brennen (1998). "Observations of shock waves in cloud cavitation". In: *Journal of Fluid Mechanics* 355, 255.

Rivera, G. and C.-W. Tseng (2000). "Tiling Optimizations for 3D Scientific Computations". In: *ACM/IEEE SC 2000 Conference (SC '00)*. IEEE.

Roe, P. L. (1981). "Approximate Riemann solvers, parameter vectors, and difference schemes". In: *Journal of computational physics* 43.2, 357.

Rossinelli, D., B. Hejazialhosseini, P. Hadjidoukas, C. Bekas, A. Curioni, A. Bertsch, S. Futral, S. J. Schmidt, N. A. Adams, and P. Koumoutsakos (2013). "11 PFLOP/s Simulations of Cloud Cavitation Collapse". In: *Proceedings of the International Conference on High Performance Computing, Networking, Storage and Analysis*. ACM, 3:1.

Rudy, D. H. and J. C. Strikwerda (1980). "A nonreflecting outflow boundary condition for subsonic Navier-Stokes calculations". In: *Journal of Computational Physics* 36.1, 55.

Saurel, R. and R. Abgrall (1999a). "A multiphase Godunov method for compressible multifluid and multiphase flows". In: *Journal of Computational Physics* 150.2, 425.

Saurel, R. and R. Abgrall (1999b). "A simple method for compressible multifluid flows". In: *SIAM Journal on Scientific Computing* 21.3, 1115.

Saurel, R., P. Cocchi, and P. B. Butler (1999). "Numerical study of cavitation in the wake of a hypervelocity underwater projectile". In: *Journal of Propulsion and power* 15.4, 513.

Saurel, R., S. Gavrilyuk, and F. Renaud (2003). "A multiphase model with internal degrees of freedom: application to shock–bubble interaction". In: *Journal of Fluid Mechanics* 495, 283.

Saurel, R., O. Le Metayer, J. Massoni, and S. Gavrilyuk (2007). "Shock jump relations for multiphase mixtures with stiff mechanical relaxation". In: *Shock Waves* 16.3, 209.

Saurel, R. and C. Pantano (2018). "Diffuse-Interface Capturing Methods for Compressible Two-Phase Flows". In: *Annual Review of Fluid Mechanics* 50.1, 105.

Saurel, R., F. Petitpas, and R. A. Berry (2009). "Simple and efficient relaxation methods for interfaces separating compressible fluids, cavitating flows and shocks in multiphase mixtures". In: *Journal of Computational Physics* 228.5, 1678.

Schmidmayer, K., S. H. Bryngelson, and T. Colonius (2020). "An assessment of multicomponent flow models and interface capturing schemes for spherical bubble dynamics". In: *Journal of Computational Physics* 402, 109080.

Schmidmayer, K., F. Petitpas, E. Daniel, N. Favrie, and S. Gavrilyuk (2017). "A model and numerical method for compressible flows with capillary effects". In: *Journal of Computational Physics*.

Schnerr, G. H., I. H. Sezal, and S. J. Schmidt (2008). "Numerical investigation of three-dimensional cloud cavitation with special emphasis on collapse induced shock dynamics". In: *Physics of Fluids* 20.4, 040703.

Senocak, I. and W. Shyy (2002). "A Pressure-Based Method for Turbulent Cavitating Flow Computations". In: *Journal of Computational Physics* 176.2, 363.

Seo, J. H., S. K. Lele, and G. Tryggvason (2010). "Investigation and modeling of bubble-bubble interaction effect in homogeneous bubbly flows". In: *Physics of Fluids* 22.6, 063302.

Shu, C.-W. (1988). "Total-Variation-Diminishing Time Discretizations". In: *SIAM Journal on Scientific and Statistical Computing* 9.6, 1073.

Shu, C.-W. and S. Osher (1988). "Efficient implementation of essentially non-oscillatory shock-capturing schemes". In: *Journal of Computational Physics* 77.2, 439.

Shu, C.-W. and S. Osher (1989). "Efficient implementation of essentially non-oscillatory shock-capturing schemes, II". In: *Journal of Computational Physics* 83.1, 32.

Shyue, K.-M. (1998). "An efficient shock-capturing algorithm for compressible multicomponent problems". In: *Journal of Computational Physics* 142.1, 208.

Silberman, E. (1957). "Sound Velocity and Attenuation in Bubbly Mixtures Measured in Standing Wave Tubes". In: *The Journal of the Acoustical Society of America* 29.8, 925.

Singhal, A. K., M. M. Athavale, H. Li, and Y. Jiang (2002). "Mathematical basis and validation of the full cavitation model". In: *Journal of fluids engineering* 124.3, 617.

Soto, Á. M., T. Maddalena, A. Fraters, D. van der Meer, and D. Lohse (2018). "Coalescence of diffusively growing gas bubbles". In: *Journal of Fluid Mechanics* 846, 143.

Stricker, L., B. Dollet, D. F. Rivas, and D. Lohse (2013). "Interacting bubble clouds and their sonochemical production". In: *The Journal of the Acoustical Society of America* 134.3, 1854.

Šukys, J., U. Rasthofer, F. Wermelinger, P. E. Hadjidoukas, and P. Koumoutsakos (2018). "Multilevel Control Variates for Uncertainty Quantification in Simulations of Cloud Cavitation". In: *SIAM J. Sci. Comput.* 40.5, B1361.

Supponen, O., D. Obreschkow, M. Tinguely, P. Kobel, N. Dorsaz, and M. Farhat (2016). "Scaling laws for jets of single cavitation bubbles". In: *J. Fluid Mech.* 802, 263.

Sussman, M., P. Smereka, and S. Osher (1994). "A Level Set Approach for Computing Solutions to Incompressible Two-Phase Flow". In: *Journal of Computational Physics* 114.1, 146.

Tagawa, Y. and I. R. Peters (2018). "Bubble collapse and jet formation in corner geometries". In: *Physical Review Fluids* 3.8.

Thibault, J. and I. Senocak (2009). "CUDA Implementation of a Navier-Stokes Solver on Multi-GPU Desktop Platforms for Incompressible Flows". In: *47th AIAA Aerospace Sciences Meeting including The New Horizons Forum and Aerospace Exposition*. American Institute of Aeronautics and Astronautics.

Thompson, K. W. (1987). "Time dependent boundary conditions for hyperbolic systems". In: *Journal of computational physics* 68.1, 1.

Thompson, K. W. (1990). "Time-dependent boundary conditions for hyperbolic systems, II". In: *Journal of Computational Physics* 89.2, 439.

Thoroddsen, S. T., K. Takehara, and T. G. Etoh (2005). "The coalescence speed of a pendent and a sessile drop". In: *Journal of Fluid Mechanics* 527, 85.

Tiwari, A., C. Pantano, and J. Freund (2015). "Growth-and-collapse dynamics of small bubble clusters near a wall". In: *Journal of Fluid Mechanics* 775, 1.

Toro, E. F. (2009). *Riemann Solvers and Numerical Methods for Fluid Dynamics: A Practical Introduction*. 3rd. Springer.

Toro, E. F., M. Spruce, and W. Speares (1994). "Restoration of the contact surface in the HLL-Riemann solver". In: *Shock Waves* 4.1, 25.

Treibig, J., G. Wellein, and G. Hager (2011). "Efficient multicore-aware parallelization strategies for iterative stencil computations". In: *Journal of Computational Science* 2.2, 130.

Trilling, L. (1952). "The collapse and rebound of a gas bubble". In: *Journal of Applied Physics* 23.1, 14.

Tryggvason, G. and S. Dabiri (2013). "Direct Numerical Simulation of Shock Propagation in Bubbly Liquids". In: *Bubble Dynamics and Shock Waves*. Springer Berlin Heidelberg, 177.

Van Leer, B. (1979). "Towards the ultimate conservative difference scheme. V. A second-order sequel to Godunov's method". In: *Journal of Computational Physics* 32.1, 101.

Van Rees, W. M., A. Leonard, D. Pullin, and P. Koumoutsakos (2011). "A comparison of vortex and pseudo-spectral methods for the simulation of periodic vortical flows at high Reynolds numbers". In: *Journal of Computational Physics* 230.8, 2794.

Van Straalen, B., J. Shalf, T. Ligocki, N. Keen, and W.-S. Yang (2009). "Scalability challenges for massively parallel AMR applications". In: *2009 IEEE International Symposium on Parallel & Distributed Processing*. IEEE.

Van Wijngaarden, L. (1968). "On the equations of motion for mixtures of liquid and gas bubbles". In: *Journal of Fluid Mechanics* 33.3, 465.

Van Wijngaarden, L. (1970). "On the structure of shock waves in liquid-bubble mixtures". In: *Applied Scientific Research* 22.1, 366.

Van Wijngaarden, L. (1972a). "One-Dimensional Flow of Liquids Containing Small Gas Bubbles". In: *Annual Review of Fluid Mechanics* 4.1, 369.

Van Wijngaarden, L. (1972b). "Propagation of shock waves in bubble-liquid mixtures". In: *Proceedings of the International Symposium on Two-Phase Systems*. Elsevier, 637.

Verma, S., G. Novati, and P. Koumoutsakos (2018). "Efficient collective swimming by harnessing vortices through deep reinforcement learning". In: *Proceedings of the National Academy of Sciences* 115.23, 5849.

Volkov, V. (2010). "Better performance at lower occupancy". In: *Proceedings of the GPU technology conference, GTC*. Vol. 10, 16.

Wang, Y.-C. and C. E. Brennen (1999). "Numerical computation of shock waves in a spherical cloud of cavitation bubbles". In: *Journal of fluids engineering* 121.4, 872.

Watanabe, M. and A. Prosperetti (1994). "Shock waves in dilute bubbly liquids". In: *Journal of Fluid Mechanics* 274, 349.

Wellein, G., G. Hager, T. Zeiser, M. Wittmann, and H. Fehske (2009). "Efficient Temporal Blocking for Stencil Computations by Multicore-Aware Wavefront Parallelization". In: *2009 33rd Annual IEEE International Computer Software and Applications Conference*. IEEE.

Wermelinger, F., U. Rasthofer, P. E. Hadjidoukas, and P. Koumoutsakos (2018). "Petascale simulations of compressible flows with interfaces". In: *J. Comput. Sci.* 26, 217.

Wermelinger, F., B. Hejazialhosseini, P. E. Hadjidoukas, D. Rossinelli, and P. Koumoutsakos (2016). "An Efficient Compressible Multicomponent Flow Solver for Heterogeneous CPU/GPU Architectures". In: *PASC '16: Proceedings of the Platform for Advanced Scientific Computing Conference*. ACM Press, 8:1.

Williams, S., J. Shalf, L. Oliker, S. Kamil, P. Husbands, and K. Yelick (2007). "Scientific Computing Kernels on the Cell Processor". In: *International Journal of Parallel Programming* 35.3, 263.

Williams, S., A. Waterman, and D. Patterson (2009). "Roofline: An Insightful Visual Performance Model for Multicore Architectures". In: *Commun. ACM* 52.4, 65.

Williamson, J. H. (1980). "Low-storage Runge-Kutta schemes". In: *Journal of Computational Physics* 35.1, 48.

Wilson, P. S. and R. A. Roy (2008). "An audible demonstration of the speed of sound in bubbly liquids". In: *American Journal of Physics* 76.10, 975.

Wood, A. B. (1930). *A textbook of sound*. G. Bell & Sons Ltd.

Xu, Z., M. Raghavan, T. Hall, M.-A. Mycek, J. Fowlkes, and C. Cain (2008). "Evolution of bubble clouds induced by pulsed cavitational ultrasound therapy - Histotripsy". In: *IEEE Transactions on Ultrasonics, Ferroelectrics and Frequency Control* 55.5, 1122.

Yamamoto, K. (2016). "Investigation of Bubble Clouds in a Cavitating Jet". In: *Mathematical Fluid Dynamics, Present and Future*. Springer Nature, 349.

Yasui, K., Y. Iida, T. Tuziuti, T. Kozuka, and A. Towata (2008). "Strongly interacting bubbles under an ultrasonic horn". In: *Physical Review E* 77.1.

Youngs, D. L. (1982). "Time-dependent multi-material flow with large fluid distortion". In: ed. by K. W. Morton and M. J. Baines. Academic Press.

Zeravcic, Z., D. Lohse, and W. van Saarloos (2011). "Collective oscillations in bubble clouds". In: *Journal of Fluid mechanics* 680, 114.

Zhang, D. Z. and A. Prosperetti (1994). "Ensemble phase-averaged equations for bubbly flows". In: *Physics of Fluids* 6.9, 2956.

Zhang, W., A. Almgren, V. Beckner, J. Bell, J. Blaschke, C. Chan, M. Day, B. Friesen, K. Gott, D. Graves, M. Katz, A. Myers, T. Nguyen, A. Nonaka, M. Rosso, S. Williams, and M. Zingale (2019). "AMReX: a framework for block-structured adaptive mesh refinement". In: *Journal of Open Source Software* 4.37, 1370.

Zhao, T., P. Basu, S. Williams, M. Hall, and H. Johansen (2019). "Exploiting reuse and vectorization in blocked stencil computations on CPUs and GPUs". In: *Proceedings of the International Conference for High Performance Computing, Networking, Storage and Analysis*. ACM.

PUBLICATIONS

Hadjidoukas, P. E., D. Rossinelli, F. Wermelinger, J. Šukys, U. Rasthofer, C. Conti, B. Hejazialhosseini, and P. Koumoutsakos (2015). "High throughput simulations of two-phase flows on Blue Gene/Q". In: *Parallel Computing: On the Road to Exascale*, 767.

Wermelinger, F., B. Hejazialhosseini, P. E. Hadjidoukas, D. Rossinelli, and P. Koumoutsakos (2016). "An Efficient Compressible Multicomponent Flow Solver for Heterogeneous CPU/GPU Architectures". In: *PASC '16: Proceedings of the Platform for Advanced Scientific Computing Conference*. ACM Press, 8:1.

Rasthofer, U., F. Wermelinger, P. E. Hadjidoukas, and P. Koumoutsakos (2017). "Large Scale Simulation of Cloud Cavitation Collapse". In: *Procedia Comput. Sci.* 108, 1763.

Šukys, J., U. Rasthofer, F. Wermelinger, P. E. Hadjidoukas, and P. Koumoutsakos (2018). "Multilevel Control Variates for Uncertainty Quantification in Simulations of Cloud Cavitation". In: *SIAM J. Sci. Comput.* 40.5, B1361.

Wermelinger, F., U. Rasthofer, P. E. Hadjidoukas, and P. Koumoutsakos (2018). "Petascale simulations of compressible flows with interfaces". In: *J. Comput. Sci.* 26, 217.

Hadjidoukas, P. E. and F. Wermelinger (2019). *A Parallel Data Compression Framework for Large Scale 3D Scientific Data*. arXiv: `1903.07761 [cs.DC]`.

Karnakov, P., F. Wermelinger, M. Chatzimanolakis, S. Litvinov, and P. Koumoutsakos (2019). "A High Performance Computing Framework for Multiphase, Turbulent Flows on Structured Grids". In: *PASC '19: Proceedings of the Platform for Advanced Scientific Computing Conference*. ACM Press.

Rasthofer, U., F. Wermelinger, P. Karnakov, J. Šukys, and P. Koumoutsakos (2019). "Computational study of the collapse of a cloud with 12500 gas bubbles in a liquid". In: *Phys. Rev. Fluids* 4 (6), 063602.

Karnakov, P., G. Arampatzis, I. Kičić, F. Wermelinger, D. Wälchli, C. Papadimitriou, and P. Koumoutsakos (2020). "Data-driven inference of the reproduction number for COVID-19 before and after interventions for 51 European countries". In: *Swiss Med. Wkly.*

Karnakov, P., F. Wermelinger, S. Litvinov, and P. Koumoutsakos (2020). "Aphros: High Performance Software for Multiphase Flows with Large Scale Bubble and Drop Clusters". In: *PASC '20: Proceedings of the Platform for Advanced Scientific Computing Conference*. The conference has been postponed by one year due to COVID-19. ACM Press.